PNNL-11899
UC-400
UC-721

Pacific Northwest National Laboratory

Operated by Battelle for the U.S. Department of Energy

Science to Support DOE Site Cleanup: The Pacific Northwest National Laboratory Environmental Management Science Program Awards

Fiscal Year 1998 Mid-Year Progress Report

May 1998

Prepared for the U.S. Department of Energy under Contract DE-AC06-76RLO 1830

PNNL-11899

DISCLAIMER

PACIFIC NORTHWEST NATIONAL LABORATORY
operated by
BATTELLE
for the
UNITED STATES DEPARTMENT OF ENERGY
under Contract DE-AC06-76RLO 1830

Printed in the United States of America

Available to DOE and DOE contractors from the Office of Scientific and Technical Information, P.O. Box 62, Oak Ridge, TN 37831; prices available from (615) 576-8401.

Available to the public from the National Technical Information Service, U.S. Department of Commerce, 5285 Port Royal Rd., Springfield, VA 22161

This document was printed on recycled paper.
(9/97)

DISCLAIMER

PNNL-11899
UC-400
UC-721

Science to Support DOE Site Cleanup: The Pacific Northwest National Laboratory Environmental Management Science Program Awards

Fiscal Year 1998 Mid-Year Progress Report

May 1998

Prepared for
the U.S. Department of Energy
under Contract DE-AC06-76RLO 1830

Pacific Northwest National Laboratory
Richland, Washington 99352

Summary

Pacific Northwest National Laboratory
June 1, 1998

Pacific Northwest National Laboratory was awarded ten (10) Environmental Management Science Program (EMSP) research grants in Fiscal Year 1996 and six (6) in Fiscal Year 1997.[a] This section summarizes how each grant addresses significant U.S. Department of Energy (DOE) cleanup issues, including those at the Hanford Site. The technical progress made to date in each of these research projects is addressed in more detail in the individual progress reports contained in this document.

This research is focused primarily in four areas: Tank Waste Remediation, Spent Nuclear Fuel and Nuclear Materials, Soil and Groundwater Cleanup, and Health Effects.

Tank Waste Remediation

Over 300 underground storage tanks containing about 350,000 cubic meters (92 million gallons) of mixed chemical and radioactive waste are located at the Hanford Site (Washington), Oak Ridge Reservation (Tennessee), Savannah River Site (South Carolina), Idaho National Engineering and Environmental Laboratory (Idaho), and West Valley Site (New York). The liquids, sludges, saltcake, and calcined solids (at Idaho) in these tanks contain about 70% (720 million curies) of the man-made radioactivity existing in the DOE complex. Remediation of this tank waste is one of the most technically complex, scientifically challenging, and potentially expensive problems facing DOE.

Hanford has 60% of the waste volume and 30% of the radioactivity for all DOE high-level waste tanks. At Hanford there are 177 underground storage tanks containing 210,000 cubic meters (54 million gallons) of high-level waste. The current baseline approach to remediating this tank waste is to retrieve the waste and then separate the solids from the liquid. Once cesium (Cs), strontium (Sr), and other radionuclides are removed from the liquid, it will become a relatively low-activity stream that can be immobilized as low-level radioactive and chemical waste. The solid, high-activity stream will be pretreated to reduce its volume (mainly through

(a) PNNL researchers are the lead principal investigators in these sixteen projects. PNNL also collaborates with researchers at other institutions on 21 other EMSP projects. However, this document does not include the annual reports for those collaborations, which are submitted through the lead institutions.

the removal of nonradioactive inorganic components such as chromium, phosphorous, and aluminum) and then immobilized as high-level radioactive waste.

Even safe storage of the waste in the tanks gives rise to technical issues. Chemical reactions in the tanks, including reactions caused by radiation and by the slow corrosion of the steel tank walls, produce gases in the waste such as hydrogen, nitrogen, nitrous oxide, ammonia, and methane. Many of these gases are flammable, toxic, or both. In addition to generating gases, the reactions degrade organic compounds in the waste, change organic fuel and oxidant concentrations, and alter the surface chemistry of insoluble colloids, influencing sedimentation and gas/solid interactions. The EMSP project **Interfacial Radiolysis Effects in Tank Waste Speciation** (page 1.1) is focused on understanding the radiolytic processes in these mixed-phase systems to determine the radiation-induced physical and chemical changes occurring in the wastes.

Most of the tanks have a layer of solids that can trap bubbles of generated gas. If too many bubbles become lodged in the solids layer it becomes buoyant, and the entire layer or pieces of it may rise to the surface and suddenly release the trapped gas. Other processes that disturb the waste may also release gas. Very large releases have the potential to create a flammable atmosphere in the headspace of a tank that, if ignited, could rupture the tank or filters in the ventilation system that control radionuclides. Determining the amount of retained gas in the tanks is therefore a critical component of evaluating the safety hazard of the tanks.

Periodic, direct measurements of the gas volume in each tank would be very expensive and, in some cases, impossible. However, previous work has established that the waste level responds to barometric pressure changes, leading to a method for estimating the volume of retained gas. Interactions between the gas bubbles and the rheologically complex waste are poorly understood, though, causing inaccuracies in this method. The objective of the EMSP project **Mechanics of Bubbles in Sludges and Slurries** (page 1.15) is to gain a fundamental understanding of these interactions and improve the accuracy of gas volume estimates.

The presence of submicron, colloidal particles in the waste complicates nearly every aspect of waste processing. They make the separation of solid and liquid waste streams difficult by forming colloidal suspensions, which may take months to settle, if at all. These suspensions can also form sediments or gels, clogging pipes and interrupting waste transfer operations.

Colloidal particles can also contaminate the liquid waste, complicating downstream processing. Radionuclides can adsorb to the particles' surfaces and radioactively contaminate the low-level liquid waste stream, forcing it to be treated as high-activity waste, thereby increasing treatment costs. In other cases, the presence of colloidal particles interferes with separations processes by plugging ion exchange columns, causing schedule delays and increased costs.

The EMSP project **Colloidal Agglomerates in Tank Sludge: Impact on Waste Processing** (page 1.31) is conducting experiments to understand and identify the chemical conditions that control the formation and agglomeration of colloidal particles. In this way, the effect that agglomerate structures have on the rheology and sedimentation properties of the waste can be quantified, and methods for manipulating agglomerate structures to optimize tank waste transfer and processing conditions can be developed. It is important to note that the new knowledge and data generated by this project will also be of benefit to the cleanup of K-Basin liquids at Hanford and of the tank wastes at the Oak Ridge Reservation and the Savannah River Site.

The removal of radionuclides to prepare the liquid waste stream for immobilization as low-level waste also presents a series of challenges. Several EMSP projects are investigating innovative approaches in the area of separation processes.

The removal of cesium appears to be straightforward, with ion exchange technologies capable of meeting the performance criteria. In conventional ion exchange processes, the cesium-bearing liquid passes through a reactor packed with a resin or other ion exchange material. The cesium binds to the resin, but not permanently. Once the resin has reached its cesium capacity, the cesium is flushed from the resin with acid and reused. However, this creates a second liquid waste stream that must be processed further (e.g., by incorporating into boro-silicate glass) for long-term storage or disposal.

The EMSP project **New Silicotitanate Waste Forms: Development and Characterization** (page 1.41) is investigating a new strategy for disposing of crystalline silicotitanate (CST) ion exchangers by in situ heat treatment with minimal or no additives to produce an alternate waste form. The CST is the most promising candidate for removal of Cs and Sr from tank wastes; however, it has been identified as a risk to vitrification due to its high level of TiO_2. This EMSP project is characterizing the phase relationships, structures, and thermodynamic and kinetic stabilities of crystalline silicotitanate waste forms and establishing a sound technical basis for understanding key waste form properties, such as melting temperatures and aqueous durability, based on an in-depth understanding of waste form structures and thermochemistry. This approach could significantly reduce the volume and costs associated with waste disposal, minimize the risk of environmental contamination during processing, eliminate problems associated with radiolytic hydrogen generation during short-term storage, and provide DOE with technical alternatives for waste disposal.

In some tanks, there may be a need to remove the lanthanides and actinides (because of their long half-lives of 10^2-10^6 years) and/or Sr, which has been complexed by organic complexing agents present in the waste. Unfortunately, there are few technologies for the selective removal of the *f*-block metals (lanthanides and actinides). The EMSP project **Architectural Design Criteria for *f*-Block Metal Sequestering Agents** (page 1.53) uses computational and experimental methods to optimize ligand architecture for *f*-block metal recognition. By

developing an accurate set of criteria for ligand architecture design, ligand structures can be targeted for synthesis, dramatically reducing the time and cost associated with metal-specific ligand development. This provides cleanup projects with more cost-effective and efficient separations agents that can reduce schedules and save money, especially the costs associated with the regeneration of separations materials and/or the disposal of spent separations materials.

Turning to the issue of Sr, one way to remove complexed Sr is to first destroy the organic complexants. The EMSP project **Ionizing Radiation Induced Catalysis on Metal Oxide Particles** (page 1.69) is developing a novel approach for organic destruction using the redox chemistry resulting from the radiation already present in the tanks. This approach has the advantages of being nonthermal and emission-free. Moreover, it is applicable to any organic-containing waste stream, and it can also make use of the currently unused Cs and Sr capsules at Hanford as radiation sources.

Current strategies for reducing the volume of the solid, high-activity waste stream involve developing methods to selectively dissolve and remove nonradioactive elements such as aluminum, phosphorus, and chromium while retaining the radioactive elements in the sludges. This partitioning is fundamentally dependent upon the chemical speciation of the elements present in the processing solutions. The EMSP project **Chemical Speciation of Strontium, Americium, and Curium in High Level Waste: Predictive Modeling of Phase Partitioning During Tank Processing** (page 1.79) addresses the problem of trivalent actinide (americium/Cs) and Sr speciation and solubility in tank liquids. The resulting data will be used to develop thermodynamic models to predict changes in chemical speciation and solubility as a result of changes in tank processing conditions. In this way, existing processes can be optimized and new processes can be developed.

Once the high-activity stream has been reduced in volume, the remaining waste, with its concentrated radionuclides, will be immobilized. However, interactions between alkali ions (such as sodium) and radionuclides in the immobilized waste that could affect their release rate are not well understood. The impact of internal radiation on the long-term performance of these immobilized forms is also unclear. And, given the time frames involved (ca. 10,000 years) the data will not be gathered from simple experimentation. The EMSP project **Ion Exchange Processes and Mechanisms in Glasses** (page 1.93) investigates ion exchange reactions and kinetics within the glass and relates those kinetics to glass structural properties. The EMSP project **Radiation Effects in Nuclear Waste Materials** (page 1.107) is focused on developing a fundamental understanding of radiation effects in glass and ceramic waste forms. The understanding and associated data from both of these projects will improve models assessing the long-term performance of these waste forms. It is also important to note that these studies will benefit the assessment of waste forms proposed for the immobilization and disposal of plutonium residues and scrap and excess weapons plutonium.

Spent Nuclear Fuel and Nuclear Materials

Another legacy of nuclear weapon production is spent nuclear fuel, plutonium residues, and scrap and excess weapons plutonium. The Department of Energy has 2500 metric tons of spent nuclear fuel (SNF) in water storage across the complex. For example, the Hanford Site K-Basins hold 2100 metric tons of spent fuel, much of it severely corroded. Similar situations exist elsewhere in the DOE complex, especially at Savannah River and Idaho National Engineering and Environmental Laboratory. The DOE plans to remove much of this fuel and seal it in canisters for "dry" interim storage for up to 75 years awaiting permanent disposition. However, chemically-bound water will remain in cracks and bound to surfaces even following proposed drying steps, leading to possible long-term corrosion of the containers and/or fuel rods themselves, radiolytic generation of H_2 and O_2 gas, which could lead to deflagration or detonation, and reactions of pyrophoric uranium hydrides. No thoroughly tested model is currently available to predict fuel behavior during pre-processing, processing, or storage. The EMSP project **Radiolytic and Thermal Process Relevant to Dry Storage of Spent Nuclear Fuels** (page 2.1) is therefore studying the radiolytic reactions, "drying" processes, and corrosion behavior of actual SNF materials and pure and mixed-phase samples. These studies will determine what is omitted from current models: radiolysis of water adsorbed on or in hydrates or hydroxides, thermodynamics of interfacial phases, and kinetics of drying.

Dried and packaged SNF will ultimately be shipped to the federal geologic repository for final disposal, while transuranic materials such as plutonium and uranium will be treated (if necessary), packaged, and shipped to the Waste Isolation Pilot Plant (WIPP) near Carlsbad, New Mexico. The EMSP project **Distribution & Solubility of Radionuclides & Neutron Absorbers in Waste Forms for Disposition of Plutonium Ash & Scraps, Excess Plutonium, and Miscellaneous Spent Nuclear Fuels** (page 2.5) is working to understand the distributions, solubilities, and releases of radionuclides and neutron absorbers in these materials after disposition. The results will provide the underpinning knowledge for developing, evaluating, selecting, and matching waste forms for safe disposal and for developing models of their long-term performance.

Soil and Groundwater Cleanup

Contaminant plumes, contaminated soils, and landfills account for some 4,800 waste sites on DOE property located in 31 states (DOE 1995). Approximately 35 million cubic meters of soil are contaminated with low-level and mixed low-level waste (ORNL 1994). Another 1.2 million cubic meters of soil is contaminated with transuranic and mixed transuranic waste. Landfills of buried waste are estimated to contain 3 million cubic meters of low-level waste. This includes 105,000 cubic meters of retrievably stored transuranic waste. Several hundred square miles of

groundwater are contaminated with a variety of radionuclides and hazardous chemicals in concentrations above drinking water standards and DOE's concentration guidelines.

Nearly 150 square miles of groundwater contamination underlies Hanford. The radioactive and hazardous wastes are dispersed through large volumes of soil and groundwater, making potential treatment by conventional soil excavation and groundwater cleanup technologies ineffective and costly. In addition, some 650,000 metric tons of solid waste is buried at Hanford.

The current baseline approach for treating contaminated groundwaters is to pump out the groundwater, treat it ex situ, and return it to the subsurface ("pump and treat"). For contaminated soils the plan is simple: dig it up and dispose of it in a controlled disposal unit. At Hanford, that unit is the Environmental Restoration Disposal Facility (ERDF).

ERDF, centrally located on the 200 Area plateau, is receiving contaminated soils and solid waste from the 100 Area. Two cells are now operating with a capacity of approximately 1.2 million cubic yards each. The potential exists for eight new cells depending upon future needs. These cells, classified as RCRA (Resource Conservation and Recovery Act) landfills, have a design life of approximately 20–30 years, which may be extended through the use of caps and/or engineered barriers.

While ex situ options may be available and effective over the short term, they are more expensive, labor intensive, and have a greater potential for worker and environmental risk than in situ methods. Consequently, there are many drivers for the development of in situ treatment, monitoring, and characterization solutions.

One class of in situ treatment approaches holding great promise uses biological organisms to effect the cleanup (bioremediation). The EMSP project **Dynamics of Coupled Contaminant and Microbial Transport in Heterogeneous Porous Media** (page 3.1) is providing fundamental data on the attachment/detachment dynamics of anaerobic bacteria in porous media under growth and growth-limiting conditions. The dynamics of attachment/detachment vary with individual bacterial species and are especially important when a contaminant is collectively degraded by bacterial consortia. This understanding of coupled contaminant and bacterial transport in actual subsurface media is critical to the design, evaluation, and success of any bioremediation or biobarrier strategy.

Another critical factor controlling the success of bioremediation efforts is the response of the subsurface microbial community and individual bacteria to the stresses encountered at contaminated sites. These stresses include low nutrient concentrations, low oxygen concentrations, and the presence of pollutants. Defining bacterial responses to these stresses presents an opportunity for improving bioremediation strategies, both with indigenous populations and genetically engineered microbes, and will reduce the cost and time required to achieve cleanup goals.

The EMSP project **Genetic Analysis of Stress Responses in Soil Bacteria for Enhanced Bioremediation of Mixed Contaminants** (page 3.13) is focused on identifying the stress-inducible genes from soil bacteria with unique degradative capabilities. Investigators will then demonstrate how the manipulation and expression of these genes will allow the degradation of trichloroethylene under low-nutrient conditions.

Non-biologically controlled processes can also contribute to the in situ treatment of subsurface contaminants. For example, many of the inorganic and organic contaminants present in the soils and groundwater at Hanford and other DOE sites can be altered, immobilized, or destroyed by reduction and oxidation reactions occurring at mineral surfaces. The EMSP project **Molecular-Level Processes Governing the Interaction of Contaminants with Iron and Manganese Oxides** (page 3.23) is a combined experimental and theoretical study. Researchers will develop a detailed understanding of specific mineral surface (iron and manganese oxides) and contaminant (chromate and chlorinated solvents) reactivities that will substantially improve models of contaminant fate and transport in geologic systems. This work will also help technology developers optimize the manipulation of geochemical reduction and oxidation processes for improved subsurface treatment.

Finally, the rate of migration of radioactive Cs in the subsurface from tank leakage or waste cribs has received considerable attention at Hanford lately. Although it is strongly sorbed by the micaceous fraction of the soil, Cs appears to be moving faster towards the groundwater and, ultimately, the Columbia River than previously thought possible. The EMSP project **Mineral Surface Processes Responsible for the Decreased Retardation (or Enhanced Mobilization) of ^{137}Cs from HLW Tank Discharges** (page 3.43) is investigating the geochemistry of Cs ion adsorption under conditions appropriate to high-level waste tank releases. High sodium concentrations in tank waste are thought to suppress all but the most selective Cs sorption sites on the frayed edges of micaceous particles. The hydroxide and aluminate compounds in high-level waste may alter these sites chemically, leading to faster transport through the soil.

Health Effects

Future land uses, regulatory requirements, stakeholder and tribal concerns, and the potential health impacts from hazardous waste and radionuclide contamination will dictate the acceptable treatment approaches and cleanup levels at Hanford and other DOE sites. Trichloroethylene (TCE), a chlorinated solvent, is one of the most common chlorinated organic contaminants at DOE sites (including Hanford, though carbon tetrachloride is a more widespread problem there). Cleanup costs for chlorinated solvents are driven most frequently by TCE because it is both widespread and is generally present at the highest concentrations on DOE sites. The EMSP project **Mechanism Involved in Trichloroethylene-Induced Liver Cancer: Importance to Environmental Cleanup** (page 4.1) is developing critical data for updating the human health and safety risk-based cleanup standards for trichloroethylene (TCE) that were developed 20 years ago. These data could

potentially allow changes in risk-based standards for TCE that could reduce complex-wide cleanup costs by several billions of dollars while still protecting humans and the environment.

References

DOE. 1995. *Estimating the Cold War Mortgage: The 1995 Baseline Environmental Management Report.* DOE/EM-0232, U.S. Department of Energy, Washington, D.C.

ORNL. 1994. *Integrated Data Base Report-1993: U.S. Spent Nuclear Fuel and Radioactive Waste Inventories, Projections, and Characteristics.* DOE/RW-0006 Rev. 10, Oak Ridge National Laboratory, Oak Ridge, Tennessee.

For more information contact:

Dr. Rod K. Quinn
Manager, Environmental Science and Technology
Pacific Northwest National Laboratory
(509) 375-6625
rod.quinn@pnl.gov

Dr. Loni M. Peurrung
Environmental Science and Technology
Pacific Northwest National Laboratory
(509) 373-0201
loni.peurrung@pnl.gov

or

Dr. Roy E. Gephart
Program Manager
Environmental and Health Sciences Division
Pacific Northwest National Laboratory
(509) 375-6754
roy.gephart@pnl.gov

Contents

1.0 Tank Waste Remediation

Interfacial Radiolysis Effects in Tank Waste Speciation 1.1

Mechanics of Bubbles in Sludges and Slurries 1.15

Colloidal Agglomerates in Tank Sludge: Impact on Waste Processing 1.31

New Silicotitanate Waste Forms: Development and Characterization 1.41

Architectural Design Criteria for *f*-Block Metal Sequestering Agents 1.53

Ionizing Radiation-Induced Catalysis on Metal Oxide Particles 1.69

Chemical Speciation of Strontium, Americium, and Curium in High-Level Waste: Predictive Modeling of Phase Partitioning During Tank Processing 1.79

Ion Exchange Processes and Mechanisms in Glasses 1.93

Radiation Effects in Nuclear Waste Materials 1.107

2.0 Spent Nuclear Fuel and Nuclear Materials

Radiolytic and Thermal Processes Relevant to Dry Storage of Spent Nuclear Fuels 2.1

Distribution and Solubility of Radionuclides and Neutron Absorbers in Waste Forms for Disposition of Plutonium Ash and Scraps, Excess Plutonium, and Miscellaneous Spent Nuclear Fuels 2.5

3.0 Soil and Groundwater Cleanup

Dynamics of Coupled Contaminant and Microbial Transport in Heterogeneous Porous Media 3.1

Genetic Analysis of Stress Responses in Soil Bacteria for Enhanced Bioremediation of Mixed Contaminants 3.13

Molecular-Level Processes Governing the Interaction of Contaminants with Iron and Manganese Oxides 3.23

Mineral Surface Process Responsible for the Decreased Retardation (or enhanced mobilization) of ^{137}Cs from High-Level Waste Tank Discharges 3.43

4.0 Health Effects

Mechanism Involved in Trichloroethylene-Induced Liver Cancer: Importance to Environmental Cleanup 4.1

Tank Waste Remediation

Interfacial Radiolysis Effects in Tank Waste Speciation

(First Year of Funding: FY 1996)

Principal Investigator

T.M. Orlando
Pacific Northwest National Laboratory
P.O. Box 999, MSIN K8-88
Richland, WA 99352
(509) 376-9420 (phone)
(509) 376-6066 (fax)
thomas.orlando@pnl.gov

Co-Principal Investigators

D. Meisel
Argonne National Laboratory
9700 South Cass Av.
Argonne, IL 60439
(630) 252-3472 (phone)
(630) 252-7068 (fax)
dani@anl.gov

D. M. Camaioni
Pacific Northwest National Laboratory
P.O. Box 999, MSIN K2-44
Richland, WA 99352
(509) 375-2739 (phone)
(509) 375-2186 (fax)
donald.camaioni@pnl.gov

Contributors and Collaborators

K. Knutsen (Assoc. Western Universities - Postdoctoral Fellow)
N. Petrik (Assoc. Western Universities - Visiting Research Scientist)
A. R. Cook (Argonne National Laboratory - Assistant Scientist)
N. Dimitrievic (Argonne National Laboratory - Visiting Scientist)
T. Schatz (Argonne National Laboratory - Postdoctoral Fellow)
N. Zevos (State University - New York, Potsdam Visiting Prof.)

Research Objective

The purpose of this program is to deliver pertinent, fundamental information that can be used to make technically defensible decisions on safety issues and processing strategies for mixed chemical and radioactive waste cleanup at U.S. Department of Energy (DOE) sites. The intent is to establish an understanding of radiolysis in mixed-phase systems typical of heterogeneous, radioactive, and chemical wastes. This is an important scientific concern with respect to understanding tank waste chemistry issues; until now, it has received relatively little attention. The importance of understanding solid-state radiolysis, secondary electron interactions, charge-transfer dynamics, and the general effect of heterogeneous solids (interface and particulate surface chemistry) on tank waste radiation processes will be demonstrated. In particular, we will investigate 1) the role of solid-state and interfacial radiolysis in the generation of gases, 2) the mechanisms of organic compound degradation, 3) scientific issues underlying safe interim storage, and 4) the effects of colloid surface-chemical properties on waste chemistry.

Research Statement

The radioactive and chemical wastes present in DOE underground storage tanks contain complex mixtures of sludges, salts, and supernatant liquids. These mixtures comprise a wide variety of oxide materials, aqueous solvents, and organic components and are constantly bombarded with energetic particles produced via the decay of radioactive ^{137}Cs and ^{90}Sr. A vital need exists to understand radiolysis of organic and inorganic species present in mixed waste tanks because these processes

- produce mixtures of toxic, flammable, and potentially explosive gases (e.g., H_2, N_2O and volatile organics)

- degrade organics, possibly to gas-generating organic fragments, even as the degradation reduces the hazards associated with nitrate-organic mixtures

- alter the surface chemistry of insoluble colloids in tank sludge, influencing sedimentation and the gas/solid interactions that may lead to gas entrapment phenomena.

Unfortunately, the mixed chemical and radiolytic nature of the problem greatly complicates the interactions, and the information available on radiolytic processes in multiphase heterogeneous systems is insufficient to develop accurate safety margins or radiolysis models that adequately describe DOE tank waste chemistry to support technically sound decision making.

Research Progress

Progress in three areas is reported: 1) radiation effects at $NaNO_3$ crystal interfaces, 2) radiation effects in aqueous suspensions of particles, and 3) reactions of organic complexants with NO_2 in water. The first two areas involve controlled radiolysis studies using pulsed, low- (5–150 eV) and high- (3 MeV) energy electron-beams at Pacific Northwest National Laboratory (PNNL) and at Argonne National Laboratory (ANL), respectively. The pulsed, low-energy electron beams probe the inelastic scattering and secondary cascading effects produced by high-energy beta and gamma radiation. Pulsed radiolysis allows time-resolved measurements of the chemical processes induced by ionizing radiation. These studies suggest that NO_2 is the dominant oxidizing species generated by radiolysis in tank wastes at the Hanford and Savannah River sites; as such, it oxidatively degrades organic waste constituents and initiates generation of flammable gas. Because little is known about its reactions with organic species in aqueous solution, some research is being focused on elucidating the kinetics and products of NO_2 reactions. The research disclosed in this report is the result of collaborations between the listed investigators, who closely coordinate their efforts on this project, another EMSP project located at ANL ("NO_x System in Nuclear Waste," PI: D. Meisel) and a project in the Tank Waste Safety Program at the Hanford Site ("Waste Aging Studies Project," PI: D. M. Camaioni).

Radiation Effects at Crystalline $NaNO_3$ Interfaces

The low-energy (5-100 eV) electron-stimulated desorption (ESD) of neutrals from $NaNO_3$ single crystals is compared with the previous state-resolved 193 nm (6.4 eV) photon-stimulated desorption (PSD) study (Knutsen and Orlando 1997a). This PSD study demonstrated that excitation of $NaNO_3$ interfaces with 193 nm photons (6.4 eV) results in the stimulated desorption of predominantly $NO(^2\Pi)$ and $O(^3P_J)$. The 193 nm (6.4 eV) valence band excitation in $NaNO_3$ solids/interfaces has been correlated with the $NO_3^-\pi^*\leftarrow\pi$ and and is below the nominal bandgap energy of ~8 eV. Excitations of this band create localized excitons, which couple to phonons and trap at surface and/or defect sites. Decomposition of these excitons results in the direct desorption of both thermal and non-thermal $NO(^2\Pi)$ and $O(^3P)$. We favor a mechanism in which surface excitons decay to produce $NO(g) + O(g) + O^-(sf)$, either in one step or via an NO_2^{*-} intermediate. This intermediate is consistent with the observation of NO_2^- as a primary bulk radiolysis product (Cunningham and Steele 1962; Cunningham 1968).

The controlled low-energy electron-beam irradiation studies also demonstrate that $NO(^2\Pi)$ and $O(^3P_J)$ are the primary direct neutral desorption products. In Figure 1, we compare the velocity distributions of the $NO(^2\Pi)$ and $O(^3P_J)$ from both 100 eV ESD and 6.4 eV PSD. The open circles are ESD data obtained with an electron beam pulse width of 200 ns. The closed circles represent PSD data obtained at a desorption laser fluence of 50 $\mu J/cm^2$. All data have been normalized to a common peak height. The data for the $O(^3P)$ show that the velocity

distributions obtained from ESD and PSD are essentially identical (Knutsen and Orlando 1997b, p. 6.4). The NO data agree very well at short times, though the ESD velocity distribution shows more population at longer flight times. No dependence of the velocity distribution on incident electron energy was observed. Comparison with the 423K Maxwell-Boltzmann distributions of the form $t^{-4}\exp(-1/t^2)$ (solid lines), where t is the time to cover the 4-mm distance from the sample to the surface to the probe laser beam, shows that both the O and NO velocity distributions are non-thermal, with a significant portion of their populations "hotter" than the $NaNO_3$ surface temperature. Both the $NO(^2\Pi)$ and $O(^3P_J)$ gave a 1-electron dependence upon incident flux, in agreement with the 1-photon dependence on desorption laser flux observed for PSD from the sample surface.

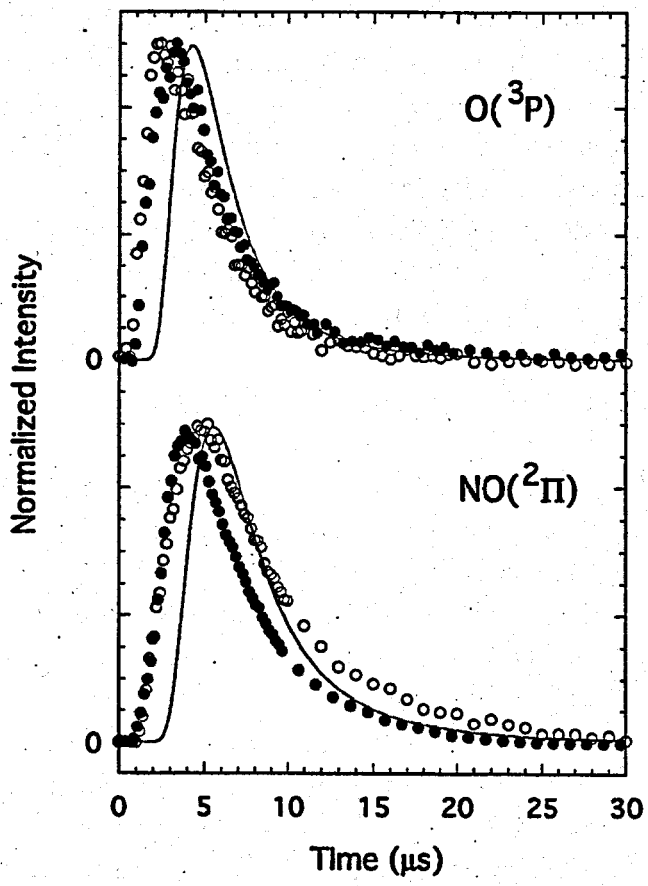

Figure 1. The velocity distribution for $NO(^2\Pi)$ and $O(^3P_J)$ from both 100 eV ESD (open circles) and 6.4 eV PSD (filled circles). The data were obtained using REMPI/TOF detection techniques and have been normalized to a common peak height for comparison. The solid lines are the 423K Maxwell-Boltzmann distributions calculated for the flight distance of 4 mm. The data demonstrate that the $NO(^2\Pi)$ and $O(^3P_J)$ velocity distributions from ESD and PSD are similar and have non-thermal components.

In addition to NO and O, some O_2(g) and NO_2(g) are produced from both 100 eV ESD and 193 nm PSD of $NaNO_3$. Unlike NO and O, we believe these latter species are produced indirectly and do not represent direct products of $NaNO_3$ decomposition. In fact, the NO_2 data are well fit by a Maxwell-Boltmann distribution at the $NaNO_3$ surface temperature of 423K, indicating interaction with the surface prior to desorption. Neither NO_2 nor O_2 shows the "hot" temperature component observed in both NO and O(^{3}P), but both show a 1-electron dependence upon electron fluence. Thus they may result from ESD processes at defect sites (such as $NO_2^- + e \rightarrow NO_2 + 2e$) or from secondary reactions of the primary products (such as $O + NO_3^- \rightarrow O_2 + NO_2^-$). Since the neutral product yields and energy distributions for ESD and PSD are similar, the final states involved in these desorption events must be similar. This is an important result because it allows us to initiate "radiation"-induced processes at $NaNO_3$ interfaces by selectively exciting the $NO_3^-\pi^* \leftarrow \pi$ band.

It can be concluded from these experiments that the primary direct radiolysis products of $NaNO_3$ solid surfaces are NO, O, and O^- (sf). Secondary (indirect) radiolysis products are O_2 and NO_2. The latter are formed below the surface in the bulk crystal but may diffuse to the surface and react with interfacial species. It is important to consider the impact that such processes would have if they occur in tank wastes. Here, the crystal surface interfaces with saturated aqueous $NaNO_3$ solutions, or possibly immiscible organic liquids, rather than vacuum. Species such as O and O^- are very reactive and probably will react with solution species at or near the interface. The O atom reacts with a variety of organics with diffusion-limited rate constants (Bucher and Scaiano 1994) and it reacts fast with nitrate and nitrite (Warneck and Worzinger 1988)

$$O + NO_3^- \rightarrow NO_2^- + O_2 \qquad k=2.2\times10^8\ M^{-1}s^{-1} \qquad (1)$$

$$O + NO_2^- \rightarrow NO_3^- \qquad k=1.5\times10^9\ M^{-1}s^{-1} \qquad (2)$$

The O^- and its conjugate acid, OH, are also very reactive with organics and with nitrite. Since nitrite concentrations are usually high in aqueous wastes, a significant fraction of the O^- generated at the solution crystal interfaces will probably convert to NO_2. Therefore, we expect that radiolysis of solid $NaNO_3$ in wastes will generate NO_x species in solution. Radiolysis of homogeneous aqueous waste solutions generate primarily OH/O^- and NO_2 (Meisel et al. 1991, 1997) such that heterogeneous and homogeneous processes appear to be complementary. We expect that immiscible organics that adhere to the crystal surfaces will be oxidized directly by O and O^-. As pointed out in an earlier study at ANL (Meisel et al. 1993), it is likely that NO reactions with organic radicals lead to the production of N_2O(g) and NH_3(g) in Hanford tank wastes. Therefore, reactions of the electron-stimulated $NaNO_3$ desorption products with organic overlayers and reactions of NO_2 with organic species in solution are currently under investigation. Progress on the latter effort is discussed in the next to last section of this report.

The generation of strongly oxidizing radicals, O and O^-, and NO at $NaNO_3$ interfaces is correlated such that organic radicals generated at the interface can react with NO to produce nitrogen-containing species. The decay of these species can lead to the production of HNO (NO^- in aqueous conditions), which can undergo recombination reactions and directly yield N_2O(g). Analogous chemistry occurs in the gas-phase photolysis of CH_3ONO (see Equations 3–5) (Heicklen 1988; Nesbitt et al. 1989). Note that Equation (5) has a slow gas-phase rate constant (4×10^{-15} cm^3 $molecule^{-1}$ sec^{-1}) (Palsberg et al. 1989); however, the combination reaction rate is likely to increase considerably at interfaces and in liquids since energy transfer will quench the dissociation reaction of the dimer, $(HNO)_2$.

$$CH_3ONO + h\upsilon \rightleftarrows CH_3O + NO \quad (3)$$

$$CH_3O + NO \rightarrow CH_2O + HNO \quad (4)$$

$$HNO + HNO \rightleftarrows (HNO)_2 \rightarrow N_2O + H_2O \quad (5)$$

The possibility of Equations 4 and 5 occurring at irradiated methanol-$NaNO_3$ is being investigated by controlled electron-beam-induced radiolysis of $NaNO_3$ surfaces containing multilayers of CH_3OH. Methanol radicals, $HOCH_2\bullet$ and $CH_3O\bullet$, ought to be generated from both direct interactions of methanol with energetic electrons and reactions of methanol with oxidizing radicals, O and O^-(sf), generated by electron impact on the nitrate interface (Equation 6).

$$CH_3OH + e^-, O\bullet, OH\bullet, \text{or } O^-(sf) \rightarrow HOCH_2\bullet + CH_3O\bullet + H/OH^-/H_2O \quad (6)$$

The methanol radicals are expected to react with NO (Equations 7 and 8) that is generated concurrently by electron stimulation of the nitrate interface. These reactions should produce N_2O, or its precursor, as well as other compounds that have been suggested to contribute to production of nitrogenous and H_2 gases in tank wastes.

$$HOCH_2 + NO \rightarrow HNO\,(HON) + CH_2{=}O \quad (7)$$

$$HOCH_2 + NO \rightarrow HOCH_2NO \quad (8)$$

$$HOCH_2NO \rightarrow HOCN + H_2O \quad (9)$$

$$HOCH_2NO \rightarrow HCO_2NH_2 \quad (10)$$

Radiation Effects in Aqueous Suspensions of Particles

To begin studying radiation chemical effects in solutions containing colloidal oxide particles, pulsed radiolysis studies of silica-loaded aqueous solutions were carried out at ANL. These pulse radiolysis studies indicate that absorption of the radiation in the solid particles may lead to the transfer of charge across the particle-liquid interface and initiate chemistry at the interface

and in the surrounding solution (Meisel et al. 1997; Schatz et al. 1998). This is demonstrated in Figure 2, which shows that yields of solvated electrons in SiO_2/water suspensions increase with SiO_2 loading. Because the fraction of energy (ionizing radiation) absorbed by the particles increases with loading, this observation suggests that the absorption of radiation by the solid particles causes electrons to be ejected into the surrounding solution. If the radiation effects were localized within silica particles, the yield of solvated electrons should decrease along the lower dashed line in the figure, which represents the dependence of the volume fraction of water on silica loading. Instead, the yields follow the average sample densities (upper dashed line) that are calculated from particle concentrations and the density of silica.

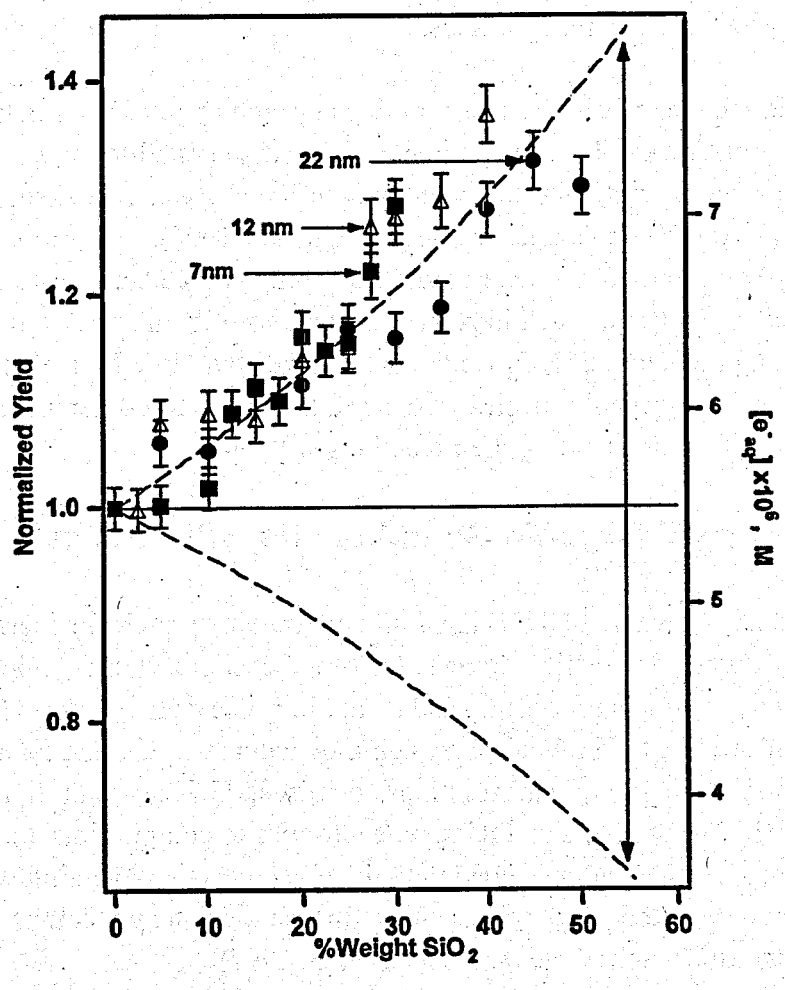

Figure 2. Observations of Solvated Electron Production from Heavily Loaded SiO_2/Water Suspensions. Data points and least-squares error estimates for each measurement are shown for three particle sizes: (■) 7 nm, (Δ) 12 nm, and (•) 22 nm. The right Y-axis shows the total concentration of e^-_{aq} generated in the cell; the left Y-axis shows the concentration normalized to the result in pure water; lower dashed curve is the dependence of water volume fraction on silica loading. The upper dashed curve is the dependence of the average sample density on silica loading.

The results have many practical implications. Most obviously, storage of nuclear material in an "inert" matrix of small particles (e.g., grout) may lead to adverse effects. If the particles are small, the enhanced absorption of energy in the matrix will lead to more pronounced aqueous radiation chemistry. For high-level radionuclides stored in suspensions in large tanks, the presence of the particles will promote generation of water radiolysis products (of particular concern is H_2) in the vicinity of the particles. This may increase the probability of retention of products near the particles, e.g., by gas bubble attachment to the particle, and may lead to serious safety concerns. On the other hand, ionizing irradiation is often considered a viable advanced oxidation technique in various cleanup operations such as water decontamination or soil remediation. Such a radiocatalytic approach, analogous to the proliferating photocatalysis, will clearly be most efficient with small particles.

The implication to tank waste chemistry of this research on interfacial radiolysis effects is that radiation absorbed by solid waste components ($NaNO_3$ crystallites and metal oxide particles) will result in chemistry at waste interfaces and in solution phases. This is significant because many of the organic waste constituents are soluble (Barney 1994). Therefore, heavily solids-laden wastes may contribute to, not deter, radiolytic aging. Since tank waste supernatant solutions are saturated or nearly saturated in $NaNO_3$, radiolysis of both solids and liquids should result in significant production of NO_2 via the metastable NO_3^{2-} ion (Meisel et al. 1991, 1997). Thus, understanding how organic species degrade in tank wastes and the impacts of their degradations must start with understanding their reactions with NO_2.

Reactions of Model Organic Complexants with NO_2 in Water

While it has been shown that NO_2 is the dominant oxidizing radical generated by radiation effects on nuclear waste, there is little knowledge of its reactions with organic compounds that were used in nuclear materials processing and stored in waste tanks. Studies have been performed at the Hanford Site to simulate waste aging by gamma-irradiating nonradioactive waste simulants (Camaioni et al. 1998), e.g., solutions containing high concentrations of $NaNO_3$, $NaNO_2$, and NaOH. The products and relative reactivities of complexants and several intermediate compounds have been determined with the objectives of explaining waste characterization data and predicting the effects of organic aging on the potential combustion hazards of organic containing nitrate-rich wastes (Meacham et al. 1997).

Complementary experiments have been performed to verify the role of NO_2 and elucidate reaction kinetics and products for development of mechanistic kinetic models. The experiments contact aqueous alkaline solutions of organic species with N_2 containing <50 ppm NO_2. The NO_2 dissolves in the solutions and hydrolyzes (Lee and Schwarz 1981) competitively with reduction by organic solutes. Preliminary experiments have surveyed the reactions of nitrilotriacetate (NTA), iminodiacetate (IDA), glycine, and formate. Products were analyzed using ^1H and ^{13}C

nuclear magnetic resonance spectroscopies and ion chromatograpy. The results show that NTA degrades via stepwise decarboxymethylation, giving mainly formate and carbonate.

$$N(CH_2CO_2^-)_3 \xrightarrow{NO_2} HN(CH_2CO_2^-)_2 \xrightarrow{NO_2} H_2NCH_2CO_2^- \xrightarrow{NO_2} HCO_2^{-2} \quad (11)$$

The high preference for production of formate over oxalate suggests that decarboxymethylation may be initiated by decarboxylation (Equations 12–14). Note that in the 1 M NaOH solutions used for these studies, formaldehyde and glyoxal convert to formate and oxalate, respectively, producing H_2 gas (Equation 15) (Karpoor et al. 1995; Ashby et al. 1993).

$$R_2NCH_2CO_2^- + NO_2 \rightarrow R_2NCH_2\bullet + CO_2 + NO_2^- \quad (12)$$

$$R_2NCH_2\bullet + NO_2 \rightarrow R_2N^+{=}CH_2 + NO_2^- \quad (13)$$

$$R_2N^+{=}CH_2 + HO^- + H_2O \rightarrow R_2NH + H_2C(OH)_2 \quad (14)$$

$$H_2C(OH)_2 + OH^- \rightarrow HCO_2^- \quad (15)$$

Formate degrades to carbonate when reacted with NO_2 but at a much slower rate than aminocarboxylates. Relative reactivities, NTA> IDA>glycine>formate, were determined by competition experiments in which each of the aminocarboxylates was oxidized in the presence of formate-^{13}C to obtain initial production rates of formate-^{12}C and carbonate-^{13}C.

We have not determined the mechanism by which NO_2 induces decarboxymethylation. However, we favor the possibility that reactions with aminocarboxylates occur by electron transfer from N followed by decarboxylation of the radical cation or radical zwiterion anion pair, $^-O_2N\ ^+NR_3$. A precedent for such a path is found in the autoxidation of trialkylamines in alkaline aqueous solutions (Chen et al. 1990), the decarboxylation of aminoacid anions by hydroxyl radical (Mönig et al. 1985), and the recently observed decarboxylations of anilinoacetate radical cations (Su et al. 1997).

In conclusion, we note that very similar results have been obtained in Hanford Waste Aging Studies (Camaioni et al. 1998), which irradiated simulated waste solutions (4 M $NaNO_3$, 1 M $NaNO_2$, and 2 M NaOH) containing aminocarboxylate/formate-^{13}C mixtures. Similar product distributions and relative reactivities were obtained from NTA, IDA, and glycine. Therefore, the NO_2 contact experiments appear to corroborate our assertion that NO_2 is the dominant species responsible for radiolytic oxidation of organic chemicals in DOE tank wastes at the Hanford and Savannah River sites.

Planned Activities

PNNL will study radiolytic processes occurring at $NaNO_3$ crystal interfaces with organic overlayers using ESD techniques. The experiments will condense thin layers of methanol on a $NaNO_3$ crystal and irradiate with 100 eV electrons. Then the crystal will be slowly warmed to desorb the organic layers into a mass spectrometer to detect and identify the products.

In collaboration with the ANL EMSP project, "The NO_x System in Nuclear Waste," studies will be continued to elucidate mechanisms of NO_2 oxidations of organic complexants and to measure relative rate constants using a reactive dissolution apparatus that passes dilute (ppm) concentrations of NO_2 through aqueous solutions of substrates. Substrates of interest include aminocarboxylates, glycolate, acetate, and formate. Extensive use will be made of isotopically labeled substrates to determine relative reactivities of competing substrates, isotope effects, and partial rate factors to oxalate, formate, and carbonate. Also, the effects of OH^- and NO_2^- on product distributions will be examined. OH^- concentration may control partioning to oxalate if electron transfer from aminocarboxylates and glycolate precedes decarboxylation. NO_2^- oxidizes radicals, so depending on concentration, different products might occur if organic radicals are oxidized by NO_2^- instead of NO_2.

At ANL, studies of the effects of particles on radiolytic yield will continue. The focus will be on the fate of holes that are initially generated in the particle. The research will investigate whether they migrate to the aqueous phase, similar to the electrons, or remain on the solid and its surface.

References

Ashby EC, F Doctorovich, CL Liotta, HM Neumann, EK Barefield, A Konda, K Zhang and J Hurley. 1993. "Concerning the Formation of Hydrogen in Nuclear Waste. Quantitative Generation of Hydrogen via a Cannizzaro Intermediate." *J Am Chem Soc.*, 115:1171.

Barney GS. 1994. *The Solubilities of Significant Organic Compounds in HLW Tank Supernate Solutions*. WHC-SA-2565-FP, Westinghouse Hanford Company, Richland, Washington.

Bucher G and JC Scaiano. 1994. "Laser Flash Photolysis of Pyridine N-Oxide: Kinetic Studies of Atomic Oxygen [O(3P)] in Solution." *J Phys Chem.*, 98:12471.

Camaioni DM, WD Samuels, JC Linehan, AK Sharma, MO Hogan, MA Lilga, SA Clauss, KL Wahl, and JA Campbell. 1998. *Organic Tanks Safety Program FY97 Waste Aging Studies*. PNNL-11670 Rev. 1, Pacific Northwest National Laboratory, Richland, Washington.

Chen MJ, JC Linehan, and JW Rathke. 1990. "Autoxidation of Trimethylamine in Aqueous Solutions." *J Org Chem.*, 55:3233.

Cunningham J. 1968. *Radical Ions*. Interscience, New York, Vol. pp. 475.

Cunningham J. and LR Steele. 1962. *Phys Rev Lett.*, 9:47.

Heicklen J. 1988. "The Decomposition of Alkyl Nitrites and the Reactions of Alkoxyl Radicals." In *Adv. in Photochemistry*, D. H. Volman, G. S. Hammond and K. Gollnich, Ed.; John Wiley Sons, Inc., New York, Vol. 14, pp. 177.

Karpoor S, FA Barnabas, SC Sauer Jr., D Meisel, and CD Jonah. 1995. "Kinetics of Hydrogen Formation from Formaldehyde in Basic Aqueous Solutions." *J Phys Chem.*, 99:6857.

Knutsen K. and TM Orlando. 1997a. "Photon-stimulated Desorption of $O(^3P)$ and $NO(^2\Pi)$ from $NaNO_3$ Single Crystals." *Phys Rev B*, 55:13246.

Knutsen K and TM Orlando. 1997b. "Low-energy (5-100 eV) Electron and Ultraviolet (6.4 eV) Photon-stimulated Desorption of Neutral Fragments from NaNO3 Single Crystals," in press.

Lee Y-N and Schwarz. 1981. "Reaction Kinetics of Nitrogen Dioxide with Liquid Water at Low Partial Pressure." *J Phys Chem.*, 85:840.

Meacham JE, AB Webb, NW Kirch, JA Lechelt, DA Reynolds, GS Barney, DM Camaioni, F Gao, RT Hallen, and PG Heasler. 1997. *Organic Complexant Topical Report*. HNF-SD-WM-CN-058 Rev. 1, Duke Engineering Services Hanford, Richland, Washington.

Meisel D, H Diamond, EP Horwitz, MS Matheson, MC Sauer Jr., and JC Sullivan. 1991. *Radiation Chemistry of Synthetic Waste*. ANL-91/40, Argonne National Laboratory, Argonne, Illinois.

Meisel D, CD Jonah, S Kapoor, MS Matheson, and MC Sauer Jr. 1993. *Radiolytic and Radiolytically Induced Generation of Gases from Synthetic Wastes*. ANL-93/43, Argonne National Laboratory, Argonne, Illinois.

Meisel D, A Cook, D Camaioni and T Orlando. 1997. "Chemistry, Radiation, and Interfaces in Suspensions of Nuclear Waste Simulants." *Photoelectrochemistry*, L Rajeshwar, A Fujishima, D Meissner and M Tomkiewicz, eds. The Electrochemical Society, pp. 347.

Mönig J, R Chapman, and KD Asmus. 1985. "Effect of the Protonation State of the Amino Group on the •OH Radical Induced Decarboxylation of Amino Acids in Aqueous Solutions." *J Phys Chem.*, 89:3139.

Nesbitt FL, WA Payne, and LJ Stief. 1989. "Kinetic Studies of the Reaction of the Hydroxymethyl Radical with NO and NO_2." *J Phys Chem.*, 93:5158.

Palsber P, J Munk, Anastasi and VJ Simpson. 1989. "Reaction of CH_2OH with O_2, NO and NO_2 at Room Temperature." *J Phys Chem.*, 93:5162.

Schatz T, AR Cook, and D Meisel. 1998. "Charge Carrier Transfer Across the Silica Nanoparticle/Water Interface." in press.

Su Z, DE Falvey, UC Yoon, and PS Mariano. 1997. "The Dynamics of α-Anilino Carboxylate and Related Cation Radical α-Heterolytic Fragmentations." *J Am Chem Soc.*, 119:5261.

Warneck P and C Wurzinger. 1988. "Product Quantum Yields for the 305-nm Photodecomposition of NO_3^- in Aqueous Solution." *J Phys Chem.*, 92:6278.

Information Access

This project and the ANL EMSP project, "The NO_x System in Nuclear Waste," are strongly coupled with the "Waste Aging Studies" project at the Hanford Site such that the basic studies are performed at ANL and PNNL and the information is continuously shared with the Tank Waste Safety Program. Information from the projects is also shared directly with Westinghouse Savannah River staff. To further facilitate the exchange of information and the immediate incorporation of results into operations, we conduct at least semi-annual "coordination meetings" in which the site operators (e.g., from Duke Engineering Services Hanford, Numatec, Westinghouse Savannah River Company, etc.) participate both as contributors and as observers. In addition, we participate in national and international meetings of scientific societies, such as the American Chemical Society, the Electrochemical Society, the American Physical Society, and the IEEE, and publish our work in the open literature. The following is a list of publications and conference presentations for the project.

Publications and Presentations

Camaioni DM, K Knutsen, JC Linehan, TM Orlando, A Cook, and D Meisel. September 8, 1997. "Some Fundamental Studies on the Effects of Radiation and Interfaces in High Level Wastes." Symposium on *Future Directions in Radioactive and Mixed Waste Management*, 214th ACS National Meeting, Las Vegas, Nevada.

Knutsen K and TM Orlando. 1998. "Low-energy (5-100 eV) Electron and Ultraviolet (6.4 eV) Photon-stimulated Desorption of Neutral Fragments from $NaNO_3$ Single Crystals." *Appl. Surf. Sci.*, in press.

Meisel D, A Cook, D Camaioni, and T Orlando. 1997. "Chemistry, Radiation, and Interfaces In Suspensions Of Nuclear Waste Simulants." *Photoelectrochemistry*, K Rajeshwar, LM Peter, A Fujishima, D Meissner, and M Tomkiewicz, eds. Electrochemical Society, Vol. 97-20, 350-7.

Orlando TM, MT Sieger, WC Simpson, and K.Knutsen. April 8-11, 1997. "Quantum-Resolved Studies of Electron-Stimulated Processes in Wide Band-Gap Materials." International Conference on Desorption Induced by Electronic Transitions (DIET) VII, Ambleside, United Kingdom.

Orlando TM, MT Sieger , WC Simpson, DP Taylor, and K Knutsen. May 19-22, 1997. "UV Photon- and Low-Energy (5-100 eV) Electron-Stimulated Processes at Environmental Interfaces." The 24th IEEE International Conference on Plasma Science, San Diego, California.

Orlando TM, DP Taylor , WC Simpson, and K Knutsen. July 21-25, 1997. "A Comparison of UV-Photon and Low-Energy Electron-Stimulated Desorption Processes from Wide Band-Gap Materials." The Fourth International Conference on Laser Ablation, COLA '97, Monterey, California.

Schatz T, AR Cook, and D Meisel. 1998. "Charge Carrier Transfer Across The Silica Nanoparticle/Water Interface." Submitted for publication in *J Phys Chem.*

Mechanics of Bubbles in Sludges and Slurries

(First Year of Funding: FY 1997)

Principal Investigators

Dr. Phillip A. Gauglitz (Lead PI)
Pacific Northwest National Laboratory
P.O. 999, MSIN K6-28
Richland, WA 99352
(509) 372-1210 (phone)
(509) 372-1861 (fax)
phillip.gauglitz@pnl.gov

Prof. Morton M. Denn, LBNL
Prof. Susan J. Muller, LBNL
Chemical Engineering Department
University of California
Berkeley, CA 94720-1462
(510)-642-0176 (phone)
(510)-642-4778 (fax)
denn@cchem.berkeley.edu

Prof. William R. Rossen
Petroleum and Geosystems Engineering Department
The University of Texas at Austin
Austin, TX 78712-1061
(512) 471-3246 (phone)
(512) 471-9605 (fax)
william_rossen@pe.utexas.edu

Dr. Guillermo Terrones
Pacific Northwest National Laboratory
P.O. Box 999, MSIN K7-15
Richland, WA 99352
(509) 375-2183 (phone)
(509) 375-3641 (fax)
g_terrones@pnl.gov

Research Objective

This project focuses on key issues associated with the flammable gas safety hazard and its role in safe storage and in future waste operations such as salt-well pumping, waste transfers, and sluicing/retrieval. The purpose of this project is to develop a basic understanding of how single bubbles (of flammable gases) behave in representative waste simulants and then develop a framework for predicting macroscopic full-tank behavior from the underlying single-bubble behavior.

The specific objectives of this research are as follows:

1. quantitatively describe the interaction of bubbles with waste materials (both sludges and slurries) to understand the physical mechanisms by which barometric pressure changes give rise to a hysteresis between level and pressure

2. develop improved methods for estimating retained gas by properly accounting for the interactions of bubbles with the waste

3. determine how to estimate waste physical properties from the observed hysteresis and the limitations of these estimates

4. determine how barometric pressure fluctuations induce slow upward migration and release of gas bubbles.

Problem Statement

Previous studies have established that the waste level of Hanford tanks responds to barometric pressure changes, the compressibility of retained bubbles accounts for the level changes, and the volume of retained gas can be determined from the measured waste level and barometric pressure changes. However, interactions between the gas bubbles and rheologically complex waste cause inaccurate retained gas estimates and are not well understood. Because the retained gas is typically a flammable mixture of hydrogen, ammonia, and nitrous oxide, accurate determination of the retained gas volume is a critical component for establishing the safety hazard of the tanks. Accurate estimates of retained gas from level/pressure data are highly desirable because direct in situ measurements are very expensive in an individual tank and impossible in many single-shell tanks. The elucidation of the bubble waste interactions will have a direct influence on improving the accuracy of gas volume estimates, will provide for more accurate models for estimating waste properties from level/pressure data, and should quantify the

effect of barometric pressure fluctuations on the slow rise and release of bubbles. The results of this research will support critical operations at the Hanford Site associated with the flammable gas safety hazard and future waste operations such as salt-well pumping, waste transfers, and sluicing/retrieval.

Research Progress

This research program, which began in late FY97, is separated into four related activities on bubble behavior, as shown schematically in Figure 1. Modeling studies on continuum materials (sludges) are being conducted from both the solid mechanics and fluid mechanics viewpoints. The solid mechanics models are being developed by Terrones at PNNL and the fluid mechanics solution approach is being developed by Denn and Muller at the University of California at Berkeley. Rossen is conducting the modeling studies of bubble behavior in particulate materials (slurries) at the University of Texas at Austin, and Gauglitz at PNNL is conducting experimental studies on both sludges and slurries. Bubbles retained in sludges and slurries have significantly different behavior, thus it is appropriate to approach modeling these materials from different viewpoints, though the experimental studies are more closely related. Progress has been made in each of these activities and is summarized in the following sections.

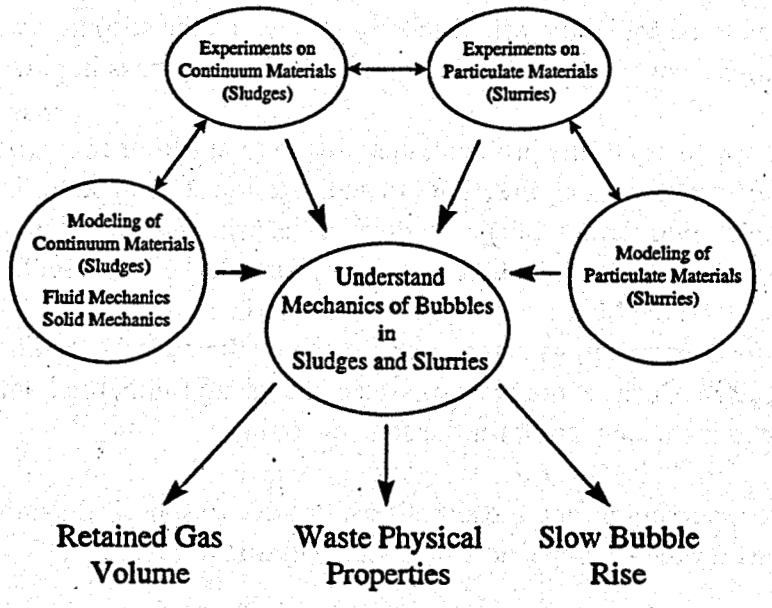

Figure 1. Interrelationship of the Individual Research Problems with the Overall Program Objectives

Modeling Continuum Materials (sludges) – Solid Mechanics for a Single Bubble

One of the objectives of this activity is to understand the effects that smooth external pressure fluctuations have on the deformation history of a single bubble imbedded in a compressible elastic-perfectly plastic isotropic medium of infinite extent. In this section, the progress made on the theoretical analysis of the deformation of a bubble in an elastoplastic material under pressure is reported.

The general situation in which the external pressure fluctuations are large enough to produce plastic zones during compression and reversed plastic zones during decompression is considered. It is assumed that the rate of change of the pressure variations acting on the medium is sufficiently small that the inertial or dynamic effects become negligible. To make for a more general model, it is assumed that the mechanical properties of the medium do not appreciably change during one full compression and decompression cycle (in reality, a sludge material returns to its original mechanical properties after some time). Under the condition of radial quasi-static expansion or contraction of the bubble, the equilibrium and the compatibility equations are used to determine the state of elastic stress and strain within the medium. To determine the plastic stresses the equations of equilibrium and the yield criterion must be satisfied. Yield is assumed to occur in the continuum according to the maximum octahedral shear stress criterion (also called the Mises criterion) in which the second invariant of the deviatoric elastic stress tensor is equal to the square of the yield stress in pure shear (Hill 1955).

Because of the symmetry of the problem, the only non-vanishing component of the displacement vector is in the radial direction. In addition, the state of stress in the angular directions is isotropic. Furthermore, the directions of the principal stresses correspond to those of the coordinate system. The implication of this correspondence is twofold. First, the state of stress is equibiaxial, thus the Mises and Tresca yield criteria are the same. Second, the radial and angular strains in the plastic regions can be represented by their corresponding logarithmic strains (Lubliner 1990). Because the plastic displacements are finite, the Lagrangian reference frame is used to describe the equation for the state of strain.

With the above assumptions and the simplifications due to spherical symmetry, the governing equations for the stresses and strains in the elastic region are

$$\begin{bmatrix} \nu & \nu-1 \\ 1 & 0 \end{bmatrix} \frac{d}{dr} \begin{Bmatrix} \sigma_r \\ \sigma_\theta \end{Bmatrix} + \frac{1}{r} \begin{bmatrix} \nu+1 & -\nu-1 \\ 2 & -2 \end{bmatrix} \begin{Bmatrix} \sigma_r \\ \sigma_\theta \end{Bmatrix} = 0$$

$$\begin{Bmatrix} \dot{\varepsilon}_r \\ \dot{\varepsilon}_\theta \end{Bmatrix} = \frac{1}{E} \begin{bmatrix} 1 & -2\nu \\ -\nu & 1-\nu \end{bmatrix} \begin{Bmatrix} \dot{\sigma}_r \\ \dot{\sigma}_\theta \end{Bmatrix}$$

where r is the radial coordinate, σ_r and σ_θ ($= \sigma_\phi$) are the radial and angular stresses, ν is the Poisson ratio, $\dot{\varepsilon}_r$ and $\dot{\varepsilon}_\theta$ are the radial and angular strain rates (dotted variables are time derivatives), and E is the Young's modulus of elasticity. The boundary and initial conditions for the elastic problem are

$$\sigma_r(a;t) = -p(t)\left(\frac{a_o}{a}\right)^3, \sigma_r(\infty;t) = -p_o - p(t)$$

$$\varepsilon_r(r;0) = \varepsilon_\theta(r;0) = 0, \sigma_r(r;0) = \sigma_\theta(r;0) = -p_o$$

where a_o is the initial bubble radius, a is the current radius, which is an unknown function of the external pressure, the external pressure exerted on the medium is periodically varied in time by an amount p about a reference pressure p_o, and $|p(t) - p_o| < p_o$.

During any given pressure sweep, the continuum in general comprises a finite plastic and an infinite elastic region. As time evolves, the alternate compression and decompression cycles create states of residual stress that constitute the initial conditions for the subsequent pressure sweep. For a given pressure sweep, two different sets of equations are solved to determine the plastic and elastic states of stress and strain. Two additional boundary conditions are introduced: the yield criterion is satisfied at the plastic-elastic boundary (which is not known a priori), and the stresses are continuous across this boundary.

When a finite plastic zone is formed, the equations for the stresses and the finite displacements are

$$\begin{bmatrix} r & 0 \\ 0 & 0 \end{bmatrix} \frac{d}{dr} \begin{Bmatrix} \sigma_r \\ \sigma_\theta \end{Bmatrix} + \begin{bmatrix} 2 & -2 \\ (-1)^n & (-1)^{n+1} \end{bmatrix} \begin{Bmatrix} \sigma_r \\ \sigma_\theta \end{Bmatrix} = \begin{Bmatrix} 0 \\ \sigma_y \end{Bmatrix}$$

$$\ln\left(\frac{r^2 dr}{r_o^2 dr_o}\right) = \frac{1-2\nu}{E}(\sigma_r + 2\sigma_\theta) + \left[\varepsilon_r + 2\varepsilon_\theta - \frac{1-2\nu}{E}(\sigma_r + 2\sigma_\theta)\right]\Bigg|_{t=\text{Onset of Yield}}$$

$$\varepsilon_r = \ln\left(\frac{dr}{dr_o}\right), \qquad \varepsilon_\theta = \ln\left(\frac{r}{r_o}\right)$$

where n is 0 or 1 during external compression or decompression, respectively (i.e., if during the first pressure sweep p(t) is a monotonically decreasing function of time and p(0) = 0, there is external decompression), r is the current radial coordinate, r_o is the original radial coordinate, and σ_y is the yield stress of the material in pure tension. The initial conditions for the plastic displacements are obtained from the state of stress-strain at the onset of yield. This is calculated by evaluating the elastic solution at the critical pressure (above which there is plastic yield). For the combined plastic and elastic problems, the boundary conditions are

$$\overset{p}{\sigma}_r(a) = -p\left(\frac{a_o}{a}\right)^3, \overset{e}{\sigma}_r(b) - \overset{e}{\sigma}_\theta(b) = (-1)^n \sigma_y$$

$$\overset{p}{\sigma}_r(b) = \overset{e}{\sigma}_r(b) \overset{p}{\sigma}_\theta(b) = \overset{e}{\sigma}_\theta(b)$$

$$\overset{e}{\sigma}_r(\infty) = -p_o - p(t)$$

where the superscripts p and e denote plastic and elastic solutions, respectively. After reaching the maximum decompression, the external pressure is increased and compression commences by re-tracing the same pressure values followed by the previous sweep. However, at a same pressure value, the state of stress during compression is different from that of decompression because of the presence of residual stresses. Analytically, the calculation of these stresses constitutes the major difficulty of the present problem. Residual stresses are the combination of the original state of stress (before the beginning of compression) and the elastic stresses originating from the departure of the state of stress from the maximum decompression point (Chadwick 1959; Hopkins 1960). The residual stresses during the compression cycle take the form

$$\begin{Bmatrix} {}_c\sigma_r \\ {}_c\sigma_\theta \end{Bmatrix} = \begin{Bmatrix} \sigma_r \\ \sigma_\theta \end{Bmatrix} + \begin{Bmatrix} {}_d\sigma_r \\ {}_d\sigma_\theta \end{Bmatrix}$$

where the left subscripts c and d refer to the total compressive stresses and the departure stresses, respectively. Initially, compression causes a state of elastic stress. This is followed by the formation of a reversed plastic zone. During this pressure sweep, the elastic and plastic equations are solved by taking into account that the extent of the new plastic zone is different from that obtained during decompression and that the bubble radius has changed because of an irrecoverable plastic displacement. Interestingly, the residual stresses, in general, cannot satisfy either the elastic or the plastic equations because they are a composite solution with one plastic and one elastic component. The equation for the plastic displacements in the reversed plastic zone is

$$\ln\left(\frac{{}_c r^2 d_c r}{r^2 dr}\right) = \frac{1-2\nu}{E}({}_c\sigma_r + 2\,{}_c\sigma_\theta) + \left[{}_d\varepsilon_r + 2\,{}_d\varepsilon_\theta - \frac{1-2\nu}{E}({}_c\sigma_r + 2\,{}_c\sigma_\theta)\right]\Bigg|_{t=\text{At Reverse Yield}}$$

A similar procedure is followed for subsequent pressure sweeps. Figure 2 shows how the bubble radius changes as the pressure component p is varied from 0 to maximum decompression to maximum compression and then back to 0. The pressure is normalized with the critical pressure for the initiation of yield during decompression (which can be approximated by $2/3\sigma_y$). In the inset of Figure 2, the external pressure component cycle exerted on the bubble is shown. During decompression, the rate of increase in the bubble radius markedly increases after the formation of a plastic zone. From the beginning of compression, the medium loads elastically up to a critical pressure below which the material loads plastically until the maximum compression

point is reached. This behavior repeats during the last decompression sweep. Notice the difference between the bubble radius at the start and at the end of the pressure cycle (the original radius is not recovered). During each pressure sweep, the medium undergoes elastic and plastic deformation.

Future work will focus on the extension of the solution to further pressure cycles. In addition, the contribution of neighboring bubbles (multi-bubble problem) to the plastic and elastic deformations will be investigated. This study will be expanded to include yield criteria that depend on the hydrostatic pressure, such as the Drucker-Prager or the Mises-Schleicher criterion.

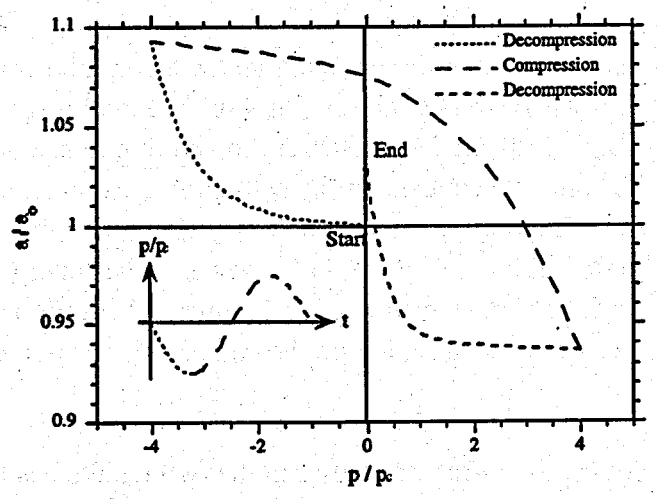

Figure 2. Bubble Radius Hysteresis Due to an External Periodic Pressure Cycle ($p_o = 1$ atm, $\sigma_y = 6$ kPa, $E = 1000$ kPa, $\nu = 0.3$)

Modeling Continuum Materials (sludges) and Simulant Rheology–Fluid Mechanics Approach

The slurries in the Hanford storage tanks are complex fluids that exhibit a yield stress and most likely deform elastically below the yield stress. We are studying the behavior of bubbles in these slurries under the influence of gravity and changing barometric pressure through a computational and theoretical effort. Specifically, we are interested in how multiple bubbles suspended in a yield-stress fluid interact, coalesce, and move. The issues involved are intuitively clear: an expanding single bubble strains the surrounding fluid to a point where the yield stress is exceeded, the fluid structure within that yielded region collapses, the fluid around the bubble flows but remains surrounded by a region that continues to deform elastically. The yielded region will continue to grow in size as the bubble grows. In an array of bubbles, the yielded

regions will interact. How this interaction occurs and what happens when the yielded regions intersect is the heart of the problem. When there is a fully connected yielded region, bubbles can move about, coalesce, and rise.

Before addressing the interactions of an array of bubbles, a number of important issues relating to complex motions of yield-stress fluids in complex geometries must first be resolved. We are beginning with a consideration of the squeezing deformation of a yield-stress fluid between finite plates. There have been relatively few solutions for Bingham-like fluids in complex geometries because of the computational difficulty associated with the unknown location of the yield surfaces. For the squeeze flow of a Bingham fluid between approaching disks, Covey and Stanmore (1981) used a lubrication approach to obtain an approximate solution that showed unyielded regions with position-dependent cross section. Lipscomb and Denn (1984) pointed out through a kinematical argument that this cannot be correct because it is impossible to satisfy velocity and stress continuity at a surface enclosing a solid body with a changing cross section. Lipscomb and Denn (1984) showed that in a squeeze flow field, which is a quasi-static flow with some dynamical similarity to bubble expansion or contraction, the system cannot yield at any point until it has yielded everywhere, and the deformation thereafter is viscous throughout the flow field. However, O'Donovan and Tanner (1984), and more recently Adams and coworkers (1997), have reported numerical solutions of squeeze flow of a yield stress fluid showing an unyielded region on the center axis in apparent contradiction to the Lipscomb-Denn analysis.

Denn[(a)] has suggested that the difference between the two results has to do with relative length scales; the Lipscomb and Denn analysis assumes flow between infinite disks; the finite-element calculations assume a finite geometry. When the disks are infinite and there is a single characteristic length (the gap spacing H), the only relevant dimensionless group is the Bingham number, $Bi = \tau_y H/\eta V$. Here τ_y is the yield stress, η is the viscosity of the material above the yield stress, and V is a characteristic velocity. For disks of finite radius R, however, the geometric ratio H/R must also be relevant. A ratio of the minimum force required to move a plate to overcome the yield stress to that required to squeeze the plates when only viscous stresses are present leads to a dimensionless group $Bi(H/R)^2$. For $H/R \rightarrow 0$ with finite Bi, we expect yielding everywhere before any flow occurs, while for $Bi \rightarrow \infty$ with finite H/R we expect an unyielded region. A transition between these two behaviors is likely for finite values of the product and is the system of practical interest. It is worth noting that the dimensionless group Bi(H/R) arises naturally in the variational analysis of Zwick et al. (1996), and it, rather than the group mentioned above, may be the relevant group for defining the flow regimes.

We have obtained an exact solution to a model problem that gives some insight into the flow field. When a Newtonian fluid is squeezed between two flat surfaces of arbitrary shape, the solution for the velocity field is in terms of an analytic function (a complex function whose real

(a) Denn MM. 1997. Personal communication.

and imaginary parts satisfy Laplace's equation and certain other relations). The values of an analytic function everywhere are determined by the conditions at "infinity"; i.e., at the outer edge of the flow regime. This establishes directly that there is a "preferred origin" for compressive flows in finite geometries and the flow is dependent on conditions far from the origin. The particular boundary conditions to be used far from the origin are not obvious.

A more thorough numerical analysis of the squeeze flow problem is planned. Initial work with a commercial finite element package, POLYFLOW, is underway. We will use convergent numerical methods to examine the effect of finite length scales on the development of unyielded regions. At present, it is not clear how these issues carry over to bubble expansion and contraction, where there is both an inner length scale defined by the bubble diameter and an outer length scale defined by the distance between bubbles. The single bubble problem will be addressed next, followed by an array of bubbles on a regular lattice, where the yielded regions may interact.

In addition, we have performed preliminary rheological characterization of the simulant sludges being used in the experimental study of bubble behavior. Figure 3 shows sample stress-strain data indicating the essential "elastic-plastic" behavior of one of these materials. This data set will ultimately provide the appropriate parameters for constitutive modeling of the slurries. A more detailed characterization of these materials is underway.

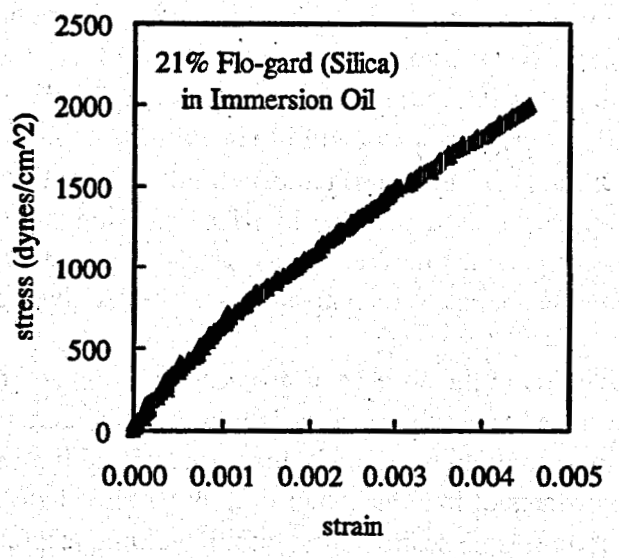

Figure 3. Typical Rheological Behavior of a Sludge Simulant from a Stress Ramp Experiment Using Parallel Plates

Modeling Particulate Materials (slurries)

Many of the wastes in the Hanford tanks are more appropriately modeled as a permeable porous medium of loosely packed beds of salt particles. The objective of this research problem is to model compressible bubble behavior in simple porous media. For simplicity, we begin with a model pore structure of a one-dimensional (1-D) network of identical biconical pores with both converging and diverging sections (Figure 4). The parameters needed to characterize the shape of an individual pore are pore length, pore-body radius, and pore-throat radius. Although the pore network is one dimensional, the shape of individual pores is of course three dimensional (3-D).

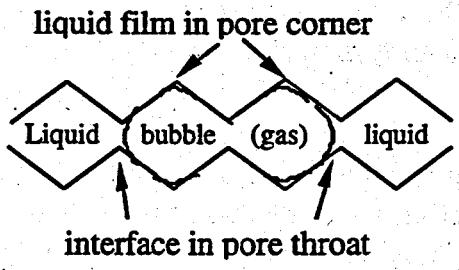

Figure 4. 1-D Model of Porespace

If a spherical gas bubble is large enough to touch all the sides of a biconical pore, its interface splits into three parts: two invading pore throats and the other pressing into the pore corner at the pore body, as depicted in Figure 4. Assuming the liquid phase surrounding the bubble is interconnected and gas pressure in the bubble is uniform, capillary pressure is the same at all interfaces. Capillary pressure for the interface penetrating a pore throat is defined by a single curvature, whereas capillary pressure for the interface pressing into the pore corner is defined by two curvatures, because this interface is not spherical. Contact angle plays an important role in determining the shapes of the various interfaces at given capillary pressure.

Three time scales are involved in the process of gas accumulation and response to barometric pressure. A long-term time scale of months or years is related to the generation of the gas phase. During this period, bubble mass and volume slowly increase at fixed liquid pressure. This process determines the initial states of bubbles when liquid pressure changes in response to barometric pressure. On a shorter time scale, hours, bubble volume responds to changes in liquid pressure at fixed mass. It is on this time scale that effective compressibility is observed. On a still shorter time scale, seconds or less, interfaces advance or retreat impulsively. These jumps occur at fixed barometric pressure *and* bubble mass. They can imply a huge (infinite) compressibility for individual bubbles; the effective compressibility of a population of bubbles includes a few that jump and many that do not. Because of these jumps, many hypothetical interface positions are not observed in a slowly growing bubble responding to barometric pressure.

The slow growth of a bubble over a period of months proceeds as follows. As the bubble expands, two interfaces at opposite ends of the bubble advance symmetrically into pore throats along the converging pore section, the interface at the pore corner approaches more and more into the corner. Maximum capillary pressure occurs when two interfaces arrive at pore throat (Figure 5), because then these interfaces have minimum radii. Only one interface proceeds into the next pore; the other moves back to the original pore. (Two interfaces in diverging pore sections are mechanically unstable; one must advance and the other retreat.) As one interface proceeds into the diverging section of the next pore, capillary pressure decreases and interfaces at the pore corners and at the opposite end of the bubble retreat further. If the bubble is large, the retreat of interfaces in pore corners means that bubble volume decreases for a time as interface position advances; in reality, a jump occurs instead of this decrease in volume. The advance of the interface continues until the interface touches the converging section of the given pore. At that time, the interface jumps to the converging section. After this jump, the shape of the bubble becomes symmetrical again, leaving one more interface at the pore corner where jump occurred.

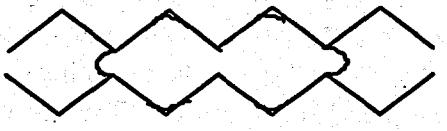

Figure 5. Point of Maximum Capillary Pressure

Since only one interface can penetrate a pore throat at one time, it is possible to conduct calculations for that interface explicitly and lump movement of all the other interfaces into effective response functions. This simplifies the calculations considerably.

Modeling of interface movement and effective bubble compressibility in a 1-D pore space is nearly complete. Parameters examined include pore shape, bubble size, contact angle, and ambient pressure. Two additional factors must be addressed in the context of this 1-D model: pore heterogeneity and bubble breakup. It will be straightforward to model a periodically constricted capillary (Figure 4) with a variety of pore-throat diameters along its length; as the bubble advances, it enters the throat on either end with the widest diameter. If capillary pressure falls sufficiently, however, bubbles may break apart internally by snapping off at narrow pore throats along their length. If capillary pressure later rises sufficiently, the two bubbles may merge again; if not, they may remain separate indefinitely.

Once modeling of bubbles in 1-D porous media is complete, we will focus on modeling the pressure-volume responses of complex gas ganglia occupying many pores in a heterogeneous 3-D pore network. Such cases are similar to the case already examined: although there are many interfaces invading pore throats, only one advances at a time (that invading the widest throat). The widest throat around the perimeter of a large bubble can be estimated from percolation

theory given the distribution of pore-throat radii. The many other interfaces on the perimeter of the bubble can be lumped together in an effective response to the movement of this one advancing interface.

Experimental Studies of Single Bubbles

The initial objective of this research activity is to quantify the effects of small pressure changes on the volume of a single bubble in a simulated sludge. The challenges of this research problem are to measure accurately the induced volume change of non-spherical bubbles while concurrently visualizing the changes in bubble shape. In this section, the apparatus and initial experimental results are described.

Figure 6 shows the apparatus for conducting the single-bubble experiments. The apparatus consists of a glass test vessel that holds the sludge simulant and bubble, a system for controlling the pressure, and video equipment for collecting visual images. The simulated sludge consisted of an immersion oil (Cargille Industries) and fine silica glass particles (Flo-Gard AB, PPG Industries). The oil and silica were selected to have matching refractive indexes (1.437) so they create a transparent sludge that is nearly crystal clear. The shear strengths of mixtures with a range of solids loading were measured with a shear vane; preliminary rheological characterization with parallel-plate geometry was also done (see Figure 3). The initial experiments described below used a simulant with 20.5 wt% silica that had a shear strength of 580 Pa.

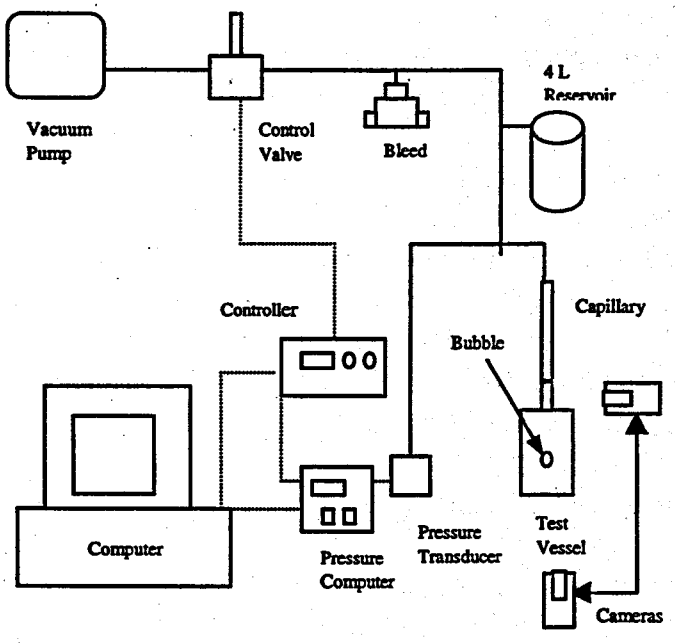

Figure 6. Apparatus for Conducting Single-Bubble Experiments

The simulated sludge was placed in the test vessel, which is a cylindrical glass tube approximately one inch in diameter and one inch long with flat glass plates on each end. A single bubble, approximately three millimeters in diameter, was added to the transparent sludge. The bubble was monitored and recorded on S-VHS video. A 1-mm inner diameter glass capillary was connected to the test vessel and filled with the immersion oil. The level change in this capillary gives the volume change of the bubble. The meniscus height was also recorded on video and was viewed to give the change in bubble volume during an experiment.

The pressure applied to the test vessel was controlled with a MKS 250 pressure controller, which makes pressure changes by adjusting a control valve (MKS 248E) that regulates a bleed flow to a small vacuum pump (Dyna-Pump, Neptune). A Paroscientific quartz transducer (245A-102,) and pressure computer (702/703) determined the system pressure with an accuracy of 0.01 psia. The pressure controller and measured pressures are interfaced to a PC-computer with LabView software (National Instruments) for data acquisition and control. While this system has been tested with automated pressure control, the initial experiments were conducted by manually adjusting the controller setting.

Figure 7 shows the preliminary results for how a single bubble changes its volume in response to cycling pressures and the bubble shapes at different points along the pressure cycles. This experiment used a 580-Pa simulant and cycled pressures between 13.0 and 8.3 psia. This pressure cycle is certainly larger than typical barometric pressure changes, but it is useful in demonstrating the bubble behavior and exaggerating the unusual bubble shapes during the expansion and compression. The experiment started at 13 psia and had one full pressure cycle followed by a second decompression.

In this experiment, the bubble expands as nearly an ideal gas, which is expected for pressure changes that are large compared with the strength of the simulant. The bubble images show that the changing bubble shape is far from an ideal spherical bubble due to the interaction of the bubble with the simulant. A particularly interesting observation is was that the location of the bubble expansion varied between the pressure cycles. The deformation of the bubble during the first decompression occurred at the bottom of the bubble (the bubble image shows a protrusion downward). During the second decompression, the top of the bubble expanded, and the bubble image shows the elongated bubble that had risen upwards. This set of images documents our first observation of slow bubble rise during a pressure cycle. Understanding in detail how this mechanism of bubble rise occurs is one of the objectives of this research.

A second interesting observation was that the bubble volume decreased between the beginning of the first and second decompressions. While this is typical of a bubble/waste interaction, other observations showed that the air bubble was dissolving into the sludge simulant. The magnitude of this gas dissolution was larger than anticipated, and in future experiments must be accounted for or the effect eliminated.

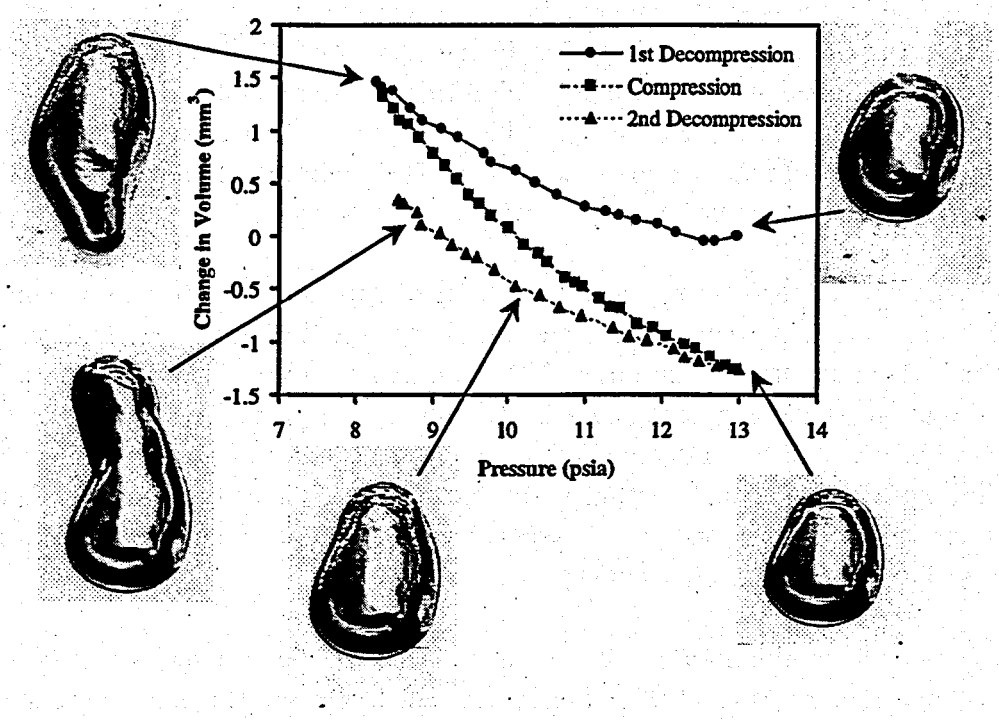

Figure 7. Change in Bubble Volume as a Function of Pressure for Decompression and Compression Cycles. Images of a few-mm-diameter bubbles are also shown at different pressures

Future experimental work will focus on completing the system integration and automation for the single-bubble experiments. Following this, a systematic series of single-bubble experiments will be conducted in simulants with a range strengths (it is particularly important to vary the ratio of pressure change to simulant strength). The transparent simulants studied so far have a narrower strength range than desired, so it is planned to test smaller particle silica materials for optical quality, refractive index matching, and ability to form stronger simulants. Multi-bubble experiments are also planned. Components for this apparatus will be purchased and assembled, and the experiments will be conducted.

Planned Activities

From an overall viewpoint, the first year of this project has been devoted to developing the mathematical and computational frameworks and experimental apparatuses and methods. Initial results have been obtained for simple models of single bubbles in both continuum (sludges) and particulate materials (slurries) and for initial experiments on single bubbles. The most substantial findings will come from the planned activities over the next (second) year as further

work is built on this framework. A detailed comparison of experimental and modeling results will be completed toward the end of the second year and the first part of the third year. The remainder of the third year will be devoted to reconciling the differences between theory and experiment, which will likely require additional experiments and numerical simulations.

References

Adams MJ, I Aydin, BJ Briscoe, and SK Sinha. 1997. "A Finite Element Analysis of the Squeeze Flow of an Elasto-Viscoplastic Paste Material." *J. Non-Newtonian Fluid Mechanics*, 71(1-2):41-57.

Chadwick P. 1959. "The Quasi-Static Expansion of a Spherical Cavity in Metals and Ideal Soils." *Quart. J. Mech. Appl. Math.*, Vol. 12, pp. 52-71.

Covey GH and BR Stanmore. 1981. "Use of the Parallel-Plate Plastometer for the Characterisation of Viscous Fluids with a Yield Stress." *J. Non-Newtonian Fluid Mech.*, Vol. 8, pp. 249-260.

Hill R. 1971. *The Mathematical Theory of Plasticity.* Oxford University Press, London.

Hopkins HG. 1960. "Dynamic Expansion of Spherical Cavities in Metals." *Progress in Solid Mechanics*, IN Snedon and R Hill, eds. North-Holland, Amsterdam, Vol. 1, pp. 85-164.

Lipscomb GG and MM Denn. 1984. "Flow of Bingham Fluids in Complex Geometries." *J. Non-Newtonian Fluid Mech.*, Vol. 14, pp. 337-346.

Lubliner J. 1990. *Plasticity Theory*, Macmillan Publishing Company, New York.

O'Donovan EJ and RI Tanner. 1984. "Numerical Study of the Bingham Squeeze Film Problem." *J. Non-Newtonian Fluid Mech.*, Vol. 15, pp. 75-83.

Zwick KJ, PS Ayyaswamy, and IM Cohen. 1996. "Variational Analysis of the Squeezing of a Yield Stress Fluid." *J. Non-Newtonian Fluid Mech.*, Vol. 63, pp. 179-199.

Presentations

Gauglitz PA and JH Konynenbelt. November 16-21, 1997. "Mechanics of Bubbles in Sludges and Slurries: Preliminary Experiments." Fluid Mechanics Poster Session, AIChE Annual Meeting, Los Angeles.

Web Site Address

http://www.doe.gov/html/em52/60451.html

Colloidal Agglomerates in Tank Sludge: Impact on Waste Processing

(First Year of Funding: FY 1996)

Lead Principal Investigator

Dr. B. C. Bunker
Pacific Northwest National Laboratory
P.O. Box 999, MSIN K8-93
Richland, WA 99352
(509) 376-1928 (phone)
(509) 376-5106 (fax)
bc.bunker@pnl.gov

Co-Investigators

Dr. J. A. Martin
Sandia National Laboratories
P.O. Box 5800
Albuquerque, NM 87185
(505) 844-9125 (phone)
(505) 844-4045 (fax)

Professor John D. Berg
Dept. of Chemical Engineering, BF-10
University of Washington
Seattle, WA 98195
(206) 543-2029 (phone)
(206) 543-3778 (fax)

Contributors

G. L. Graff (PNNL)
A. S. Lea (PNNL)
K. D. Keefer (PNNL)
D. R. Rector (PNNL)
J. M. Tingey (PNNL)
S. Stenkamp (U. of W.)
K. M. Hill (SNL)
D. A. Adolf (SNL)

Research Objective

Insoluble colloidal sludges in hazardous waste streams such as tank wastes can pose serious problems for waste processing, interfering with retrieval, transport, separation, and solidification procedures. Properties of sediment layers and sludge suspensions such as slurry viscosities, sedimentation rates, and final sediment densities can vary by orders of magnitude depending on the particle types present, the degree to which the particles agglomerate or stick to each other, and on a wide range of processing parameters such as solution shear rates, pH, salt content, and temperature. The objectives of this work are to

- understand the factors controlling the nature and extent of colloidal agglomeration under expected waste processing conditions
- determine how agglomeration phenomena influence physical properties relevant to waste processing including rheology, sedimentation, and filtration
- develop strategies for optimizing processing conditions via control of agglomeration phenomena.

Problem Statement

Disposal of millions of gallons of existing radioactive wastes is a major remediation problem for the U.S. Department of Energy (DOE). Although radionuclides are the most hazardous waste constituents, the components of greatest concern from a waste processing standpoint are insoluble sludges consisting of submicron colloidal particles. Depending on processing conditions, these colloidal particles can form agglomerated networks having high viscosities that could clog transfer lines or produce high volumes of low-density sediments that interfere with solid-liquid separations such as settle-decant operations during sludge washing and leaching. Under different conditions, the particles can be dispersed to form very fine suspended particles that will not sink during settle-decant operations and thus can foul and contaminate downstream components such as ion exchangers or filtration systems. The formation and properties of viscous sludge layers appear to be highly significant in the retention and periodic release of potentially flammable or explosive gas mixtures from the so-called "burping" tanks. Colloidal agglomerates are also important to the processing and remediation of other waste streams, including the sludges present in fuel storage basins such as the K-Basins at Hanford. Given the wide range of waste chemistries present at Hanford and other DOE sites, it is impractical to measure the properties of all possible sludge compositions under all potential processing conditions to design effective treatment procedures. Instead, a framework needs to be established to allow sludge property

trends to be predicted on a sound scientific basis. The underlying principles of colloid chemistry and physics provide such a framework, allowing us to predict and eventually control the physical properties of sludge suspensions and sediment layers in tank wastes and other waste processing streams.

Research Progress and Implications

Components of this research program include: 1) understanding the nature of the primary particles and agglomerates that compose tank sludge, 2) determining how particle and agglomerate distributions influence the physical properties of sludge, 3) understanding the critical interparticle interactions that control agglomerate distributions and slurry properties, and 4) developing chemical and physical methods to deliberately manipulate agglomerate structures during various waste processing steps. Work on the first two components has largely been completed. Work is in progress to understand how interparticle interactions influence agglomeration and sludge properties. Deliberate manipulation of colloidal interactions will be a primary program focus in FY 1999. Below are research highlights for items 1 through 3. Item 4 is discussed under Planned Activities.

Particles and Agglomerates in Actual Tank Sludge

Work done before this year demonstrated that Hanford sludges consist largely of submicron ($< 10^{-6}$ m) primary particles of hydrated oxides of Al, Fe, U, Zr, Mn, Cr, Ni, and Ti. Small particles of insoluble salts such as apatite ($Ca_5(PO_4)_3OH$), uranium phosphate, aluminum phosphate, bismuth phosphate, and the zeolite cancrinite are also present. In existing tanks, and in most proposed tank processing schemes, the particles are in contact with highly basic (pH 10–14), high ionic strength (0.1–10 M) salt solutions (mainly $NaNO_3$ and NaOH). In such solutions, the electrical double layers associated with charged sites in particle surfaces collapse, and the electrostatic repulsions that can disperse particles of like charge disappear. Therefore, under most tank waste processing conditions, the particles composing most sludges are predicted to be attracted to each other (van der Waals attraction dominates), resulting in extensive particle agglomeration. Most of the work performed in this project involves examining model suspensions containing mixtures of one or two of the major components found in actual wastes and studying how agglomeration influences physical properties such as viscosity and sedimentation. Experimental results on the simple systems are rationalized using theoretical models that describe particulate suspensions. Property models developed from theory and experiment on the simple suspensions are then applied to explain the limited results that have been obtained on actual tank wastes.

Agglomerate Structures: Impact on Sludge Properties

The key to understanding sludge properties is the realization that the agglomerates are fractal objects whose mass scales as R^D, where R is the agglomerate size and D is the fractal dimension. For a diffusion-limited aggregate, D = 1.8; a dense three-dimensional object would have a fractal dimension of 3. Fractal agglomerates can have an enormous impact on slurry properties because fractal objects have lower densities and occupy much more space than dense particles at the same solids loading. The solids loading within an individual agglomerate, Φa, is given by the expression $\Phi a = (R/r)^{D-3}$, where r is the primary particle size. As shown in Figure 1, Φa can vary over three orders of magnitude depending on the ratio of the agglomerate size to the primary particle size and the fractal dimension. When agglomerates fill the solution and begin to contact each other (at a solids loading referred to as the "percolation threshold," or "gel point" [$\Phi g = 0.17\ \Phi a$]), slurry viscosities can increase by orders of magnitude. In laboratory-scale tests, sediment densities are usually not much greater than Φg because sedimentation is slow above the gel point. Work on this project has shown that fairly accurate values for Φg can be calculated for both single component slurries and actual tank wastes if r, R, and D are determined experimentally.

For this program, primary particle size distributions have been determined using transmission electron microscopy (TEM), and agglomerate size distributions have been estimated using static light scattering on dilute suspensions. Direct measurements of the fractal dimension D have not yet been made (see Planned Activities). Based on literature studies on model systems, D = 2.2 has been used to model slurry properties (the theoretical value for a rearranged reaction-limited

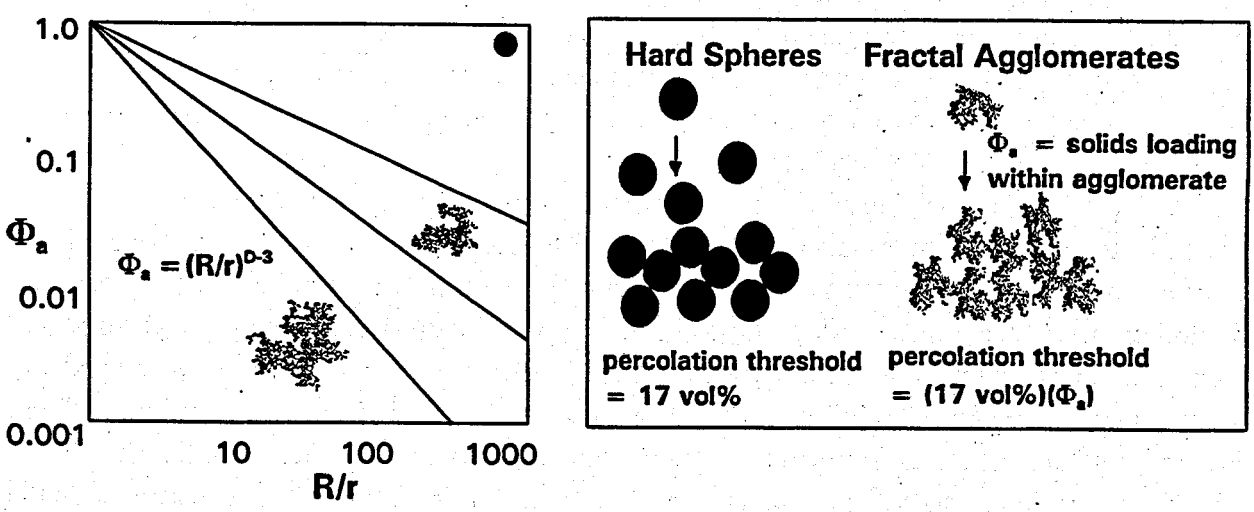

Figure 1. a) Solids Loadings Within Fractal Agglomerates as a Function of R/r and D

b) Packing of Ideal Spheres and Fractal Agglomerates

aggregate). Using experimental r and R values and D = 2.2, sediment densities have been successfully predicted to within about 20% for single component systems as well as actual sludges; solids loadings at which slurry viscosities will exceed the desired maximum of around 100 centipoise within around 30%; and sedimentation velocities in settle-decant operations to within a factor of around 5. In terms of general trends, the least tractable slurries are those containing the smallest primary particles (10 nm particles are common in actual tank sludges), the largest agglomerate sizes, and the smallest fractal dimensions. Such slurries can have viscosities in excess of 10,000 centipoise at solids loadings as low as 1 vol%, which corresponds to the lowest sediment densities. At the other extreme, slurries containing noninteracting primary particles larger than 10 μm can exhibit viscosities below 100 centipoise even at 30 vol% and pack to form dense sediments having solids loadings exceeding 35 vol%. Of the 20 or so distinct Hanford wastes examined to date, most exhibit gel points of from 1–8 vol% consistent with the fine primary particles observed in most sludges using TEM. For the finest sludges, dilution factors as high as 20 may be required to avoid plugging pipes and transfer lines with viscous colloidal gels, generating millions of gallons of additional waste requiring treatment and ultimate disposal.

Interparticle Interactions: Impact on Sediment Densities

While we can now predict sludge properties if agglomerate structures are known, we cannot yet predict what agglomerate structures will be present under a given set of processing conditions. To make such predictions, we need to develop models that relate agglomerate structures to interparticle interaction potentials. Interaction potentials are critical to controlling sludge properties because they control 1) whether primary particles are dispersed or agglomerated, 2) what agglomerate sizes and structures are stable, and 3) the ease with which agglomerates can be consolidated, deformed, or disrupted. The focus of research at Pacific Northwest National Laboratory (PNNL) during FY 1998 has been on attempting to understand the relationships between interaction potentials and sediment densities in the high-salt, high-pH regime representative of most tank wastes. Work done before FY 1998 showed that changes in salt content from sludge washing and leaching operations can change sediment volumes by as much as a factor of 2, having an enormous impact on processing tank utilization and separation efficiencies. The practical goal is to be able to predict and control sediment densities in basic salt solutions. This regime is also of significant scientific interest because interaction potentials in such solutions cannot be described using classical electrical double-layer theory (the double layers collapse in high ionic strength solutions).

During sedimentation, individual agglomerates sink until they come into contact with each other near the percolation threshold. At solids loadings above the percolation threshold (Φg), the sediment layer can continue to settle by collapsing under its own weight. In a full-scale tank,

such collapse can be significant, resulting in higher sediment densities than are indicated by lab-scale testing. By determining the volume occupied by the sediment as a function of applied pressure (varied by changing the sediment mass or via centrifugation), it is possible to extract values for the gel point and the compressive yield stress of the sediment (which is a measure of how deformable and compressible the sediment is.) Once these parameters are known, sediment densities can be predicted for a wide range of processing geometries, including extrapolation from laboratory-scale tests to sedimentation in a one million-gallon tank.

First, experiments were conducted to determine how salt content influences sediment densities. Sedimentation studies were conducted on 1.3-μm primary particles of gibbsite [$Al(OH)_3$] suspended in sodium nitrate solutions at different salt concentrations and pH values. At pH 4 and with no salt present, the primary particles of gibbsite are dispersed. Because the particles are relatively large, they settle within a few days. The dispersed particles pack efficiently as they settle, yielding a sediment with a density of 50 vol% (the theoretical maximum solids loading for packed spheres is 63 vol%). Such sediment would be ideal for maximizing the efficiency of solid-liquid separations. In contrast, the same gibbsite particles suspended in 0.1 M $NaNO_3$ yield a sediment density of only 4 vol% solids (consistent with 6–7 μm fractal agglomerates each containing around 30 primary particles). This means that the agglomerated sludge occupies over 10 times more space and contains 24 times the volume of nonremovable interstitial liquids than the sediment formed from the dispersed sludge, which has an adverse impact on the efficiency of solids-liquids separations.

Interestingly, as salt concentrations are increased still further to 5 M, sediment densities increase to 5.1 vol%, suggesting that "short-range" or "hydration" forces associated with adsorbed salt layers might be weakening the interactions between particles. High salt concentrations could also change sediment densities by changing agglomerate structures. To investigate the role of adsorbed ions on interparticle interactions, systematic variations were made in the cations and anions present in dissolved salts to examine whether specific ions were more effective than others in weakening sediment structures. Gibbsite particles were suspended in aqueous solutions containing various salts ($NaNO_3$, NaCl, CsCl, LiCl, $Mg(NO_3)_2$, $CaCl_2$, and $BaCl_2$) as a function of pH (pH 4 – 14) and salt concentration (10^{-2} M – 5 M) (Figure 2). All salts tested promote sediment compression at concentrations above 1 M. While anion (Cl^- for NO_3^-) and cation (Li^+ or Cs^+ for Na^+) substitutions have no apparent effect, salts of divalent cations (Mg^{2+}, Ca^{2+}, Ba^{2+}) all promote sediment compression. Most dramatic is the effect of $CaCl_2$, which yields sediments having a solids loading of over 15 vol% (twice the particle density seen in $NaNO_3$ solutions). The effect is not merely an ionic strength effect, as $BaCl_2$:NaCl mixtures having the same ionic strength but different Ba:Na show greater compression as the Ba content is increased. The results suggest that heavily hydrated cations can act as "molecular ball bearings," allowing agglomerates to deform and compact. The results represent one example of how it may be possible to use chemical additives to control sludge behavior. Work performed at

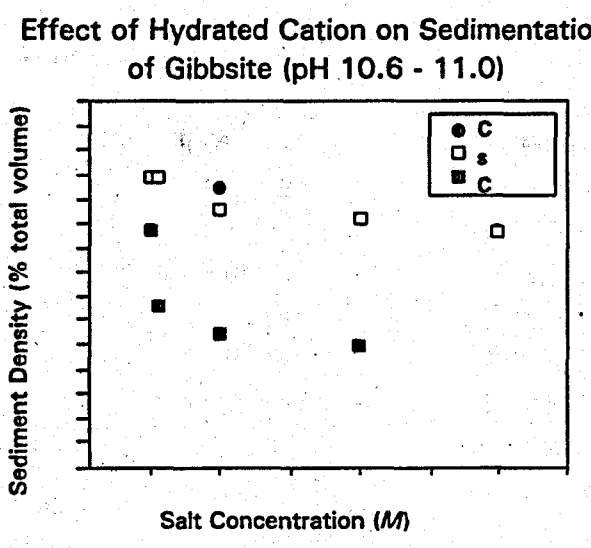

Figure 2. Volume Occupied by Sediment Layers as a Function of the Presence of Various Salts

the University of Washington on this project is being directed at understanding how organic molecules called steric stablizers function in the high salt regime of tank wastes. Once the factors controlling steric stabilization at high ionic strength are understood, it may be possible to manipulate sludge behavior with low concentration of such organic additives.

The focus of research at Sandia National Laboratory (SNL) during FY 1998 has been on understanding the relationships among interparticle forces, agglomeration, and slurry viscosities. Rheology measurements have been conducted on model slurries consisting of 0.7-μm silica spheres suspended in a solvent consisting of 25% formamide and 75% benzyl alcohol. (The solvent system has been selected to index-match the silica spheres for light-scattering measurements of agglomerate structures in FY 1999.) In this solvent system, the particles are normally dispersed. Agglomeration can, however, be induced by adding ammonium hydroxide, which collapses the electrical double layers in this solvent just as salt does in tank waste. By systematic variation of the interparticle potential and the solids loading, the rheological behavior of the suspensions can be altered to yield Newtonian solutions as well as slurries that are either shear thinning (viscosity decreasing with shear rate) or shear thickening (viscosity increasing with shear rate). When the silica spheres are dispersed, slurry viscosities are low and the behavior is nearly Newtonian until solids loadings exceed around 30 vol% solids (Figure 3). Such behavior would be ideal for retrieval and transport operations (viscosities below 1 poise are desired). At high solids loadings, shear actually forms particulate chains that resist fluid motion, resulting in shear thickening solutions. Agglomerated slurries (Figure 4) exhibit behavior in sharp contrast to the dispersed slurries. At low shear rates, slurry viscosities exceed the desired 1 poise until the solids loading is below around 8 vol%. However, while slurry viscosities are high, the agglomerated systems are shear thinning. Here, solution agitation disrupts existing agglomerates, lowering slurry viscosities.

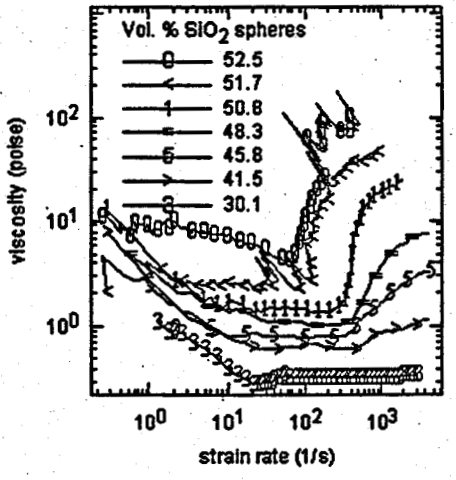

Figure 3. Rheology for Suspensions of Silica Spheres in 0.003 M NH_4OH as a Function of Solids Loading (vol%)

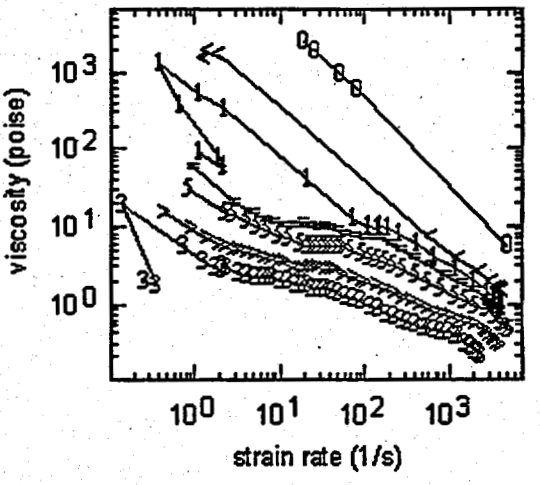

Figure 4. Rheology for Suspensions of Silica in Spheres in 0.3 M NH_4OH as a Function of Loading (vol%)

Planned Activities

While work performed to date suggests that short-range forces are important in controlling the properties of tank sludge, quantitative models do not yet exist to predict sludge properties such as sediment densities or slurry viscosities based on interaction potentials. Complementary activities in progress to develop predictive tools include:

Short-range forces – interaction potentials will be measured between surfaces relevant to tank waste disposal using a surface-forces apparatus. Initial experiments will measure the forces between two mica plates (representative of aluminosilicates in tank wastes) in various concentrated salt solutions down to separation distances of a few angstroms to determine the magnitude of the short-range hydration forces. Subsequent experiments will involve examining mica surfaces coated with other oxides such as aluminum oxide using techniques such as molecular beam epitaxy.

Measurement of agglomerate sizes – light-scattering experiments will be conducted on dilute gibbsite suspensions mirroring the sedimentation experiments described above. The results will provide an independent estimate of Φg to compare with values obtained via sedimentation and will establish whether changes in agglomerate sizes contribute to changes in sediment density.

Measurement of agglomerate structures – Our small-angle x-ray scattering (SAXS) equipment is now in operation. SAXS measurements will be performed on zirconia suspensions in both static and sheared solutions to determine how different salts influence the fractal dimension and size of agglomerates representative of the least tractable tank wastes (e.g., those containing submicron particles). SAXS measurements will be complemented by light-scattering measurements performed at SNL.

Modeling of agglomerate properties – Computer codes have been developed at PNNL and SNL using Brownian dynamics that can be used to calculate the kinetics of diffusion-limited aggregation of primary particles, provide information regarding steady-state agglomerate sizes and structures, and calculate the ease of deformation of agglomerates as a function of the magnitude of interaction potentials and bonding between particles. The models will be refined using the experimentally determined interaction potentials, agglomerate structures, and compressive yield stress data described above.

Once quantitative models and experimental methods are in place to determine interparticle interaction potentials, predict agglomerate structures based on interaction potentials, and predict properties based on agglomerate structures, the primary focus of the project will shift to deliberate modification of sludge suspensions to optimize properties for retrieval, transport, and sedimentation processes.

Publications

Bunker BC, J Liu, DR Rector, GL Graff, PA Smith, PJ Bruinsma, L Song, XS Li, JD Virden, NG Colton, JR Philips, KD Keefer, and JM Tingey. 1998. "Fractal Colloidal Agglomerates in Nuclear Tank Wastes: Impact on Waste Properties and Processing." Submitted to *Science*.

Stenkamp VS and JC Berg. 1997. "The Role of Long Tails in Steric Stabilization and Hydrodynamic Layer Thickness." Langmuir, **13**, 3827.

Hill KM, JE Martin, and DA Adolf. 1998. "Rheology of Colloidal Suspensions and Its Implication for Tank Waste Processing." Proceedings of *Materials Research Society Symposium*, Spring 1998. San Francisco, California.

New Silicotitanate Waste Forms: Development and Characterization

(First Year of Funding: FY 1997)

Principal Investigator

Dr. Mari Lou Balmer
Pacific Northwest National Laboratory
P.O. Box 999, MSIN K8-93
Richland, WA 99352
(509) 372-4693 (phone)
(509) 376-5106 (fax)
lou.balmer@pnl.gov

Co-Investigators

Dr. Tina Nenoff
Sandia National Laboratories
P.O. Box 5800
Alburquerque, NM 87185-0709
(505) 844-0340 (phone)
tmnenof@sandia.gov

Prof. Alexandra Navrotsky
Department of Chemical Engineering and Material Science
University of California-Davis
Davis, CA 95616
(916) 752-3292 (phone)
anavrotsky@ucdavis.edu

Dr. Yali Su
Pacific Northwest National Laboratory
P.O. Box 999, MSIN K8-93
Richland, WA 99352
(509) 376-5290 (phone)
(509) 376-5106 (fax)
ya.su@pnl.gov

Contributors and Collaborators

Bruce Bunker (PNNL)

Research Objective

The objective of this program is to identify new waste forms and disposal strategies specific to crystalline silicotitanate (CST) secondary waste that is generated from Cs and Sr ion-exchange processes, in particular, in situ heat treatment of CSTs to produce an alternate waste form. Waste forms that are developed in this work will offer an alternative to current disposal plans, which call for recombining the separated Cs- and Sr-loaded CST into the high-activity waste streams, then dissolving it in borosilicate glass. The goals of the program are to reduce the costs associated with CST waste disposal, to minimize the risk of contamination to the environment during CST processing, and to provide DOE with technical alternatives for CST disposal. Because there is uncertainty in repository availability and in waste acceptance criteria, it is likely that Cs- and Sr-loaded ion exchangers will require short-term storage at Hanford or that new scenarios for long-term storage or disposal of nuclides with relatively short half-lives (such as ^{137}Cs and ^{90}Sr) will arise. Research activities in this program will generate information on the durabilities and stabilities of thermally consolidated CSTs so that the potential of these options as viable storage or disposal scenarios can be evaluated. The technical objectives of the proposed work are to fully characterize the phase relationships, structures, and thermodynamic and kinetic stabilities of CST waste forms and to establish a sound technical basis for understanding key waste form properties, such as melting temperatures and aqueous durability, based on an in-depth understanding of waste form structures and thermochemistry.

Research Statement

Plans are in place to retrieve, separate, and immobilize radioactive waste contained in 177 underground storage tanks at the Hanford Site. Likewise, nuclear wastes at other DOE sites across the country must be immobilized in a stable waste form for storage in underground repositories. A viable waste form must be chemically durable under environmental storage conditions (aqueous environments are of primary concern) and thermally stable under repository conditions over a geologic time scale. In addition, an adequate waste form should be capable of incorporating specific waste feeds to form a stable glass or ceramic material with a minimum of dilution (to minimize waste volumes) and be easy to process under remote-handling conditions. Relatively low processing temperatures and simple heat-treatment cycles are desirable.

Borosilicate glass has been chosen as the baseline host for immobilization of high-activity waste (HAW) at the Hanford Site. However, CST, the most promising candidate for removal of Cs and Sr from tank wastes, has been identified as a risk to the borosilicate vitrification process. Rutile (TiO_2) in the CST promotes crystallization and immiscible phase separation and affects the redox state and solubility of uranium in glass (Ewest and Wiese 1987; Galakhov et al. 1988;

Bickford et al. 1990; Plodinec 1980). Because of this, a TiO_2 limit of 1 wt% is set for borosilicate waste glass at the Savannah River Defense Waste Processing Facility (DWPF) (see Plodinec 1980). If these high levels of waste dilution are required to stabilize CST waste, the volume of expensive high-activity borosilicate waste glass produced for subsequent storage will be substantially increased. Dissolution of the CST in borosilicate glass (as opposed to direct thermal conversion) necessitates removal and transfer of the CST from the column, mixing with glass frit, and melting. Each of these steps significantly increases the risk of contamination to workers or the environment. The volume of HAW can be minimized, and the process can be simplified by converting the separated, compositionally homogenous loaded exchanger into an alternative waste form, rather than recombining it with the HAW for dissolution in glass.

Cesium-loaded silicotitanate ion exchangers contain the basic ingredients that can form a ceramic or glass at high temperature. The premise of this work is that, for CST ion exchange waste, waste forms can be tailored to specific waste feeds, rather than attempting to tailor waste feeds to a single waste form. Direct in situ, thermal conversion of the CST will consolidate and immobilize the loaded ion-exchange particulates, minimize handling risks, and remove water and hydroxyl groups, thus eliminating radiolytic hydrogen generation during storage.

The research strategy for developing an alternative waste form for CSTs is based on an understanding of ceramic and glass structures and phase stabilities. The key components of the research include:

- determination of stable and metastable phases that form from heat treatment of the CST and development of phase diagrams for the component systems
- characterization of the structures of ceramic and glass waste-form candidates
- development of structure-property relationships to provide predictive capabilities of key performance parameters, including aqueous leach resistance, melt temperatures, melt viscosities, and ease of crystallization for select waste forms
- determination of the enthalpies and free energies of formation of key compounds by high-temperature oxide melt solution calorimetry.

Research Progress

Durability of Thermally Converted CST

The durabilities of several Cs-loaded, thermally converted CST waste forms have been measured. Universal Oil Products (UOP) CSTs, designated IE-911, were ion-exchanged for 5 and 12 wt% Cs using two methods. In the first method, as-received IE-911 was exchanged for Cs using CsOH solutions. In the second method, IE-911 was pre-treated with NaOH solution until the pH of the eluting solution was higher than 12.5, then exchanged using CsOH solution. Pretreatment of NaOH is recommended by UOP. While the maximum loading on the CST is likely to be only 5 wt% Cs, samples were loaded to 12 wt% Cs to exaggerate potential Cs loss during leaching and to facilitate phase identification of Cs-containing compounds. The Cs-exchanged materials were heat-treated to temperatures ranging from 500°C to 1000°C, analyzed by x-ray diffraction (XRD) for phase selection, then characterized for chemical durability. Chemical durability was measured using the standard product consistency test (PCT) and the MCC-1 leach test. The PCT, which specifies the use of powders in solution, can yield high solution concentrations of leached elements and concomitant reduction of dissolution rates to yield unrealistically high durabilities. The MCC-1 test, which suspends a pellet in solution, yields conservative durabilities because solution concentrations of the elements are comparatively low and leaching continues during the entire leach period.

Figure 1 shows the PCT aqueous leach rate of Cs as a function of time for IE-911, which was Na-exchanged, 12 wt% Cs-exchanged, and heat-treated over a range of temperatures. The leach rates were extremely low, ranging from 10^{-8} to 0.002 g/m^2•day. The untreated, 500°C and 900°C treatments exhibited the lowest Cs leach rates, and the total fraction of Cs released for these samples was less than 1 wt% after seven days. These thermally converted waste forms are several orders of magnitude more durable than borosilicate glass. Standard engineering assessment (EA) borosilicate glass shows a seven-day leached concentration of alkali of 13.3 g/L (there is no Cs in this standard, only Na) (Ferrara et al. 1997). By comparison, IE-911 heat-treated to 900°C has a seven-day Cs concentration of 0.008 g/L or, in the worst case for the 700°C heat treatment, the seven-day Cs concentration is 0.175 g/L. For additional comparison, a borosilicate glass formulation, R7T7, which contains 1.42 wt% Cs and a total alkali content of 13.26 wt%, has a Cs leach rate of 0.16 g/m^2•day (Nogues et al. 1984).

As measured by the PCT test, the aqueous durability behavior for both as-received and Na-exchanged IE-911 loaded to 5 wt% and 12 wt% Cs did not show any significant differences. Leach rates measured using the MCC-1 test were even lower than those measured by the PCT test, as expected.

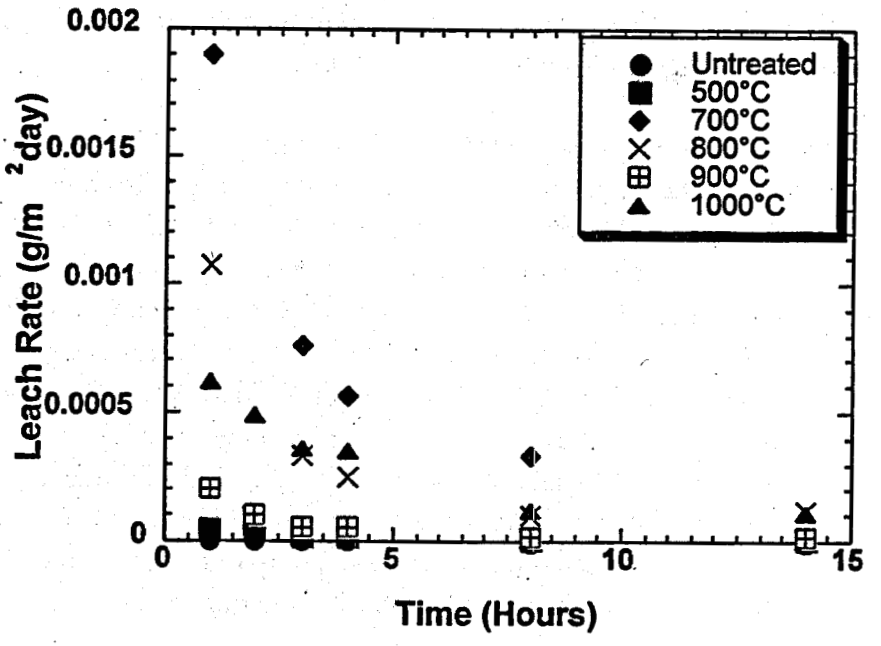

Figure 1. PCT Aqueous Leach Rate for Waste Forms Synthesized by Heat-Treating CST IE-911 over a Range of Temperatures. Before heat treatment, IE-911 was treated with NaOH and exchanged for 12 wt% Cs.

The durability tests show that heat-treated IE-911 with no additives can result in a chemically durable waste form. The durability or Cs mobility is related to the crystal structure of the Cs-containing compounds. X-ray, transmission electron microscopy (TEM), and nuclear magnetic resonance (NMR) studies were initiated to identify the phases and the local environment of the Cs in this compositionally complex exchanger.

Phase Selection of Thermally Converted CST

Phase stability and crystal chemistry studies for compositions related to the exchanger are vital to predicting long- and short-term performance of waste forms. Cesium-loaded IE-911 contains six or more constituents, including Cs_2O, Na_2O, SiO_2, TiO_2, a binder, and proprietary components. While the phase relationships between some of the binary and ternary components of the CST are available in the literature, the phase selection and durabilities of more complex compositions that represent the loaded exchanger are unknown.

X-ray diffraction of heat-treated IE-911 powders shows that the single-phase metastable ion exchanger structure is destroyed above 500°C; then, at higher temperatures, stable multiphase crystalline mixtures precipitate. A large amorphous fraction appears at temperatures between the destruction of the low-temperature phase and the reprecipitation of the stable high-temperature phase. This amorphous regime corresponds to the lowest leach rates. At 900°C, where a large

portion of the sample is crystalline, high durabilities are measured. At 1000°C, partial melting occurs and the leach rate increases slightly.

Many of the structures of the phases in the crystalline mixture could be matched to existing compounds. However, several peaks in the pattern could not be identified and therefore represent a new phase or phases. In addition, the structures of phases that were identified do not match any compounds that contain Cs. It was concluded that the Cs is either located in a residual amorphous phase or in solid solution with one of the crystalline compounds identified. Cesium-133 magic angle spinning NMR measurements were performed to reveal the local environment around the Cs atom. Figure 2 shows the NMR spectra for NaOH-treated, Cs-exchanged IE-911, heat-treated over a range of temperatures. It can be seen from the spectra that the Cs environment in the as-received exchanger is destroyed above 500°C. Broadening of the peak at 500°C indicates that the material is becoming amorphous. At 700°C, a new Cs-containing phase forms, and by 800°C, the peak representing the original Cs environment is completely gone. The single, sharp, high-temperature peak indicates that the Cs is in only one crystalline environment.

We suspect that the Cs may be contained in a sodium titanate phase, $Na_2Ti_6O_{13}$, because the relative intensity of several XRD peaks was observed to change as a function of increasing Cs-loading. An XRD simulation with Cs substitution on the Na site showed that these peaks are affected by Cs concentration. To confirm that the Cs is in solid solution with this compound, a series of $(Na,Cs)_2Ti_6O_{13}$ compounds will be synthesized and the experimental XRD and Cs NMR will be compared with phases observed in heat-treated IE-911.

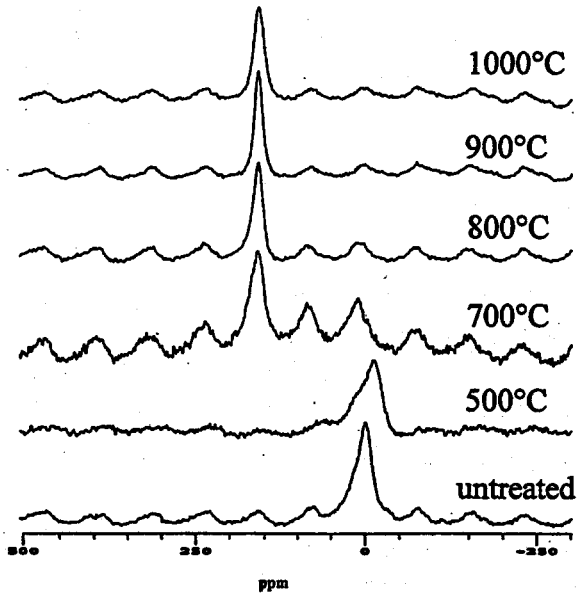

Figure 2. ^{133}Cs MAS NMR Spectra for NaOH-Treated, 12 wt% Cs-Exchanged IE-911, Heat-Treated over a Range of Temperatures

Phase equilibria studies in the model system Cs_2O-TiO_2-SiO_2 are being performed to identify the stable compounds in this system and to determine their compositional regions of stability (Su et al. 1998; Balmer et al. 1997a, 1997b; McCready et al. 1997; Grey et al. 1997). The phase relationships for compositions related to the ion exchanger will provide information necessary for setting optimal composition and temperature regimes for processing the final waste form and will elucidate the effects of minor compositional variations. The current understanding of the phase equilibria is illustrated in Figure 3. Single-crystal growth experiments have produced a new tetragonal structure that is similar to cubic pollucite (1:2:4 Cs_2O-TiO_2-SiO_2) but with extended TiO_2 solubility. In addition, a new compound with stoichiometry 1:1.2:1.7 Cs_2O-TiO_2-SiO_2 has been identified. Crystal structure determination of these new compounds is underway.

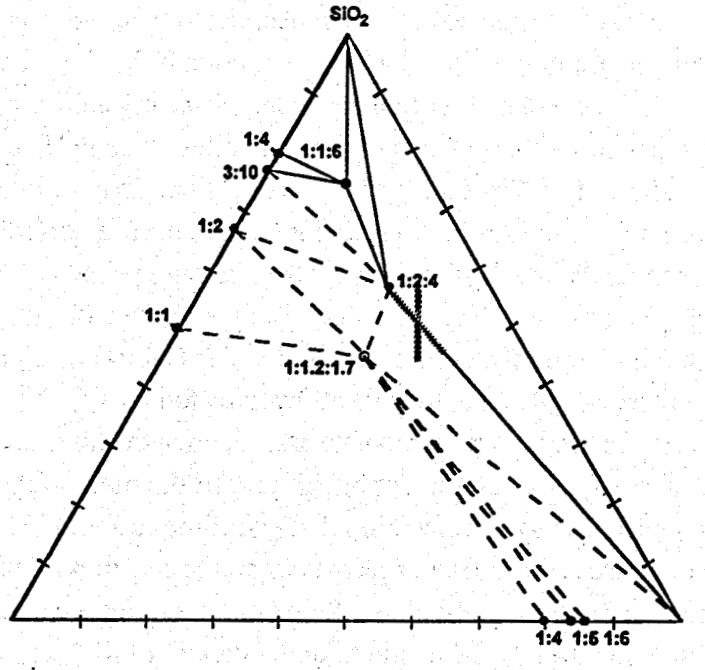

Figure 3. Phase Equilibrium Diagram for Cs_2O-TiO_2-SiO_2

Thermogravimetric and differential thermal analysis of Cs-exchanged and Na,Cs-exchanged IE-911 was performed to determine decomposition and crystallization temperatures. This analysis revealed that all molecular water is desorbed by 400°C and that hydroxyl groups are removed near 800°C. Therefore, the risk of radiolytic hydrogen production during short- or long-term storage is eliminated by heat-treating the ion exchanger to temperatures above 800°C. The volume reduction of a pellet heat-treated to 900°C is 40%.

Metastable Cs_2O-TiO_2-SiO_2 Phase Selection

Hydrothermal synthesis techniques have been used to search the Cs_2O-TiO_2-SiO_2 phase space in an attempt to synthesize phases that may crystallize during the formation of a CST-derived ceramic. The phases synthesized under hydrothermal conditions (low temperature, solution mixtures) generally tend to be metastable and in larger quantities than those synthesized at high temperatures (>700°C). These phases are of interest because 1) their stability will be compared to high-temperature phases and 2) they will be used in thermodynamic studies to help develop models of phase equilibria.

Early procedures were directed toward the hydrothermal synthesis of the Cs/Si/Ti analog of the mineral pollucite. This phase has not been synthesized to date; however, two new phases have been synthesized and are now being characterized (A and B). Results show that phase A is a condensed (BET: 29 m^2/g) cesium silicotitanate. This phase crystallizes (>90% purity) as clear rod-like crystals that contain no internal H_2O molecules. The PCT leach tests performed on this phase for 10 days showed <0.2% Cs loss from the original Cs composition, which was 30% by weight; effectively no Cs was lost due to leaching. Furthermore, after PCTs, Phase A showed no crystallographic change. Work continues to synthesize pure phase A for thermodynamic studies. Phase B is an open "zeolitic" cesium silicotitanate phase with needle-like crystals. Thermal data show that it contains internal water molecules (10 wt%). X-ray diffraction and scanning electron microscopy (SEM) data have allowed us to identify this phase B in the impure product mixture. Work continues to better isolate and identify this phase. Phase A appears to be a condensed phase that grows out of the reaction mixture of the metastable phase B. With monitoring by XRD, phase B is synthesized in 2.5 days; if the reaction is allowed to continue for five days, a mixture of phases A and B are present; when the reaction mixture is allowed to continue for 10 days, the product is only phase A. As crystallographic studies continue to refine the structures, particular attention will be paid to understanding this phase transformation.

Thermodynamic Studies Using Solution Drop Calorimetry

Thermodynamic studies on a known sodium titanosilicate $(Na(Ti_4O_4)(SiO_4)_2\,(OH)\text{-}4H2O)$ have been performed in an effort to begin developing the data necessary for modeling of phase equilibria and comparing the stabilities for new phases. A heat of formation (H_f) for this material was determined to be -508 ± 15.33 kJ/mol.

Summary

The first seven months of work have shown that a very durable waste form can be achieved by a simple heat treatment of the Cs-loaded ion exchanger with no additives. Direct thermal conversion reduces the total volume of waste generated from the ion exchanger and dramatically

simplifies processing. Heat treatment of the ion exchanger coarsens fines, reducing inhalation risk, and removes water, eliminating radiolytic hydrogen production. The IE-911 CST ion exchanger is compositionally complex. The heat-treated waste forms that show excellent durability consist of a mixture of crystalline phases, some of which have not been previously characterized. Preliminary results indicate that the Cs resides in solid solution in a crystalline sodium titanate.

Planned Activities

Future work will concentrate on identifying all Cs-containing phases in the heat-treated waste forms and determining their thermodynamic stabilities so that long-term predictions of durability can be made. A solid solution series of $(Cs,Na)Ti_6O_{13}$ compounds will be synthesized for analysis by XRD, NMR, and solution drop calorimetry. The stability of Cs-containing compounds that radioactively decay to ^{137}Ba is of concern. When Cs-containing phases have been identified and characterized, solid solutions such as $(Ba, Cs, Na)_2Ti_6O_{13}$ will be synthesized and analyzed for stability, chemical durability, crystal structure type, and Cs environment. Crystal growth studies revealed that there is a tetragonal phase with composition near the cubic pollucite phase. Diffraction and differential scanning calorimetry studies will be performed on this phase to determine if there is a low-temperature cubic-to-tetragonal transition. Hydrothermal synthesis methods have revealed two new phases. Variations in reaction conditions will be attempted to synthesize phase pure samples for XRD and thermochemical analysis.

References

Balmer ML, BC Bunker, LQ Wang, CHF Peden, and Y Su. 1997a. "Solid State ^{29}Si MAS NMR of Titanosilicates." *J. Phys. Chem.*, 101(45):9170-9179.

Balmer ML, Q Huang, A Santoro, and R Roth. 1997b. "Neutron Powder Diffraction Study of the Crystal Structure of $CsTiSi_2O_{6.5}$." *J. Sol. State Chem.*, 130:97-102.

Bickford DF, A Applewhite-Ramsey, CM Jantzen, and KG Brown. 1990. "Control of Radioactive Waste Glass Melters: I, Preliminary General Limits at Savannah River." *J. Am. Cer. Soc.*, 73(10):2896-2902.

Ewest E and H Wiese. 1987. "High Level Liquid Waste Vitrification with the PAMELA Plant in Belgium." In IAEA-CN-48/177, pp. 269-280. International Atomic Energy Agency, Vienna.

Ferrara DM, MK Andrews, JR Harbour, TL Fellinger, DT Herman, KM Marshall, and PJ Workman. 1997. *Vitrification of Ion Exchange Material.* WSRC-TR-97-00320, Westinghouse Savannah River Corp., Aiken, South Carolina.

Galakhov FY, VT Vavilonova, VI Aver'yanov, and TV Slyshkina. 1988. "An Experimental Determination of the Region of Liquid-Liquid Phase Separation in the Li_2O-Al_2O_3-TiO_2-SiO_2 System." Translated from *Fiz. khim. Stekla,* 14(1):38-46.

Grey IE, RS Roth, and ML Balmer. 1997. "The Crystal Structure of $Cs_2TiSi_6O_{15}$." *J. of Sol. State Chem.,* 131:38-42.

McCready DE, ML Balmer, and KD Keefer. 1997. "Experimental and Calculated X-Ray Powder Diffraction Data for Cesium Titanium Silicate, $Cs_2Ti_2Si_4O_{13}$: A New Zeolite." *Powder Diffraction,* 12(1):40-46.

Nogues JL, EY Vernaz, and N Jacquet-Francillon. 1984. *The Scientific Basis for Nuclear Waste Management,* Vol. 44, CM Jantzen, JA Stone, and RC Ewing, eds. Materials Research Society, Pittsburgh, Pennsylvania.

Plodinec MJ. 1980. "Development of Glass Compositions for Immobilization of Savannah River Plant Waste." *Scientific Bases for Nuclear Waste Management,* CJM Northrup Jr. ed. Vol. 2, pp. 223-229.

Su Y, DE McCready, and ML Balmer. 1998. "Calculated X-Ray Powder Diffraction Pattern for Cesium Titanium Silicate, $Cs_2TiSi_6O_{15}$." Submitted to *Powder Diffraction.*

Publications

Y Su, DE McCready, and ML Balmer. 1998. "Calculated X-Ray Powder Diffraction Pattern for Cesium Titanium Silicate, $Cs_2TiSi_6O_{15}$." Submitted to *Powder Diffraction.*

ML Balmer, BC Bunker, LQ Wang, CHF Peden, and Y Su. 1997. "Solid State ^{29}Si MAS NMR of Titanosilicates." *J. Phys. Chem.,* 101(45):9170-9179.

Presentations

Balmer ML. March 29-April 2, 1998. "Evaluation of Thermally Converted Silicotitanate Waste Forms." 215th Annual Meeting of the American Chemical Society, Dallas.

Nenoff TM. March 29-April 2, 1998. "CST's: Stability and Use as an Alternative Waste Form." 215th Annual Meeting of the American Chemical Society, Dallas.

Architectural Design Criteria for f-Block Metal Sequestering Agents

(First Year of Funding: FY 1996)

Principal Investigator

Dr. Benjamin P. Hay
Pacific Northwest National Laboratory
P.O. Box 999, MSIN K9-77
Richland, WA 99352
(509) 372-6239 (phone)
bp_hay@pnl.gov

PNNL Contributors

Dr. Omoshile Clement
Dr. David A. Dixon
Dr. Gregg J. Lumetta
Dr. Linfeng Rao
Dr. Brian M. Rapko

External Collaborators

Prof. D. Max Roundhill
Department of Chemistry
Texas Tech University
Lubbock, TX 79409-1061
(806) 742-3067 (phone)
uldmr@ttacs.ttu.edu

Prof. Robin D. Rogers
Department of Chemistry
The University of Alabama
Tuscaloosa, AL 35487-0336
(205) 348-4323 (phone)
rdrogers@ua1vm.ua.edu

Prof. Robert T. Paine
Department of Chemistry
University of New Mexico
Albuquerque, NM 87131
(505) 277-1661 (phone)
rtpaine@unm.edu

Prof. Kenneth N. Raymond
Department of Chemistry
University of California at Berkeley
Berkeley, CA 94720
(510) 642-7219 (phone)
raymond@garnet.berkeley.edu

Contributors

Dr. Bruce K. McNamara (Post Doctoral Research Associate)
Dr. Giovanni Sandrone (Post Doctoral Research Associate)
Dr. Pier L. Zanonato (Visiting Scientist, University of Padova, Italy)

Research Objective

The objective of this project is to provide the means to optimize ligand architecture for f-block metal recognition. Our strategy builds on an innovative and successful molecular modeling approach in developing polyether ligand design criteria for the alkali and alkaline earth cations. The hypothesis underlying this proposal is that differences in metal ion binding with multidentate ligands bearing the same number and type of donor groups are primarily attributable to intramolecular steric factors. We propose quantifying these steric factors through the application of molecular mechanics models.

The proposed research involves close integration of theoretical and experimental chemistry. The experimental work entails synthesizing novel ligands and experimentally determining structures and binding constants for metal ion complexation by series of ligands in which architecture is systematically varied. The theoretical work entails using electronic structure calculations to parameterize a molecular mechanics force field for a range of metal ions and ligand types. The resulting molecular mechanics force field will be used to predict low-energy structures for unidentate, bidentate, and multidentate ligands and their metal complexes through conformational searches. Results will be analyzed to assess the relative importance of several steric factors including optimal M-L length, optimal geometry at the metal center, optimal geometry at the donor atoms (complementary), and conformation prior to binding (preorganization). An accurate set of criteria for the design of ligand architecture will be obtained from these results. These criteria will enable researchers to target ligand structures for synthesis and thereby dramatically reduce the time and cost associated with metal-specific ligand development.

Problem Statement

Critical tasks in the cleanup of U.S. Department of Energy (DOE) sites include processing radioactive wastes for disposal in long-term storage, remediation/restoration of environmental sites resulting from radioactive contamination, and decontamination/decommissioning of nuclear facilities. Because the radioactive components, most of which are metals, are typically present in very low concentrations, it is desirable to remove them from the bulk of the contaminated source (process waste stream, groundwater, soil) and concentrate them to minimize the volume of radioactive material destined for permanent subsurface disposal and thus minimize disposal costs. One group of radionuclides, the actinides, which are pervasive throughout the DOE complex, is of special concern. In particular, thorium, uranium, neptunium, plutonium, americium, and curium with half-lives ranging from 10^2 to 10^6 years can all be found in various DOE

wastes, contaminated soils and groundwaters, and contaminated facilities. Lanthanide elements are also of concern because they form an important group of fission products that can persist in radioactive wastes for decades (e.g., ^{152,154,155}Eu).

Organic ligands with a high degree of metal ion specificity are essential components for developing separations processes for metal ions. Over the past 50 years, much research has focused on the discovery of selective ligands for f-block metal separations; both neutral and ionic ligands have been examined. Despite past success in the discovery of ligands that exhibit some degree of specificity for the f-block metal ions, the ability to further control binding affinity and selectivity remains a significant challenge to the synthetic chemist. The approach for developing these ligands has involved lengthy and costly experimental programs of organic synthesis and testing, which, in the absence of reliable methods for screening compounds before synthesis, requires an extensive research effort. Criteria for accurately selecting target ligands would result in much more effective use of resources.

Research Progress

This project combines a theoretical and experimental approach to developing ligand design criteria for selective complexation of f-block metal ions. These criteria will address how to best connect donor functionality to achieve metal ion recognition in multidentate ligands. For the f-block metal ions, donor groups of interest include amides, phosphine oxides, pyridine N-oxides, and catechols. Scoping studies were performed on these ligands during the first year of the project, FY 1997. A decision was made to focus solely on amides. Ligands containing the amide functional group are currently used in DIAMEX (an actinide separation process used for treatment of commercial reprocessing wastes) and TRUEX (actinide separation process under testing for use in tank waste cleanup at Idaho National Engineering and Environmental Laboratory).

The DIAMEX process uses a diamide ligand as the actinide extractant. Diamides such as malonamide and succinamide contain two oxygen donor groups and can form bidentate complexes. A bidentate ligand is the simplest case in which the issue of binding site organization arises. There are three structural variables that can affect binding site organization in a diamide: the length of the bridge between the two amides, the degree of bridge alkylation, and the steric bulk of the alkyl groups attached to the nitrogen. Understanding the effect of these structural variables on metal ion complexation provides criteria for optimizing the performance of multidentate amide ligands. In FY 1998 our research focuses on the synthesis and characterization of diamides and their complexes, the development and application of methods to measure ligand

binding affinities for f-block metals, and the development of a force field model for these ligands and their metal complexes. The goal is to generate structure-function data and to correlate these data with the molecular mechanics model. In a parallel effort, Prof. D. Max Roundhill is preparing a series of calixarene amides and studying their behavior as metal ion extractants. We plan to use the molecular mechanics model to examine the metal binding site organization in these complex polyamides.

Synthesis and Characterization

We have prepared the diamides **1** - **12** in multigram quantities (see Figure 1). Compounds **5**, **6**, **10**, **11**, and **12** are previously unreported. All have been characterized by ^{1}H and ^{13}C NMR spectroscopy, IR spectroscopy, and GC-MS. These diamides represent the three types of structural variation. The bridge length is varied in **1** and **2**, and in **3** and **4**. The degree of bridge alkylation is varied in **3**, **5**, and **6**, in **7** and **8**, in **9** and **10**, and in **4** and **11**. The steric bulk of the alkyl groups attached to the nitrogen is varied in **1**, **3**, **7**, **9**, and **12**.

The coordination chemistry of diamides with lanthanides has been explored with emphasis on the parent compounds **1** and **2** (presentation 12; publication 9). Solid state structural information was obtained by single-crystal x-ray diffraction and thermogravimetric analysis (TGA). The question of whether or not the solid state structures are maintained in solution was addressed through the use of infrared (IR) spectroscopy. The crystal structures determined in this work are shown in Figure 2. Although there have been several prior determinations of lanthanide malonamide structures, no crystal structures had been reported for **1** with lanthanide nitrates. In addition, we have obtained the first crystal structures for any lanthanide succinamide complex and have discovered that lengthening the bridge leads to a rich and varied coordination chemistry.

TGA analysis reveals that the reaction of lanthanide nitrates with **1** yields 2:1 ligand:metal species for all the lanthanides examined (La, Nd, Gd, and Yb). The structures for La, Nd, and Gd have been determined by single crystal x-ray diffraction and were found to be monomeric with two bidentate chelating diamides, consistent with previous literature reports. Titrations of lanthanide nitrates with **1** or **3** are consistent with the formation of a 2:1 species in solution as evidenced by the FTIR spectra. No evidence for any higher L:M species is observed.

The reaction of lanthanide nitrates with **2** is more complicated. TGA analyses revealed that a 2:1 ligand:metal species occurs only with the early lanthanides (La and Ce). Single crystal x-ray diffraction revealed a *polymeric* material with one chelating bidentate diamide bound solely to one

Varied Bridge Length

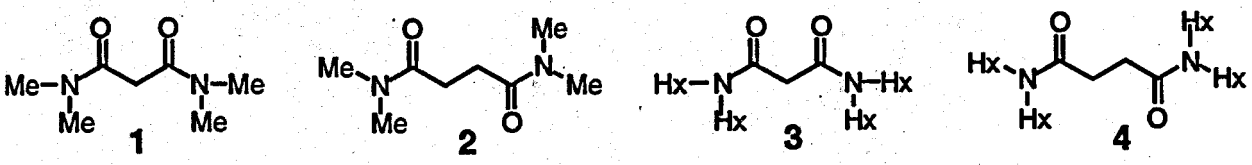

Varied Bridge Alkylation

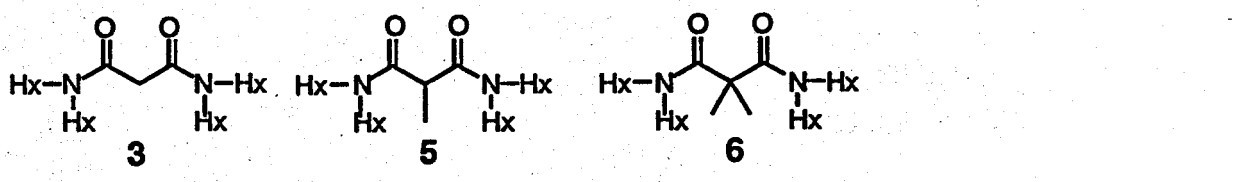

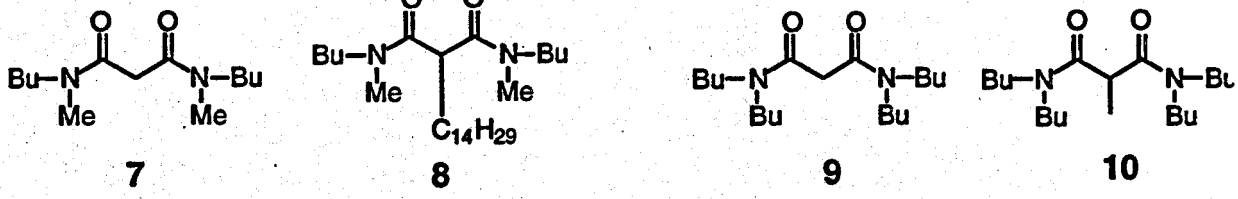

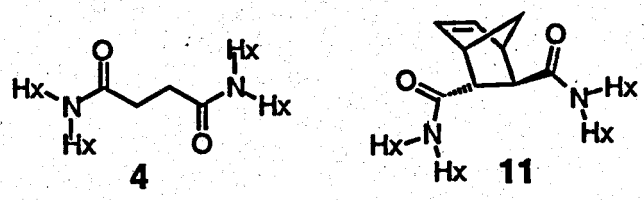

Varied N-Alkylation

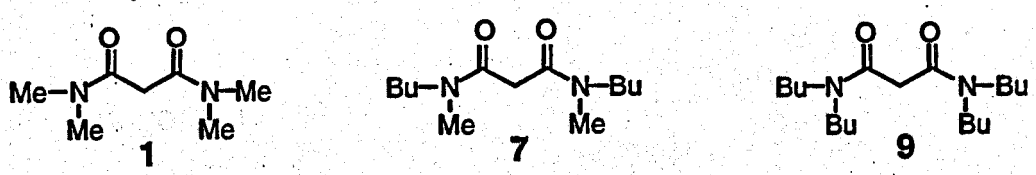

Figure 1. Diamide Derivatives Prepared for this Study

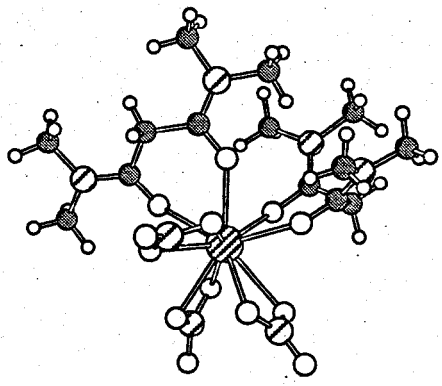

$[M(1)_2(NO_3)_3]$
(M = La, Nd, Gd)

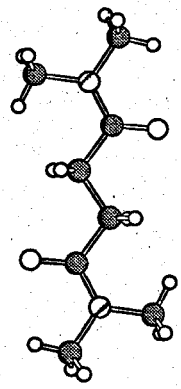

2

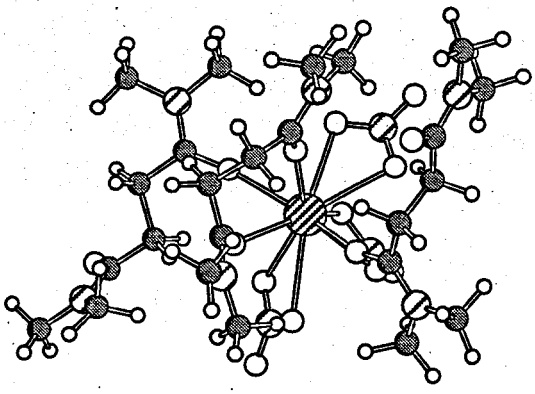

$[M(2)_2(NO_3)_3]_n$ (M = La,Ce)

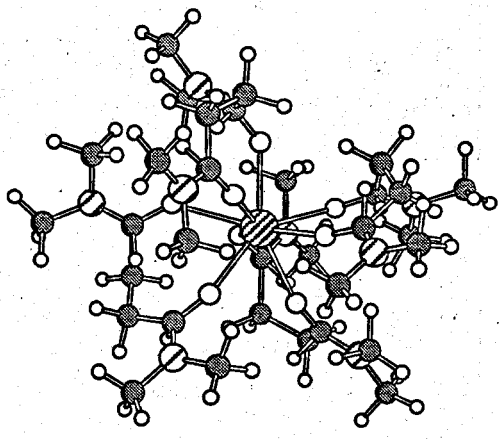

$[M(2)_4(ClO_4)_3]$ (M = Eu, Nd)

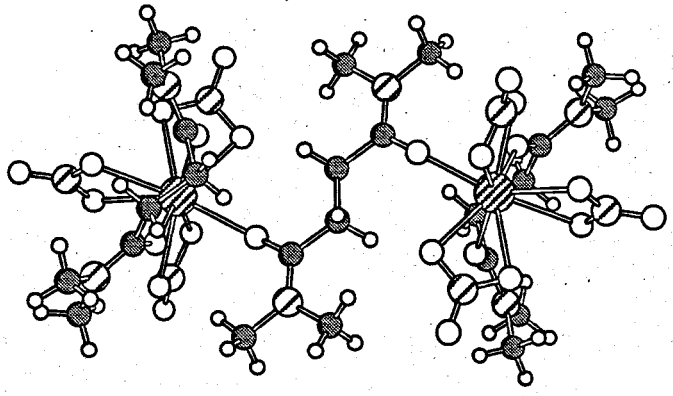

$[M_2(2)_3(NO_3)_6]$ (M = Ce, Pr, Nd, Gd, Yb)

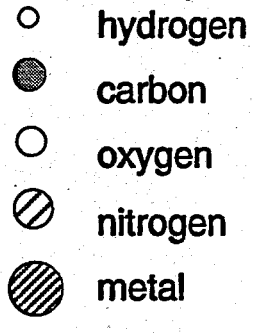

Figure 2. X-Ray Crystal Structures for **2** and Lanthanide Complexes of **1** and **2**

metal and the second bridging between two metals. IR spectroscopic titration of lanthanide nitrates with **2** is consistent with the formation of a 2:1 species in solution with no evidence for any higher L:M species.

TGA analysis reveals a different stoichiometry, a 3:2 ligand to metal ratio, for complexes of **2** with the lanthanides Pr, Nd, Gd, Yb, and Lu. The structures of the Pr, Nd, Gd, and Yb compounds have been determined by single crystal x-ray diffraction and were found to be *dimeric*, with one bidentate diamide bound to a single metal and a bidentate diamide bridging two metals. Curiously, a crystal containing this stoichiometry was also isolated for Ce. With the exception of La and Ce, IR spectroscopic titration of lanthanide nitrates with **2** or **4** is consistent with the formation of the 3:2 species in solution with no evidence for any higher L:M species.

Ce appears to be a special (and transitional) lanthanide in its reaction with **2**. Although IR and TGA analyses indicate it is predominantly the 2:1 ligand-to-metal product, crystals for both the 2:1 and 3:2 compound were isolated. No evidence was found for multiple stoichiometries with any of the other lanthanides.

If non-coordinating counteranions are present, such as triflate or perchlorate, TGA analysis of the products formed in the presence of excess **2** reveals a 4:1 ligand:metal complex with Eu and Nd. Single crystal x-ray diffraction revealed a monomeric species with four bidentate chelating diamides. IR spectroscopic titration of lanthanide perchlorates with **2** is consistent with the formation of a 4:1 species in solution with no evidence for any higher L:M species.

Binding Affinities

A literature search was performed to locate any information regarding single-phase stability constants for amide complexes of lanthanides or actinides and solution structural information on such complexes. This search revealed that not only are there no existing structure-stability data sets but no stability constant data for f-block metal ions with pure amide ligands. Given that the amide group is neutral over a wide pH range, this situation reflects the general difficulty of determining stability constants for non-ionizable ligands. Generation of structure-function data require that the relative metal binding affinities should be determined under identical experimental conditions of solvent, counter ion, and temperature. A variety of methods for the determination of metal-amide binding constants were investigated in FY 1997. These methods include electronic spectroscopy, IR spectroscopy, use of ion selective electrodes, calorimetry, and solvent extraction. Of these methods, solvent extraction and calorimetry were found to be the most applicable.

Calorimetry has yielded the first measurements of diamide binding constants with any metal ion (presentations 4, 5, 15; publication 12). The formation constants for 1:1 ligand:metal complexes, K, have been determined for $Eu(ClO_4)_3$ with **1**, **2**, **3**, **6**, **7**, and **12** in 10% DMSO/90% acetonitrile solution buffered to ionic strength 0.1 M at 25°C. The results are presented in Table 1. A decrease in the formation constant by a factor of 3.7 occurs on lengthening the bridge by one methylene group, as shown in the comparison of **1** and **2**. Comparing **3** and **6** demonstrates that dialkylation of the methylene bridge causes a drop in the formation constant of at least 2 orders of magnitude. Data for **1**, **3**, **7**, and **12** illustrate that the formation constant steadily decreases as the steric bulk of N-alkyl groups increases.

A method for analyzing liquid-liquid extraction data has been reported (publication 6). This method can be used to obtain the overall equilibrium constant for the organic phase reaction $M^{x+} + x\ NO_3^- + y$ ligand $\rightarrow M(NO_3)_x(L)_y$. This method is being applied to $Eu(NO_3)_3$ and $UO_2(NO_3)_2$. Preliminary measurements have been performed on the extraction of Eu from acidic aqueous nitrate solutions into tert-butylbenzene containing either **3**, **4**, or **6** (presentations 2, 5).

Table 1. Formation Constants for $Eu(ClO_4)_3$

Ligand	Formation Constant, M^{-1} ($\pm 3\ \sigma$)	
1	21.9	(1.1)
2	5.9	(1.2)
3	3.5	(1.3)
6	<0.1	
7	11.0	(1.2)
12	1.2	(1.2)

A ligand:metal ratio of 2:1 is observed for **3**, which is consistent with the x-ray data on malonamides. However, a ligand:metal ratio of 3:1 is observed for **4**, which is a stoichiometry that has not been observed in the solid state. This method cannot be used to measure the impact of lengthening the bridge directly because of the differing ligand:metal ratios in **3** and **4**. However, when comparing **3** and **6**, dialkylation of the central methylene causes a drop of at least three orders of magnitude in the distribution value. The same trend is observed by calorimetry.

Preliminary measurements also have been performed on the extraction of $UO_2(NO_3)_2$ from acidic aqueous nitrate solutions into tert-butylbenzene containing either **4**, **6**, or **11** (presentations 2, 5). Extraction constants range from 0.1 to 100 with **4** > **11** > **6**. A 2:1 ligand:metal ratio is observed in all four cases. Experimental efforts using TGA, x-ray crystal structures, and IR spectroscopy are currently in progress to identify the structures of these species.

Calix[4]arene Amides

A series of eight calixarene amide derivatives have been prepared and characterized (publications 1, 7). Solid phase structures for two of these compounds have been determined by single crystal x-ray diffraction (publication 7). The use of these ligands as metal ion extractants is under investigation (presentations 8, 9; publications 1, 5, 8). For example, geometrically isomeric 1,2- and 1,3-tert-butylcalix[4]arene amides disubstituted with (dibutylcarbamoyl)methoxy groups have been structurally characterized by ^1H and ^{13}C nuclear magnetic resonance (NMR) spectroscopy. Two non-interconverting conformers of the 1,2-isomer have been isolated. The 1,3-isomer and the two 1,2-isomers have been used to extract the uranyl ion into toluene and isooctane. The degree of the extraction depended on the particular conformer of the calixarene. As highlighted in a science/technology concentrate in C&E News, March 2, 1998, this is the first example in which such conformer effects on the extraction of the uranyl ion have been observed.

Modeling

Our approach uses a molecular mechanics model to relate ligand structure to metal ion binding affinity. Precedence for this approach is documented in an exhaustive review on the application of molecular mechanics to obtain structure-function relationships in coordination chemistry (presentation 14, publication 2). Using a molecular mechanics model requires the development of an extended force field to handle the specific system under study. In this case, force field development has required the refinement of existing amide parameters and the generation of new parameters for the metal-amide interactions. This has been accomplished using both electronic structure calculations and experimental data (crystal structures). Because the design of selectivity involves both an affinity for the target metal and a rejection of competing metal ions, the MM3 model needs to be applicable not only to f-block metals but to other metals. For this reason, our model has been designed to evaluate amide complexes with metal ions throughout the periodic table.

Ab initio DFT and molecular orbital theory calculations were used to examine the structure, vibrational modes, and bonding of the various metal ions to simple unidentate and bidentate amides. These calculations yielded ground state geometries and potential energy surfaces that provided a starting point for the refinement of the MM3 parameters through empirical fitting to

crystal structure data, as described below. Because of their expense, the electronic structure calculations were focused on simple complexes of representative metal ions selected to cover a range of charge, size, and metal electronic configuration. Density functional theory has been used to calculate the structures of a variety of amides and metal ion complexes at local and nonlocal levels with at least polarized valence double zeta basis sets. Frequencies have been calculated for all species to determine if they are minimal and as an aid in calibrating force field development. The initial calculations were done with just a naked metal ion binding to the amide, but this gave M-O distances that were far too short to compare with crystal structure data. Calculations were then done on $[M(OH_2)_m]^{n+}$ for the optimal value of m (m = 4 - 6 for small alkali and alkaline earth cations and transition metals). N,N-dimethylacetamide was then substituted for one H_20, and the structures were reoptimized to yield data that could be compared with crystal structures directly. In addition, the geometries of three complexes observed in crystal structures were optimized at the DFT level to examine the effect of other ligands in the coordination sphere. Good agreement was obtained with the crystal structures. Although most calculations were focused on the alkali, alkaline earth, and transition metals, calculations have been initiated on Th(IV). The geometries of $[Th(OH_2)_6]^{4+}$ and $[Th(N,N\text{-dimethyl-acetamide})(OH_2)_5]^{4+}$ have been done with one effective core potential (ECP) basis set. Work is continuing on validating the ECP and basis set for thorium. These calculations have been done with the computer codes NWChem and DGauss. This work has provided extensive testing of the new code NWChem being developed at the Wiley Environmental and Molecular Science Laboratory (EMSL) at PNNL.

Initial parameters obtained through electronic structure calculations were refined to give the best fit to crystal structures. An exhaustive survey of the Cambridge Structural Database identified suitable metal-amide structures for MM3 parameter refinement and validation. In addition, a statistical analysis of bond lengths, bond angles, and torsion angles was performed as a function of the degree of alkylation of the amide functional group and the type of metal ion in the amide complex. Orientational preferences of the coordinated amide ligand were evaluated in terms of M-O-C bond angles and M-O-C-N torsion angles. This evaluation led to the first recognition of the geometric requirements for amide binding (publication 3). A marked difference was observed in the structural features of the transition metals versus the f-block metal ions, suggesting that ligand architecture can be manipulated to optimize selectivity for the actinides over the transition metals.

The review of the structures of metal complexes with monodentate amides established that metal ions prefer to lie in the plane of the amide group and cis with respect to the C_a-substituent (where C_a is the carbonyl carbon) (publication 3). This result is consistent with *ab initio* electronic structure calculations on the binding of a proton to the lone pair of the carbonyl that

shows the same orientation (publication 13). This orientation places the C_a-substituent in close contact with other ligands in the complex. It is therefore important that the amide force field correctly model the rotation about the C_a-C bonds with respect to the location of the minima as well as the barrier heights to reproduce the structures of the metal-amide complexes. In a number of cases, however, the default MM3 amide parameters failed to yield observed ligand conformations. *Ab initio* DFT and molecular orbital theory calculations were used to obtain the rotational potential surfaces for C_a-C bond rotation in acetamide, propanamide, 2-methylpropan-amide, and 2,2-dimethylpropanamide. These data were used to refine the MM3 torsional parameters (presentation 10, publication 11).

The performance of the extended MM3 model for metal-amide complexes has been validated by comparison of calculated and observed structural features. Fifty-six crystal structures, including those shown in Figure 2, were used in this comparison. In addition to f-block metal ions (lanthanides, Th(IV), U(IV), U(VI)), this set of structures included complexes with alkali, alkaline earth, and transition metals. We found that each metal ion requires a different set of parameters. A unique feature of this parameterization is that the metal-dependent parameters are correlated with the ionic radius, charge, and electronegativity of the metal ion. Therefore, the resulting MM3 model can be applied to any metal ion for which these properties are known. For the 56 crystal structures examined to date, the model computes a mean average deviation of ±0.035 Å for M-O bond lengths, ±5 deg for M-O-C angles, and ±15 deg for M-O-C-X torsion angles (X = H, C, or N) (presentations 6, 11; publication 10).

The degree of alkylation affects both the steric and electronic characters of the amide functional group. Steric and electronic factors both influence the strength of metal ion complexation. Although the molecular mechanics model allows a quantitative evaluation of steric effects, it does not address the changes in oxygen basicity that accompany structural modifications. A series of electronic structure calculations has been performed on eight monoamides to evaluate the effect of alkylation on oxygen basicity. Calculated proton affinities are in good agreement with experimental gas phase values where available (publication 13). Gas-phase metal ion binding affinities also have been calculated for this series of amides with Li(I), Mg(II), Sc(III), and $[Zr(OH_2)_8]^{++}$.

Planned Activities

Research efforts will continue to focus on the amide function group for the remainder of this fiscal year and into FY 1999.

A series of structurally varied diamide derivatives has been synthesized and their complexes with the lanthanides have been characterized. Characterization of actinide complexes is in progress. Additional succinamide derivatives will be prepared to evaluate the effect of the degree of bridge alkylation. Limited structure-function data have been obtained for the three types of structural variations present in diamides. The structure-function data sets will be expanded by the continued application of calorimetry and solvent extraction methods to measure additional binding constants. Additional calixarene amides will be prepared and characterized. Binding constants for the complexation of the amides with f-block metal ions will be determined by microcalorimetry.

A molecular mechanics model for metal-amide complexes has been developed and validated. This model is currently being applied to evaluate the degree of binding site organization for metal ions as a function of structural variation in diamides. Conformational analyses of malonamide and succinamide derivatives will be performed. All geometries and their relative energies obtained with the MM3 model will be verified by geometry optimizations and frequency calculations obtained from electronic structure calculations. Ligand strain energies will be evaluated for all the diamides for which binding affinities have been measured. Comparison of binding affinity with ligand strain will indicate to what extent ligand steric demands influence complex stability. The results of this study will be used to evaluate the extent of improvement that can be obtained by the structural modification of diamides.

Electronic structure calculations will be extended to a wide range of f-block elements, both actinides and lanthanides. This effort will benefit from work being done under the MICS (Mathematics, Information and Computer Sciences) computational "Grand Challenge" in Relativistic Quantum Chemistry in terms of method development and from a recent allocation of computer time on the EMSP Computing Facility's massively parallel IBM SP computer system.

On completion of our study of the amide functional group, the same methodology will be applied next to phosphine oxides.

Presentations

(1) Rapko BM. April 1997. "Extraction of f-Elements by Phosphine Oxide/Pyridine N-Oxide Ligands." 213th ACS National Meeting, San Francisco, California.

(2) Lumetta GJ, BK McNamara, and E Burgeson. June 1997. "Amide Complexes of f-Block Elements." 21st Annual Actinide Separations Conference, Chartleston, South Carolina.

(3) Rao L, Y Xia, BM Rapko, and PL Martin. June 1997. "Synergistic Extraction of Eu(III) and Am(III) by TTA and the Neutral Donor Extractants CMPO and NOPOPO." 21st Annual Actinide Separations Conference, Chartleston, South Carolina.

(4) Zanonato PL, and L Rao. September 1997. "Complexation of Eu(III) by N, N,N',N'-tetraalkyldiamides." 214th ACS National Meeting, Las Vegas, Nevada.

(5) Rapko BM, GJ Lumetta, BK McNamara, L Rao, and PL Zanonato. October 1997. "Determination of Actinide and Lanthanide Binding Constants with Amides and Diamides." Tenth Symposium on Separation Science and Technology for Energy Applications, Gatlinburg, Tennessee.

(6) Clement O, G Sandrone, DA Dixon, and BP Hay. March 1998. "A MM3(96) Force Field for Metal-Amide Complexes." 215th American Chemical Society Meeting, Dallas, Texas.

(7) Lumetta GJ, BK McNamara, and BM Rapko. April 1998. "Binding of Amide Ligands to f-Block Elements." Twenty-Second Annual Actinide Separations Conference, Chattanooga, Tennessee.

(8) Roundhill DM. May 1998. "New Macrocycles for Selective Ion Exchange." Metals Adsorption Workshop, Cincinnati, Ohio.

(9) Yordanov AT, NJ Wolf, HF Koch, and DM Roundhill. June 1998. "Sulfur and Nitrogen Derivatized Calix[4]Arenes as Selective Phase Transfer Extractants for Heavy Metals and Oxyions." 2nd Fargo Conference on Main Group Chemistry, Fargo, North Dakota.

(10) Hay BP, DA Dixon, and G Sandrone. June 17-20, 1998. "A Modified MM3(96) Force Field for Simple Amides and Diamides." Abstract submitted for the Northwest Regional ACS Meeting, Richland, Washington.

(11) Clement O, G Sandrone, DA Dixon, and BP Hay. June 17-20, 1998. "A MM3(96) Force Field for Metal-Amide Complexes." Abstract submitted for the Northwest Regional ACS Meeting, Richland, Washington.

(12) Rapko BM, BK McNamara, and RD Rogers. June 17-20, 1998. "Coordination Chemistry of Lanthanide Salts with N, N, N', N'-Tetramethylsuccinamide and N, N, N', N'-Tetrahexylsuccinamide." Abstract submitted for the Northwest Regional ACS Meeting, Richland, Washington.

(13) Lumetta GJ, BK McNamara, and BM Rapko. June 17-20, 1998. "Binding of Diamide Ligands to f-Block Elements." Abstract submitted for the Northwest Regional ACS Meeting, Richland, Washington.

(14) Hay BP. August 23-27, 1998. "A Points-on-a-Sphere Approach to Model Metal-Ligand Interactions with an Extended MM3 Model." Abstract submittted for the 216th ACS National Meeting, Boston, Massachusetts.

(15) Rao L, P Zanonato, and P Di Bernardo. August 23-27, 1998. "Thermodynamics of Europium(III) Complexation with Alkyl-Substituted Diamides in Organic Solvents." Abstract submittted for the 216th ACS National Meeting, Boston, Massachusetts.

Publications

(1) Falana OM, HR Koch, DM Roundhill, GJ Lumetta, and BP Hay. 1998. "Synthesis and Extraction Studies of 1,2- and 1,3-Disubstituted Butylcalix[4]Arene Amides with Oxyions: Geometric and Conformational Effects." *J. Chem. Soc. Chem. Communl*, pp. 503-504.

(2) Hay BP, and O Clement. 1998. "Metal Complexes." in *Encyclopedia of Computational Chemistry*, P. von Rague Schleyer, ed. John Wiley and Sons, London, in press.

(3) Clement O, BM Rapko, and BP Hay. 1998. "Structural Aspects of Metal-Amide Complexes." *Coordination Chemistry Reviews*, in press.

(4) Rao L, Y Xia, BM Rapko, and PF Martin. 1998. "Synergistic Extraction of Eu(III) and Am(III) by Thenoyltrifluoroacetone and Neutral Donor Extractants: Octyl(Phenyl)-N,N-Diisobutylcarbonyl-methylphosphine Oxide and 2,6-Bis(Diphenylphosphino)methyl Pyridine N,P,P Trioxide." *Solvent Extraction and Ion Exchange*, in press.

(5) Yordanov A, and DM Roundhill. 1998. "Solution Extraction of Transition and Post-Heavy and Precious Metals by Chelate and Macrocyclic Ligands." *Coord. Chem. Rev.*, in press.

(6) Lumetta GJ, BM Rapko, and BK McNamara. 1998. "Using Excel© to Analyze Liquid-Liquid Extraction Equilibria." Submitted for publication in the *Journal of Chemical Education.*

(7) Wolf NJ, EM Georgiev, AT Yordanov, BL Whittlesey, HF Koch, and DM Roundhill. 1998. "Synthesis of Lower Rim Amine and Carbamoyl Substituted Calixarenes as Transfer Agents for Oxyions between an Aqueous and a Chloroform Phase." Submitted for publication in *Inorganic Chemistry.*

(8) Yordanov AT, NJ Wolf, EM Georgiev, HF Koch, OM Falana, and DM Roundhill. 1998. "Derivatized Calix[4]arenes as Selective Phase Transfer Extractants for Heavy Metal and Oxyion Salts." Submitted for publication in *Comments on Inorganic Chemistry.*

(9) McNamara BK, GJ Lumetta, BP Hay, BM Rapko, and RD Rogers. 1998. "Coordination Chemistry of Lanthanide Nitrates with N,N,N,N-Tetramethylsuccinamide." Submitted for publication in *Inorganic Chemistry.*

(10) Clement O, G Sandrone, DA Dixon, and BP Hay. "A MM3(96) Force Field for Metal-Amide Complexes." Submitted for publication in *Inorganic Chemistry.*

(11) Sandrone G, DA Dixon, and BP Hay. 1998. "C(sp2)-C(sp3) Rotational Barriers in Simple Amides: H_2N-C(=O)-R, R = Methyl, Ethyl, i-Propyl, t-Butyl." Submitted to the *J. Phys. Chem.*

(12) Rao L, P Zanonato, and P Di Bernardo. 1998. "Studies of Europium(III) Complexation with Tetramethylmalonamide and Tetramethylsuccinamide in Organic Solvents by Calorimetry and Optical Spectroscopy." *Inorg. Chim. Acta*, manuscript in preparation.

(13) Dixon DA, G Sandrone, and BP Hay 1998. "Computational Studies of Cation Binding to Amides. I. Proton Binding Affinity." *J. Phys. Chem.*, manuscript in preparation.

Ionizing Radiation-Induced Catalysis on Metal Oxide Particles

(First Year of Funding: FY 1996)

Principal Investigator

Teresa A. Fryberger
Pacific Northwest National Laboratory
P.O. Box 999, MSIN K8-84
Richland, WA 99352
(509) 376-6688 (phone)
(509) 376-6742 (fax)
teresa.fryberger@pnl.gov

Co-Investigators

Scott A. Chambers (PNNL)
John L. Daschbach (PNNL)
Michael A. Henderson (PNNL)
Charles H.F. Peden (PNNL)
Yali Su (PNNL)
Yong Wang (PNNL)

Contributors and Collaborators

Prof. Miguel E. Castro
Dept. of Chemistry
University of Puerto Rico
Mayuagues, Puerto Rico 00680
(787) 832-4040, ext 3134 (phone)
mi_castro@rumac.upr.clu.edu

Prof. Abhaya K. Datye
Director, Center for Microengineered Materials
University of New Mexico
Albuquerque, NM 87131
(505) 277-0477 (phone)
Datye@unm.edu

Research Objective

This project focuses on a novel approach for destroying organics found in high-level mixed waste at U.S. Department of Energy (DOE) sites. In this project we propose that organics can be destroyed by reduction/oxidation (redox) chemistry resulting from electron-hole (e^-/h^+) pairs generated in stable, wide bandgap semiconductors via interactions with ionizing radiation (α,β,γ). Conceptually, this process is an extension of visible and near-UV photocatalytic processes known to occur at the interfaces of narrow bandgap semiconductors in both solution and gas phases. In these processes, an electron is excited across the energy gap between the filled and empty states in the semiconductor. The excited electron does reductive chemistry, and the hole (from where the electron was excited) does oxidative chemistry. The energy separation between the hole and the excited electron reflects the redox capability of the e^-/h^+ pair and is dictated by the energy of the absorbed photon and the bandgap of the material. Ionizing radiation overcomes optical transparency limitations associated with visible and near-UV illumination (γ-rays penetrate much farther into a solution than UV/visible light) and permits the use of wider band-gap materials (such as ZrO_2) that possess potentially greater redox capabilities than those with narrow bandgap materials.

Planned experiments will extend the body of knowledge about e^-/h^+ pair chemistry of semiconducting metal oxide (MO) materials by 1) examining the influence of surface structure, defects, and dopants on the photocatalytic activity of narrow bandgap materials (TiO_2); and 2) by expanding these studies to wider bandgap materials (ZrO_2) that are virtually unexplored in terms of their e^-/h^+ pair chemistry. Experiments are being conducted in three areas: 1) γ-radiocatalysis of reactant-colloidal metal oxide solutions, 2) photoelectrochemical studies at model MO electrodes, and 3) photochemical studies in ultra-high vacuum (UHV) and high pressures on model MO surfaces. An outcome of this proposed work will be a more thorough evaluation of ionizing radiation in the catalytic remediation of organics (and other problem species) in high-level mixed waste.

Problem Statement

High-level radioactive waste storage tanks located at DOE sites contain significant amounts of organic components (solid and liquid phases) in the form of solvents, extractants, complexing agents, process chemicals, cleaning agents, and a variety of miscellaneous compounds. These organics pose several safety and pretreatment concerns. This is particularly true in the case of the Hanford Site, where all currently proposed tank waste cleanup alternatives encounter potential safety or pretreatment problems associated with organics. Needed are remediation technologies that would significantly reduce the amounts of problem organics without resulting

in toxic or flammable gas emissions and without requiring thermal treatments. These restrictions pose serious technological barriers for current organic destruction methods that rely on oxidation achieved by thermal or chemical activation.

Research Progress

Probing the Mechanism of EDTA Radiocatalysis

In the previous year, we observed that the yield of γ–ray-induced destruction of EDTA in solution increased significantly if oxygen and a colloidal suspension of TiO_2 were present. Both oxygen and TiO_2 were necessary to see this increased EDTA destruction, as shown in Figure 1. Without TiO_2, about 19% of the EDTA in an aerated solution were destroyed after a 1 mrad exposure toγ–rays, but with a 0.1 g/ml suspension of TiO_2 the level of EDTA destruction increased to near 50%. We have, however, observed that this process is very pH-dependent. As the pH is increased (more basic solutions) the difference between the blank experiment (no TiO_2 present) and that with TiO_2 present became zero. We interpret this to mean that as the pH increases the surface charge on each TiO_2 particle becomes increasingly negative, and anionic species, such as EDTA, are unable to directly interact with the surface. This effect is overcome if EDTA is complexed with a cation such as Sr^{2+}. Figure 1 shows that at a pH of 9 the level of EDTA destruction is approximately the same after a 1 mrad exposure with or without TiO_2. If

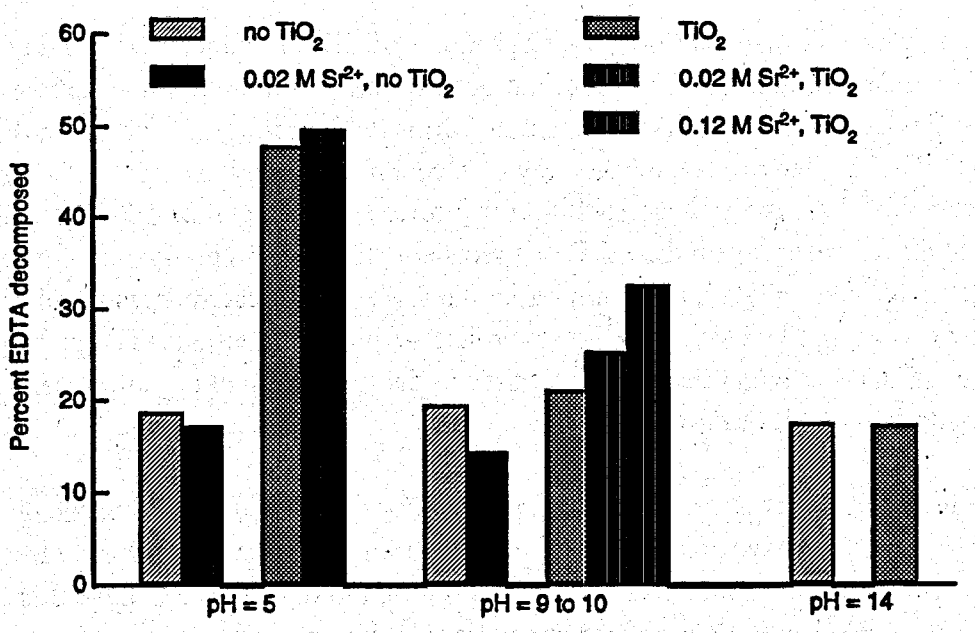

Figure 1. Percent Decomposition of Various Aerated 0.02 M EDTA Solutions after 1 mrad Irradiation with γ–Rays

the solution is made with 0.2 M in Sr^{2+} the level of EDTA destruction increases to about 25% after a 1 mrad exposure, while a 0.12 M solution increases the level to over 30%. We interpret this to mean that complexed EDTA is an electrostatically neutral solution species and is therefore insensitive to the negative charge on a TiO_2 particle at high pH. We have also observed that Cu^{2+} ions produce the same effect as Sr^{2+}, which is consistent with EDTA complexing with 2+ cations in general. This finding has great significance for the radio- and photo-catalytic destruction of complexants such as EDTA because pH effects can be negated. The effect is minimal at a pH of 5, where the surface charge on TiO_2 is close to zero. These results are also consistent with UV photo-oxidation studies conducted by Professor Abhaya Datye's group at the University of New Mexico.

We have also undertaken to characterize the solution and gas-phase products from radiocatalytic destruction of EDTA over TiO_2. Although several products have been observed from solution radiolysis in the absence of TiO_2, there is a significant increase in the yields of EDTA and formic acid as well as a decrease in the yield of oxalic acid when TiO_2 is present. Assuming that charge transfer occurring between the γ–ray excited TiO_2 surface and the adsorbed EDTA species is responsible for EDTA decomposition, we expect that the anchoring group of the molecule is most susceptible to TiO_2-mediated oxidation. Based on comparisons with the binding of carboxylic acids such as formic and acetic acids to TiO_2, we expect that EDTA should bind to the surface through only one of its four carboxyl groups due to steric issues. Therefore, the production of EDTA is consistent with this model in that one acetate moiety is preferentially decomposed per EDTA molecule destroyed.

Because formic acid was one of the major products of EDTA radiocatalysis and because we wish to better understand the mechanism of radiocatalysis, we have undertaken studies of smaller probe molecules. Our initial results indicate that formic acid, acetic acid, and ethanol are all insensitive to the presence of TiO_2 in the γ–ray experiments; that is, the extents of γ–ray radiolysis are the same for these molecules in solution regardless of the presence of TiO_2. This result for formic acid is consistent with the EDTA experiments that show a gradual evolution of this species with increasing radiation dose, implying that formic acid accumulates in solution without being further decomposed. This result, however, is also surprising because UV photolysis conducted by us and in several published accounts indicates that small organics such as formic acid are rapidly photo-oxidized over TiO_2.

Although we do not yet understand the absence of γ–ray-induced radiocatalytic destruction of these small organics, we have observed that impregnating TiO_2 with 0.5% Pt increases the rate of formic acid decomposition threefold over that of solution radiolysis. We believe this is a thermal effect because the yields of CO_2 produced are equivalent irrespective of the presence of γ–ray irradiation. During these γ–ray irradiation experiments we also observed significant yields of hydrogen gas that were not observed without platinized TiO_2 present or without irradiation. This

hydrogen did not arise from photoreduction of water on the platinized TiO_2 because identical experiments in the absence of formic acid did not yield hydrogen.

In an effort to determine the role that various excitation mechanisms play in the γ–ray experiments over TiO_2, we have conducted controlled experiments with small organic molecules over TiO_2 single crystal surfaces in UHV. One possible mechanism that might occur in solution is the effect of secondary electron-induced chemistry resulting from absorption of the high-energy radiation. For example, a Compton electron, formed by absorption of a γ–ray, can produce up to 10^4 100 eV electrons through subsequent ionization and loss processes. These electrons should be very effective at breaking bonds. To determine the cross-sections and thus the relative rates for electron-induced decomposition of small organics on TiO_2, we conducted a series of experiments focusing on the 100 eV electron irradiation of methanol on TiO_2(110). These experiments were done in collaboration with Professor Miguel Castro from the University of Puerto Rico.

Methanol was chosen as the organic probe molecule for these experiments because it is the simplest organic that has no thermal decomposition on TiO_2(110). Although we have not examined this species in γ–ray experiments, we expect that its behavior is similar to that of ethanol, which was not sensitive to γ–ray-induced radiocatalysis over a TiO_2 suspension. Figure 2 shows a schematic of the various methanol-related surface species that have been detected on the TiO_2(110) surface in the absence of electron exposure. About 65% of the monolayer is composed of molecularly bound methanol, but most of this desorbs from the surface below 300K. The remainder of the monolayer is methanol molecules that have dissociated to adsorbed methoxyl groups and protons added to the substrate oxygen to make bridging hydroxyl groups. On the vacuum-annealed surface, about 30% of the methoxyl groups end up in oxygen vacancy

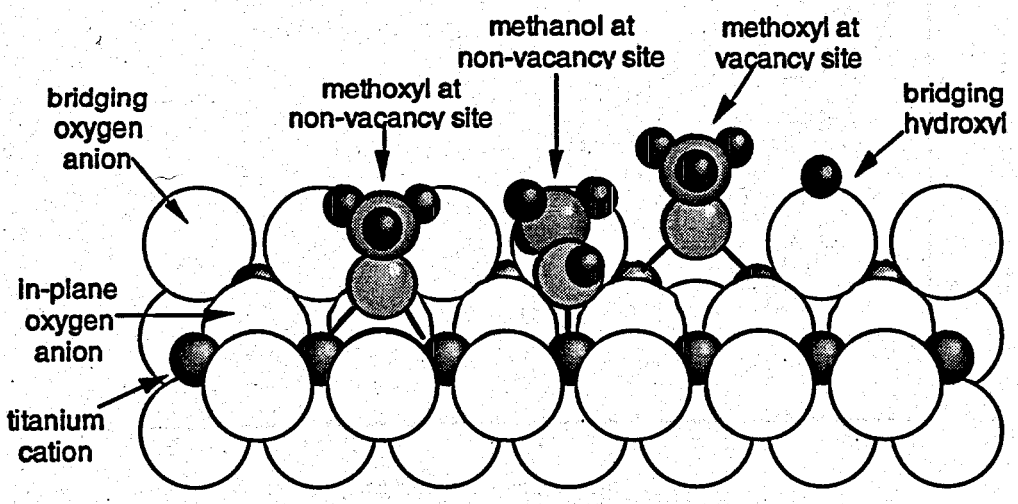

Figure 2. Schematic Model of the Various Forms of Adsorbed Methanol on the Vacuum-Annealed Surface of TiO_2(110)

sites, 70% are adsorbed at non-vacancy sites, are shown in Figure 2. Both types of methoxyls recombine with the deposited protons to regenerate molecular methanol. This occurs at 350K for the non-vacancy methoxyls and 480K for the vacancy methoxyls.

By careful dosing and preheating, the TiO_2(110) surface was prepared with these various species, and the sensitivity of each to electron irradiation was determined by monitoring the signal in each of their respective TPD states as a function of electron exposure. Molecularly adsorbed methanol left no detectable carbon-containing fragments on the surface after activation with 100 eV electrons. Instead, the parent and/or its carbon-containing fragments were ejected from the surface, leaving unoccupied surface sites. The ejected carbon-containing species were not ions because only H^+, OH^+ and H^- were detected during electron irradiation. In contrast, electron irradiation of both vacancy and non-vacancy methoxyl species resulted in adsorbed formaldehyde at the same respective binding sites. Formaldehyde molecules bound at vacancies were resistant to further electron-induced decomposition, whereas those bound at non-vacancies were further decomposed (probably to gaseous CO).

Figure 3 shows the cross-section data taken as a function of 100-eV electron exposure. The data indicate that, although molecular methanol was decomposed with the lowest cross-section (1.7×10^{-16} cm^2), its cross-section was only a factor of 2.5 less than that for the gas phase dissociative ionization of methanol with 100 eV electrons. This indicates that the TiO_2(110) does not

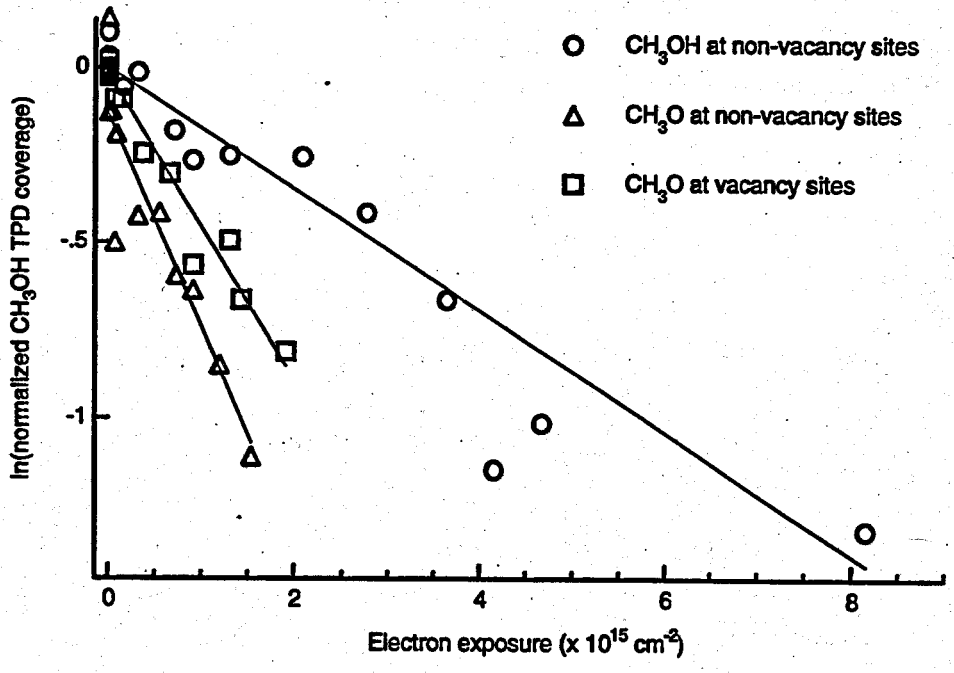

Figure 3. Cross Sections Plots for the 100 eV Electron Induced Decomposition of Various Methanol-Related Species Adsorbed on the Vacuum-Annealed Surface of TiO_2(110)

significantly perturb the electronic structure of methanol, nor does it quench the excited states of methanol that result from electron impact ionization. The cross-sections for methoxyl decomposition were approximately equivalent (about 5 x 10^{-16} cm^2), indicating that the excited states of these more tightly bound fragments are also not significantly quenched by the TiO_2(110) surface.

Although these large cross-sections suggest that small organics like methanol should readily decompose on TiO_2 surfaces exposed to 100 eV electrons, it does not appear that the γ–ray studies show the same type of reactivity. This suggests that secondary electrons with energies above the ionization potentials of most organics (about 10 to 20 eV) are not generated in significant concentrations when TiO_2 suspension are irradiation with γ-rays. The chemistry associated with less than 10 eV electrons has not been examined in this study but is planned for the next year of this project.

Probing the Mechanism of UV Photocatalysis

It is commonly held among photocatalytic researchers that the dominant mechanism associated with the semiconducting oxide photoeffect is the generation and subsequent chemistry of electron-hole pairs. Studies have been conducted on the photoexcitation mechanism, charge carrier dynamics, surface and bulk trap states, effects of dopants in bending bands, and charge transfer processes occurring at the surface once electron-hole pairs are formed. Much of our effort has been focused on determining whether this accepted mechanism also applies to γ–ray radiocatalysis. Recently, however, we have also been exploring alternative processes that might explain photooxidation outside of the traditionally held electron-hole pair mechanism. For example, it is well known that UV irradiation of TiO_2 materials results in photodesorption of oxygen from the surface of the oxide and the generation of Ti^{3+}-related surface defects. These photon-generated defects have not been produced with sufficient surface concentrations to permit characterization; however, it is also well known that oxygen vacancy sites can be made in the 0.05 to 0.15 mL coverage regime by thermal annealing. These vacancy defects are also associated with Ti^{3+} sites, as shown in the electron energy loss spectroscopy (ELS) data of Figure 4. The fully oxidized surface has a bandgap of about 3.2 eV, as seen from the ELS spectrum in Figure 4a. The signal between 3 and 10 eV corresponds to excitation of valence band electrons into the conduction band. After annealing at 850K (Figure 4b), a bandgap state appears at 0.85 V that is caused by Ti^{3+} sites located in energy just below the conduction band edge. This intense loss feature arises from only about 0.08 mL of oxygen vacancies indicating that the cross-section for exciting these electrons into the conduction band is considerably greater than that of the valence band electrons. The bandgap Ti^{3+} sites are really reoxidized by exposure to molecular oxygen at room temperature (Figure 4c). This oxidation temperature appears to regenerate the fully oxidized surface; however, TPD reveals that low-temperature oxidation of oxygen vacancies does not yield the same surface as that of high-temperature oxidation.

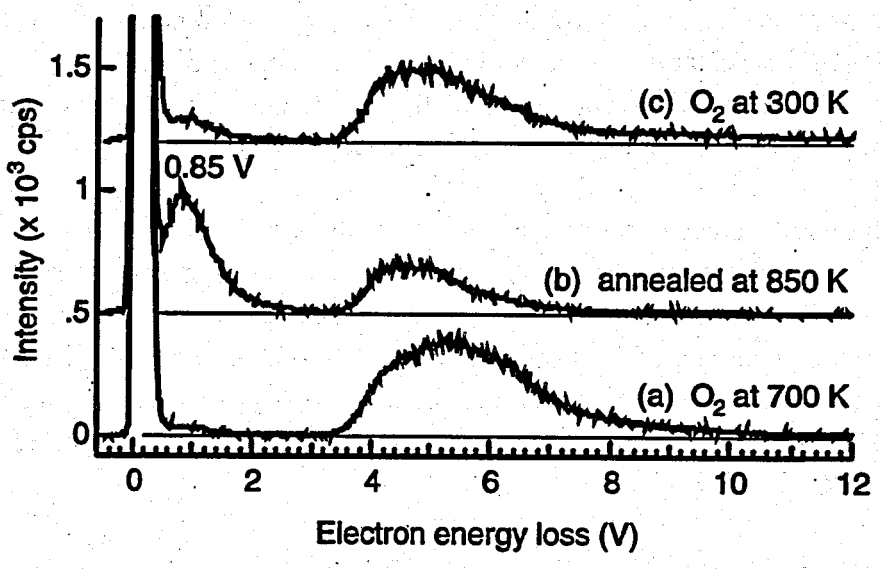

Figure 4. Electron Energy Loss Spectra Using 20 eV Primary Electrons for TiO_2(110) after (a) Oxidation at 700K, (b) Annealing in Vacuum at 850 K, and (c) Oxidation of (b) at 300K

Using water as a probe molecule, data in Figure 5 address the effect of oxidation temperature on the surface chemistry of TiO_2(110). Figure 5a shows a typical water TPD spectrum obtained from the vacuum-annealed surface of TiO_2(110). The state at 270K is due to molecularly bound water at Ti^{4+} sites, and the weaker signal at 500K is from water dissociation at oxygen vacancy

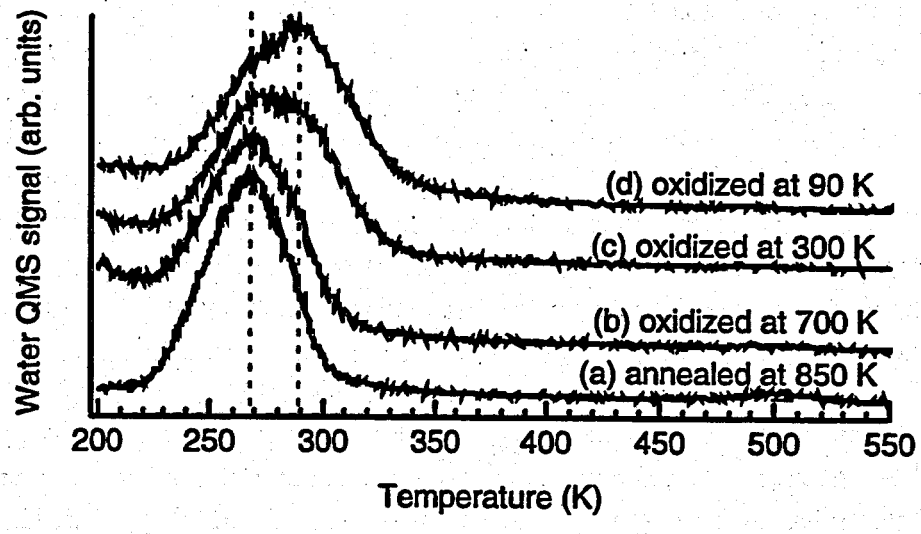

Figure 5. Water TPD Spectra from the TiO_2(110) Surface after (a) Vacuum Annealing at 850K, (b) Oxidation of (a) at 700K, (c) Oxidation of (a) at 300K, and (d) Oxidation of (a) at 90K

sites. The 500K TPD state is absent after oxidation of the vacancies with O_2 at 700K (Figure 5b) indicating that the surface is fully oxidized. Although the vacancy state is also absent after oxidizing the surface at 300K (Figure 5c) or at 90K (Figure 5d), a new water TPD state is now present at 290K. Using $^{18}O_2$ to oxidize the surface, we determined that this new 290K state of water is attributable, in part, to dissociated water. This implies that a previously undetected species is left on the surface after low temperature oxidation. Based on these results, we conclude that this species is an oxygen adatom. Preliminary results indicate that this oxygen adatom oxidizes coadsorbed N_2 to N_2O.

The discovery of a highly reactive oxygen adatom formed from the interaction of O_2 with surface defects opens the door for consideration of photo-oxidation mechanisms other than that of electron-hole pairs. Coupling this with the fact that UV photons may generate surface oxygen vacancies provides exciting new possibilities for explaining UV photo-oxidation phenomena over TiO_2 photocatalysts.

Planned Activities

We will focus on the following areas in the next year:

1. Continue studies directed at determining the mechanism of the γ-ray radiocatalysis effect over TiO_2 and ZrO_2. These will include more studies involving small probe molecules but also expand into the area of photoreduction of metals. This effort will include looking at new TiO_2-based materials such as 15Å wide particles of anatase obtained from Dupont and mesoporous materials grown in-house by Scott Elder.

2. Begin work on growth of model ZrO_2 materials by molecular beam epitaxy that will be used to probe the photodynamics and charge carrier properties of wider bandgap materials.

3. Continue probing the role of oxygen vacancies and reactive oxygen species in the photooxidation of organics over single crystal TiO_2 substrates. For example, we will further probe the oxidation of N_2 with oxygen adatoms and expand this work to consider organics such as acetone and propylene.

4. Explore the ability of low-energy (below 10 eV) electrons to activate adsorbed molecules such as methanol on the surface of TiO_2(110).

Publications

Alam M, MA Henderson, PD Kaviratna, GS Herman, and CHF Peden. 1998. "Chromyl Chloride Chemistry at the TiO_2(110) Surface." *J. Phys. Chem.*, B102:111.

Epling WS, CHF Peden, MA Henderson and U Diebold. 1998. "Evidence for Oxygen Adatoms on TiO_2(110) Resulting from O_2 Dissociation at Vacancy Sites." *Surf. Sci.*, in press.

Henderson MA, S Oreto-Tapia, and ME Castro. 1998. "Electron-Induced Decomposition of CH_3OH on the Vacuum Annealed Surface of TiO_2(110)." *Surf. Sci.*, in press.

Su Y, Y Wang, JL Daschbach, TB Fryberger, MA Henderson, J Janata, and CHF Peden. 1998. "Gamma-Ray Destruction of EDTA Catalyzed by Titania." *J. Adv. Oxid. Technol.*, in press.

Taylor DP, WC Simpson, K Knutsen, MA Henderson, and TM Orlando. 1998. "Photon Stimulated Desorption of Cations from Yttria-Stabilized Cubic ZrO_2(100)." *Appl. Surf. Sci.*, in press.

Presentations

Henderson MA. 1998. "Probing the Surface Chemistry of Single Crystal Metal Oxides with Water." 215th National Meeting of the American Chemical Society, Dallas, invited.

Peden CHF. September 1997. "The Growth, Structure and Surface Chemistry of Oxide Films as Model Surfaces." 17th National Congress of the Mexican Surface Science and Vacuum Society, Mazatlan, Mexico, invited.

Peden CHF. April 1998. "Water Adsorption and Reaction as a Probe of Oxide Surface Structure and Chemistry." Department of Chemistry, Texas A&M University, College Station, Texas, invited.

Su Y, Y Wang, JL Daschbach, MA Henderson, TB Fryberger, and CHF Peden. 1997. "Radiocatalytic degradation of organic contaminants in colloidal TiO_2 and ZrO_2 suspensions." Third International Conference on TiO_2 Photocatalytic Purification and Treatment of Water and Air, Orlando, Florida.

Su Y, Y Wang, MA Henderson, JL Daschbach, TB Fryberger, and CHF Peden. 1997. "Radiocatalytic degradation of organic contaminants in TiO_2 suspensions." 214th National Meeting of the American Chemical Society, Las Vegas.

Development of Fundamental Data on Chemical Speciation and Solubility for Strontium and Americium in High-Level Waste: Predictive Modeling of Phase Partitioning During Tank Processing

(First Year of Funding: FY 1996)

Principal Investigators

Dr. Andrew R. Felmy
Pacific Northwest National Laboratory
P.O. Box 999, MSIN K9-77
Richland, WA 99352
(509) 376-4079 (phone)
(509) 376-3650 (fax)
ar.felmy@pnl.gov

Dr. Gregory Choppin
Florida State University
Department of Chemistry, B-164
Tallahassee, FL 32606-3006
(904) 644-3875 (phone)
(904) 644-8281 (fax)
Choppin@chem.fsu.edu

Dr. David A. Dixon
Pacific Northwest National Laboratory
P.O. Box 999, MSIN K1-83
Richland, WA 99352
(509) 372-4999 (phone)
(509) 375-6631 (fax)
da.dixon@pnl.gov

Dr. James A. Campbell
Pacific Northwest National Laboratory
P.O. Box 999, MSIN P8-08
Richland, WA 99352
(509) 376-0899 (phone)
(509) 376-2329 (fax)
ja.campbell@pnl.gov

Research Objective

Pacific Northwest National Laboratory (PNNL) and Florida State University (FSU) are investigating the speciation of Sr and Am/Cm in the presence of selected organic chelating agents (ethylenediaminetetraacetic acid (EDTA), N-(2-hydroxyethyl)ethylenediaminetriacetic acid (HEDTA), nitrilotriacetic acid (NTA), and iminodiacetic acid (IDA)) over ranges of hydroxide, carbonate, ionic strength, and competing metal ion concentrations present in high-level waste tanks. The project comprises several integrated research tasks that approach the problem of chemical speciation using macroscopic thermodynamic measurements of metal-ligand competition reactions, molecular modeling studies to identify structures or complexes of unusual stability, and mass spectrometry measurements of complex charge/mass ratio that can be applied to mixed metal-chelate systems. This fundamental information is then used to develop thermodynamic models that allow us to predict changes in chemical speciation and solubility that can occur in response to changes in tank processing conditions. In this way new approaches can be developed to address fundamental problems in aqueous speciation and to provide useful and practical information for tank waste processing.

Problem Statement

Current strategies for reducing the total volume of radioactive tank waste requiring disposal at Hanford and other DOE sites call for developing methods to selectively dissolve and remove nonradioactive elements such as Al, P, and Cr while retaining or precipitating the radioactive elements, including Sr and the actinide elements, in the tank sludges. This partitioning between solids and precipitates is fundamentally dependent upon the chemical speciation of the elements present in the tank processing solutions. Of particular importance is separation of the radioactive and hazardous actinide elements and fission products from the sludges and supernatants, particularly from supernatants containing high concentrations of strong chelating agents that can act to solubilize the actinides and fission products and interfere with subsequent metal ion extraction processes. Specifically, the fundamental understanding of chemical speciation reactions gained from these studies is needed to propose methodologies for removing Sr and Am/Cm from organic chelates present in high-level tank waste, via competition, displacement, or other reactions, without developing costly and potentially hazardous organic destruction technologies.

Research Progress and Implications

This section describes the progress of the PNNL studies. The research at FSU, which is currently focused on the speciation of Cm and Am under similar hydroxide and carbonate conditions, will be reported by Professor Choppin in a separate document. The PNNL research progress is summarized in three areas: Sr speciation, trivalent actinide speciation, and supporting studies. The supporting studies focus on solution calorimetry, isopiestic measurements, and applications of capillary electrophoresis-mass spectrometry. The chemical systems described in the Sr speciation section are divided into systems without chelators and systems with chelators.

Studies on Sr speciation

Unraveling the speciation reactions of Sr in complex tank waste requires studies of speciation reactions in the presence and absence of chelators. Speciation reactions in four chemical systems were studied: Na-Sr-OH-H_2O, Na-Sr-CO_3-H_2O, Na-Ca-OH-H_2O, Na-Ca-CO_3-H_2O, and the mixed system Na-Sr-Ca-OH-CO_3-H_2O with and without added chelators. Only the results for the Sr-containing systems are summarized in this report. The data for the systems containing Ca are included in the open literature. The systems including Ca and Sr were studied to begin addressing the issue of metal ion competition and displacement of Sr from the chelates. Ca was chosen for these initial studies because it is present in large amounts in tanks waste, and Ca^{2+} has approximately two orders of magnitude higher affinity for the organic chelators than Sr^{2+}.

Na-Sr-OH-H_2O

Although the hydrolysis of Sr^{2+} is known to be relatively weak, these conclusions are based upon experiments at relatively low total base concentration (<01 M) and several possible species (i.e., $SrOH^+$, $Sr(OH)_2(aq)$, $Sr(OH)_3^-$...) could be present at higher base concentration (e.g., several molal). To address this issue we examined the solubility of $Sr(OH)_2{\cdot}8H_2O$ in NaOH solutions extending to high base concentration. These results show lower solubilities than those predicted solely with Pitzer's form of the extended Debye-Huckel equation. It was therefore impossible to fit these experimental data to any combination of equilibrium constants for Sr-OH species. Interestingly, density functional theory (DFT) calculations on $Sr(H_2O)_n^{2+}$ clusters generated by removing a proton from $Sr(H_2O)_8^{2+}$ to form $Sr(H_2O)_7OH^+$ (Figure 1) show that the hydroxyl group is more closely associated with bound water molecules than with the central Sr^{2+} cation. These calculations indicate that even the successive addition of water molecules can delocalize the hydroxyl group from the central Sr^{2+} cation, indicating that associations of hydroxyl with Sr^{2+} are so weak as to be overcome by the hydrogen bonding with just the first solvation shell. Our

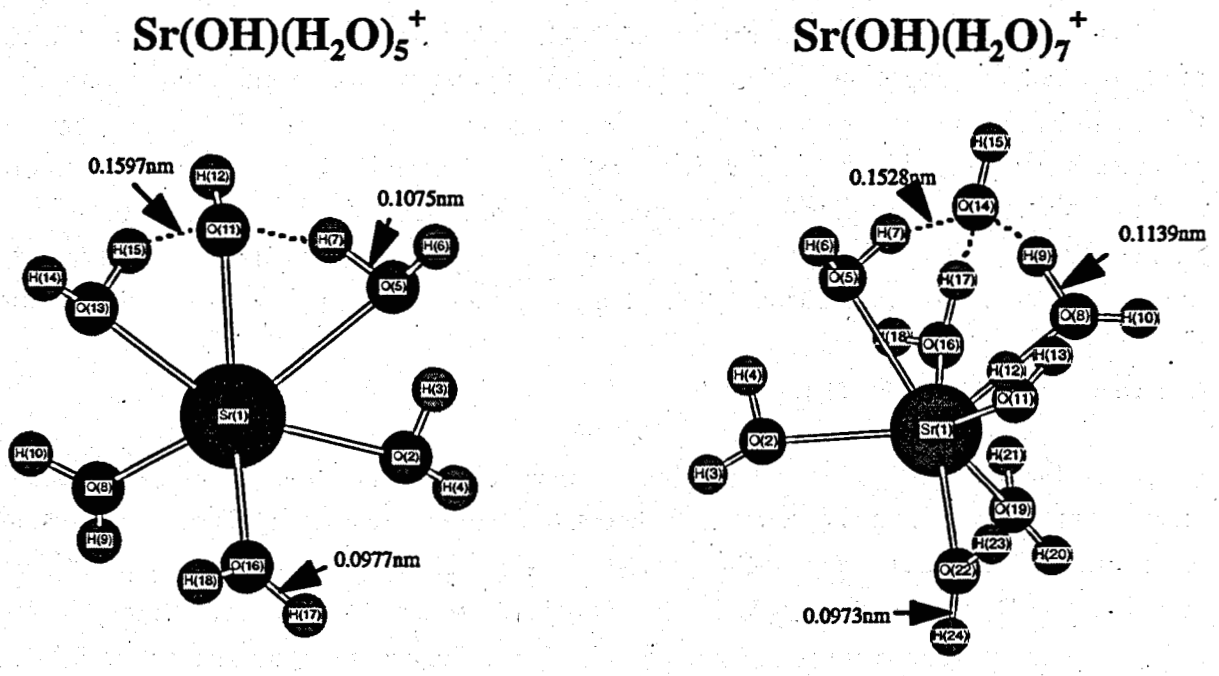

Figure 1. Structures of Gaseous $Sr(H_2O)_5OH^+$ and $Sr(H_2O)_7OH^+$ Calculated by DFT

thermodynamic model for this system therefore describes the observed non-idealities in the solution phase free energy solely by the use of Pitzer ion-interaction parameters in the activity coefficients expressions.

Effects of Chelators

In the presence of added chelators, the solubility data for $Sr(OH)_2{\cdot}8H_2O$ as a function of added NaOH and in the presence of 0.1 M added chelate (Figure 2) show that, in the case of EDTA and HEDTA, essentially all of the added chelate is complexed with Sr and that even high base concentration has little effect on the displacement of Sr from the these chelates. In the case of added IDA, the results with and without added chelate show that the solution speciation is dominated by Sr-IDA complexes. Apparently, the hydrolysis of Sr^{2+} is too weak to effectively displace the weakest chelators even at very high base concentration.

The addition of the organic chelates affects the speciation reactions in quite different ways depending upon the specific chelate studied (Figure 2). In the case of IDA, the observed solubilities are essentially the same as those observed without added chelator, indicating that only aqueous Sr^{2+} or Sr-CO_3 complexes are present. The aqueous Sr-IDA complexes are too weak to

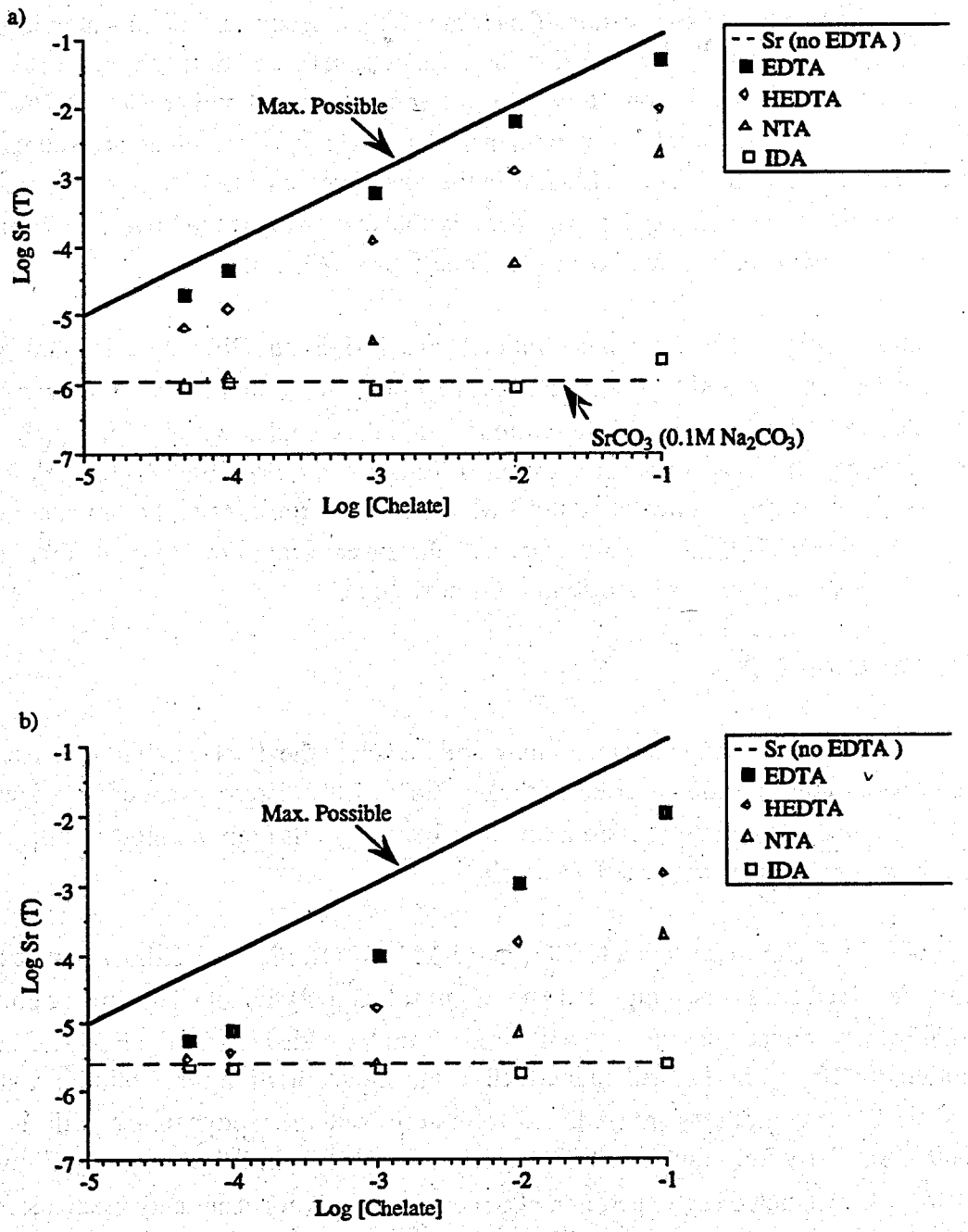

Figure 2. Effects of Added Na_2CO_3 on the Displacement of Sr from the EDTA Chelate: a) 0.1 M Na_2CO_3 solutions, b) 1.0 M Na_2CO_3 solutions. Note the complete displacement of Sr from IDA at high carbonate and the displacement of 0.001 M NTA at high carbonate.

out-compete carbonate for the Sr^{2+} cation. This same effect is seen to a limited extent in the case of NTA, where the carbonate complexes dominate the aqueous speciation at added NTA concentrations less than 0.001 M but become the dominant Sr complexes at higher added NTA. The same trend of increasing Sr complexation with increasing stability of the aqueous Sr-chelate complexes continues for HEDTA and EDTA. In the specific case of EDTA, not only is all of the Sr present as Sr-EDTA complexes but, with the possible exception of the lowest concentrations of added EDTA, there is only a small concentration of "free" EDTA.

The addition of higher Na_2CO_3 concentrations (e.g., 1 M, Figure 2b) results in a uniform and competitive shift in the solubility and speciation reactions. The results for NTA show a substantially enhanced displacement of the Sr from the Sr-NTA complex with Sr-NTA complexation being important only at NTA concentrations >0.01 M. Similarly, Sr- HEDTA complexes are now important only at concentrations >0.0001 M. Sr-EDTA complexes still dominate the speciation of Sr in these solutions even at very low chelate concentrations (e.g., 0.0005 M), although most of the EDTA present in solution is now "free."

$Na\text{-}Sr\text{-}Ca\text{-}OH\text{-}CO_3\text{-}H_2O$

The presence of other competing metal ions could result in the displacement of Sr from the organic chelates. In this section the effects of added Ca^{2+} on the displacement of Sr^{2+} from the chelates is described. Calcium was chosen for study because of its high thermodynamic stability with the important chelates and weak hydrolysis.

The results for $SrCO_3$ with added $CaCO_3$ in 0.1 M Na_2CO_3, Figure 3a, show 1) that essentially all of the added EDTA is complexed with Ca in solution, 2) the total aqueous Sr concentration is significantly reduced because of competition from the added Ca for the EDTA, 3) solution concentration of $<10^{-3}$ M EDTA will be ineffective in complexing Sr in these solutions, and 4) the aqueous Sr concentrations are predicted accurately using thermodynamic equilibrium relationships. Similarly, the results for $SrCO_3$ with added $CaCO_3$ in 1.0 M Na_2CO_3, Figure 3b, also show that the predicted and experimental Sr concentrations are accurately predicted, even though the electrolyte medium has changed significantly.

The results for Na_3HEDTA show essentially the same features as the results for EDTA in that 1) Ca is effective in displacing Sr from the HEDTA chelate, 2) HEDTA concentrations of $<10^{-3}$ M HEDTA will be ineffective in complexing Sr in these solutions and 3) the Sr-HEDTA concentration is accurately predicted.

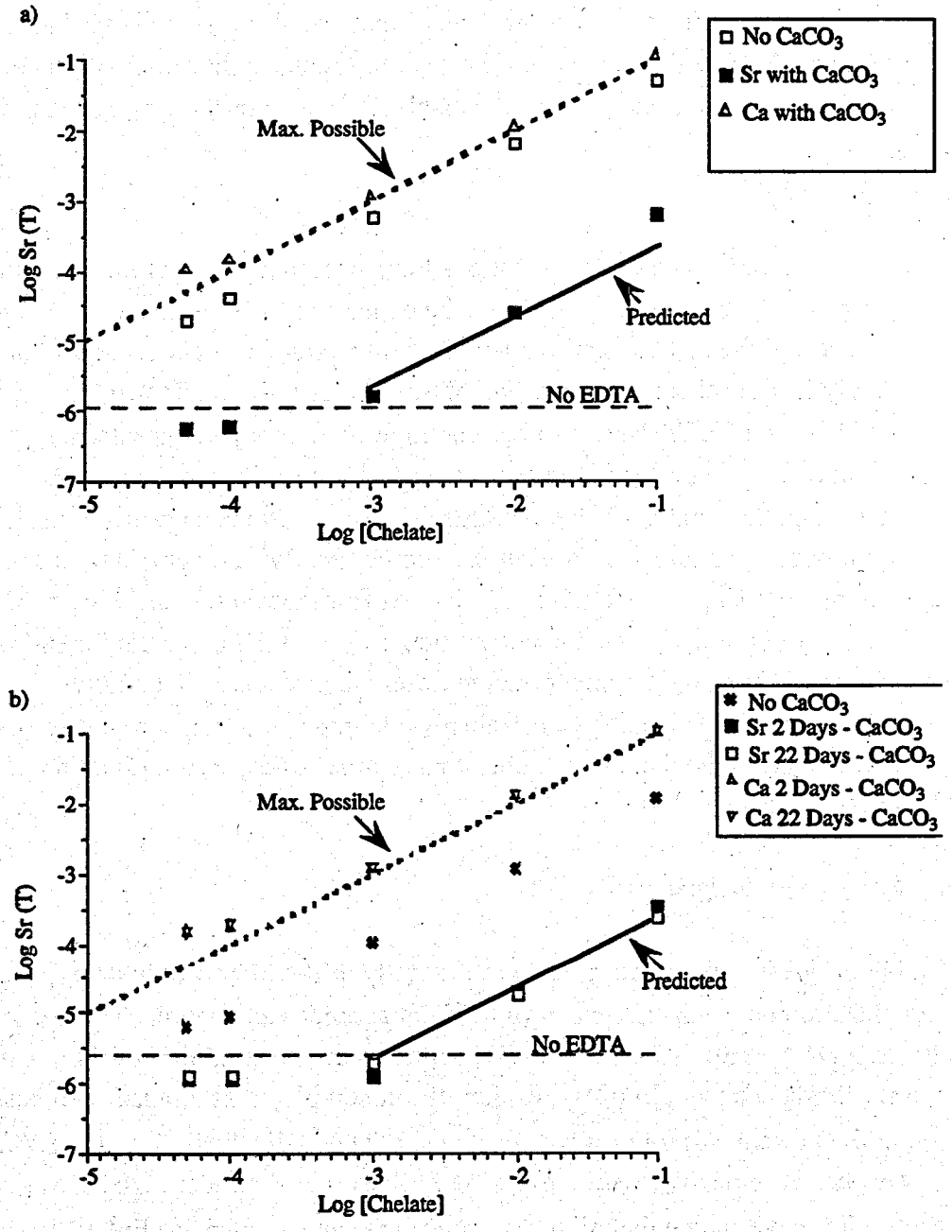

Figure 3. Effects of Added $CaCO_3$ (c) on the Displacement of Sr from the EDTA Chelate: a) 0.1 M Na_2CO_3 Solutions, b) 1.0 M Na_2CO_3 Solutions

The results for NTA are not as dramatic. The predicted concentrations still follow the thermodynamic predictions, but the displacement reactions of Sr by Ca from the NTA are much less effective because of the decreased stability of the Ca-NTA complexes relative to the Sr-EDTA and Sr-HEDTA complexes. This lower stability means that not all of the added NTA is tied up with Ca, leaving "free" NTA in such solutions. This greatly reduces the competition between Ca-NTA and Sr-NTA complexes and reduces the displacement of Sr-NTA by added Ca.

Summary of Sr Studies

These results have some interesting implications for processing basic/carbonate solutions such as those in high-level tank waste. First, given the expected range in chelate concentrations present in tank waste and the fact that carbonate is present in significant concentration in all tanks, it is not likely that the chemical speciation of Sr or NTA will be affected by the presence of IDA. Only HEDTA and EDTA appear to be present at high enough concentrations and form strong enough complexes to significantly impact the speciation of Sr in tank waste. Such results are important in limiting the number of chemical species that need to be considered in chemical modeling of tank processing strategies. In addition, competition with other metal ions present in such solutions, in this case Ca, can effectively displace Sr from the strong chelating agents HEDTA and EDTA, depending upon the concentration of Sr and the competing metal ions. This result indicates that metal ion displacement may represent an acceptable alternative to costly and hazardous organic destruction technologies in reducing the impacts of organic chelates in tank processing, especially given the fact that the chelators represent only a small fraction of the total organic carbon in tank waste.

Trivalent Actinide Studies

Considerable progress has also been made in the study of the effects of hydrolysis and carbonate complexation on the displacement of trivalent actinides and actinide analogs from the organic chelates: EDTA, HEDTA, NTA, and IDA. Studies on the solubility of Eu (a trivalent actinide analog) compounds [e.g., $Eu(OH)_3(c)$] have been completed as a function of base concentration in the presence of four organic chelates, EDTA, HEDTA, NTA, and IDA. $Eu(OH)_3(c)$ was chosen for study because of its very low solubility under high base concentration. These studies have shown that high base concentration can displace Eu(III) from all of the organic chelates studied. The effective NaOH concentration for the displacement reaction is dependent on the nature of the specific chelate studied and the chelate concentration. For example, Figure 4 shows the solubility data for $Eu(OH)_3(c)$ in the presence of different concentrations of EDTA, which is the most difficult chelate to displace. Comparisons of soluble Eu(III) concentrations in the presence and absence of EDTA show that increasing NaOH concentration

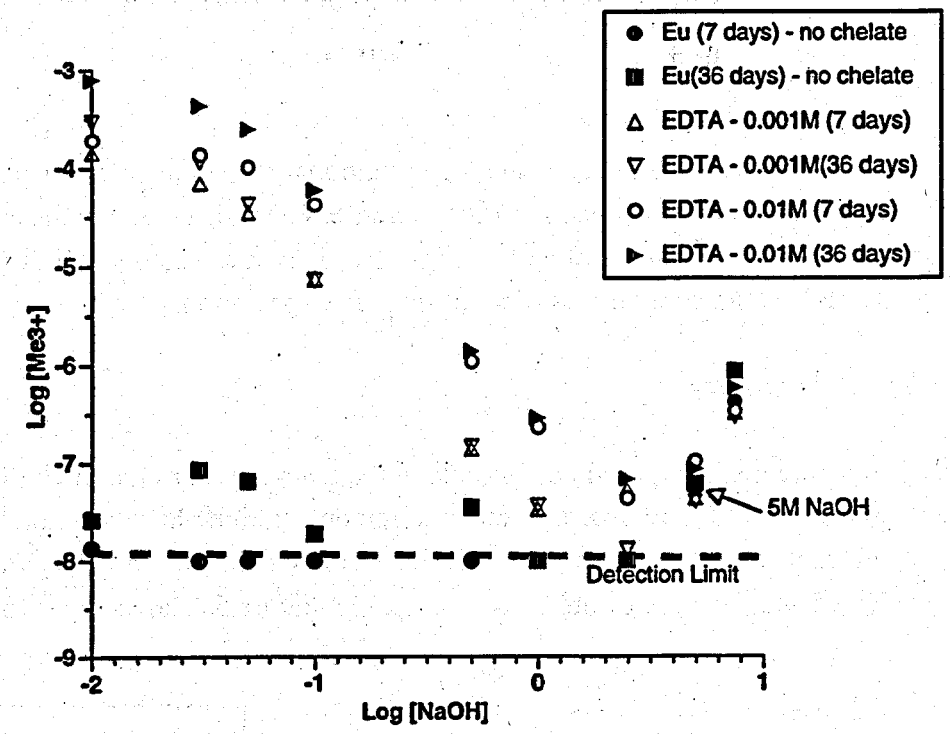

Figure 4. The Solubility of $Eu(OH)_3(c)$ in the Presence and Absence of EDTA. Note the dissolved Eu(III) concentration at high base concentrations is identical both in the presence and absence of chelate, indicating that Eu(III) has been completely displaced from the chelate.

Eu(III) from the EDTA chelate and that at NaOH concentrations ≥ 5 M all of the Eu(III) is removed from EDTA solutions (e.g., [EDTA]≤ 0.01 M). At higher base concentration the solubility of $Eu(OH)_3(c)$ increases, but this is a result of the formation of soluble hydrolysis species (e.g., $Eu(OH)_4^-$, ...). Similar results have been found for the other chelates with, as expected, IDA being the easiest chelate to displace. Complete displacement of 0.01 M IDA solution occurring in 0.03 M NaOH, indicating that IDA is not of concern in complexation of trivalent actinides at typical tank supernatant concentrations of 2 M NaOH. Such data are needed to develop accurate thermodynamic models for trivalent actinide species under high base conditions and to provide useful practical data for processing engineers.

In addition to the studies of $Eu(OH)_3(c)$, studies have also been initiated on the solubility of $EuPO_4(c)$ in the presence of the same four organic chelates: EDTA, HEDTA, NTA, and IDA. $EuPO_4(c)$ were chosen for study owing to very low solubility in the presence of phosphate.

The presence of phosphate must be considered since it occurs in significant concentration in most waste tank sludges. Only the first sampling of these suspensions has been completed.

Supporting Studies

In addition to the extensive experimental and computational modeling studies performed under the Sr and trivalent actinide studies, significant progress has been made in the areas of solution phase calorimetry, mass spectrometry, and isopiestic measurements. All three of these areas of study directly enhance our studies of solution phase speciation.

Solution Phase Calorimetry

Calorimetric measurements are used both to extend the temperature range of validity of our thermodynamic models and to provide useful information on solution phase reaction kinetics. Studies of reaction kinetics are possible because the heat of reaction is a sensitive parameter that can be directly studied as a function of time. As an example, Figure 5a shows the measured heat

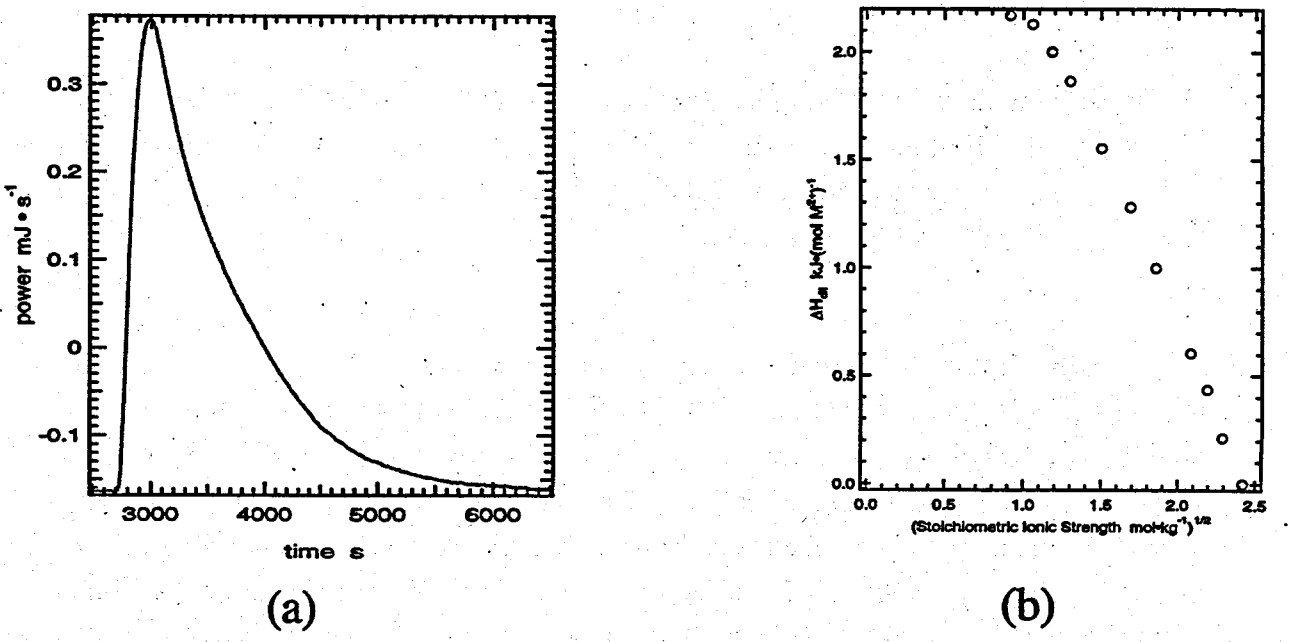

Figure 5. (a) Enthalpy of Exchange Measurement for $SrEDTA^{2-}$ by Carbonate Complexed Ca^{2+} in the Presence of Crystalline $CaCO_3$(c) (solutions contained 0.01 M EDTA, 0.1 M NaOH, and 0.1 M Na_2CO_3); (b) Enthalpy of Dilution Measurements of Na_4EDTA-NaOH-H_2O Mixtures

of reaction for the exchange of chelated $SrEDTA^{2-}$ by carbonate complexed Ca^{2+} under representative basic and carbonate conditions shown in Figure 4 (e.g., 0.01 M EDTA, 0.1 M NaOH, and 0.1 M Na_2CO_3). These data indicate that the exchange reaction is extremely rapid, being essentially complete in 1.5 hours. This information is useful for developing temperature-dependent thermodynamics models for the organic chelate reactions; it also provides useful kinetic information on the exchange of potentially kinetically inhibited species.

In addition to the kinetic information, enthalpy of dilution measurements have been conducted on Na_4EDTA-NaOH-H_2O mixtures (see Figure 5b) to allow the activity coefficient expressions to be extrapolated over the range of temperatures (25–100°C) needed to develop tank waste processing strategies.

Isopiestic Measurements

Isopiestic studies of electrolyte solutions is a well established technique for obtaining direct information on the activity of water, which in turn through the use of the Gibbs-Duhem relation yields direct information of the solution phase activity coefficients of the species involved. The method is particularly useful at high electrolyte concentrations such as those relevant to this research. Therefore, as part of this study extensive isopiestic measurements have been made of osmotic coefficients in the mixed NaOH-Na_4EDTA systems (Figure 6). These data are being used to develop better thermodynamic models (i.e., Pitzer ion interaction coefficients) for Na^+-$EDTA^{4-}$ and OH^--$EDTA^{4-}$ interactions.

Mass Spectrometry

As part of this study, solution speciation reactions are planned using capillary electrophoresis-mass spectrometry (CE-MS). CE-MS offers the potential of determining the mass/charge ratio of complexes that may be present in mixed metal-chelate systems where unraveling complex spectral signatures will be difficult or impossible. Our initial results with CE-MS have proven effective in identifying Co(II)/Co(III)EDTA complexes in negative ion mode from mixed electrolyte solutions. This represents the first known combination CE separation with mass spectrometry detection of metal-organic complexes under negative ion conditions that we are aware of. These results will be presented at the American Society for Mass Spectrometry Meeting in Orlando, Florida. The results of these preliminary studies represent a major step forward in combining the advantages of CE separation and mass spectrometry detection under negative ion conditions.

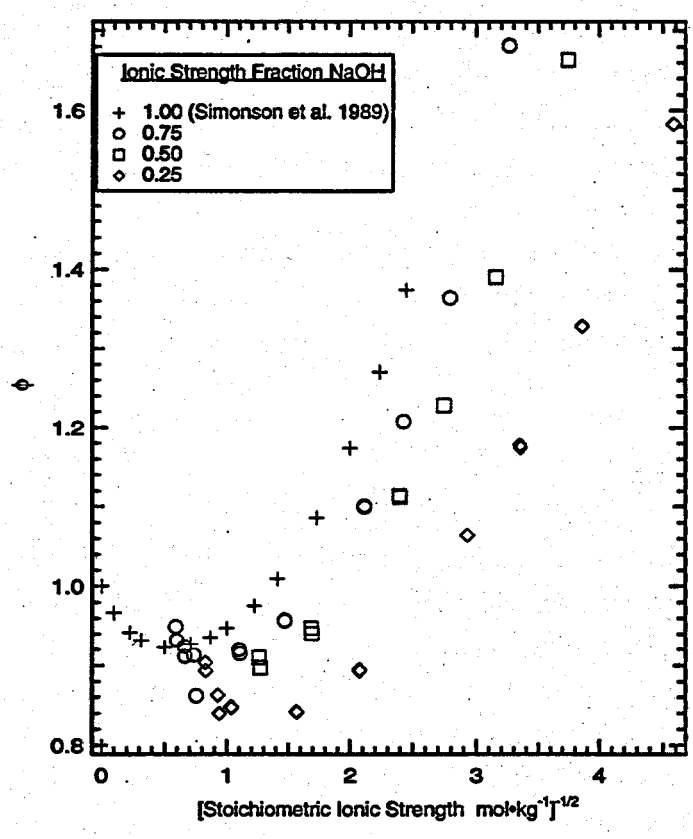

Figure 6. Isopiestic (osmotic coefficient) Measurements of Mixed NaOH-Na_4EDTA Solutions Covering a Broad Range in Mixing Fractions at 50°C

Studies are currently under way to apply these methods to the analysis of additional metal-organic complexes (both mixed metal and mixed chelator) and metal-organic complexes in solutions with high ionic strengths, such as those in waste tanks.

Planned Activities

Studies at PNNL on the competitive effects of hydrolysis and carbonate complexation of Sr with the organic chelates at 25°C have been largely completed and published. This effort has resulted in several journal articles and scientific presentations (see below). Initial experiments have also been completed with trivalent actinide analogs [using $Eu(OH)_3(c)$]. Significant progress has also been made in the areas of solution calorimetry, mass spectrometry, and isopiestic studies. Plans for FY 1999 call for completing the temperature-dependent thermodynamic model for Sr in the mixed chelate systems, completing the studies that have been initiated on the

$EuPO_4(c)$, and publishing the results on the $Eu(OH)_3(c)$ in mixed chelate systems and those of solution phase calorimetry. Plans for FY 1999 also call for extending the CE/MS studies to high ionic strength solutions. Support for studies in outer years will be required to extend the trivalent actinide model to higher temperatures (>25°C), unravel the speciation of tetravalent actinides [especially Pu(IV)], and verify the modeling predictions and speciation measurements (CE/MS) in tank waste, specifically complex concentrates from the Hanford Site.

Publications and Presentations

Felmy AR, DA Dixon, JA Campbell, and MJ Mason. September 7–11, 1997. *The Effects of OH, CO_3, and Ca on the Displacement of Sr from the EDTA Chelate: Implications for Waste Processing.* Abstract presented at the ACS National Meeting, Las Vegas.

Felmy AR, and MJ Mason. 1998. "The Displacement of Sr from Organic Chelates by Hydroxide, Carbonate, and Calcium in Concentrated Electrolytes." *J. Solution Chemistry,* 27(5):435-454.

Felmy AR, and MJ Mason. August 9–15, 1998. *The Aqueous Complexation of Eu(III) with Organic Chelating Agents at High Base and High Ionic Strengths: Metal-Chelate Displacement Induced by Hydrolysis and Precipitation Reactions.* Abstract accepted for presentation at the 53rd Calorimetry Conference, Midland, Michigan.

Felmy AR, DA Dixon, and MJ Mason. August 4–8 1997. *The Complexation of Alkaline Earth Cations by Organic Chelates at High Ionic Strength: Competitive Effects of Hydrolysis and Carbonate Complexation.* Abstract presented at the 52nd Calorimetry Conference, Asilomar, California.

Felmy AR, DA Dixon, and MJ Mason. 1998. "Hydrolysis and Carbonate Complexation of Alkaline Earth Cations: Consistency of Thermodynamic and Molecular Modeling Results." *J. Chem Thermodynamics* (in press).

Felmy AR, DA Dixon, JR Rustad, LM Onishi, and MJ Mason. August 4–8, 1997. *The Use of Molecular Modeling Calculations to Improve the Development of Thermodynamic Models: Hydrolysis, Carbonate, and EDTA Complexation of Alkaline Earth Cations.* Abstract presented at the 52nd Calorimetry Conference, Asilomar, California.

Oakes CS, and AR Felmy. August 4–8, 1997. *Thermodynamics of [Na_4EDTA+NaOH]{aq}, Including New Isopiestic Measurements to 373K.* Abstract presented at the 52nd Calorimetry Conference, Asilomar, California.

Oakes CS, SM Sterner, and AR Felmy. 1998. *Thermodynamic Properties of Aqueous Solutions of Calcium Nitrate* [$CaNO_3)_2$] to 425K and to Ionic Strengths in Excess of 24 mol·Kg^{-1}. Manuscript in PNNL clearance process. Pacific Northwest National Laboratory, Richland, Washington.

Petersen CE, JA Campbell, AR Felmy, KL Wahl, and JW Finch. May 31–June 4, 1998. *Analysis of Metal-Organic Complexes Using* CE/MS. Presented at the ASMS Meeting in Orlando, Florida.

Sterner SM, AR Felmy, JR Rustad, and KS Pitzer. 1997. *Thermodynamic Analysis of Aqueous Solutions Using 'INSIGHT.'* PNWD-SA-4436, Pacific Northwest National Laboratory, Richland, Washington.

Sterner SM, A Felmy, and KS Pitzer. 1998. "Correlation of Thermodynamic Data for Aqueous Solutions to Very High Ionic Strengths Using 'INSIGHT': Vapor-Saturated Water Activity in the System $CaCl_2$-H_2O to 250°C and Solid Saturation." *Proceedings of the Thirteenth Symposium on Thermophysical Properties* (in press).

Ion Exchange Processes and Mechanisms in Glasses

(First Year Funding: FY 1997)

Principal Investigator

Dr. B. P. McGrail
Pacific Northwest National Laboratory
P.O. Box 999, MSIN K6-81
Richland, WA 99352
(509) 376-9193 (phone)
(509) 376-2210 (fax)
Pete.McGrail@pnl.gov

PNNL Contributors

D. R. Baer
J. G. Darab
M. H. Engelhard
C. W. Lindenmeier
S. Thevusathan

External Collaborators

K. Ivanov (LBNL)
D. K. Shuh (LBNL)

Research Objective

Recent performance assessment calculations of a disposal system at Hanford, Washington, for low-activity waste glass show that a sodium ion exchange reaction can effectively increase the radionuclide release rate by over a factor of 1000 and so is a major factor that limits waste-loading. However, low-temperature ion exchange has not been thought to be important in recent analyses of waste glass durability. The objective of this work is to develop an understanding of the processes and mechanisms controlling alkali ion exchange and to correlate the kinetics of the ion exchange reaction with glass structural properties. A fundamental understanding of the ion exchange process is sought to developing lower ion exchange-rate glasses that would remain durable at higher-alkali waste loading.

Research Statement

This multidisciplinary research program involves two primary tasks to develop an understanding of the processes and mechanisms that control sodium ion exchange in waste-glass materials: 1) reaction mechanisms and 2) glass structure correlations. The objective of the reaction mechanisms task is to identify specific ion exchange mechanisms by using surface analytical techniques to probe the distribution of selected elements in the hydrated layers on glass surfaces. Differences in the uptake and distribution of selected isotopes will provide a signature characteristic of specific ion exchange reactions. The objective of the glass structure task is to determine whether differences in key structural properties, such as the number of nonbridging oxygens (NBO), bonding of alkali to other elements in the glass, and alkali coordination, can be correlated with differences in measured rates of alkali exchange. Both tasks are discussed in detail in the following sections.

An overview of the research plan is given in Figure 1. To simplify interpretation of the kinetics measurements and glass structure analyses, three series of simple glasses in the Na_2O-Al_2O_3-B_2O_3-SiO_2 family will be examined, where the amounts of Na, Al, B, and Si are systematically varied along compositional joins. Selective substitutions of network modifiers, such as CaO, ZrO_2, and La_2O_3, will also be made in the base glass to change the bonding coordination of Na^+ with network intermediate sites. Differences in the structural properties of these glasses will then be correlated with observed changes in the sodium ion exchange kinetics. It is the *combination* of the glass structure correlations with the identification of the ion exchange reaction mechanisms that provides the underpinning scientific basis for formulation of glasses with lower rates of alkali ion exchange. This new understanding of ion exchange processes and mechanisms will be evaluated at the conclusion of this research project in the formulation and testing of a low ion exchange-rate glass with a 25-wt% Na_2O loading.

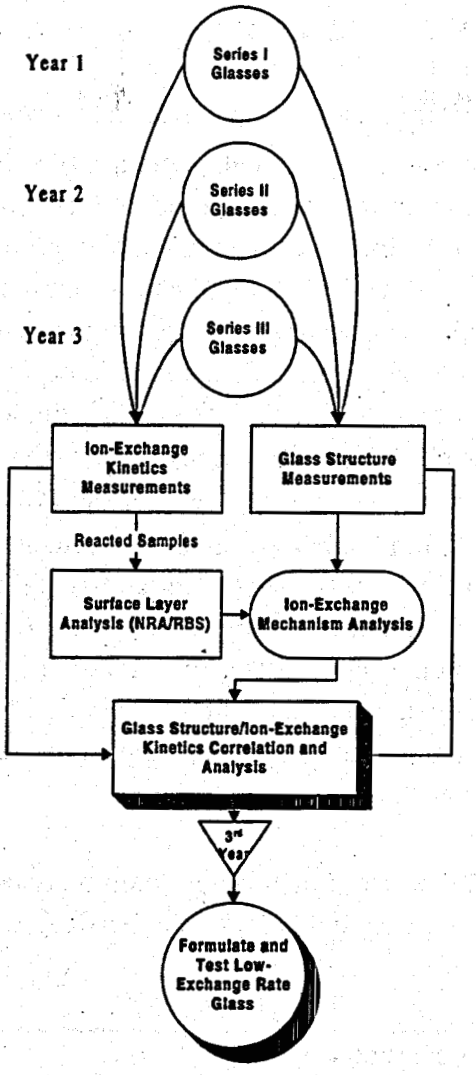

Figure 1. Research Plan Flow Chart

Research Progress

Project Status

This project was initiated in FY 1998 and is being performed cooperatively by PNNL and Lawrence Berkeley National Laboratory (LBNL). Progress in the first eight months has primarily focused on three activities: 1) developing and manufacturing the Series I glasses, 2) characterizing these glasses, and 3) designing, building, and testing the flow-through cells that will be used for the ion exchange kinetics measurements. A few scoping measurements of isotope distributions have also been completed with nuclear reaction analysis (NRA) and elemental depth profiles using Rutherford backscattering spectroscopy (RBS).

Series I Glass System Development

The objective of the glass formulation scheme used in this work was to allow for sufficient variation in the distribution of Na^+ in representative glasses (i.e., Na^+ distributed between ^{Q3}Si non-bridging oxygen and four-coordinated Al) in order to assess the effects of glass structure chemistry and, in particular, of the local environment of sodium on the properties of the glass. After several test melts, a $33.33Na_2O$-$66.67SiO_2$ (composition in mol%) baseline glass composition was selected. This formulation contains the largest amount of Na_2O possible to theoretically maintain no more than one NBO per Si atom (i.e., all the Si occurs as ^{Q3}Si). A set of sodium aluminum silicate glasses was then designed to keep the fraction of metals in the glass that are network formers (f_M^N) constant at 0.50 while varying the distribution of Na^+ between association with ^{Q3}Si non-bridging oxygen sites (f_{Na}^{Q3}) and four-coordinated Al sites (f_{Na}^{Al}). Based on the $33.33Na_2O$-$66.67SiO_2$ composition, which was given the nomenclature NaSiO-X, five Na_2O-Al_2O_3-SiO_2 glasses were formulated with the concentrations of Al_2O_3 ranging from 0 to 20 mol%, batched in 100+ gram quantities using Na_2CO_3, Al_2O_3 and SiO_2, melted at 1500°C for one hour in air, then quenched on a stainless steel plate. All melts except one (NaSiO-20.0Al, see below) were visually homogeneous and readily pourable, and they yielded a clear, visibly homogenous glass. Table 1 summarizes the target composition as well as the f_{Na}^{Q3} and f_{Na}^{Al} theoretically determined for these glasses.

Table 1. Composition, Theoretical Fractions of Sodium Associated with NBOs (f_{Na}^{Q3}) and Tetrahedrally Coordinated Al (f_{Na}^{Al}), and NMR Results Obtained for the Series I Glasses

Sample	Composition (mol%)			f_{Na}^{Q3}	f_{Na}^{Al}	Peak Position (ppm)	
	Na_2O	Al_2O_3	SiO_2			^{29}Si[(a)]	^{27}Al[(b)]
NaSiO-X	33.33	-[(c)]	66.67	1.00	-	-87±1	-
NaSiO-5.0Al	35.00	5.00	60.00	0.86	0.14	-86±1	+61±1
NaSiO-10.0Al	36.67	10.00	53.33	0.73	0.27	-81±1	+61±1
NaSiO-15.0Al	38.33	15.00	46.67	0.61	0.39	-78±1	+62±1
NaSiO-20.0Al [(d)]	40.00	20.00	40.00	0.50	0.50	-	-
α-Al_2O_3	-	100.00	-	-	-	-	+12±1

(a) Tetramethylsilane (TMS) was used as a ^{29}Si NMR reference.
(b) $AlCl_3$ was used as a ^{27}Al NMR reference.
(c) - indicates "not applicable."
(d) The NaSiO-20.0Al glass did not form a homogeneous melt and was thus not considered further.

The NaSiO-X, NaSiO-5.0Al, NaSiO-10.0Al, and NaSiO-15.0Al glasses were crushed and remelted at 1500°C for one hour, cast into bars, then annealed. Subsequently, coupons with dimensions 1.0 x 1.0 x 0.05 cm were cut from the annealed bars, polished in mineral oil using 600-grit SiC paper, and then ultrasonically cleaned in ultrapure acetone and ethyl alcohol. These samples were used for ion-exchange rate measurements.

Series I Glass Characterization

NMR Studies

As the glass composition is systematically changed from that of NaSiO-X to that of NaSiO-15.0Al, a greater amount of the Na^+ is transferred from being associated with ^{Q3}Si sites to being associated with network-forming Al sites, which will presumably affect the rate of Na^+ ion exchange. Samples of these glasses, as well as reference materials, were analyzed using ^{27}Al solid-state NMR to indirectly confirm this distribution of Na^+. The results are summarized in Table 1. As with other low-level waste-based glass compositions we have studied (Darab et al. 1997), each of the glasses studied here exhibited only a single, broad, asymmetric ^{27}Al NMR peak at 61±1 ppm. A peak at this position is indicative of tetrahedrally coordinated Al as opposed to octahedrally coordinated Al, which occurs at 12 ppm (see Table 1).

The ^{27}Al NMR results confirm that all of the Al in these four glasses occurs as tetrahedrally coordinated network-forming sites, presumably by association with charge-compensating Na^+ ions. Based on this presumption and the target concentration of Al_2O_3 and Na_2O in these glasses, the f_{Na}^{Al} values have been determined (Table 1). Assuming that the remaining Na^+ is associated with ^{Q3}Si, the f_{Na}^{Q3} values have also been calculated.

Similarly, ^{29}Si solid state NMR spectra were obtained for each of these glasses. As in previous studies on related glass systems, only a single, relatively broad but symmetric ^{29}Si NMR peak was observed. The ^{29}Si NMR peak position systematically shifts from -87 ppm for the NaSiO-X glass to -78 ppm for the NaSiO-15.0Al glass (see Table 1, above) due to the substitution of Al_2O_3 for SiO_2. This range of chemical shifts is typical of ^{Q3}Si.

X-Ray Absorption Spectroscopy Studies

Several preliminary investigations have been carried out to determine the best technique and necessary experimental parameters to obtain structural information from sodium x-ray absorption and related synchrotron radiation methodologies. These studies were initiated early in the project, before preparing the actual sample materials to be used for the ion exchange studies. These experiments were performed at the Advanced Light Source (ALS) on beamline 8.0 undulator in the soft x-ray emission (SXE) fluorescence endstation. The SXE technique was used to determine whether electronic information could be obtained from resonant sodium K-edge

excitation to provide insight on the local sodium structural environment (Nordgren and Wassdahl 1995). This was the first time the Na K-edge had been investigated in this manner. Although the first results were interesting and suggested that this might be a viable method to obtain structural information, careful follow-on experiments determined that the width of the Na fluorescence line prevents the extraction of useful structural data from materials with a limited amount of order.

A new experimental approach to obtain x-ray absorption fine structure (XAFS) data from the Na K-edge has been explored using the high-photon-energy capabilities of a spherical grating monochromator (SGM) matched with an undulator source of the ALS. To the best of our knowledge, these are the first studies to take advantage of these new opportunities. All previous studies have employed double-crystal monochromators to perform Na XAFS (McKeown et al. 1985). Figure 2 shows smoothed Na XAFS spectra collected at the ALS in fluorescence detection mode from the test glasses and a reference material. Differences in the near edge region of the spectra are obvious. The data from the extended portion of the Na XAFS spectra are being processed and theoretically fit to determine whether the data obtained from this experimental approach is of high enough quality to permit the extraction of the Na structural parameters.

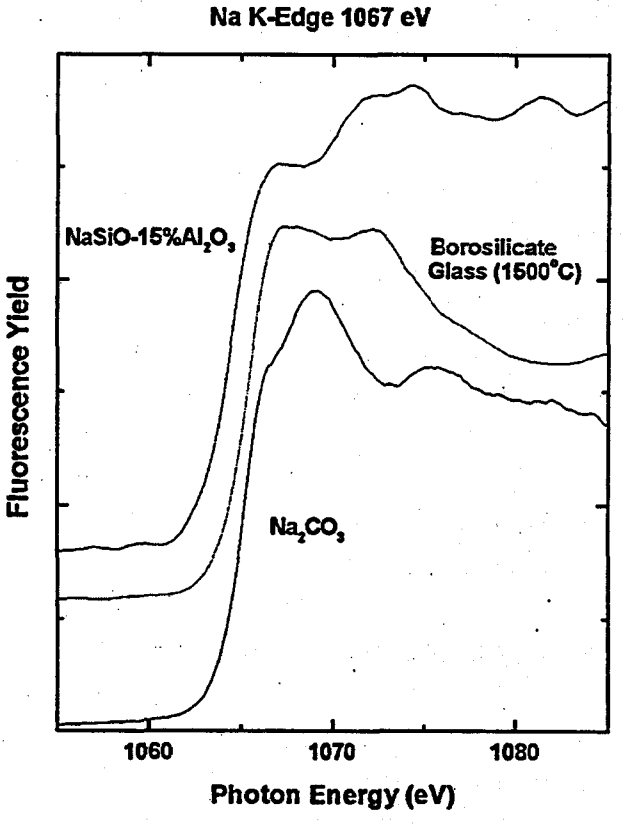

Figure 2. Experimental Sodium K-edge Spectra from Two Glasses and a Disodium Carbonate Reference Collected in Fluorescence Mode on Beamline 8 at the Advanced Light Source

The investigation of the Na K-edge by SXE and XAFS stimulated the simultaneous investigation of boron speciation at the K-edge by the same techniques because B is a constituent of interest in the Series II glasses to be evaluated next year. The structural characterization of boron is of particular importance because knowledge of the interactions between B, O, Na, Al, and Si is essential for building a fundamental understanding of glass durability (Bates et al. 1994). The only other viable method to obtain local structural information is NMR. However, NMR requires specially formulated glasses to avoid paramagnetic interferences, whereas real glasses may be used in SXE and XAFS investigations. The focus of boron studies in glasses is to determine the amount of three- versus four-coordinate boron. A schematic depiction of local boron environments and bonding is shown in Figure 3. The XAFS spectroscopy of the B K-edge has been well characterized, and the distinctive π^* electronic feature characteristic of the B sp^2 environment provides a signature of three-coordinate boron (Terminello et al. 1994). The differences in boron coordination between two identical glass-melt compositions, one processed at 1300°C and the other at 1500°C, are shown in Figure 4. The data were collected in the total electron yield mode, thereby slightly emphasizing the near-surface contribution from boron. The ratio of the peak intensities indicates that the 1300°C glass has about 1.7 times more boron in three-coordinate environments than in the 1500°C glass.

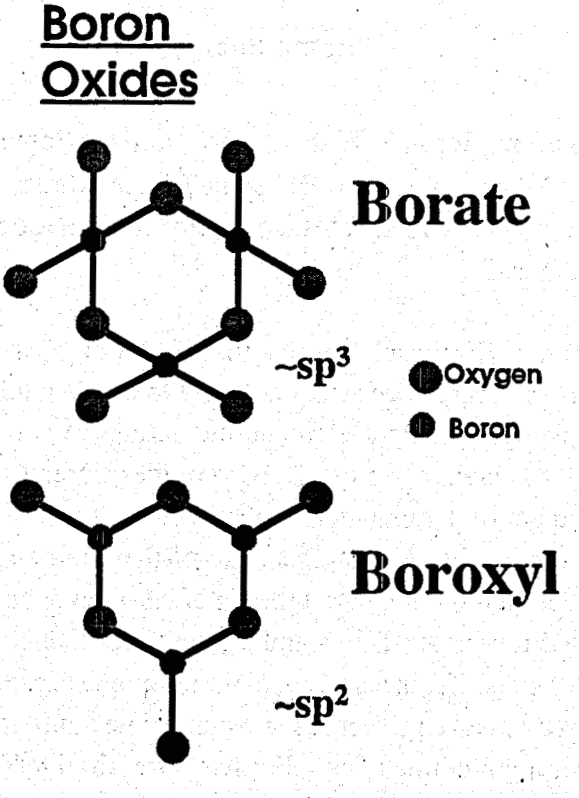

Figure 3. Schematic Representation of Two Common Boron Coordination Environments with Oxygen in Waste Form Glasses. The coordination environment in borate is approximately sp^3, whereas boroxyl bonding is more sp^2 in nature.

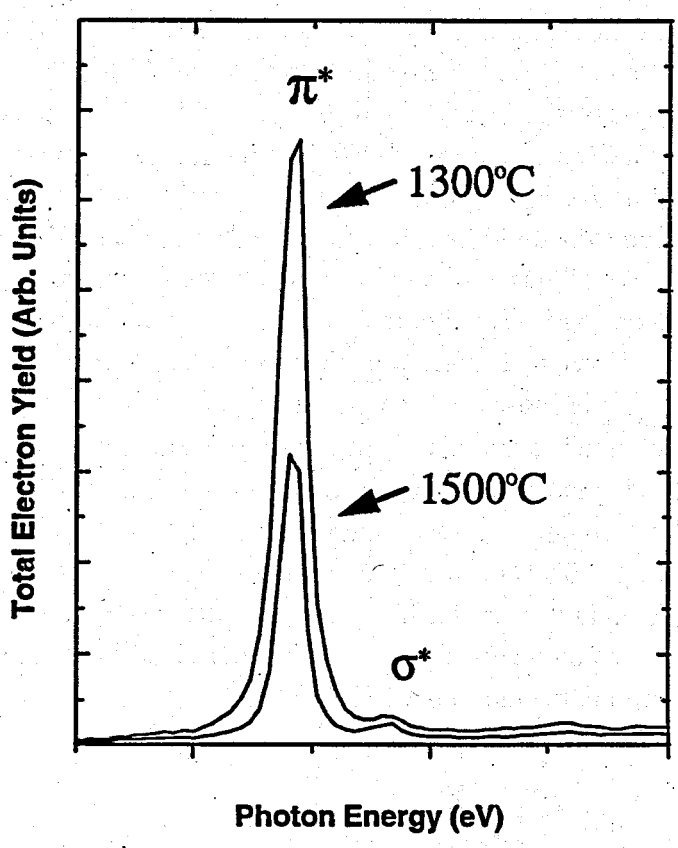

Figure 4. Comparison of the Boron K-Edge Spectra from the Same Borosilicate Glass Melt Composition Processed at Two Different Temperatures. The intensity of the B π^* feature from the glasses indicates a different coordination environment of B in the respective glasses.

The results of these studies firmly substantiate that XAFS of glass constituents will provide the structural information component necessary not only to understand the role of Na in the ion-exchange process but for many other light-element interactions in glasses. Although this speciation knowledge is difficult to obtain directly, XAFS provides a means to do so even in glasses that contain a full complement of paramagnetic constituents. It has been shown that XAFS spectra at the Na K-edge can be obtained using a state-of-the-art undulator beamline at the ALS, thus providing a convenient method of characterizing at least the near-edge region. The Na near-edge spectra show greatly different structures among the glasses, and theoretical approaches are being used to understand these differences. Evaluation of the extended-XAFS data will determine whether this experimental arrangement is an appropriate approach for the determination of Na metrical parameters throughout this study. Furthermore, similar XAFS studies at the B K-edge have been shown to be of great utility and suggest that investigations at the oxygen and aluminum K-edges for selected glasses are desirable. This knowledge will be valuable for establishing a fundamental understanding of the influence of glass structure on ion exchange.

Ion-Exchange Kinetics

An accurate measurement of the rate of Na ion exchange from the test glasses is one of the key challenges on this project. The experiments must be performed under controlled conditions of constant pH, temperature, and solution composition. To accomplish this, a flow-through experimental design was selected. However, these design challenges had to be overcome: 1) glass coupons must be used to provide samples for surface-layer-depth profiling; 2) several coupons must be exposed to the leachant solution simultaneously to provide a time-sequenced set of samples for analysis; and 3) fluid volumes need to be minimized because D_2O^{18} will be used in some tests, and it is expensive. The flow-through reactor design developed to meet these challenges is shown in Figure 5. It employs a single-pass flow-through column made of polyetheretherketone (PEEK) and contains five compartments, or "cells," to hold individual glass coupons of about 1.0 x 1.0 x 0.3 cm in size. Each cell is independently accessible by removing its stainless steel cover and Teflon seal. The column is orientated vertically, with the influent moving up through the column. For tests run at elevated temperature, the column is shrouded in a thermally controlled blanket and heated with a Kapton heater. Thermal control is performed using an Omega programmable controller and type T thermocouple. Influent is delivered to the system using a Kloehn programmable syringe pump.

Although flow-through testing was just initiated at the time this report was prepared, the results from a test with the NaSiO-15.0Al glass provide a good indication as to how the apparatus will perform. Three coupons of the prepared test glass were placed in the column, with operational parameters set at 40°C and flow rate at 1.0 mL/d (0.04 mL/h). A silicate buffer solution of 10^{-3} M Tris (THAM) + 5.25 x 10^{-4} M HCl+ and 2.8 x 10^{-3} M H_4SiO_4 was used. The pH of this buffer was 8.07 ± 0.10, measured at room temperature. Before the start of the tests,

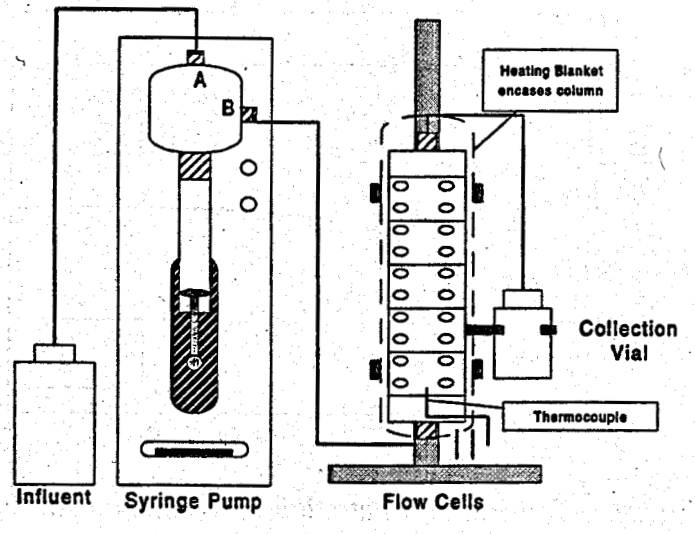

Figure 5. Schematic of Multichamber Flow-Through Column for Ion Exchange Kinetics Tests

several mL of the silicate buffer were allowed to flush through the column and effluent samples were collected for analysis. After putting the glass in the column chambers, resealing the lids, and restarting the solution flow, effluent samples were collected periodically over about five days. Effluent samples were analyzed by inductively coupled plasma atomic emission spectroscopy (ICP-AES).

After subtracting background Na levels in the buffer, measured Na and Si concentrations are plotted in Figure 6. The Si concentrations remained approximately constant, as expected for the saturated buffer solution. The Na concentrations approached a steady-state concentration (the goal of this test design) of about 31.7 ± 4.7 mg/L. This corresponds to a Na release rate of 2.4 x 10^{-8} ± 3.5 x 10^{-9} mol Na/m²·s. The Na release rate for this simple glass is about three orders of magnitude faster than the long-term ion-exchange rate we have measured in static tests on typical low-activity waste glasses at this same temperature. However, the static tests were conducted in deionized water, where the pH rises 2 to 3 units higher than in these tests. Because ion exchange rates are expected to be a strong function of pH, rates in the pH 8 flow-through experiments are expected to be higher.

Isotopic Depth Profiling

Trial tests were performed of the isotope-specific surface spectroscopies that will be used to characterize distribution of labeled-water species in hydrated glass surface layers. These measurements are made using a Van de Graaff accelerator and nuclear reactions D(d,p) ^{3}He, ^{18}O (p, α) ^{15}N for deuterium and oxygen analysis and Rutherford backscattering spectroscopy (α,α) to measure alkali loss or surface buildup. The NaSiO-10Al and NaSiO-15Al glasses were exposed to 30 mL of water made up from 10 mL of ($D_2{}^{18}O$ - 97.46 at% ^{18}O and 76.4% D) and 20 mL of

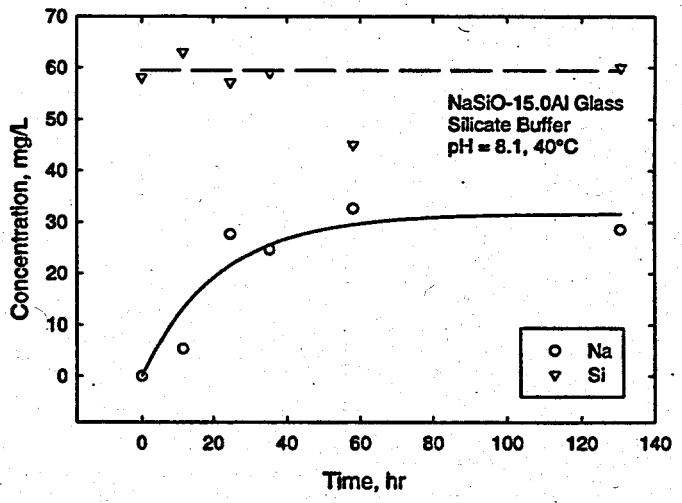

Figure 6. Effluent Concentrations as a Function of Time in Flow-Through Test Using Silicate Buffer at 40°C

($D_2{}^{16}O$ 99% D). Samples of these glasses were exposed for 220 hours at 50°C under static conditions. Specimens were then removed from solution, dried, coated with about 20 nm of carbon, and inserted into vacuum.

Figure 7 shows D(d,p) ^{3}He nuclear reaction data with peaks for deuterium and oxygen. The changes in amplitude and width of the deuterium peak relate to the concentration and depth of the deuterium penetration into the glass. For the deuterium measurement, the surface appears at the lower kinetic energy side of the peak, while the higher-energy proton comes from deeper into the material. Both glasses showed considerable amount of deuterium uptake. The amplitude of the deuterium signal indicates the amount of deuterium adsorbed near the surface, while the tail indicates the amount of penetration into the material. Although the surface intensity for the 15 mol% Al glass is about 4x that of the 10 mol% Al glass, the D decreases quickly with depth into the glass. For the 10 mol% Al glass, there is much less D at the surface, but there is considerable penetration. These results are consistent with the expected differences in durability of these glasses. We conclude from these preliminary results that the NRA technique appears to be viable for studying D and O uptake in these glasses.

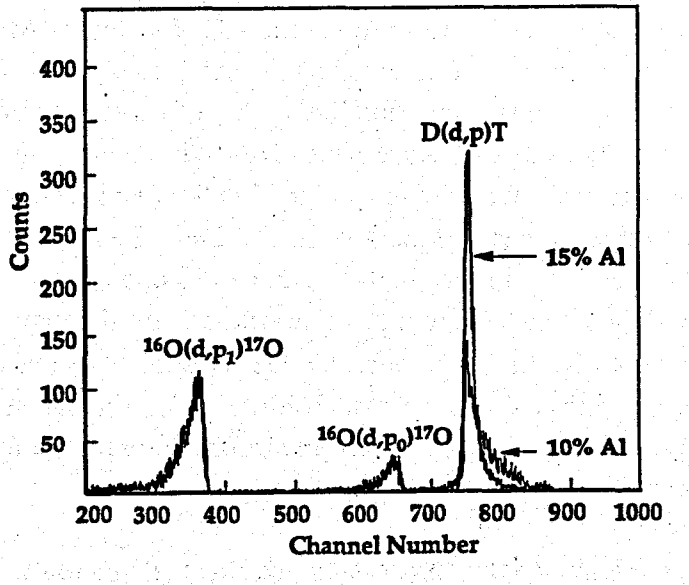

Figure 7. Results from Nuclear Reaction Analysis of NaSiO-10Al and NaSiO-15Al Glasses Reacted in Labeled Water at 50°C for 250 hours

Planned Activities

The observed variation of the ^{29}Si NMR chemical shift value with respect to glass composition is likely due to variation in the electronic interactions within the glass network, an indicator of the bonding characteristics within the network. For example, the delocalization of the excess

charge on a Na^+ stabilized tetrahedrally coordinated Al through its neighboring network-formers may influence the associated bonds; thus, it may influence how easily Na^+ can ion-exchange with a hydronium ion and how readily the network is hydrolyzed by diffusing water molecules. Indeed, a review of the available NMR and PCT chemical durability data on other low-activity waste glasses indicates at a very rudimentary level that as the ^{29}Si chemical shift value becomes less negative, the durability of sodium borosilicate and sodium boroaluminosilicate glasses increases. Thus, the next step is to correlate the ^{29}Si NMR chemical shift values with the more precisely determined glass properties measured during the course of this project. The planned study of the Series II glasses, incorporating B_2O_3, will be a key database of information to test these glass structure/property correlations.

Flow-through experiments in H_2O and D_2O are now in progress on the Series I glasses, and most will be completed by the end of this fiscal year. We hope to complete tests on the NaSiO-X glass in $D_2{}^{18}O$ as well. We are also making new glasses that contain a chemical tracer (Mo) so that we can subtract any Na released by matrix hydrolysis (not by ion exchange) in the flow-through tests.

There is a scheduled experimental beam run at the ALS in which XAFS will be collected in fluorescence detection mode from the Series I glasses at the Na K-edge. The results of these Na investigations, the theoretical simulations, and the quality of the structural parameters obtained will determine the approach used for characterizing Na environments for the duration of the project. The Na structural information derived from the XAFS will be used to establish the baseline parameters for the exchange studies. At the same time, the B K-edge will be investigated by both total yield and fluorescence detection methods to compare B coordination environments from the near-surface region and the bulk. This will be done with glasses that have had the B coordination previously examined by NMR. In this manner, the B π^* response will be correlated to the NMR results and the B K-edge yields calibrated to an absolute scale. Enough results will have been obtained after these experiments to provide baseline information for the ion exchange experiments and for the preparation of manuscripts.

Experimental, theoretical, and data processing activities related to the Na K-edge XAFS investigations will remain the primary activities for the next two years of the project. This research effort will develop into a more regular activity. It may become necessary to develop, acquire, or have more routine access to a fluorescence detector. The experimental activities will remain focused at the ALS unless the data quality in the extended-XAFS proves insufficient to extract metrical parameters. This will be determined by the end of the first year. In that event, the experiments may switch to beamline 3-3 at the Stanford Synchrotron Radiation Laboratory. Should the Na XAFS experiments and data processing proceed without complications, the scope of the studies could be expanded to include K-edge XAFS studies of oxygen and aluminum in the glasses in the later years of the project.

Publications and Presentations

There have been no publications submitted from this project yet. We expect publishable results from the sodium near-edge data in combination with theoretical modeling and ion exchange work late in the calendar year. At least two abstracts will be submitted to the MRS Fall Meeting in Boston as well as papers for the symposium proceedings.

Preliminary results of the boron and sodium near-edge studies have been shown with other data from waste-form studies in the following presentations:

DK Shuh. May 16, 1998. "Radionuclide Environmental Chemistry." Foothill College, invited.

DK Shuh. April 17, 1998. "Synchrotron Radiation Techniques for the Investigation of Environmental Materials Science." MRS Spring Meeting, San Francisco, California, invited.

References

Bates JK, CR Bradley, EC Buck, JC Cunnane, WL Ebert, X Feng, JJ Mazer, DJ Wronkiewicz, J Sproull, WL Bourcier, BP McGrail, and MK Altenhofen. 1994. *High Level Waste Borosilicate Glass: A Compendium of Corrosion Characteristics.* DOE-0177, U.S. Dept. of Energy, Office of Waste Management, Washington, D.C.

Darab JG, X Feng, JC Linehan, and PA Smith. 1997. "Composition-Structure Relationships in Model Hanford Low-Level Waste Glasses." In *Transactions of the American Ceramic Society,* Vol. 72, V Jain and D Peeler. eds. American Chemical Society, Columbus, Ohio.

McKeown DA, GA Waychunas, and GE Brown, Jr. 1985. *J. Non-Cryst. Solids* 74:325.

Nordgren J and N Wassdahl. 1995. *J. Electron Spectros. Related Phenom.* 72:273.

Terminello LJ, A Chaiken, DA Lapiano-Smith, and T Sato. 1994. *J. Vac. Sci. Technol.,* A 12:2462.

Radiation Effects in Nuclear Waste Materials

(First Year of Funding: FY 1996)

Project Manager and Principal Investigator

Dr. William J. Weber
Pacific Northwest National Laboratory
P.O. Box 999, MSIN K2-44
Richland, WA 99352
(509) 375-2299 (phone)
(509) 375-2186 (fax)
bill.weber@pnl.gov

Co-Investigator

Dr. L. René Corrales
Pacific Northwest National Laboratory
P.O. Box 999, MSIN K1-96
Richland, WA 99352
(509) 375-6410 (phone)
(509) 375-6631 (fax)
rene.corrales@pnl.gov

PNNL Contributors

N.J. Hess
R.E. Williford
H.L. Heinisch
G.D. Maupin
M.J. Schweiger
S. Thevuthasan
Y. Gao
J. Song (Post Doctoral Fellow)
R. Devanathan (Post Doctoral Fellow)
W. Jiang (Post Doctoral Fellow)
B. Begg (Visiting Scientist)
R. Van Ginhoven (Student)

External Contributors

R.B Bircher (ANL)
X. Chen (ANL – Post Doctoral Fellow)
M. Nastasi (LANL)
S. Grigull (LANL – Post Doctoral Fellow)
S.D. Conradson (LANL)
W. Dmowski (University of Pennsylvania)

External Collaborators

R.C. Ewing (University of Michigan)
L.A. Boatner (ORNL)
A.D. Trifunac (ANL)
D.E. Day (University of Missouri)
J.D. Gale (Imperial College)
H. Jónsson (University of Washington)
M.C. Weinberg (University of Arizona)
D.L. Griscom (Naval Research Laboratory)

Research Objective

The objective of this multidisciplinary, multi-institutional research effort is to develop a fundamental understanding of radiation effects in glass and ceramics at the atomic, microscopic, and macroscopic levels. Current research addresses many of the scientific issues identified in the reports of two recent DOE panels (Weber et al. 1997, 1998). The goal of this effort is to provide the underpinning science and models necessary to assess the performance of glasses and ceramics designed for the immobilization and disposal of high-level tank waste, plutonium residues, excess weapons-grade plutonium, and other highly radioactive waste streams. Studies are focused on the effects of ionization and elastic collisions on defect production, defect interactions, diffusion, solid-state phase transformations, and gas accumulation using actinide-containing materials, gamma irradiation, ion-beam irradiation, and electron-beam irradiation to simulate the effects of α-decay and β-decay on nuclear waste materials. This program exploits a variety of structural, optical, and spectroscopic probes to characterize the nature and behavior of defects, defect aggregates, and phase transformations. Computer simulation techniques are also used to determine defect production processes, defect energies, and defect/gas diffusion and interactions. A number of irradiation facilities and capabilities are used, including user facilities at other national laboratories, to study the effects of irradiation under different conditions.

Problem Statement

A significant challenge facing the environmental management and restoration activities at DOE facilities is the stabilization and immobilization of high-level tank waste, high-level sludge in the fuel storage basins, and plutonium (Pu) residues/scrap. In addition, the immobilization and disposal of surplus weapons-grade Pu is becoming a growing technological and political issue that is historically and politically tied to environmental management and restoration activities. These high-level wastes will be converted to glass or glass-ceramic waste forms for permanent disposal in a geologic repository. A key challenge is to develop predictive strategies and models, based on sound scientific understanding, to fully assess long-term performance. Self-radiation effects from α-decay and β-decay can significantly impact long-term performance. Waste forms for the disposal of Pu residues/scrap, surplus weapons-grade Pu, and other high-actinide waste streams may differ significantly in composition from the waste forms for high-level tank wastes and will produce significantly higher radiation doses and helium. The current baseline data and scientific understanding of radiation effects in glass, glass-ceramics, and crystalline phases are critically lacking. Without a fundamental understanding of radiation effects at the molecular, microscopic, and macrosopic levels, meaningful predictions of performance are not possible. This lack of understanding of the radiation damage processes that occur in nuclear waste materials makes it

impossible to extrapolate the limited existing data bases to larger doses, lower dose rates, different temperature regimes, and different glass compositions or ceramic structures.

Research Progress

There has been extensive progress under this project, and work to date has resulted in a number of publications, which are listed at the end of this report. Highlights of the research over the past year are presented below.

Theory, Simulations, and Modeling

Modeling and Simulations of Excitons in Network Materials

A novel semi-empirical methodology has been developed to model and simulate electron-hole pair formation in materials such as silicon and silica. This methodology takes advantage of two distinct approaches to examine the effects of the excited electrons in a network structure. Both approaches require including the hypervalent states of the atoms, which can be occupied by an excited electron, into the model Hamiltonian. Since the goal is to model excitons, only the low-lying orbitals need to be considered. These hypervalent orbitals have energies that are above the Fermi level and hence represent states in the conduction (or delocalized) band. For silicon atoms, the low-lying hypervalent states are the *4s* and *3d* orbitals, and for oxygen, the *3s* and *3p* orbitals. In the work to date, only the *ns* hypervalent orbitals are considered for the sake of simplicity.

The first approach simply determines the force contributions of the electron-hole pairs on the atoms, as if the electron and hole were localized at specific atom sites. The second approach uses a time-dependent Hubbard model to propagate the electron-hole pair through the network with the ions in a fixed configuration. (Details of this methodology are described in a paper being prepared for publication.) The current objective is to couple the two methods in order to determine the extent of the lattice relaxations that lead to stabilization and destabilization of the electron-hole pair. Stabilization will lead to self-trapped excitons (STE), and destabilization will lead to radiative decay. Nonradiative decay is also strongly affected by lattice relaxation, as in the stabilization of defects in an amorphous structure versus that in a crystalline structure. For example, this model predicts that a single exciton will not be stabilized by lattice distortions in the structures of either silicon or quartz; hence, it will not readily lead to a STE. Whenever there is a biexciton (i.e., two excitons interacting with one another), a bond will be broken in either silicon or quartz, thereby creating a STE state. If there are defects present, such as vacancies, other pathways exist that can lead to nonradiative decay processes, such as the breaking of bonds.

In amorphous silicon and silica, very different processes occur. Amorphous silicon behaves very similarly to crystalline silicon, which is no surprise given the similarities of the local structures. The presence of stretched and compressed bonds does appear to localize an exciton, since the probability amplitudes for transfer of the electron and hole are strongly affected by the bond lengths. The relaxation of the lattice, however, is small, and the exciton is only self-trapped as a biexciton, as in the crystal. In amorphous silica, the distorted bonds lead to localization (i.e., effectively an STE), but, in addition, there is a significant amount of lattice relaxation. The force calculations indicate a preference for breaking bonds to form vacancy-interstitial pair defects, accompanied by large lattice relaxation effects. In quartz, the stiffness of the lattice does not lead to significant relaxation effects. In the silica glass, however, relaxation can readily occur at some positions and less readily at others. This is because at given points across the network there are significant local structural differences in density, ring structure, bond lengths, bond angles, and electrostatic fields, among other factors. In a glass, the local structure has a distribution that can be related to the different crystal structures, including the high-density phases as well as the more open zeolite and gel structures.

This modeling effort continues to focus on determining the role of excitons in the formation and propagation of defects in silica glass. The pathways for the formation of various defects, using both the ground-state and excited-state forces and energetics, are being characterized. In this manner, it should be possible to ascertain the role excitons play in the actual formation of defects. In addition, by coupling this methodology with other methods, it will become possible to explore the formation and migration barriers of the defects. Initial calculations indicate that the migration barrier of a vacancy is actually lowered whenever an electron-hole pair interacts with the vacancy.

This simulation effort is strongly coupled with and leveraged by ongoing BES-funded work in the development of semi-empirical methodologies to simulate amorphous networked materials. Because of these coupled efforts, the simulation of excitons in binary silicate materials will begin soon. Collaboration with Prof. Hannes Jónsson (Department of Chemistry, University of Washington) has been initiated to study the energetics and dynamics of the triplet and singlet states of excitons in silica glass. This collaborative effort was awarded a minimum of 125,000 CPU node hours of computational support per year (over 3 years) on the 512-node IBM SP2 parallel computational platform, which is part of the Molecular Science Computational Facility at the Environmental and Molecular Sciences Laboratory at Pacific Northwest National Laboratory (PNNL).

Defect Energies in Crystalline Ceramics

Activities under this task are focused on using computational methodologies to determine fundamental defect energies in complex ceramics relevant to nuclear waste applications. Such defect energies are often difficult to determine experimentally, particularly for multi-cation

ceramics. Two fundamental energy parameters important to radiation effects are the threshold displacement energies for the various cations and anions and the migration energies of radiation-induced defects (e.g., interstitials and vacancies). Both energy minimization methods and molecular dynamic simulations can be used in determining these energies. Initial work under this project has used energy minimization methodology, as described below. Computational-intensive molecular dynamic (MD) simulations, which are currently being developed and applied to ceramics under a Basic Energy Sciences (BES)-sponsored project at PNNL, will be used in studies of ceramics relevant to nuclear waste applications once the refinement of the inter-atomic potentials is completed.

Threshold displacement energies, E_d, and defect migration energies, E_m, are fundamental parameters controlling defect production, defect migration, and the kinetics of microstructure growth and phase transformations. These energies are not easily determined experimentally for many ceramic materials; however, advances in computational methodologies and their application to ceramics materials provide a means to determine these energies for a number of ceramic materials of interest. This project uses the energy-minimization methodology incorporated into the GULP code (General Lattice Utility Program, by J.D. Gale, Imperial College, London) to determine E_d and E_m for ceramics of interest. In fact, this project was the first to apply such methodologies to the determination of E_d values in ceramics, and the results (Williford et al. 1998) are in excellent agreement with known experimental values (within 14%).

The GULP code, which is being utilized in collaboration with its author (J.D. Gale), is an energy minimization code that employs the well-documented Mott-Littleton model (Mott and Littleton 1938) for isolated (as opposed to periodic) defects. The polarization induced by charged defects in the lattice is treated with the Dick-Overhauser shell model (Dick and Overhauser 1958), which includes the important coupling between short-range repulsion and ion polarization, preventing excessive polarization of the ion. GULP also includes several useful libraries of inter-atomic potentials. Two of its many options are particularly useful in the present work. For determining E_d, the ion "translate" option permits the movement of a selected ion to a point along a prescribed vector, after which the lattice is relaxed to determine if the ion returns to its original position or assumes a new equilibrium position, such as at an interstitial site. For determining defect migration energies, GULP contains a useful "transition" state option. Some results are highlighted below.

Zircon

Computer simulation techniques, as described above, have been used to provide the only available estimates of E_d values in zircon because no experimental data are available. Several different sets of interatomic potentials (Chandley et al. 1992; Gay and Rohl 1995) have been used to model the structure and perform the simulations (Williford et al. 1992). Based on the calculations at this time, the recommended displacement energies for zircon are given in Table 1.

These values are now being used by several groups to determine the displacement dose in zircon under different types of irradiation, thus providing an accepted method for comparison of different irradiation data sets.

Table 1. Minimum Threshold Displacement Energies, E_d, for Zircon

Specific Ion	E_d (eV)
Zr	79
Si	23
O	47

The migration of defects controls both transport processes and the kinetics of phase transformations (e.g., amorphization) and microstructural evolution (e.g., bubble formation). The GULP code is especially suited for finding the transition states (saddle points) associated with the energy barriers for interstitial and vacancy migration in the crystal structure. The objective is to fully characterize the defect migration energies for all three species; however, initial results have focused on the oxygen, using the Gay and Rohl potentials (Gay and Rohl 1995). Results to date indicate that oxygen vacancy migration occurs by hopping between corners of nearest silica tetrahedra. This minimum energy pathway for migration of the oxygen vacancy is diffusionally isotropic with activation energies of 1.2 to 1.3 eV. Recently, Watson and Cherniak (1997) have reported an activation energy of 4.6 eV with no diffusional anisotropy for oxygen self-diffusion in natural zircons, so additional refinement of the potentials may be needed.

Pyrochlores

The pyrochlores structures, $Gd_2Ti_2O_7$ and $Gd_2Zr_2O_7$, are also of interest as actinide host phases. Computer-simulation studies of these structures have been initiated, and work has focused on activation energies for oxygen vacancy migration, for which there are data in the literature. Migration energies for oxygen vacancy migration in these structures range from about 0.2 eV (see Catchen and Rearick 1995) to 0.9 eV (see Tuller 1992). These differences in migration energies may be caused by impurities, disorder, defect clustering, or combinations thereof. The results of recent computer simulations under this project are shown in Table 2, with and without cation disorder, and are in reasonable agreement with experimental data (Tuller 1992; Catchen and Rearick 1995).

Table 2. Oxygen Vacancy (48f) Migration Energies Calculated with and Without Cation Disorder

	$Gd_2Ti_2O_7$		$Gd_2Zr_2O_7$	
		With Disorder		With Disorder
Gulp Results	0.93 eV	0.72 eV	0.42 eV	0.93 eV
Exp. Data		0.74 eV	0.17-0.32 eV	0.88 eV

Evolution of Damage from Alpha Particles and Alpha-Recoil Cascades

The goal of this effort is to study the fundamental processes of radiation effects in crystalline ceramics using dynamic and kinetic computer simulation techniques. Work currently focuses on zircon because of the availability of experimental data and other computationally determined parameters (e.g., E_d and E_m values). Alpha decay of actinides results in the formation of energetic alpha particles and recoil nuclei. Damage produced in the crystalline structures by these particles can be studied at the atomic level using the binary-collision-approximation computer code MARLOWE, which allows input of the actual crystal structure. In the case of zircon, MARLOWE has been used to calculate initial cascade morphology and damage production. The damage production from alpha particles can be accurately modeled with MARLOWE if the threshold displacement energies are known. In the case of the alpha-recoil displacement cascade, MARLOWE is less accurate since it only models the collisions as a series of two-body collisions. Nonetheless, the results are still useful, providing information on cascade morphology and energy deposition. Ideally, molecular dynamic (MD) simulations would be used for studying damage production in the alpha-recoil cascade, but reliable interatomic potentials are not readily available for most materials. Molecular dynamic simulations of damage processes from displacement cascades in zircon will begin under this project later this summer.

Kinetic Monte Carlo (KMC) simulations will be used to follow the evolution of the radiation-induced defect population at the atomic (or near-atomic) scale over times and distances much longer than possible with MD, potentially up to geologic time scales. The KMC simulations require input from MD and static (energy-minimization) simulations and experimental data (when such data are available), i.e., such input as migration energies, binding energies, interaction energies, and initial defect configurations produced in the cascades.

At present, the development of the MD and KMC simulations for zircon are being done in tandem. The KMC code will be used for vital parameter sensitivity studies, gradually incorporating MD results as available. The initial version of the KMC simulation code for zircon has been written, and it is presently being tested. This KMC code for zircon was built from the

ALSOME (atomic level simulation of microstructure evolution) code that was originally developed under a fusion energy project for defect accumulation studies in monatomic metals. The ALSOME code has been very successful (under fusion support) in simulating the formation, dissolution, and migration of point defect clusters in metals under irradiation conditions. Recent results on copper (Heinisch and Singh 1998) are in good agreement with experimental measurements by electron microscopy. The KMC code developed for zircon must follow defect diffusion on the sublattices of three types of atoms. Radiation-induced amorphization due to defect accumulation is one of the primary features to be modeled and understood.

In the present KMC simulation code for zircon, a very simple model of defect diffusion and interaction is being assumed initially. The present KMC simulation code for zircon follows the "hopping" kinetics of individual defects on the crystal lattice but does not deal explicitly with the interactions of individual atoms. Defects are assumed to "hop" only on their own sublattices. Although antisite defects can be dealt with if necessary, this is not presently thought to be required. Interstitial atoms are said to be "associated" with a lattice site, i.e., as they migrate, the exact positions of interstitial atoms are not monitored but are instead associated with the nearest lattice site in their sublattice. Vacancy and interstitial defects that become nearest neighbors (on their own sublattice) are recombined. Defect clustering is not explicitly dealt with. Same-type defects may be next to each other, but presently no binding is assumed, nor are any special defect-complex configurations. The test volume has periodic boundaries, and cascades occur randomly in space and time at a predetermined average rate. After each cascade occurs, the cascade region is searched for amorphization based on defect density, since experimental evidence (Weber et al. 1994) suggests that amorphous regions might form where cascades overlap. Regions with defect densities above a critical value are assumed to be "amorphous," and defect migration ceases within these regions. This code can be adjusted and augmented to include more realistic features than the present basic model.

Cascades used as input to the KMC code currently come from binary collision simulations using the MARLOWE code. MARLOWE portrays what happens during the first 0.1 ps of the cascade process, during which the recoil energy is shared among atoms until no atom has enough energy to permanently displace another. The considerable rearrangement of atoms, as the cascade region cools to the crystal temperature over the next several picoseconds, must be modeled with the many-body MD simulations. MARLOWE provides a reasonably good description of the extent of the defect distribution produced in the cascade. However, it does not accurately give the final number of defects and the relative placement of vacancy and interstitial defects, which might be important to their subsequent disposition.

After testing the KMC code, parameter variation studies will be initiated to assess the reasonableness of the present simple model relative to a range of values expected for defect

migration energies. Even this simple model might prove useful in assessing the effects of dose and dose rate on the observed differences in amorphization of natural, Pu-doped, and ion-irradiated zircons.

Experimental Studies

Pu-Containing Glasses and Ceramics

Studies have continued on Pu-containing zircon and a suite of compositionally identical Pu-doped (1 wt%) waste glasses prepared with different α-activities by varying the $^{239}Pu/^{238}Pu$ isotopic ratio. The stored energy measured in these glasses as a function of cumulative dose is shown in Figure 1. The stored energy at the highest dose is nearly the largest ever measured in a nuclear waste glass and shows no evidence of saturation. This stored energy could provide a driving force for enhanced dissolution. Leaching studies of these glasses and the Pu-zircons will be proposed in a renewal or follow-on study, since budget constraints prevent undertaking such work under the existing three-year effort.

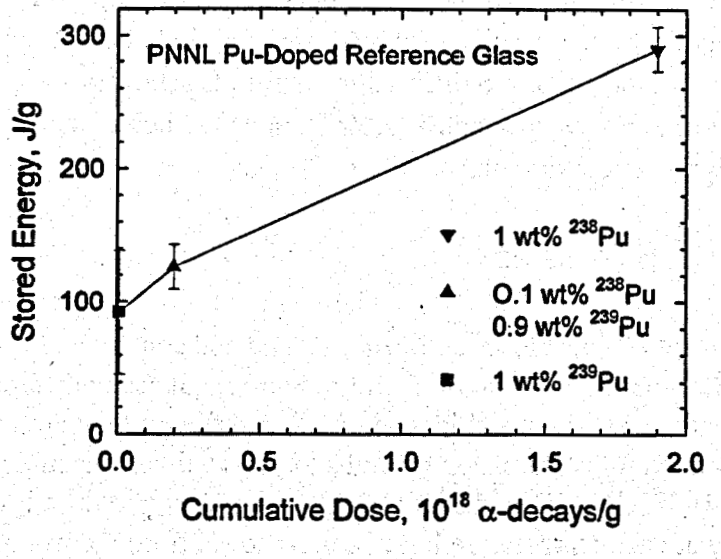

Figure 1. Stored Energy as a Function of Cumulative Dose

EXAFS and XANES measurements and data analyses of these Pu-containing glasses and zircons have continued. Analysis of the EXAFS and XANES spectra indicates that the local environment around the cations exhibits different degrees of disorder as a result of the cumulative α-decay dose. In the Pu-doped glasses, cations with short cation-oxygen bonds show little effect from self-radiation, whereas cations with long cation-oxygen bonds show a greater degree of disorder with increasing dose. In the fully amorphous Pu-zircon samples, the cations reside in two distributions, one that is similar to a highly disordered zircon and a second that has

Zr-Zr distances that are similar to baddeleyite, the monoclinic form of ZrO_2. In addition, the uranium daughter in the fully amorphous state is present as U(IV) and resides in a site unlike that of the Pu parent, suggesting that it is not in thermal equilibrium with the host. In both the fully amorphous zircon (^{238}Pu sample) and in the fully crystalline zircon (^{239}Pu sample), the Pu is present as Pu(III), as opposed to the expected Pu(IV) state, and resides in a site that is very similar to $PuSiO_4$, the plutonium analog of zircon. This valence state for Pu in the zircon samples is most probably due to the reducing conditions employed during the original sintering (flowing helium). In an upcoming study, samples of these zircons will be heat-treated in air at elevated temperatures (~1500°C) and measured to confirm oxidation of the Pu to Pu(IV).

Diffuse x-ray diffraction and pair distribution function analyses have also been performed. Data analysis indicates that inter-atomic distances at a short range can be identified by the pair distribution functions, as long as the element concentration is greater than about 5%. The effect of radiation damage in the glasses is most pronounced in the range of 0.28 to 0.3 nm, which comes from the O-O and some M-O correlations. The local atomic order in amorphous zircon is similar to that found in fully crystalline zircon, except that the structure is heavily disordered and long-range correlations are lost, which is mostly likely associated with random orientation of the basic structural units. Additional analyses are planned to finalize this work. Neutron diffraction studies of the Pu-doped zircon have also been performed by J. A. Fortner (ANL) as part of an interlaboratory collaboration. Neutron diffraction results also show no evidence for crystallinity, and peaks corresponding to the expected Si-O, Zr-O, and O-O bond lengths are observed. Data refinement and analysis are continuing.

Gamma-Irradiation Studies

Temperature-controlled capsules have been designed and constructed for irradiation studies using the PNNL (^{60}Co) gamma-irradiation facility. Samples of seven different glasses have been prepared, cut into wafers, polished, and loaded into four different temperature-controlled capsules for long-term gamma irradiation (months to years). Each capsule is held at a different temperature (50°C, 100°C, 150°C, and 200°C). Glasses exposed to dose levels of about 2.5×10^7 Gy and 7.5×10^7 Gy at each temperature have been removed from the irradiation facility and are undergoing extensive characterization. Density measurements indicate no significant changes in volume. Raman, polarized Raman, UV-VIS, and FTIR spectroscopies have been carried out on the lowest dose glass samples, and some results are briefly described below. Electron paramagnetic resonance (EPR) and transmission electron microscopy characterization of these samples is planned. Characterization of the higher-dose glass samples (7.5×10^7 Gy), which have been only recently removed from the gamma facility, has been initiated. Even higher-dose glass samples, which have already been exposed to 1.0×10^8 Gy, are continuing to be irradiated and will be removed for characterization in 3 to 6 months. As part of a collaboration, some space in the gamma capsules is being made available to the EMSP project at the University of Arizona (M. Weinberg) for studies on radiation-induced phase separation.

The Raman, polarized Raman, UV-VIS-NIR, and FTIR spectra from each of the glass compositions exhibit significant differences because of the compositional differences in the glasses and the resulting effect on the structure of the silicate glass. Initial spectroscopic analyses indicate only minor changes in the Raman, polarized Raman or FTIR spectra between the non-irradiated samples and those irradiated to a cumulative dose of 2.5×10^7 Gy. However, significant differences are observed between the nonirradiated and irradiated samples in the 400- to 700-nm region of the UV-VIS-NIR optical absorption spectra of the sodium borosilicate glass compositions. Furthermore, these radiation-induced variations display systematic dependencies on the temperature at which the gamma irradiation occurred, as shown in Figure 2. At this time, the changes in optical absorption in the 400- to 700-nm region are believed to originate from electronic defects. It is anticipated that the nature of these defects can be fully characterized using EPR spectroscopy as part of a collaboration with the EMSP project at the Naval Research Laboratory (D. Griscom).

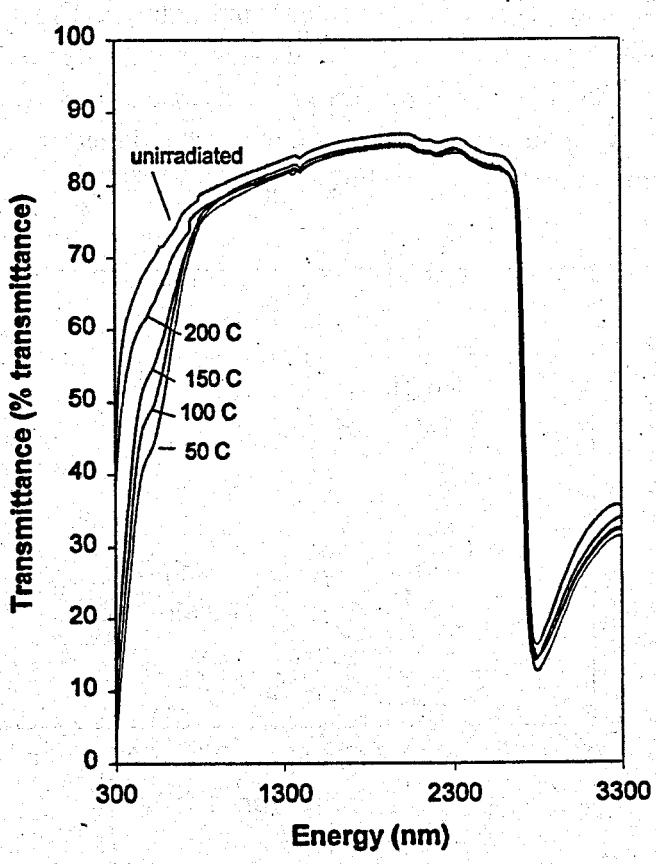

Figure 2. UV-VIS-NIR Spectra of Unirradiated and Gamma-Irradiated NBS-1 Glass, which consists of 65 wt% SiO_2, 19 wt% B_2O_3, and 17 wt% Na_2O. This glass displays decreased transmittance in 400 to 700 nm region at the lowest irradiation temperature, suggesting that the responsible defect anneals at the higher irradiation temperatures.

Electron and Ion Irradiation Studies

PNNL Studies

Irradiation studies at PNNL or by PNNL staff have focused on zircon ($ZrSiO_4$), pyrochlore ($Gd_2Ti_2O_7$), and perovskite ($SrTiO_3$) using the ion accelerator facility at PNNL or the HVEM-Tandem user facility at ANL. Studies will determine the temperature dependence of amorphization for different ions species, defect annealing kinetics, and changes in mechanical properties using a pico indenter. Samples include single crystals, single crystal films, and polycrystalline monoliths. Recent data obtained at ANL on the temperature dependence of amorphization in zircon and pyrochlore are shown in Figure 3. Studies have also shown that ion beam-induced recrystallization of fully amorphous $Gd_2Ti_2O_7$ occurs at 800°C under 1-MeV Kr^+ irradiation. Pico indentations of $Gd_2Ti_2O_7$ irradiated at PNNL with 4-MeV Au^+ ions indicate a 15% decrease in elastic modulus and a 42% decrease in hardness. Cross-sectional transmission electron microscopy of these samples is planned to determine the depth dependence of the damage. Single-crystal $Gd_2Ti_2O_7$ thin films have recently been successfully grown (see below) and will be used for in situ studies of damage accumulated and recovery, using in situ Rutherford backscattering spectrometry and ion channeling methods (RBS/C).

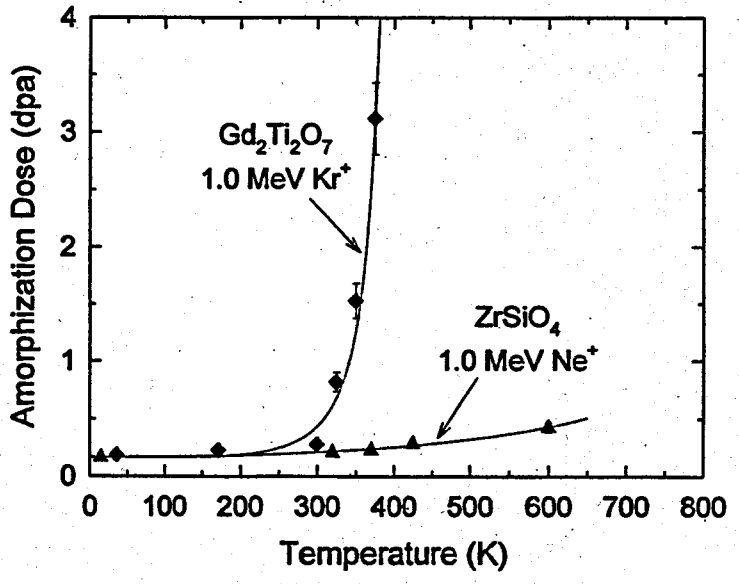

Figure 3. Temperature Dependence of Amorphization

The accumulation and recovery of ion beam-induced disorder in $SrTiO_3$ have been studied using in situ RBS/C at the PNNL accelerator facility within the Environmental and Molecular Sciences Laboratory. Low-energy (~400 keV) irradiation was performed with several ion species, including He^+, O^+, Ti^+, and Au^+, over a range of fluences and temperatures. Isochronal

annealing studies were carried out for 20 minutes across the temperature range from -90°C to several hundred degrees. Preliminary analysis indicates that the total defect concentration on the Sr and Ti sublattices exhibits an exponential dependence on the annealing temperature.

The recovery processes for defects on the O sublattice appear to be faster. In addition, almost complete recovery of the perfect crystal was observed at room temperature after a very low fluence O^+ irradiation.

ANL Studies

In order to assess the potential and mechanisms of gas bubble formation in nuclear waste storage glasses, an alkali silicate glass and NBS-1 glass were implanted in situ with inert gas atoms (50-keV Xe) at temperatures between 200°C and 600°C in a Hitachi-9000 transmission electron microscope (TEM) at Argonne National Laboratory. Bubble formation and growth were determined from TEM images taken intermittently during the irradiations. The effects of 300-keV electron irradiation on bubble formation and growth were studied during intermittent and simultaneous electron and ion irradiation. An example of the formation and growth of Xe bubbles in NBS-1 at 200°C is shown in Figure 4a. The bubbles are spherical and homogeneously distributed and result from the random agglomeration of Xe atoms, which is an indication of low gas atom and bubble mobility. Modeling by rate theory suggests that recoil resolution of gas atoms from bubbles plays an important role in bubble growth. As the implantation dose increases, bubbles grow by random gas accumulation until nearby bubbles interact and coalesce. An effect of ionizing irradiation on bubbles in NBS-1 glass is shown in Figure 4b, where the Xe implantation dose is the same as in Figure 4a but intermittently exposed to 300-keV electron irradiation. The results show that intermittent exposure to energetic electrons results in an increased density of smaller bubbles compared with Xe implantation without an intervening electron irradiation. This indicates a retardation of bubble growth due to the intervening ionization dose produced by the electron beam. Continuous TEM observations during Xe implantation show that Xe bubble growth is even more reduced by continuous electron irradiation. Possible mechanisms responsible for these effects are under investigation.

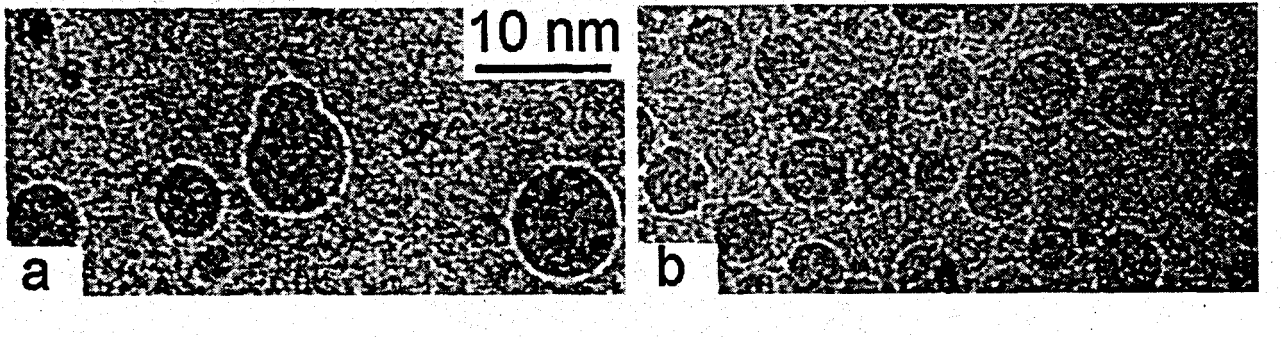

Figure 4. NBS-1 Glass Irradiated at 200°C with 50-keV Xe^+ Ions to 90 Ions/nm^2: a) Without Electron Irradiation and b) with Electron Irradiation

As the temperature is increased, bubbles form and grow more readily. Above a threshold dose, the total volume of gas bubbles observed in alkali silicate glasses increases superlinearly with increasing ion dose. The threshold dose is defined by the requirement that bubbles grow to sizes that are visible, approximately 1 nm. The temperature dependence of the threshold dose is shown in Figure 5. The decrease of threshold dose with increasing temperature indicates increasing Xe and bubble mobility. Rate theory modeling of the bubble size distribution as a function of temperature and dose will yield diffusional parameters for atomic Xe and bubbles.

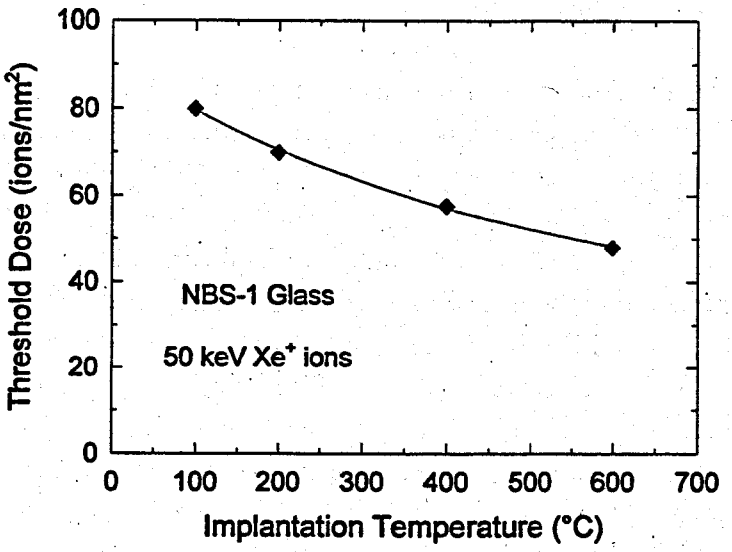

Figure 5. Threshold Dose for Bubble Formation

LANL Studies

The in situ ion-beam facility at LANL combines a 100- to 400-keV ion beam for materials irradiation with a MeV ion beam for in situ compositional and structural analysis, using the RBS/channeling technique. Two limitations of the method are 1) that it cannot discriminate between amorphous and polycrystalline structures and 2) that it does not provide information on details of crystal structure. To enhance the capabilities of this facility for structural analysis, a x-ray diffraction system has been installed on the in situ ion beam chamber and is currently undergoing testing. With this new feature, the LANL facility will have a unique international capability to investigate ionirradiation-induced structural changes in solid matter. The potential benefits of this project include the ability to study the dynamics of damage accumulation in nuclear waste materials and the irradiation-induced crystalline-to-amorphous transformations in ceramic waste phases.

The x-ray system operates according to the energy-dispersive diffraction method. In contrast to the conventional XRD, this technique uses the continuous component of the radiation spectrum generated in an x-ray tube in conjunction with an energy-sensitive detector. With the scattering geometry fixed, the characteristic Bragg reflections of the analyzed crystal show up at different energies in the spectrum obtained from the detector. In the case of a polycrystalline sample with random orientation, all reflections are analyzed at the same time, without the necessity of time-consuming angular scans. The high speed of analysis and the comparatively simple design make this technique particularly well suited for in situ analysis during ion irradiation. Figure 6 shows the arrangement of the analyzing x-ray beam and energy dispersive detector relative to the implanting beam and RBS/channeling beam line. The present geometry allows grazing incidence XRD at near-normal irradiation, which ensures the best sensitivity of the x-ray probe to near-surface structural modifications generated by the ion beam.

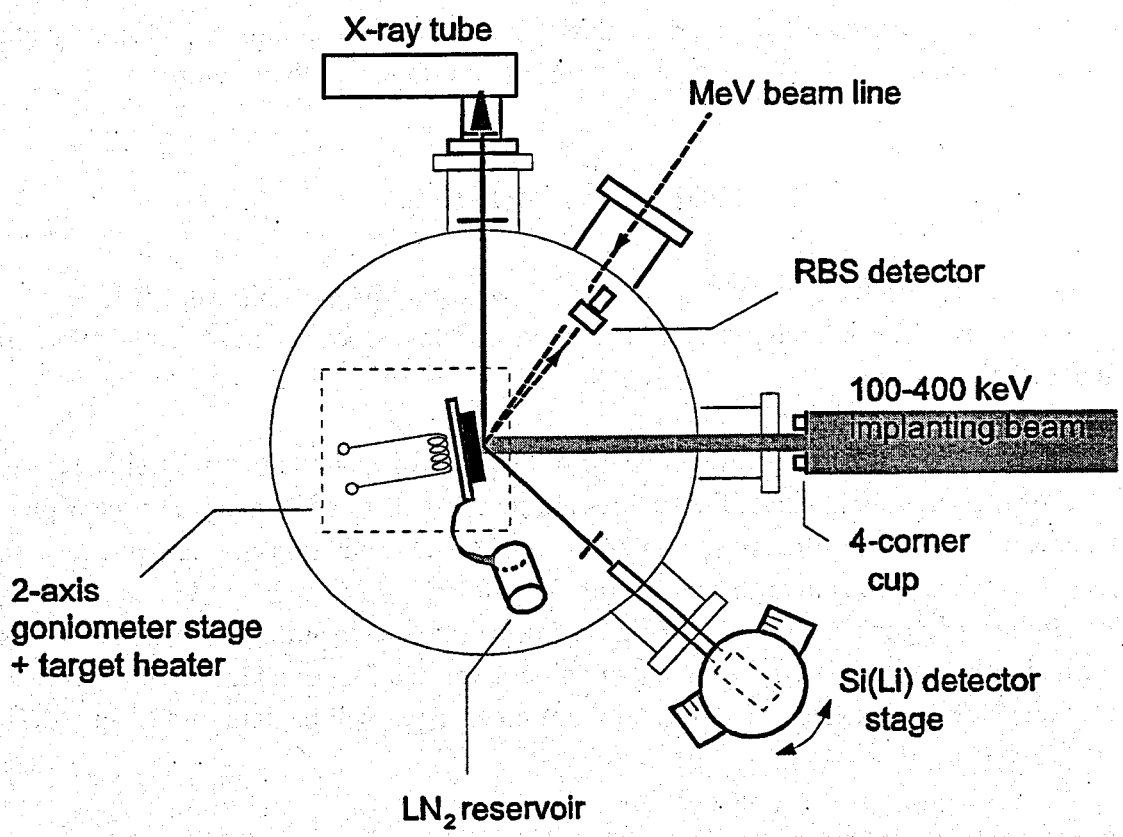

Figure 6. Schematic of Upgraded LANL In Situ Irradiation Facility

Single Crystal Growth and Reference Samples

Fundamental studies of ceramics often require the use of single crystals to obtain intrinsic materials parameters and detailed understanding of radiation effects. Single crystals of many

oxide systems of interest are not readily available. Consequently, the growth of single crystals or single crystal films has become a necessary part of this project. Epitaxial films of $Gd_2Ti_2O_7$ are currently being grown under this project by metal-organic chemical vapor deposition (MOCVD), using single-crystal, yttrium-stabilized zirconium oxide (YSZ) as a substrate. A direct liquid-source injection system is used to deliver metal-organic precursors of Gd and Ti in the MOCVD processing. $Gd(C_{11}H_{19}O_2)_3$ and titanium isopropoxide are used as the precursors for Gd and Ti, respectively. Thermal deposition of the precursors under optimum conditions (substrate temperature, chamber pressure, flow rates, oxygen partial pressure) leads to formation of epitaxial $Gd_2Ti_2O_7$ films. Use of oxygen plasma during the growth reduces the deposition temperature and prevents carbon contamination. Ion channeling measurements of films grown to date show excellent crystallinity and suitability for studies of radiation effects, which are scheduled.

During the past year, standard reference glasses have been provided to an EMSP project at Argonne National Laboratory (A. Trifunac) as part of an informal collaboration.

Planned Activities

All the above research efforts will continue as described. Much of this work will be submitted to journals for publication over the next year. Some specific activities and approximate timetables are given below.

In July 1998, the modeling effort will begin simulations of excitons in binary silicate materials. At the same time, simulation studies on the energetics and dynamics of the triplet and singlet states of excitons in silica glass will be initiated. MD simulations of damage processes from displacement cascades in zircon will begin this summer. In early FY 1999, parameter variation studies using the KMC code for zircon will be initiated to assess the reasonableness of the present simple model relative to a range of values expected for defect migration energies. Threshold displacement energies and defect migration energies will be determined for $Gd_2Ti_2O_7$ by January 1999.

Characterization of glass samples irradiated with gamma radiation to 75 MGy will be initiated in June 1998. The higher dose samples will be removed for testing in November 1998 after receiving a dose of 150 MGy. In addition to characterization already performed, electron paramagnetic resonance (EPR) and transmission electron microscopy characterization will be performed.

In June/July of 1998, the Pu-zircons will be heat treated in air at elevated temperatures (~1500°C), and EXAFS/XANES measurements will be performed to confirm oxidation of the Pu(III) to Pu(IV). Additional analyses on the diffuse scattering data will be completed by October 1998, and the results will be submitted to a journal for publication.

Studies of defect accumulation and amorphization will be initiated on $Gd_2Ti_2O_7$ single crystal films and on polycrystalline $Gd_2Zr_2O_7$ in August 1998. Studies of defect recovery and ionization-enhanced recrystallization will be initiated on $SrTiO_3$ at the same time. Studies of helium and oxygen bubble formation in glasses will be initiated in July 1998.

References

Catchen GL and TM Rearick. 1995. *Phys. Rev.*, B 52:9890.

Chandley P et al. 1992. *J. Chem. Soc. Dalton Trans.*, p. 1579.

Dick BG and AW Overhauser. 1958. *Phys. Rev.*, 112:90.

Gay DH and AL Rohl. 1995. *J. Chem. Soc. Faraday Trans.*, 91:925.

Heinisch HL and BN Singh. 1998. *J. Nuclear Materials,* in press.

Mott NF and MJ Littleton. 1938. *Trans. Faraday Soc.*, 34:485.

Tuller HL. 1992. *Sol. State Ionics*, 52:135.

Watson EB and DJ Cherniak. 1997. *Earth and Planetary Science Letters*, 148:527.

Weber WJ, RC Ewing, CA Angell, GW Arnold, AN Cormack, JM Delaye, DL Griscom, LW Hobbs, A Navrotsky, DL Price, AM Stoneham, and MC Weinberg. 1997. *J. Materials Research,* 12:1946.

Weber WJ, RC Ewing, CRA Catlow, T Diaz de la Rubia, LW Hobbs, C Kinoshita, H Matzke, AT Motta, M Nastasi, EKH Salje, ER Vance, and SJ Zinkle. 1998. *J. Materials Research,* 13:1434.

Weber WJ, RC Ewing, and LM Wang. 1994. *J. Materials Research*, 9:688.

Williford RE, R Devanathan, and WJ Weber. 1998. *Nuclear Instruments and Methods*, B 141:98.

Publications

Weber WJ and LR Corrales. 1997. "Radiation Effects in Nuclear Waste Materials." *Science to Support DOE Site Cleanup: The Pacific Northwest National Laboratory Environmental Management Science Program Awards* PNNL-11589, Pacific Northwest National Laboratory, Richland, Washington, pp. 43-52.

Weber WJ, NJ Hess, SD Conradson, and JD Vienna. 1997. "Self-Radiation Effects in Glass and Ceramic Waste Forms for the Stabilization and Disposition of Plutonium." *Plutonium Futures - The Science.* LA-13338-C, Los Alamos National Laboratory, Los Alamos, New Mexico, pp. 25-26.

Weber WJ, RC Ewing, and A Meldrum. "The Kinetics of Alpha-Decay-Induced Amorphization in Zircon and Apatite Containing Weapons-Grade Plutonium or Other Actinides." 1997. *Journal of Nuclear Materials*, 250:147-155.

Williford RE, R Devanathan, and WJ Weber. 1998. "Computer Simulation of Displacement Threshold Energies for Several Ceramic Materials." *Nuclear Instruments and Methods*, B 141:98-103.

Hess NJ, WJ Weber, and SD Conradson. 1998. "U and Pu L_{III} XAFS of Pu-Doped Glass and Ceramic Waste Forms." *J. Alloys and Compounds,* in press.

Hess NJ, WJ Weber, and SD Conradson. 1998. "X-ray Absorption Fine Structure of Aged, Pu-Doped Glass and Ceramic Waste Forms." *Scientific Basis for Nuclear Waste Management XXI*, IG McKinley and C McCombie, eds. Mater. Res. Soc. Symp. Proc. 506, Warrendale, Pennsylvania, pp. 169-176.

Hess NJ, WJ Weber, and SD Conradson. 1998. "X-ray Absorption Fine Structure of Aged, Pu-Doped Glass and Ceramic Waste Forms." *Journal of Nuclear Materials,* in press.

Corrales LR and J Song. 1998. "Semi-empirical methodology to simulate exciton processes in glasses." *Proc. of the CEA/VALRHO Summer School on Glass: Scientific Research for High Performance Containment,* in press.

Devanathan R, WJ Weber, and LA Boatner. 1998. "Response of Zircon to Electron and Ne^+ Irradiation." *Phase Transformations and Systems Driven far from Equilibrium*, E Ma, P Bellon, M Atzmon, and R Trivedi, eds. Mater. Res. Soc. Symp. Proc. 481, Warrendale, Pennsylvania, in press.

Presentations

Weber WJ. February 20, 1997. "Radiation Effects from the Incorporation of Plutonium in Glasses and Ceramics" (invited seminar). Los Alamos National Laboratory, Los Alamos, New Mexico.

Weber WJ, NJ Hess, SD Conradson, and JD Vienna. August 25-27, 1997. "Self-Radiation Effects in Glass and Ceramic Waste Forms for the Stabilization and Disposition of Plutonium." Topical Conference on *Plutonium Futures - The Science*, Santa Fe, New Mexico.

Corrales LR and J Song. September 1997. "Molecular Dynamics Simulations of Excitons in Glasses." CEA/VALHRO Summer School, Mejannes le Clap, France.

Williford RE, R Devanathan, and WJ Weber. September 14-19, 1997. "Computer Simulation of Displacement Threshold Energies for Several Ceramic Materials." 9th International Conference on *Radiation Effects in Insulators*, Knoxville, Tennessee.

Hess NJ, WJ Weber, and SD Conradson. September 21-26, 1997. "U and Pu L_{III} XAFS of Pu-Doped Glass and Ceramic Waste Forms." International Conference on *Actinides '97*, Baden-Baden, Germany.

Hess NJ, WJ Weber, and SD Conradson. September 28 - October 3, 1997. "X-ray Absorption Fine Structure of Aged, Pu-Doped Glass and Ceramic Waste Forms." MRS Symposium on *Scientific Basis for Nuclear Waste Management XXI*, Davos, Switzerland.

Corrales LR. October 1997. "Lattice Theories and Molecular Dynamics Simulations of Glasses." Department of Chemistry, University of Maryland, College Park, Maryland.

Corrales LR. October 1997. "Molecular Dynamics Simulations of Defects and Excitons in Glasses." American Ceramics Society, Glass and Optical Materials Division Meeting, Williamsburg, Virginia.

Weber WJ. December 1, 1997. "Radiation Effects in Glass and Ceramic Waste Forms" (invited seminar). Massachusetts Institute of Technology, Cambridge, Massachusetts.

Devanathan R, WJ Weber, and LA Boatner. December 1-5, 1997. "Response of Zircon to Electron and Ne^{+} Irradiation." Materials Research Society Annual Meeting, Boston.

Weber WJ. December 11, 1997. "Radiation Effects in Glass Waste Forms" (invited seminar). Argonne National Laboratory, Argonne, Illinois.

Weber WJ. January 8, 1998. "Radiation Effects in Crystalline Waste Form Phases" (invited seminar). Idaho National Engineering and Environmental Laboratory, Idaho Falls, Idaho.

Song J and LR Corrales. March 16-20, 1998. "Simulation of Exciton Processes in Networked Materials." March APS National Meeting, Anaheim, California.

Weber WJ, RC Ewing, and A Meldrum. March 30–April 3, 1998. "Radiation Effects in Nuclear Waste Ceramics." American Chemical Society Annual Meeting, Dallas.

Weber WJ. April 3–4, 1998. "Radiation Effects from Alpha Decay in Nuclear Waste Ceramics" (invited plenary lecture). American Nuclear Society Northern Student Conference, Ann Arbor, Michigan.

Weber WJ. April 19–22, 1998. "Effects of Radiation on Solid Nuclear Waste Forms" (invited plenary lecture). DOE Workshop on Research Needs and Opportunities in Radiation Chemistry, Chesterton, Indiana.

Weber WJ and R Devanathan. May 4-6,1998. "Effects of Alpha Decay on Crystalline Ceramic Waste Forms." American Ceramic Society Meeting, Cincinnati, Ohio.

Spent Nuclear Fuel and Nuclear Materials

Radiolytic and Thermal Processes Relevant to Dry Storage of Spent Nuclear Fuel

(First Year of Funding: FY 1997)

Principal Investigator

Dr. Steven C. Marschman
Pacific Northwest National Laboratory
P.O. Box 999, MSIN P7-27
Richland, WA 99352
(509) 376-3569
steve.marschman@pnl.gov

Co-Investigators

Dr. Theodore E. Madey
Rutgers University
P.O. Box 849
Piscataway, New Jersey 08855-0849
(732) 445-5185
madey@physics.rutgers.edu

Dr. Peter E. Haustein
Brookhaven National Laboratory
P.O. Box 5000
Upton, New York 11973
(516) 344-4340
haustein@bnldag.ags.bnl.gov

Dr. Thomas M. Orlando
Pacific Northwest National Laboratory
P.O. Box 999, MSIN K8-88
Richland, Washington 99352
(509) 376-9420
Thomas.Orlando@pnl.gov

Dr. James P. Cowin
Pacific Northwest National Laboratory
P.O. Box 999, MSIN K8-88
Richland, Washington 99352
(509) 376-6330
jp.cowin@pnl.gov

Research Objective

This project involves basic research in chemistry and physics aimed at providing information pertinent to the safe long-term dry storage of spent nuclear fuel (SNF), thousands of tons of which remain in water storage across the DOE complex. The Hanford Site K-Basins alone hold 2300 tons of spent fuel, much of it severely corroded, and similar situations exist at Savannah River and Idaho National Engineering and Environmental Laboratory. DOE plans to remove this fuel and seal it in overpack canisters for "dry" interim storage for up to 75 years while awaiting permanent disposition. Chemically bound water will remain in this fuel even after the proposed drying steps, leading to possible long-term corrosion of the containers and/or fuel rods themselves, generation of H_2 and O_2 gas via radiolysis (which could lead to deflagration or detonation), and reactions of pyrophoric uranium hydrides. No thoroughly tested model is now available to predict fuel behavior during preprocessing, processing, or storage. In a collaborative effort among Rutgers University, Pacific Northwest National Laboratory, and Brookhaven National Laboratory, we are studying the radiolytic reaction, drying processes, and corrosion behavior of actual SNF materials and of pure and mixed-phase samples. We propose to determine what is omitted from current models: radiolysis of water adsorbed on or in hydrates or hydroxides, thermodynamics of interfacial phases, and kinetics of drying. A model will be developed and tested against actual fuel rod behavior to ensure validity and applicability to the problems associated with developing dry storage strategies for DOE-owned SNF.

Research Progress

Relevant oxide surfaces of UO_2, ZrO_2, and Al_2O_3 have been prepared and characterized by x-ray photoelectron spectroscopy. Measurements are being made of the desorption of water from these surfaces, using accurate thermal desorption methods to elucidate the effects of temperature on the surface–water interaction. Interfacial nuclear decay and radiolysis processes that either affect the structural integrity of relevant materials or evolve flammable gases have been studied on Al_2O_3 and ZrO_2 surfaces using intense radioactive sources with radiochemical tracer techniques. Processes for generating thin (0.1-mm) uranium oxide films have been developed using three different processes: metal sputtering, electrodeless plating, and thermal treatment of uranyl nitrate deposited from solution on tungsten. Such films have been characterized by electron microscopy, revealing in partially nitrated specimens "shrink cracks" that may have profound implications for their chemical reactivity. A promising computational model of the effects of particle size and sample thickness has been developed and substantiated with experiments on MgO and TiO_2 powders.

The breakdown of zirconia films (important to the integrity of Zr-alloy fuel-rod cladding) under extreme radiation conditions has been systematically studied using low-energy electron and photon bombardment of well-characterized ZrO_2 surfaces. These studies have clarified the mechanism of oxygen removal from such surfaces, which involves the ionization of shallow metal cation core levels followed by interatomic Auger decay and resulting in the formation and rapid ejection of O^+ ions. Simpler one- and two-electron processes can lead to the desorption of neutral and molecular oxygen. These complex processes are being studied using sensitive laser detection schemes to determine the exact quantum-state distributions of the species produced. Controlled radiolysis of water-covered ZrO_2 surfaces has begun, to clarify the interaction of adsorbates with secondary electrons, electron–hole pairs, and excitons near the surface. Preliminary experiments do not suggest enhancement of hydrogen production from adsorbed water, but this needs confirmation. A related study of the radiolysis of water adsorbed on a series of powdered oxides using ^{60}Co gamma irradiation reveals that the hydrogen yield from radiolysis can be significantly greater, approximately equal to, or significantly less than the yield from pure gas phase water, depending on the specific oxide involved, and this can be correlated with the bandgap of the oxide. A mechanism has been proposed that accounts for these differences, based on the migration of excitons to the surface and their resonant coupling with the water adsorption complex.

Planned Activities

The thermal and electron-stimulated desorption kinetics of water from well-characterized UO_2 surfaces will be measured using radiotracer techniques with tritiated water. The surface radiolysis studies with radioactive sources will be extended to uranium oxide systems. High-intensity 10-MeV femtosecond electron pulses will be used to simulate the effects of beta ray and resulting cascades of lower-energy electrons. A final agreement on radiological protocols for the Environmental and Molecular Sciences Laboratory will allow UO_2 samples to be studied with the full array of instrumentation available there. The powder drying model will be tested against other oxides, including those of uranium. The radiation chemistry of zirconia will soon be extended to alumina and oxides of uranium. The influence of radiolysis on adsorbate materials will be clarified, and these experiments will be extended to uranium oxides.

Publications

Petrik NG, AB Alexandrov, AI Vall, and TM Orlando. 1998. *Gamma Radiolysis of Water on Oxide Surfaces: Parameters Controlling the Energy Transfer*, in press.

Distribution and Solubility of Radionuclides and Neutron Absorbers in Waste Forms for Disposition of Plutonium Ash and Scraps, Excess Plutonium, and Miscellaneous Spent Nuclear Fuels

(First Year of Funding: FY 1997)

Principal Investigator

Dr. X. Feng
Pacific Northwest National Laboratory
P.O. Box 999, MSIN P8-37
Richland, WA 99352
(509) 373-7284 (phone)
(509) 376-1638 (fax)
x.feng@pnl.gov

Contributors and Collaborators

H. Li (PNNL)
L.L. Davis (PNNL)
L. Li (PNNL)
J.G. Darab (PNNL)
D.K. Shuh (LBNL)
R.C. Ewing (UM)
L.M. Wang (UM)
E.R. Vance (ANSTO)
P.G. Allen (LBNL)
J.J. Bucher (LBNL)
N.M. Edelstein (LBNL)
I.M. Craig (LBNL)
M.J. Schweiger (PNNL)
J.D. Vienna (PNNL)
D.M. Strachan (PNNL)
B.C. Bunker (PNNL)

Research Objective

The objective of this research is to develop a basic understanding of the distribution and solubility of radionuclides and neutron absorbers in waste forms and their release from waste forms by studying the local structural environments of these constituents in representative materials.

Research Statement

A systematic study of the distribution and solubility of radionuclides and neutron absorbers and their release from waste forms is being undertaken through the study of materials with spectroscopic techniques such as ultraviolet-visible (UV-VIS), x-ray absorption fine structure (XAFS), and nuclear magnetic resonance (NMR). The materials being studied are silica-based glasses, ceramics, and vitreous ceramics. Specific examples of these materials were selected to be relevant to DOE/EM and DOE/MD needs.

Research Progress

This project was initiated in fiscal year (FY) 1998. Scientists from Pacific Northwest National Laboratory (PNNL) are collaborating with scientists at Lawrence Berkeley National Laboratory (LBNL), the University of Michigan, and the Australian Nuclear Science and Technology Organization (ANSTO). At PNNL, the effects of the oxidation states of plutonium (Pu) and uranium (U) on their solubility in silica-based glasses are being studied. Glasses are prepared under oxidizing and reducing environments. At LBNL, oxidation states and the local structural environments of Pu and U in glasses prepared at PNNL are being studied with the XAFS spectroscopic method. At the University of Michigan, the solubility of Cs in polycrystalline zirconolite ($CaZrTi_2O_7$) and (100) yttria-stabilized [9.5 mole%] zirconia (ZrO_2) single crystals are being studied with the ion implantation method. At ANSTO, efforts have been devoted to the study of the mechanism by which U is incorporated into zirconolite. In addition, near single-phase samples of zirconolite ($CaZrTi_2O_7$), pyrochlore ($CaCeTi_2O_7$ and $Gd_2Ti_2O_7$), monazite ($NdPO_4$), zircon ($ZrSiO_4$), perovskite ($CaTiO_3$), and spinels ($MgAl_2O_4$ and $MgFe_2O_4$) have been fabricated at ANSTO and will be used later to study the partitioning of Pu, U, and Gd in vitreous ceramics. The results obtained to date are discussed in detail in following sections.

Effect of Plutonium Redox [Pu(III)/Pu(IV)] on Pu Solubility in Borosilicate Glass

The effect of redox on Pu solubility is being systematically studied in silicates, borosilicates, and lanthanide borosilicates. Initial work has focused on a borosilicate with the composition (in mass%) Al_2O_3 4.07, B_2O_3 13.23, Cs_2O 1.02, Fe_2O_3 4.74, Gd_2O_3 11.30, K_2O 1.53, Li_2O 4.09, Na_2O 5.12, P_2O_5 2.14, SiO_2 42.76. Under oxidizing conditions, the solubility limit of PuO_2 was found to be less than 10 mass% when the glass was melted in air at temperatures between 1300 and 1500°C; crystalline PuO_2 was found in all oxidized glass samples by using powder XRD analysis. Under reducing conditions (graphite powder added to the melt) at 1400°C, however, the PuO_2 solubility limit (in terms of the oxide loading) in the same glass was determined to be at least 25 mass%. Glasses amorphous to XRD were obtained from three melts with PuO_2 loading of 10, 15, and 25 mass%.

The oxidation states of Pu in both oxidized and reduced glasses with 10 mass% PuO_2 loading were determined with XAFS. The Pu L_{III} x-ray absorption spectra were collected at the Stanford Sychnotron Radiation Laboratory (SSRL) on a wiggler beamline 4-1 with a Si (220) monochromator. Spectra were collected in the transmission or fluorescence modes using a four-pixel Ge detector developed at LBNL. Because higher harmonics interfere with clean spectra, these higher harmonics were rejected by detuning the monochromator by 50%. Powdered glass specimens (-325 mesh) dispersed in boron nitride were contained in a quaternary sample containment system for safety. Glass samples that contained Pu were analyzed as thin chips to prevent dispersion of the material. Data reduction was accomplished with the EXAFSPAK suite of computer codes developed at SSRL.

Figure 1 shows Pu L_{III} X-ray absorption spectra of glasses with 10 mass% PuO_2 (Pu16MC3) melted under oxidizing conditions at 1500°C and reducing conditions at 1400°C. Standard reference spectra for Pu(IV) and Pu(III) are included in the figure for comparison. In the oxidized glass, Pu(IV) is the dominant species; the relative proportion is estimated to be about 90% (Darab et al. 1997). In the reduced glass, Pu(III) is the major species; the proportion of Pu(III) is estimated to be about 95%. Combining the solubility data of Pu in the oxidized and reduced glasses with the XAFS spectra, we concluded that Pu(III) is much more soluble than Pu(IV) in the borosilicate system investigated. In the literature, it has been reported that PuO_2 is soluble to 22 mass% in an alkali silicate glass when it is melted in vacuum (Aldred 1980). It is very likely that the finding obtained from this study on the Pu solubility limit is also applicable to silicate glass systems.

In summary, solubilities of plutonium oxide have been demonstrated to be at least 25 mass% in the borosilicate glass when the glass is melted under reducing conditions at 1400°C. This is the highest solubility for Pu oxide that has been reported in literature. It has also been demonstrated for the first time that Pu(III) is much more soluble than Pu(IV) in the borosilicate glass

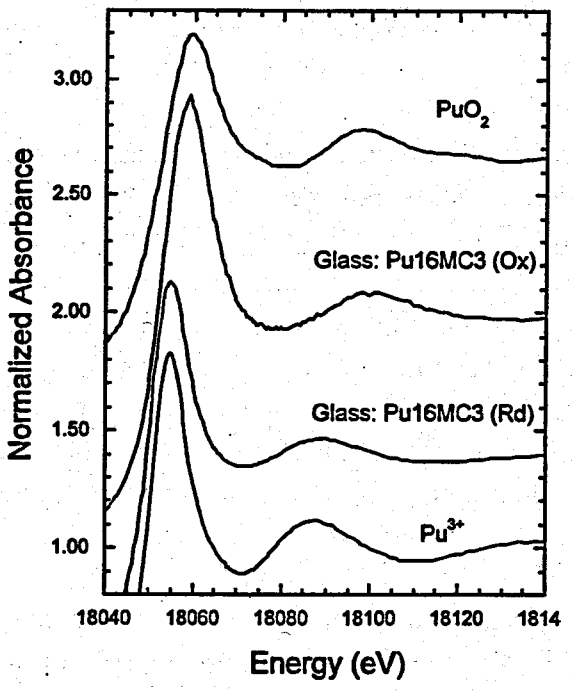

Figure 1. Normalized Plutonium L_{iii} Near-Edge Spectrum from a Borosilicate Glass Containing 10 Mass% Pu Oxide Prepared under Reducing Conditions Compared to Well-Characterized Pu Reference Spectra for the Trivalent and Tetravalent Oxidation States (the oxidized PU borosilicate spectrum is reproduced from Darab et al. 1997)

system. The significance of these results on the development of waste form for immobilization of Pu-rich materials has yet to be determined. Also to be determined are the structural roles of Pu(III) and Pu(IV) in the glass and have neutron absorbers such as Gd(III) affect the solubility of Pu(III) and Pu(IV) in the glass.

Effects of Sodium Content and Redox on Uranium Solubility in Silicate Glass

Uranium solubility in silicate glasses is being studied as well. The initial work has involved a National Institute for Standards and Testing (NIST) standard soda-lime (SL) glass, SRM 1830. Uranium in the form of UO_3 was added to this glass to make glasses with U concentrations from 10 to 40% (Table 1). Ten grams of each glass were melted at 1500°C for two hours. Measurements with XRD showed that glasses with 30 mass% UO_3 (SL-U30) or less were completely amorphous, while U_3O_7 (or $U_2O_5 \cdot UO_2$) crystallites were detected in glasses with 31 mass% UO_3 or greater. By raising the glass basicity of the baseline glass through Na_2O doping (SL-U40A, Table 1), however, we were able to make a glass that was completely amorphous at 40 mass% UO_3. This higher solubility of U in the SL-U40A glass does not appear to be the result of a change in the valence state of U (Table 1). These results suggest that U(V) solubility increases with the basicity of the glass.

Table 1. Compositions (mass%) of Soda-Lime Silicate Enriched with UO_3 and Preliminary Results on U Solubility and Valence

Glass ID	SL-U10	SL-U20	SL-U30	SL-U31	SL-U34	SL-U38	SL-U40	SL-U40A	SL-U40R	SL-U40RA
Al_2O_3	0.11	0.10	0.08	0.08	0.08	0.07	0.07	0.07	0.07	0.07
CaO	7.70	6.85	5.99	5.91	5.65	5.31	5.14	4.71	5.14	4.71
Fe_2O_3	0.11	0.10	0.08	0.08	0.08	0.08	0.07	0.07	0.07	0.07
K_2O	0.04	0.03	0.03	0.03	0.03	0.02	0.02	0.02	0.02	0.02
MgO	3.51	3.12	2.73	2.69	2.57	2.42	2.34	2.15	2.34	2.15
Na_2O	12.38	11.00	9.63	9.49	9.08	8.53	8.25	12.56	8.25	12.56
SO_3	0.23	0.21	0.18	0.18	0.17	0.16	0.16	0.14	0.16	0.14
SiO_2	65.76	58.46	51.15	50.42	48.23	45.30	43.84	40.19	43.84	40.19
TiO_2	0.01	0.01	0.01	0.01	0.01	0.01	0.01	0.01	0.01	0.01
UO_3	9.98	19.96	29.94	30.94	33.93	37.92	39.92	39.92	39.92	39.92
Crystals	N	N	N	Y	Y	Y	Y	N	Y	Y
Average valence	5	5	5	5	5	5	5	5	4	4

Melting a glass containing 40 mass% UO_3 under reducing conditions (SL-U40R, Table 1) yielded glasses with predominantly U(IV). The U solubility in SL-U40R and SL-U40AR was less than in glass SL-U40A. This further suggests that the solubility of U(V) is higher in this soda-lime silica glass than U(IV). The local structural environments of uranium in the silicate glasses are being further studied in the same manner as the plutonium glasses discussed above.

The average valence state of U in the SL glasses discussed above was estimated using XAFS. Figure 2 shows U L_{III} x-ray absorption spectra obtained from the SL glasses. Initial inspection shows that glasses prepared under oxidizing conditions with 10–40 mass% UO_3 yielded remarkably similar spectra except for the systematic increase in white line. The oxidation state of U in these glasses more closely resembles that of U_3O_8 than UO_2, characteristic of a mixture of oxidation states in the glasses. In contrast, the uranium in the U40R series glasses is significantly more reduced. The overall line shape, energy position, and presence of the actinyl signature (Schreiber and Coolburgh 1995) indicate that uranium in the SL-U40RA glass is nearly all tetravalent and in SL-U40R that a significant fraction is tetravalent. Furthermore, the extended XAFS clearly identifies U(IV) in the SL-U40R series glasses from U-U scattering as UO_2. The estimated average valence of U in the oxidizing glass is 5, compared with about 4 in the reducing SL-U40R and SL-40RA glasses (cf. Table 3).

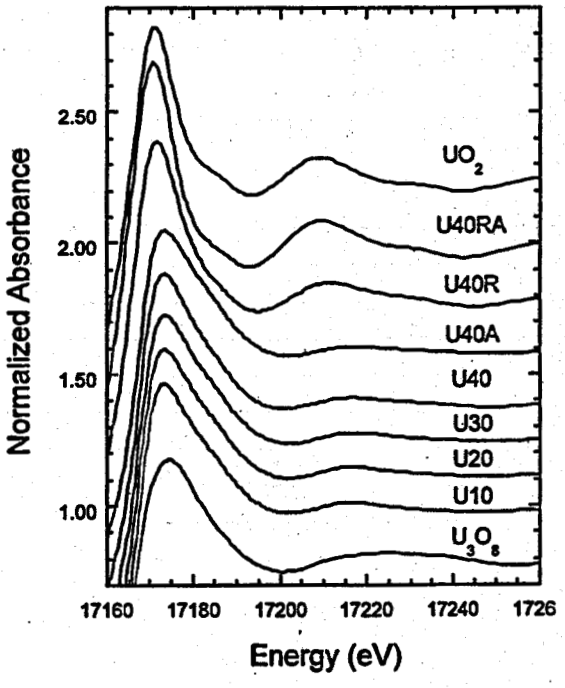

Figure 2. Normalized Uuranium L_{III} Near Edges from the soda-lime silicate glasses as a function of uranium oxide loading between 10-40 mass% UO_3, glass processing redox conditions, and composition along with appropriate reference uranium oxides (the spectra are individually labeled with the weight percent of UO_3, special reducing processing conditions by the inclusion of R, and excess Na_2O represented by A in the designation, respectively).

Composition Effects on HfO_2 and Gd_2O_3 Solubilities in Borosilicate Glass

Both Hf and Gd are neutron absorbers that are needed in waste forms for the disposition of Pu to avoid criticality. Therefore, it is important to study the solubility of Hf and Gd in these glasses and the effect of adding these elements on the solubility of Pu. For the study, we are using simple, four-component glasses. Their compositions derive from the Pu16MC3 and consist of SiO_2, Al_2O_3, B_2O_3, and Na_2O in the baseline glass plus HfO_2 and Gd_2O_3. The glasses studied to date, expressed in terms of absolute molar concentrations, are xB_2O_3-$20Na_2O$-$5Al_2O_3$-$60SiO_2$ (x from 5 to 20), $15B_2O_3$-xNa_2O-$5Al_2O_3$-$60SiO_2$ (x from 10 to 30), and $15B_2O_3$-$20Na_2O$-xAl_2O_3-$60SiO_2$ (x from 2 to 15). Hence, the effects of B_2O_3, Na_2O, and Al_2O_3 on the solubility of HfO_2 and Gd_2O_3 can be determined.

Tables 2 and 3 provide the target compositions (mass%) of the glasses with HfO_2 and Gd_2O_3 at their solubility limits with ±1% experimental uncertainty. The solubility limits of HfO_2 and Gd_2O_3 were determined at 1450 and 1560°C, respectively. The HfO_2 solubility is unaffected by B_2O_3 concentration for a fixed Na_2O/Al_2O_3 molar ratio of 4 but increases linearly with the net

Table 2. Glass Compositions (mass%) and Preliminary Results on Compositional Effects on Solubility Limits of HfO_2

Systems	xB_2O_3-$20Na_2O$-$5Al_2O_3$-$60SiO_2$				$15B_2O_3$-xNa_2O-$5Al_2O_3$-$60SiO_2$				$15B_2O_3$-$20Na_2O$-xAl_2O_3-$60SiO_2$ $60SiO_2$			
x (mol)	5	10	15	20	10	15	20	30	2	5	10	15
Target Glass Composition (mass%)												
SiO_2	44.3	42.3	39.4	37.4	51.8	45.1	39.4	34.4	37.9	39.4	41.2	42.3
Al_2O_3	6.3	6.0	5.6	5.3	7.3	6.3	5.6	4.9	2.1	5.6	11.7	17.9
B_2O_3	4.3	8.2	11.4	14.5	15.0	13.1	11.4	10.0	11.0	11.4	11.9	12.3
Na_2O	15.2	14.6	13.6	12.9	8.9	11.7	13.6	17.7	13.0	13.6	14.2	14.5
HfO_2[a]	30.0	29.0	30.0	30.0	17.0	24.0	30.0	33.0	36.0	30.0	21.0	13.0

(a) The solubility values were determined within ±1 mass% accuracy.

Table 3. Glass Compositions (mass%) and Preliminary Results on Compositional Effects on Solubility Limits of Gd_2O_3

Systems	xB_2O_3-$20Na_2O$-$5Al_2O_3$-$60SiO_2$				$15B_2O_3$-xNa_2O-$5Al_2O_3$-$60SiO_2$				$15B_2O_3$-$20Na_2O$-xAl_2O_3-$60SiO_2$ $60SiO_2$			
x (mol)	5	10	15	20	10	15	20	30	2	5	10	15
Target Glass Composition (mass%)												
SiO_2	42.6	37.5	32.7	28.3	51.2	34.3	32.7	29.8	31.4	32.7	33.9	42.3
Al_2O_3	6.0	5.3	4.6	4.0	7.23	4.9	4.6	4.2	1.8	4.6	9.6	17.9
B_2O_3	4.1	7.3	9.5	10.9	14.8	9.9	9.5	8.6	9.1	9.5	9.8	12.3
Na_2O	14.7	12.9	11.2	9.7	8.9	8.9	11.2	15.4	10.8	11.2	11.7	14.5
Gd_2O_3[a]	33.0	37.0	42.0	47.0	18.0	42[b]	42[b]	42[b]	47.0	42.0	35.0	13.0

(a) The solubility values were determined within ±1 mass% accuracy.
(b) The solubility limits of Gd_2O_3 in $15B_2O_3$-xNa_2O-$5Al_2O_3$-$60SiO_2$ (x=15,20,30) glasses are preliminary results and were determined within ±2.5 mass% accuracy.

Na_2O concentration (net moles of Na_2O = moles of total Na_2O - moles of Al_2O_3) at a fixed B_2O_3/Al_2O_3 molar ratio of 3. The Gd_2O_3 solubility was affected by the Na_2O or B_2O_3 concentrations in the following way. The solubility of gadolinium increases nonlinearly with the net Na_2O content when the B_2O_3/Al_2O_3 molar ratio is fixed at 3 but linearly with B_2O_3 concentration when the Na_2O/Al_2O_3 molar ratio is fixed at 4. Furthermore, the solubility limits of HfO_2 and Gd_2O_3 significantly decrease as the Al_2O_3 concentration increases, possibly as a result of the decrease in the net Na_2O concentration.

Under reducing conditions, the total soluble Pu(III) plus Gd(III) in the Pu16MC3 glass is close to the Gd(III) solubility obtained in the simplified four-component borosilicate glass (cf. Table 3). This solubility comparison suggests the possibility of using Gd(III) as a surrogate to

study Pu(III) solubility in the glass. Additional tests are planned to determine the solubility of PuO_2 in the four-component borosilicate glass under reducing conditions. Further spectroscopic characterization of the glasses continues to quantify the local environments of Pu(III) and Gd(III) in these glasses.

Structure of Lanthanide Borosilicate Glasses Containing Pu, U, and Surrogates

Lanthanide borosilicate (LaBS) glasses (potential waste forms for PuO_2) of general composition (in mol%) $9.6LN_2O_3$-$4.5RDO_x$-$1.0HfO_2$-$2.3CaO$-$20.1Al_2O_3$-$16.1B_2O_3$-$46.4SiO_2$ (where LN_2O_3 represents lanthanide oxides and RDO_x represents the UO_3 or the PuO_2 surrogates HfO_2 or CeO_2) were prepared at PNNL and analyzed by LBNL and PNNL collaborators using XAFS techniques. These glasses were melted in air at 1550°C for four hours. The XAFS results are now being analyzed.

For the LaBS glass with $9.6La_2O_3$ and $5.5HfO_2$, ^{11}B, ^{27}Al, and ^{29}Si solid-state NMR spectra were obtained at PNNL. Although there are no alkali ions present to act as charge-compensating species and allow three-coordinate B and six-coordinate Al to be transformed to four-coordinate network-forming species in the glass, preliminary NMR results indicate that a significant proportion of the B does occur as a four-fold, tetrahedrally coordinated species and that the Al occurs mostly as four-coordinated species.

Two glasses of composition $9.6Gd_2O_3$-$4.5PuO_2$-$1.0HfO_2$-$2.3CaO$-$20.1Al_2O_3$-$16.1B_2O_3$-$46.4SiO_2$ were also prepared—one melted under reducing conditions (using graphite powder) and the other melted in air (oxidizing conditions). Preliminary XAFS results obtained by LBNL researchers on these glasses indicated that the Pu in the glasses was predominantly Pu(III) for the reducing melt and predominantly Pu(IV) for the oxidizing melt.

Cesium Ion Implantation in Zirconolite and Zirconia

Zirconolite ($CaZrTi_2O_7$) and zirconia (ZrO_2), especially yttria-stabilized cubic zirconia, are potential nuclear waste forms. Zirconia has been considered for the inert fuel matrix/waste form concept for burning and disposition of excess plutonium from nuclear weapons. Therefore, it is important to understand the distribution and solubility of radionuclides and neutron absorbers in the structure of these phases.

During this fiscal year, we have initiated a study of the solubility and distribution of Gd and Cs in zirconolite and yttria-stabilized zirconia with in situ transmission electron microscopy (TEM) during ion beam implantation. Gadolinium is a neutron absorber and Cs is a typical fission product; the solubility and distribution of the latter is especially interesting for the zirconia inert fuel matrix/waste form concept. During the fission of ^{239}Pu, the resulting fission

products are projected to reside on the interstitial sites in the crystalline lattice. Because it is not practical to generate these products by actual fission, we have selected ion implantation as the best alternative to simulate the generation of fission products within these materials. Ion implantation is a powerful tool for introducing excess interstitials and, in that sense, a useful tool for this type of study. Also, radiation damage of the crystal structure can be studied during ion beam implantation. In situ TEM allows direct observation of the dynamic microstructural changes during ion implantation. The solubility of the implanted species in the host matrix can be studied with high dose implantation at various temperatures while carefully observing the possible formation of the secondary phases within the primary crystalline material. However, since the first attempt to obtain a useful current of the Gd beam from an ion implanter at Argonne National Laboratory (ANL) failed, this report can include only preliminary results on Cs ion implanted zirconolite and yttria-stabilized zirconia.

The polycrystalline zirconolite sample was obtained from the PNNL, and a (100) yttria-stabilized (9.5 mole%) cubic zirconia single crystal plate (0.5 mm thick) was purchased from the Atomic Chemicals Corporation (Farmmingdale, New York). Thin section samples for TEM were prepared from the two materials by mechanical polishing followed by argon ion milling. The energy of the argon beam was kept at below 4 keV. A thin carbon film (~20 nm) was deposited on the surface of the TEM sample to prevent electrical charging during TEM.

To determine the appropriate ion energy to use in the implantation of Cs, Monte Carlo computer simulations were performed with the TRIM-96 to determine the ion range and displacement damage. Cesium ion implantation and in situ TEM during the implantation were conducted at Argonne National Laboratory in the IVEM-Tandem Facility where a 650 keV ion implantor was linked to a Hitachi H-9000 electron microscope. A zirconolite sample was first implanted at room temperature to a fluence of 6×10^{16} ions/cm^2, and an additional 6×10^{16} ions/cm^2 was added later at 500°C with a double-tilt heating stage. The yttria-stabilized zirconia sample was implanted with Cs^+ to 1×10^{17} ions/cm^2 at 200°C. The flux of the Cs^+ was kept at 5×10^{12} Cs^+/cm^2/s. The maximum observed temperature rise of the sample during implantation was ~50 °C. The final ion fluence of 1×10^{17} ions/cm^2 corresponds to over 25 at% Cs and over 300 displacement per atom (dpa) in the implanted region of both materials.

In situ TEM was performed during the ion implantation with a 300-keV electron beam. Several samples have been irradiated at intermediate doses for ex-situ high-resolution TEM (HRTEM) and analytical TEM (AEM) analysis at the University of Michigan. Ex-situ HRTEM was performed with a JEOL 4000 EX HRTEM operating at 400 kV and AEM was performed with a Philips CM12 microscope with a energy dispersive x-ray spectroscopy (EDS) analyzer.

At room temperature, amorphization of zirconolite (indicated by the appearance of a diffuse halo in the electron diffraction pattern) was observed after a dose of less than 1 dpa (3×10^{14} ions/cm^2), consistent with earlier studies on radiation-induced amorphization in

zirconolite. However, the electron diffraction pattern (insert in Figure 3) still contains the diffraction maxima characteristic of crystalline materials even after 5 x 10^{16} ions/cm^2. This is because the depth affected by the implanted ions (~ 50 nm) is small compared with the thickness penetrable by the 300 keV electrons from which the diffraction pattern (~ 200 nm) is generated. After 5 x 10^{16} ions/cm^2, small precipitates, ~5 nm in diameter, were observed. At this ion fluence, the average concentration of Cs in the implanted region has exceeded 14 at%, and the peak displacement damage is already above 150 dpa. An additional 5 x 10^{16} Cs^+/cm^2 were implanted at 500°C, above the critical amorphization temperature of zirconolite. This caused the amorphous zirconolite to crystallize by epitaxial regrowth from the undamaged region. The precipitates grew slowly in size to ~20–30 nm and density (~10^{15}/cm^3) as shown in Figure 3. In some areas, small voids (~20 nm) were observed. Ex situ analytical TEM confirmed that at least some of the larger precipitates contain substantial amounts of Cs. However, detailed phase identification of these small particles has yet to be performed.

The yttria-stabilized zirconia was implanted with Cs^+ at 200°C. A high density of dislocation loops was observed with bright-field TEM after 1 x 10^{16} ions/cm^2 (Figure 4). Some of these loops are quite large (200–300 nm Figure 4), and the edges seem to be decorated by

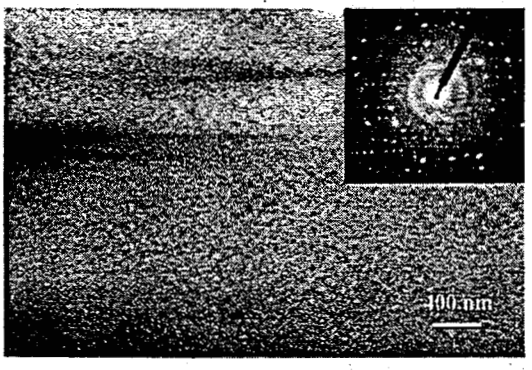

Figure 3. Bright-Field TEM Image Showing SmallPrecipitates Formed in Zirconolite after 70 Cs+ Ion Implantation to 1 × 10^{17} Ions/cm^2 at Room Temperature. The inserted selected area electron diffraction pattern was taken after implan tation to 5 × 10^{16} ions/cm^2 at room temperature showing a mixed amorphous and crystalline microstructure.

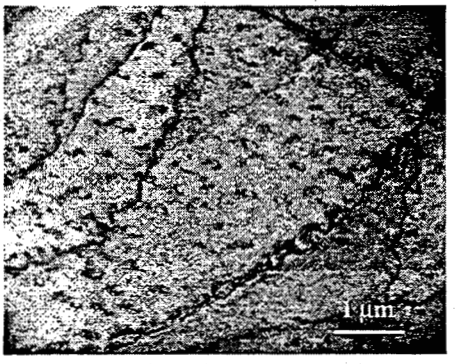

Figure 4. Bright-Field TEM of 9.5 mol% YO_2 Stabilized ZrO_2. Large dislocation loops are observed after 70 keV Cs^+ implantation to 1 × 10^{16} ions/cm^2 at 200°C.

nanometer-sized precipitates. After 5 x 10^{16} ions/cm^2, a high density of small defect clusters was observed around the bend contours where the two beam diffraction conditions for imaging the strain field induced by the clusters were satisfied (Figure 5). However, the sample remained crystalline with the cubic structure even after 1 x 10^{17} ions/cm^2 (Figure 6). The density of the defect clusters reached (~10^{19}/cm^3), but their size remained small (<30 nm), as shown in Figure 6. These high-density defect clusters were stable during the subsequent annealing at 500°C. The exact nature of these defect clusters has not been resolved. Although no apparent Cs-containing precipitates were identified with AEM, detailed analysis of HRTEM images has indicated that the defect cluster may have the characteristics of an interstitial type dislocation loop; i.e., it contains an extra atomic plane (Figure 7). The implanted Cs may have precipitated in two dimensions as small extra plane discs, which can be the source of the dislocation loops. However, the extra planes causing the dislocation loops may also be from displaced Zr or O atoms. If the extra plane discs are not made from the implanted Cs atoms, the solubility of Cs in zirconia may be higher than 25 mole% at 200°C. Detailed AEM and HRTEM analyses are continuing on this and other implanted zirconia samples.

Incorporation of U in Polycrystalline Zirconolite

The intention is to study in detail the incorporation of U(IV) into zirconolite at the Ca and Zr sites and to examine whether U could be incorporated as U(V) or U(VI) by suitable charge-balancing mechanisms.

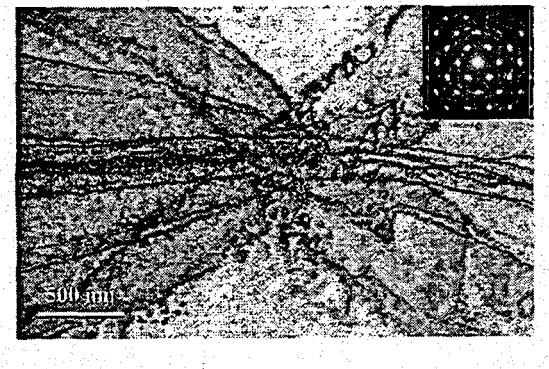

Figure 5. Bright-Field TEM of 9.5 mol% YO_2 Stabilized ZrO_2 after 70 keV Cs^+ Implantation to 5×10^{16} ions/cm^2 at 200°C

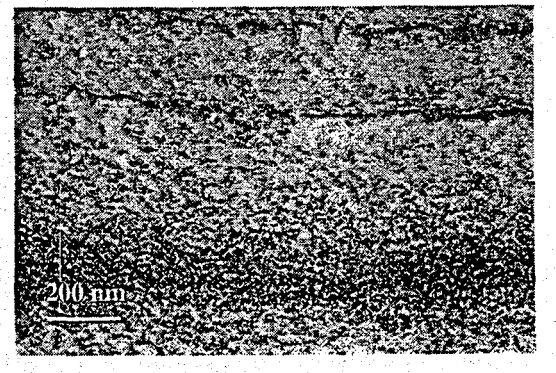

Figure 6. Bright-Field TEM Image of Defect Cluster Formed in 70 keV Cs^+ Implanted 9.5 mol% YO_2 Stabilized ZrO_2 after 1 × 10^{17} ions/cm^2 at 200°C

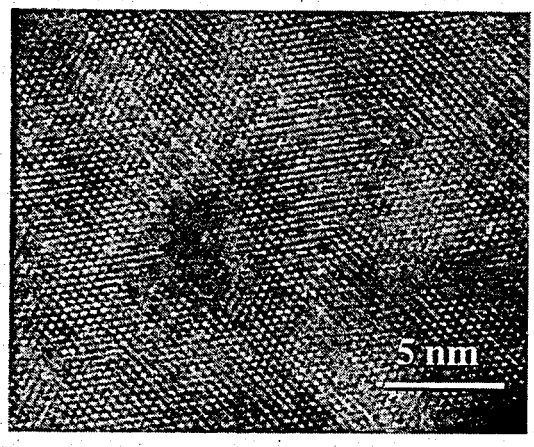

Figure 7. HRTEM Image of Radiation Damaged Lattice Structure of a 70 keV Cs^+ Implanted 9.5 mol% YO_2 Stabilized ZrO_2 after 1×10^{17} ions/cm^2 at 200°C

A set of zirconolite samples with nominal $CaZr_{1-x}U_xTi_2O_7$ stoichiometry ($0 < x < 0.5$) was made by the ANSTO alkoxide nitrate preparation route, calcining in argon at 750°C for one hour and finally firing at 1400°C for one day in an argon atmosphere with a measured $P_{O2} \sim 10^{-5}$ atm. Scanning electron microscopy (SEM) showed that the zirconolites were >99% phase pure, except that different zirconolite polytypes were frequently present. The XRD analyses showed that the zirconolite changed from the 2M polytype at low values of x to the 4M polytype for $x > 0.2$. Samples with higher U concentrations will be fabricated to locate the zirconolite/pyrochlore phase boundary. Samples with $x = 0.05$, 0.2 and 0.5 were found to melt congruently at 1550°C in argon if the product had a phase makeup similar to the sintered material. However, the microstructures were generally inhomogeneous in detail, as expected for slow cooling of a primary solid solution. Small admixtures (<1%) of $CaTiO_3$ or TiO_2 were present in both the ceramic and melted samples; this was presumed to be due to small deviations from exact zirconolite stoichiometry of the starting mixtures.

Samples with $x = 0.1$ and 0.2 formula units of U(IV) nominally substituted into the Ca site, with charge balance being effected by Mg or Al substitutions on the Ti sites were also found to be near single phase in the SEM after similar preparation routes. The measured chemical compositions of the zirconolite were close to the target values; however, samples in which 0.3 formula units of U were substituted showed significant amounts of alumina, brannerite and fluorite-structured $(U,Zr)O_2$ as extra phases. Samples with $x = 0.1$ or 0.2 formula units of U substituted in the Zr site nominally as U(V) or U(VI), with Mg or Al substitutions in the Ti sites, were also fabricated. Some of these samples were also refired in air at 1400°C to promote the

formation of the higher valence states. However the compositions of the major zirconolite phases were consistent with U(IV) substituting in the Ca site as well as the Zr site, and no essential differences were observed in air-fired samples relative to those fired in argon. As expected on this model, there was additional Ca-bearing material present (perovskite). Some XANES measurements are planned in July to expicitly try to examine the U valence states in selected samples.

References

Aldred AT. 1980. *J. Non-crystalline Solids*, 40:347-352.

Darab JG, H Li, MJ Schweiger, JD Vienna, PG Allen, JJ Bucher, NM Edelstein, and DK Shuh. 1997. *Plutonium Futures - The Science*. Conference Transactions, LA-13338-C, Los Alamos National Laboratory, Los Alamos, New Mexico, pp. 143-145.

Schreiber HD and MT Coolburgh. 1995. *J. Non-Cryst. Solids*, 181:225.

Soil and Groundwater Cleanup

Dynamics of Coupled Contaminant and Microbial Transport in Heterogeneous Porous Media

(First Year of Funding: 1996)

Principal Investigators

Dr. Timothy R. Ginn
172 Everson Hall
University of California, Davis
Davis, CA 95616-5294
(916) 752-1707
trginn@ucdavis.edu

Dr. Madilyn M. Fletcher
Belle W. Baruch Institute for Marine Biology and Coastal Research
University of South Carolina
Columbia, SC 29208
(803) 777-5288
fletcher@biol.sc.edu

Dr. Ellyn M. Murphy
Pacific Northwest National Laboratory
P.O. Box 999, MSIN K3-61
Richland, WA 99352
(509) 375-5914 (phone)
(509) 375-6954 (fax)
ellyn.murphy@pnl.gov

Dr. John H. Cushman
Department of Mathematics & Department of Agronomy
Purdue University
West Lafayette, IN 47907
(317) 494-8040
jcushman@math.purdue.edu

Collaborators

Dr. Donald M. Friedrich
Pacific Northwest National Laboratory
P.O. Box 999, MSIN K8-96
Richland, WA 99352
(509) 376-9637 (phone)
(509) 376-3650 (fax)
dm.friedrich@pnl.gov

Dr. David R. Boone
Department of Environmental Science and Engineering
Oregon Graduate Institute of Science & Technology
20000 Northwest Walker Rd
Beaverton, OR 97006
(503) 690-1146
boone@ese.ogi.edu

Contributors

Paula van Schie (Post-Doctoral Research Assistant, USC)
Robert Smits (Post-Doctoral Research Assistant, Purdue)
Zheming Wang (Post-Doctoral Research Assistant, PNNL)

Research Objectives

Dynamic microbial attachment/detachment occurs in subsurface systems in response to changing environmental conditions caused by contaminant movement and degradation. Understanding the environmental conditions and mechanisms by which anaerobic bacteria partition between aqueous and solid phases is a critical requirement for designing and evaluating in situ bioremediation efforts. This interdisciplinary research project will provide fundamental information on the attachment/detachment dynamics of anaerobic bacteria in heterogeneous porous media under growth and growth-limiting conditions. Experiments will provide information on passive and active attachment/detachment mechanisms used by growing anaerobes capable of reductive dechlorination. Theoretical representations of these attachment/detachment mechanisms will be incorporated into existing flow and transport models that incorporate heterogeneity effects and can be used to predict behavior at field scales. These mechanistic-based models will be tested against experimental data provided through controlled laboratory experiments in heterogeneous porous media in large (meter-scale) 2-dimensional flow cells. In addition to a mechanistic-based predictive model, this research will lead to new theories for the transient spatial distribution of microbial populations and contaminant plumes in heterogeneous porous media, improving our ability to design staged remediation strategies for dealing with mixed contaminants.

Problem Statement

The central challenge of in situ remediation strategies is the control of the transient spatial distribution of contaminants and remediation reagents (e.g., nutrients or microorganisms) in the presence of natural physical and chemical heterogeneities. Current predictive tools rely almost exclusively on the representation of passive attachment/detachment processes (e.g., filtration, sedimentation) with the bacterium treated as an inert biocolloid. One of the most intractable aspects of bioreactive transport, however, is active microbial partitioning (e.g., attachment/detachment) under growth and transport in physically and chemically heterogeneous systems. Active attachment/detachment is associated with microbial physiologic response to changes in local aqueous concentrations of nutrients and electron acceptors: this process is treated rarely in field-scale bacterial transport theories, and not at all in available predictive tools.

Understanding coupled contaminant and bacterial transport in real media is critical to the success of potential future bioremediation/biobarrier strategies at DOE sites. Disposal of chlorinated hydrocarbons has generated extensive contaminant plumes in sand/gravel aquifers at

DOE's Savannah River Site (SRS) in South Carolina and Paducah Gaseous Diffusion Plant (PGDP) in Kentucky, and such organic solutes interact with natural environments in coupled complex ways that have serious ramifications for remediation. For example, during the SRS in situ bioremediation demonstration, 90% of the increase in methanotroph biomass arising from degradation of trichloroethylene (TCE) partitioned into the aqueous phase. Initially, this methanotroph population was primarily attached to solid surfaces. If this partitioning behavior during bioremediation were understood and could be predicted, the knowledge could be exploited to effectively distribute the biomass across a contaminated area and to plan an injection network to minimize costly well construction and dampen or eliminate microbially induced reductions in hydraulic conductivity. This basic knowledge on the transport response of microorganisms is required for any subsurface remediation involving microbes, including staged approaches that sequentially degrade and immobilize multiple contaminants. Staged approaches (temporal or spatial) can exploit the different transport properties of distinct microbial populations and are especially well suited to DOE mixed contaminant problems.

The purpose of the proposed research is to address the limitations in understanding reactive contaminant transport and dynamic bacterial attachment/detachment under growth and growth-limiting conditions in natural porous media. This research will assess the coupled degradation and transport processes involving biological agents. It will focus on the active and passive attachment/detachment and transport processes of anaerobic microorganisms involved in TCE degradation, including their persistence under transient variations in substrate and electron-acceptor availability. Experiments will be performed in natural geologic materials that display general physical and chemical heterogeneity patterns representative of TCE-contaminated sandy media at SRS and at PGDP. The goals of the research are to develop basic knowledge of the fundamental relationship between contaminant transport and active bacterial transport and attachment/detachment under transient local chemical conditions. This knowledge will afford a quantitative understanding of the transient spatial distribution of contaminants and microbial populations during contaminant degradation and microbial growth in physically and chemically heterogeneous media. To accomplish this, the research includes an integrated effort to develop predictive models of contaminant transport and degradation in heterogeneous media using a combined multiscale experimental and theoretical approach.

Research Progress

The work on this project is being coordinated among six different investigators at five institutions. A consortium of anaerobic dechlorinating microorganisms was selected: *Desulfomonile tiedjei*, *Desulfovibrio* (G-11), *Syntrophobacter wolfei*, and *Methanospirillum*

hungateii. To date, much of the adhesion work has focused on *D. tiedjei* and *Desulfovibrio*. Progress has also been made on in situ fluorescence detection of methanogens in porous media.

Adhesion Behavior of Anaerobes

Thus far, the adhesion characteristics of three anaerobes (*D. tiedjei*, *Desulfovibrio G11*, and *S. wolinii*) have been tested, with greatest emphasis on *D. tiedjei*. Results have demonstrated interesting contrasts among these strains, which will be useful when designing experiments for consortium transport. First, the three organisms demonstrate very different attachment properties: *D. tiedjei* adheres in highest numbers, whereas *Desulfovibrio G11* adheres only when it is actively growing, and *S. wolinii* adheres in extremely low numbers. Second, the adhesion of *D. tiedjei* remains the same whether the cells are actively growing or starved, whereas that of *Desulfovibrio* is reduced when the cells are starved. Finally, the three organisms are morphologically distinct, with considerable differences in size and shape, which makes them relatively easy to distinguish microscopically.

Previous studies with aerobic organisms have demonstrated that cell adhesiveness can be affected by different nutrient conditions, such as types and concentration of available nutrients, carbon:nitrogen ratios, and degree of starvation of the organisms. The variability in adhesion with nutrient conditions varies with the organism; some show little change while others demonstrate significant changes in adhesiveness. Thus, adhesion properties of anaerobic organisms might be expected to alter with their physiological state. The adhesive properties of *D. tiedjei* and *Desulfovibrio G-11* were assessed in batch kinetic assays, using flat coupons of glass and siliconized or iron-coated glass as test substrata. Test conditions include cells freshly grown in a nutrient-rich medium and cells starved in MSNS-PIPES buffer (a dilute buffer solution more representative of nutrient levels found in groundwater). *Desulfovibrio G-11*, a motile butyrate-degrading organism, showed greater adhesion when nutrients were present in solution than when the microorganisms were starved (Figure 1a). This behavior is the opposite of that observed in column and flow cell experiments with an aerobe, *Pseudomonas cepacia*. For this aerobe, partitioning to the aqueous phase, and hence transport, increases in the presence of nutrients. *Desulfovibrio G-11* showed little change in attachment to negatively (silica) versus positively (iron oxide) charged surfaces, while *D. tiedjei* showed greater attachment to iron-oxide surfaces.

Additional features of the attachment of these organisms will increase the complexity of modeling their transport. Both *D. teidjei* and *Desulfovibrio G11* demonstrate significant detachment rates after initial attachment has occurred. The kinetics of attachment/detachment and factors that affect these rates will be a near-term focus for experimentation. Also, sedimentation of cells has been found to influence attachment numbers on the top side of surfaces. Thus, cell

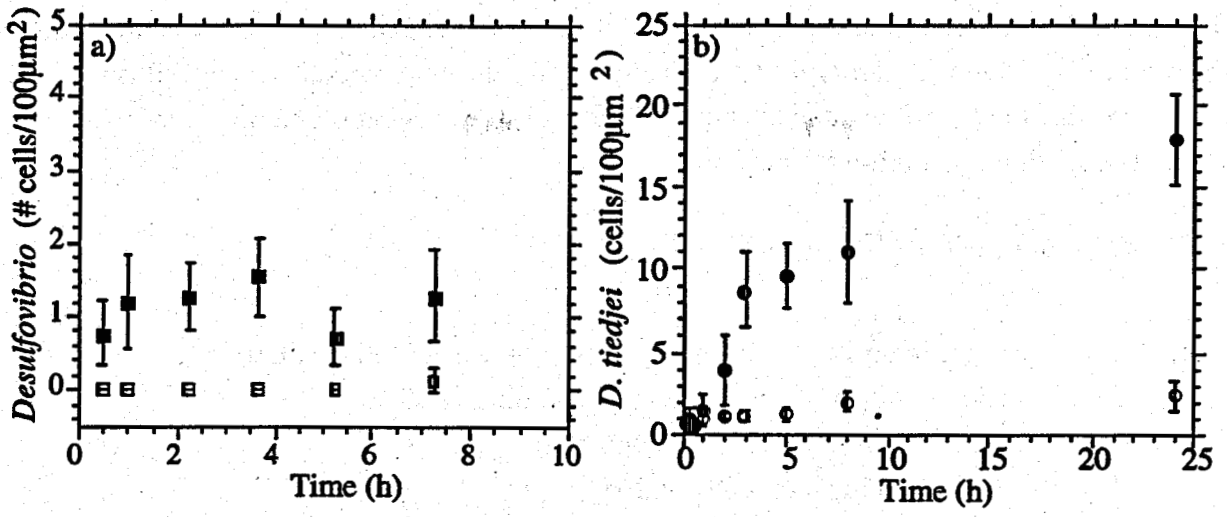

Figure 1. The Solid Squares in (a) Show the Adhesion of *Desulfovibrio* Under Active Metabolic State Compared with the Adhesion of Resting Cells (open squares). The solid circles show the number of *D. tiedjei* cells that adhered to the top side of the surface compared to the number of cells that adhered to the bottom side of the surface (b).

mass and sedimentation must be accounted for in model development, particularly for the relatively large *D. tiedjei*. Experiments are underway to measure the density of these micro-organisms under active and starved conditions (Figure 1b).

Additional experiments are underway to describe the adhesion characteristics *of Syntrophobacter wolfei*. These experiments are being performed by Dr. Paula van Schie under the guidance of Dr. Fletcher.

Stochastic Representations of Bacterial Transport in Porous Media

A microflow chamber is being constructed at PNNL for use with the confocal microscope to determine the residence time of anaerobic bacteria on porous media. To quantitatively evaluate these experiments, a model of microbial dynamics in the porous media has been developed at Purdue University by Dr. Robert Smits under the direction of Dr. Cushman. This multidimensional mathematical model depicts sticky Brownian motion with drift, as a general representation of microbial transport with attachment/detachment. This model has been implemented on the computer. A sticky Brownian motion with drift allows a particle (e.g., microbe) to diffuse by classical Brownian motion in a pressure-induced convective field, except when it hits a wall. When it hits the wall, it sticks for a random period of time, which is dictated by a probabilistic stickiness condition. Therefore, this model predicts the location in space of a microorganism as a

function of the random force, the drift, and the boundary force. The random force is the diffusive, Brownian-like motion (e.g., motility) and kinematic dispersion in porous media; drift is the convection due to water flow; and the boundary force is the sticking probability dependent on space. The resulting random-walk model is

$$dX_t = \sigma(X_t)dN_t + \mu(X_t)dt + \rho(X_t)dK_t \quad (1)$$

where dX_t = change in position of microorganism (Lagrangian cell location)
dN_t = scale of random force where s is the scaling factor
μ = velocity term (convective, chemotatic)
dK_t = random forcing term on boundary
ρ = stickiness, scaling on the forcing term.

The basic advantage of this random-walk approach is that it can be upscaled.

In Situ Spectroscopy

A laser and fiber optic system has been constructed to observe real-time biomass distribution in porous media. This system takes advantage of the natural fluorescent properties of methanogens (e.g., cofactor F_{420}) or genetically engineered microorganisms containing a green fluorescent protein. In the prototype system designed by Zheming Wang and Don Friedrich at PNNL, an optical fiber carrying the excitation beam and four additional optical fibers measuring the fluorescence emission are mounted on a collar that moves up and down along the outside of a glass column containing saturated sand. Eventually, the optical fibers will be embedded in the intermediate-scale flow cell containing porous media. The prototype system has been tested with microspheres that fluoresce in the blue region like the methanogens and with *Pseudomonas cepacia* containing the green fluorescent protein. Because of the scattering of the light by the sand particles, it is difficult to determine how deep the beam travels within the sand column. Therefore, we evaluated the breakthrough curves scanned along the length of the column with the breakthrough curve at the end of the column to determine whether the interior breakthrough curves were representative. The results for the fluorescent microspheres are shown in Figure 2a. As the pulse of microspheres moves along the length of the column, some tailing is observed, and an increase in effective macrodispersion is also observed with increasing distance along the column. The fitted dispersion using either the experimental or fitted velocity confirms this increase in dispersion along the length of the column (see Figure 2b). The characteristics of the interior breakthrough curves are consistent with the breakthrough curve at the end of the column, suggesting that the laser fiber optic system is observing a "representative" breakthrough curve with no discernible edge effects at the glass column and sand interface.

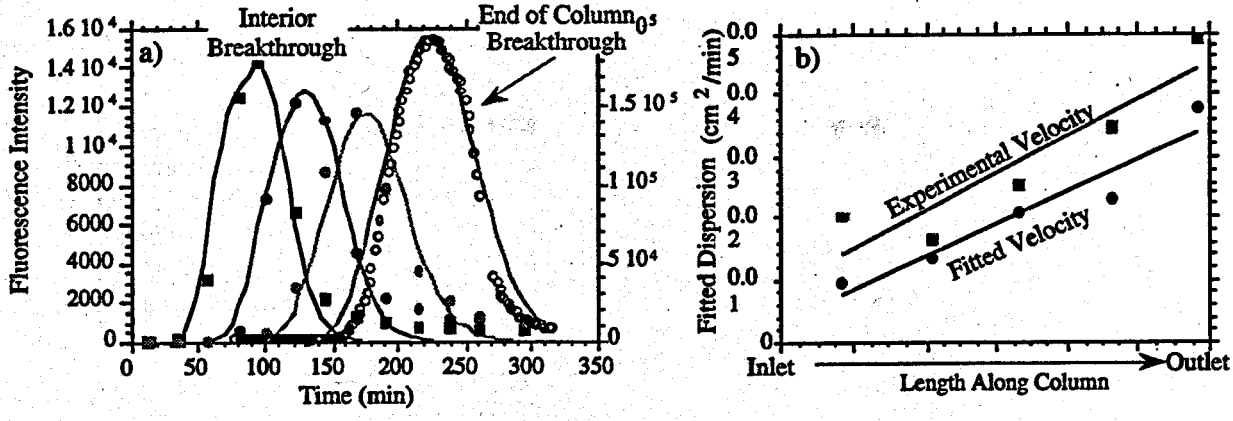

Figure 2. The Breakthrough of Carboxylated, 1-Micron Microspheres in a Sand Column is Shown in (a). The interior breakthrough curves are taken at different locations along the length of the 20-cm column (5.7, 10.6, and 15.6 cm, respectively) using the laser fiber optic system. The end-of-column breakthrough curve represents the 20-cm distance and is measured on a spectrophotometer (hence, the two different fluorescence intensity scales). The increase in the fitted dispersion is shown in (b), using either the experimental velocity or the fitted velocity.

Design of Flow Cell Experiments

A new large flow cell is nearing completion at the University of California at Davis. This flow cell will be approximately 1 meter long by 20 cm wide by 50 cm high and will accommodate a representative heterogeneity pattern found in the eastern Atlantic coastal plane (Oyster Site, Virginia). The flow cell has been set up with a dual flow system so that a mirror image of the heterogeneity pattern can be packed in the flow cell. This design will allow us to simultaneously run a "control" with every flow cell experiment. For example, starting with a porous medium containing a consortium of bacteria, a contaminant pulse could be injected into half of the flow cell while dilute groundwater continues to flow through the other half of the flow cell. The effect of the contaminant pulse on transport of the anaerobic microbial community can be rigorously evaluated by direct comparison to the bacterial transport behavior on the control side of the flow cell. This represents a vast improvement in previous flow cell designs.

A representative heterogeneous flow field was constructed using air permeability and grain-size distribution data (see Figure 3) to create a numerical representation of the flow field. This flow field is characterized by a darker region that has a higher permeability than the lighter region; however, the overall hydraulic conductivity varies by less than one order of magnitude, which is

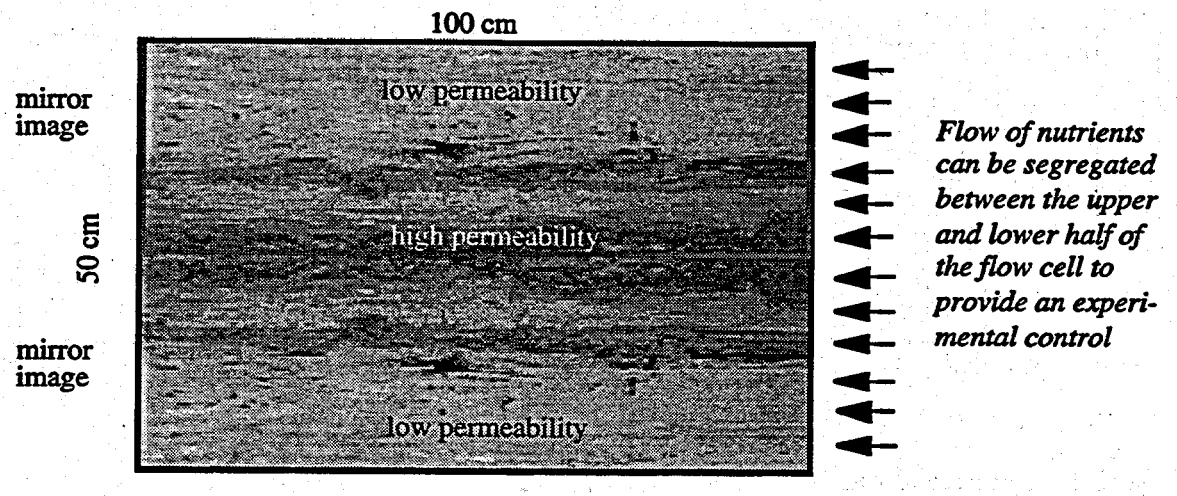

Figure 3. Heterogeneity Pattern Superimposed in New Flow Cell - Dark areas have higher permeability than light areas.

characteristic of sediments at the Oyster Site. This numerical flow field was used to conduct a theoretical experiment that demonstrates the relative effect of dynamic attachment/ detachment of bacteria on the degradation of a contaminant plume. We define kinetic attachment/ detachment as a partitioning process that arises from cell division and growth and can be described by determining a forward (attachment) and reverse (detachment) rate kinetic within a growth model. Numerically, the concentration of aqueous (mobile) and attached (immobile) bacteria are represented as follows:

$$\phi\frac{\partial C_m}{\partial t}+\nabla\cdot(C_m V) = \nabla\cdot[D\nabla C_m] + \mu C_m\left[\frac{C_{e^-}}{K_{e^-}+C_{e^-}}\right] - K_f C_m + K_r C_i \tag{2}$$

$$\frac{\partial C_{im}}{\partial t} = \mu C_{im}\left[\frac{C_{e^-}}{K_{e^-}+C_{e^-}}\right] + K_f C_m - K_r C_{im} \tag{3}$$

where C_m, C_{im} = concentration of mobile and immobile bacteria
C_{e^-} = concentration of electron donor or acceptor
$\emptyset$ = porosity
D = dispersion tensor (cm^2/h)
μ = specific growth rate of bacteria [$1/h$]; subscripts denote different microbial species
Y = yield coefficient (biomass (protein) per mass propionate); subscripts denote different populations

K_{e^-} = half-saturation constant for electron donors and acceptors (ppm)

K_f, K_r = forward (attachment) and reverse (detachment) kinetic rate (1/h); subscripts denote different microbial populations

Dynamic attachment/detachment occurs when the forward and reverse rate kinetic varies with metabolic activity. In the mechanistic description below, the forward attachment kinetic varies inversely with the specific growth rate; or as growth activity increases, aqueous partitioning of the bacteria increases.

$$\phi\frac{\partial C_m}{\partial t}+\nabla\cdot(C_m V) = \nabla\cdot[D\nabla C_m] + \mu C_m\left[\frac{C_{e^-}}{K_{e^-}+C_{e^-}}\right]-K_f C_m\left(1-\left[\frac{C_{e^-}}{K_{e^-}+C_{e^-}}\right]\right)^n+K_r C_{im} \quad (4)$$

$$\frac{\partial C_{im}}{\partial t} = \mu C_{im}\left[\frac{C_{e^-}}{K_{e^-}+C_{e^-}}\right]+K_f C_m\left(1-\left[\frac{C_{e^-}}{K_{e^-}+C_{e^-}}\right]\right)^n-K_r C_{im} \quad (5)$$

A numerical experiment was conducted to determine whether dynamic partitioning affects the overall degradation of a contaminant plume. Two anaerobic bacteria were used in the consortium: *Syntrophobacter*, which degrades propionate to formate and hydrogen; and *D. tiedjei*, which uses formate as an electron donor and dechlorinates hydrocarbons as an electron acceptor. In one experiment, both *Syntrophobacter* and *D. tiedjei* were controlled by kinetic attachment/ detachment rates; in the second experiment, *Syntrophobacter* attachment was dynamic (varying with metabolic activity) and *D. tiedjei* attachment remained kinetic.

A pulse (or plume) of chlorinated hydrocarbon was injected into the bottom portion of the flow cell, which contained a mirror image of the heterogeneity pattern. In Figure 4, the breakthrough curves and profiles of the plume moving through the flow cell are shown. The contaminant showed an early breakthrough through the high-permeability portion of the sediment-followed by a secondary peak of the contaminant moving through the lower-permeability zone under kinetic attachment/detachment. When *Syntrophobacter* undergoes dynamic attachment/ detachment, only contaminant traveling through the high-permeability zone reaches the end of the flow cell; contaminant moving through the lower-permeability zone is completely degraded. This same pattern can be seen in the profiles of the flow cell taken at different time intervals. At 35 hours, the concentration of contaminant moving through the low permeability region is significantly reduced; and by 40 hours, the contaminant is completely degraded in this region. The enhanced degradation under dynamic conditions is due to the aqueous partitioning of *Syntrophobacter*, which results in an increasing population of this propionate-degrading organism as the contaminant plume moves along the flow path. In this example, the rate of propionate

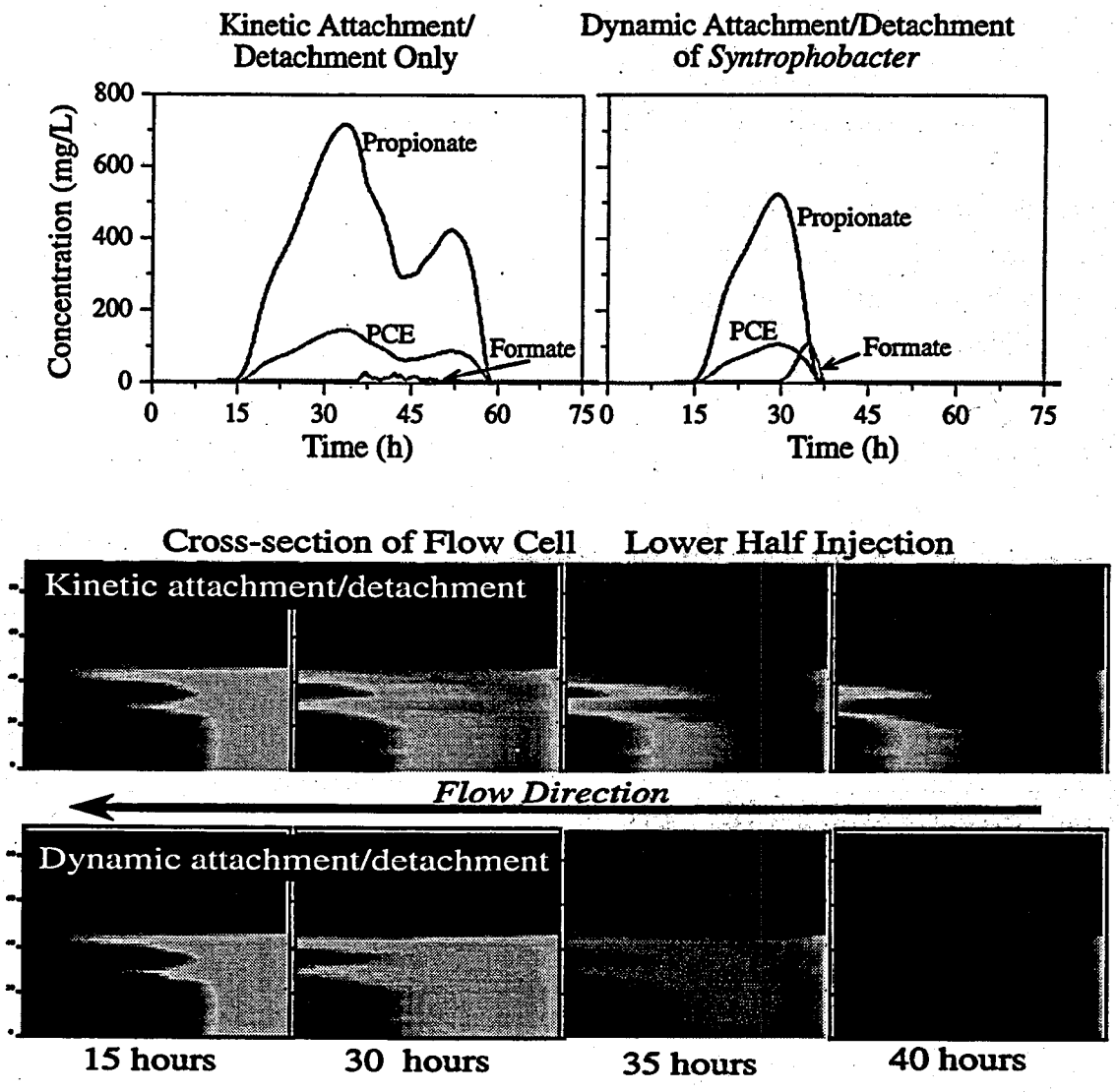

Figure 4. The Top Graphs Show the Breakthrough of Propionate, Formate, and Perchloroethylene (PCE) at the End of the Flow Cell Shown in Figure 3. The cross-sectional profiles show the interior location of the PCE plume at the different times. The highest concentration is light while the lowest concentration is gray.

degradation was limiting the metabolic activity of *D. tiedjei*, which promotes the dechlorination reaction. This example clearly illustrates the importance of dynamic attachment/detachment in intrinsic bioremediation.

Publication and Presentations

Cushman JH and BX Hu. 1997. "Solutions to the Stochastic Transport Problem of $O(\sigma_v^N)$ for Conservative Solutes." *Stochastic Hydrology and Hydraulics*, 11:297-302.

Cushman JH and TR Ginn. 1998. "Reactive contaminant transport in the saturated zone." Groundwater Hydrology Handbook, JW Delleur, ed. CRC Press (in press).

Ginn TR. 1998. Comment on "Stochastic Analysis of Oxygen-Limited Biodegradation in Three-dimensionally Heterogeneous Aquifers," by F. Miralles-Wilhelm et al., *in press, Water Resources Research.*

Ginn TR, and EM Murphy. 1998. "The Influence of Subsurface Heterogeneity on Biodegradation." Invited Review for *Soil Science Society of America Journal.*

Murphy EM, TR Ginn, FJ Brockman, and DR Boone. 1997. "Growth Effects on the Partitioning and Transport of Bacteria." American Geophysical Union Fall Meeting, *EOS Transactions*, 78(46):F231.

Murphy EM, and TR Ginn. 1996. "The Role of Passive and Active Partitioning in Microbial Transport in Natural and Contaminated Systems." American Geophysical Union Fall Meeting, *EOS Transactions.*

Smits RG and JH Cushman. 1998. " Application of sticky Brownian motion to microbial dynamics in porous media." Submitte to Random walks.

Smits RG and JH Cushman. 1998. "Application of sticky Brownian motion to microbial dynamics in porous media." Submitted to Upscaling via a central limit theorem.

van Schie PM, DR Boone, and M Fletcher. May 17-21, 1998. "Adhesion of Biodegradative Anaerobic Bacteria to Solid Surfaces." 98th general meeting of the American Society for Microbiology, Atlanta, Georgia.

Genetic Analysis of Stress Responses in Soil Bacteria for Enhanced Bioremediation of Mixed Contaminants

(First Year of Funding: FY 1996)

Principal Investigator

Kwong-Kwok Wong, Ph.D.
Pacific Northwest National Laboratory
P.O. Box 999, MSIN P7-56
Richland, WA 99352
(509) 375-5097 (phone)
kk.wong@pnl.gov

Collaborator

Jerome J. Kukor, Ph.D.
Biotechnology Center, Foran Hall
Cook College Campus, Rutgers University
The State University of New Jersey
59 Dudley Road, New Brunswick, NJ 08901-8520
(732) 932-8165, ext. 108 (phone)
kukor@aesop.rutgers.edu

Contributors

Susan Varnum (Postdoctoral fellow, PNNL)
Meng L Markillie (Technical Specialist, PNNL)

Research Objective

The purpose of this project is to provide fundamental knowledge on stress-responsive genes and the survival of soil and subsurface bacteria under stress conditions. This information will be particularly useful in developing successful bioremediation strategies. Stress-inducible genes and promoters will be identified from two soil bacteria, *Deinococcus radiodurans* and *Sphingomonas aromaticivorans* F199. These organisms represent two phylogenetically distinct groups of soil bacteria, each of which has specific features of interest for bioremediation. *D. radiodurans* exhibits high resistance to external stress including ionizing radiation; F199 is a deep subsurface (Savannah River Site) organism with unique degradative capabilities. The project will also investigate 1) probes for assessing expression of these stress-responsive genes, 2) identification of specific genetic elements that can be used for engineering effective degradative expression systems, and 3) generation of a *D. radiodurans* GEM expressing TCE (trichloroethylene)-degrading activity that is decoupled from growth.

Problem Statement

To realize the full potential of bioremediation, an understanding is needed of the microbial community and individual bacterial responses to the stresses encountered at contaminated sites. Knowledge about genetic responses of soil and subsurface bacteria to environmental stresses, which include lack of nutrients, lack of oxygen, and mixed pollutants, will allow extrapolation of basic principles to field applications using indigenous bacteria or genetically engineered micro-organisms. Defining bacterial responses to those stresses presents an opportunity for improving bioremediation strategies, both with indigenous populations and genetically engineered microbes, and should contribute to environmental management and restoration actions that would reduce the cost and time required to achieve DOE-EM's cleanup goals.

Enhanced in situ removal of hazardous wastes by stimulating the growth of indigenous bacteria with nutrients has been demonstrated. However, how much and how often to apply these supplements has been determined only empirically. And controlled and reproducible degradation of pollutants in the environment has been difficult to achieve. Genes inducible by low nutrient and low oxygen conditions can serve as markers for determining the minimum amount of supplements needed. The disappearance and reappearance of such stress responses will determine how much and when nutrients and oxygen need to be applied.

Applying genetically engineered organisms in bioremediation requires the design of gene expression systems that function under environmental conditions and are cost-effective. The promoter, the genetic regulatory element that directs the use of the gene, plays the central role in

gene expression systems. The ideal promoter for environmental applications possesses two qualities: 1) it does not require the addition of exogenous compounds for activation, and 2) it is active under nutrient-limited conditions and not dependent on cell growth for activity. Using stress-induced promoters to control expression of degradative genes allows induction under the environmental conditions encountered and effectively decouples the activity of the promoter from the requirement for cell growth.

Research Progress

Analysis of the Starvation Responses of *Sphingomonas Aromaticivorans* F199

Insufficient nutrients in the environment limit the degradative ability of the bacteria. Enhanced in situ removal of hazardous wastes by stimulating growth of indigenous bacteria with nutrients has been demonstrated. However, the effect of adding nutrients must be monitored. Using *S. aromaticivorans* as a model, we investigated the effects of adding nutrient to starved cells in terms of protein expression, rRNA, and gene expression pattern on catabolic plasmid pNL1.

S. aromaticivorans cells were starved in reconstituted well water without carbon and nitrogen sources for nine months. Nutrient (TGY medium) was added to the starved cell, and proteins were extracted from the cell culture after 4, 8 and 24 hours. Extracted proteins were analyzed using SDS-PAGE (Figure 1). Only a few major proteins were present. Few changes were detectable four hours after the nutrient was added, but several prominent proteins appeared after eight hours, suggesting that there is a lag time before starved cells respond to nutrient supplement. These identified proteins may be useful for monitoring the bioremediation process during biostimulation with nutrient supplements.

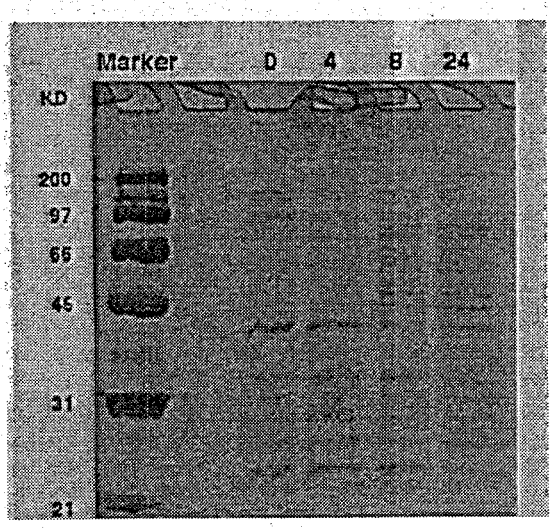

Figure 1. Analysis of Proteins Released by SDS Lysis of Starved *Sphingomonas aromaticivorans* F199 Cells at 0, 4, 8 and 24 Hours after Nutrient was Added to the Cultures

During further analysis of total RNA isolated from starved cells and recovery cells (24 hours after nutrient was added to starved cells), the size of rRNA molecules (both 16S and 23S rRNA) had decreased (Figure 2). It is possible that rRNA has undergone fragmentation under starvation conditions. We are now attempting to determine the sequences of the 16S and 23 rRNA from both starved cells and recovery cells. By comparing the rRNA sequences of these cells, we might be able to develop oligonucleotide probes useful for monitoring the number of recovery cells that are metabolically active during bioremediation.

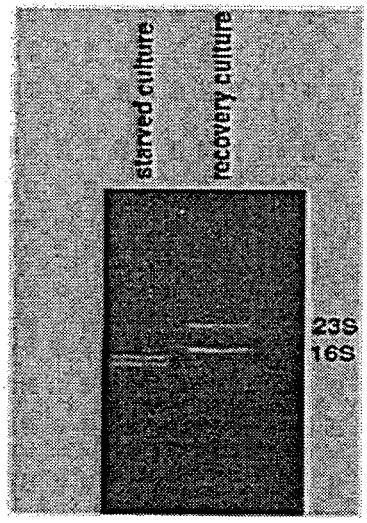

Figure 2. Analysis of rRNA of Starved Culture and Recovery Culture

S. aromaticivorans carries a catabolic plasmid, pNL1, which encodes genes for the degradation of a variety of aromatic compounds such as naphthalene, biphenyl and xylene. A plasmid library of 1 to 2 kb fragments, derived from sonicated pNL1 DNA, was used for making a dot blot. Flourescein-labeled cDNA probes, derived from both starved and recovery cells, were used for hybridization with the dot blots containing the plasmid library. Figure 3 shows that a few genes on the catabolic plasmid pNL1 are still relatively active in the starved cells. These starvation-active genes respond more robustly to the nutrient supplement. Apparently, most of the catabolic genes were not activated by the nutrient, suggesting that, although the nutrient supplement stimulates the growth of the bacteria, it does not necessarily stimulate the biodegradative activities of the bacteria. Alternative strategies need to be developed for stimulating the biodegradative activities of indigenous bacteria.

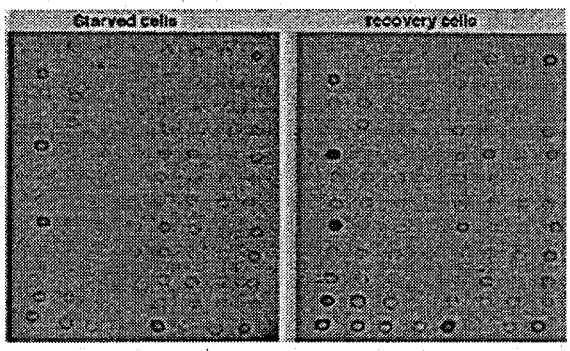

Figure 3. Identification of Genes on the Catabolic Plasmid pNL1 that are Induced after Nutrient was Added to Starved Cells

Analysis of the stress responses of *Deinococcus radiodurans* R1

RNA from *D. radiodurans* was harvested from cells grown for 0, 4, 15, and 21 days in starvation media. RAP-PCR was performed, screening 11 different arbitrary primers; and 12 tentative differentially expressed genes were identified. Sequencing revealed that 10 of the genes were either 16S or 23S RNAs. RT-PCR revealed that clone 3-5 was expressed 3-fold higher in 21-day starved cultures than in zero day cultures (Figure 4).

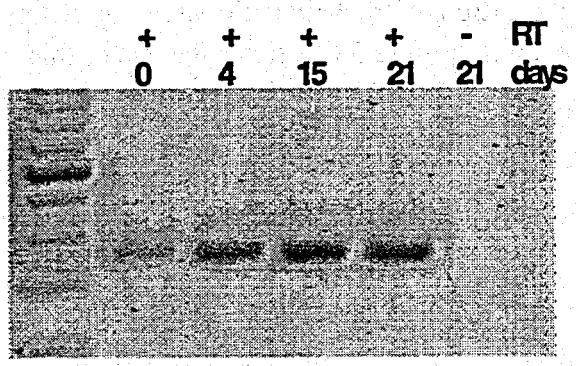

Figure 4. RT-PCR Analysis of Clone 3-5 under Nutrient-Limiting Conditions

Sequence analysis of the clone 3-5 revealed a high level of sequence identity with transposase. Five full-length copies of transposase were found in the *D. radiodurans* genome. Because this putative transposase gene is expressed at a high level during starvation conditions, a fusion was generated between its promoter and Tbu. An initial transformation experiment resulted in extremely slow growth of *D. radiodurans* with this construct.

We searched the nearly complete *Deinococcus* genome sequence databank with other microbial genes involved in the nutrient-stress response to identify additional stress-responsive genes in *D. radiodurans*. The following five *Escherichia coli* genes showed significant similarities to genes from *D. radiodurans*: a sigma factor; phage-stress protein (*pspA*); alkyl hydroperoxide reductase C protein (*ahpC*); cold shock protein (cspA); and *ftsK*. Experiments are in progress to

confirm the stress inducibility of these putative genes. Promoters from these genes will be used to express toluene 3-monooxygenase enzyme complex in *D. radiodurans* to degradation of TCE under starvation or environmental stress conditions.

Development of Genetic Methods to Engineer *S. aromaticivorans* and *D. radiodurans*

Transformation and transposon mutagenesis in *S. aromaticivorans F199*

Several transformation methods have been tried. *S. aromaticivorans* F199 was successfully transformed with a boardhost plasmid pRK404 to become tetracycline-resistant using the electroporation method. The electroporation steps were optimized to obtain high transformation efficiency. Using the tetracycline-resistant *S. aromaticivorans* strain, transposon elements Tn*5* were delivered into the chromosome of the bacterium via conjugation. These genetic methods will allow scientists to engineer *S. aromaticivorans* for better performance in bioremediation.

Duplication insertion for *D. radiodurans R1*

We have developed a modification of duplication insertion to create insertional mutations in the *D. radiodurans* genome, called duplication inactivation. Figure 5 illustrates the use of this method to inactivate a target gene.

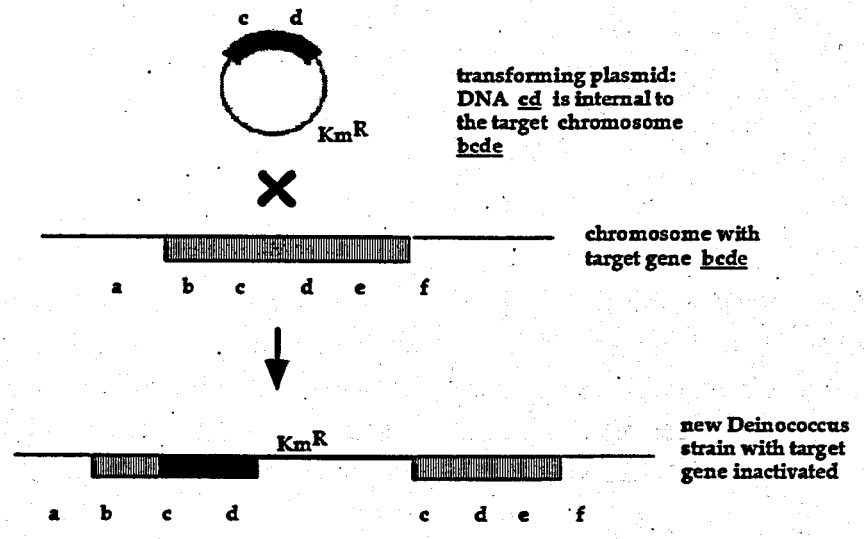

Figure 5. Duplication Insertion. The transforming construct is readily generated by ligation of the E. coli KmR-containing plasmid with chromosome fragments of *D. radiodurans* DNA. Upon transformation, integration of the plasmid occurs.

We have found several factors to be important to the success of this method:

- The plasmid must be unable to replicate autonomously in *D. radiodurans* cells.
- The drug-resistant marker on the plasmid must be recognized and expressed by *D. radiodurans.*
- The cloned *Deinococcus* DNA fragment cannot cross over the left side or right side of the gene but must be derived entirely from the internal portion of the targeted gene.

An adaptation of this method results in generation of a transcriptional or operon fusion placing an intact foreign gene (i.e., reporter or biodegradative gene) downstream from the transcriptional start signals of the target gene. The result is that the foreign gene is expressed under the control of the target gene promoter. In this case the cloned DNA fragment would be **ef** instead of **cd** (Figure 5); in other words, the 3-ft end of the gene with flanking 3-ft sequences. The resultant transformant retains a complete copy of the target gene with the foreign gene inserted downstream.

TCE is degraded aerobically by various toluene-monooxygenase enzymes, including toluene-3-monooxygenase (Tbu). We have obtained the gene encoding Tbu from Dr. Ron Olsen and inserted it into the pCR-Blunt cloning vector to generate a new plasmid, pCR-Blunt-Tbu. The insertion of a target gene into this plasmid can be used in transformation experiments to insert an intact Tbu gene into the *D. radiodurans* genome.

Several approaches have been pursued to identify appropriate promoters for the expression of the Tbu gene in *D. radiodurans*. The first gene identified, sigma factor, encodes an important regulatory protein. RNA polymerase, the enzyme complex responsible for transcription, is composed of multiple subunits, including the sigma factor. Sigma factor permits the holoenzyme to recognize promoter elements and initiate transcription at these sites. Sigma^{70} is the major sigma factor used during exponential growth, whereas sigma^{38} is an alternative sigma subunit considered to be the central regulator of gene expression in the stationary phase. Based on sequence comparisons, we are not able to discern whether the identified sigma factor in *D. radiodurans* is a sigma^{70}- or sigma^{38}-type factor. However, because both sigma factors are expressed during the stationary phase, they are both candidate promoters for the expression of a degradative gene under nutrient-limiting conditions. Therefore, in order to express the Tbu gene under the control of the sigmaX promoter, we have inserted the 3-ft end and 220 bp of 3-ft flanking sequences of sigmaX into the pCR-Blunt-Tbu plasmid. Transformation of this plasmid into *D. radiodurans* produced a strain of *Deinococcus*, expressing Tbu as determined by RT-PCR (Figure 6, lanes 5 and 6).

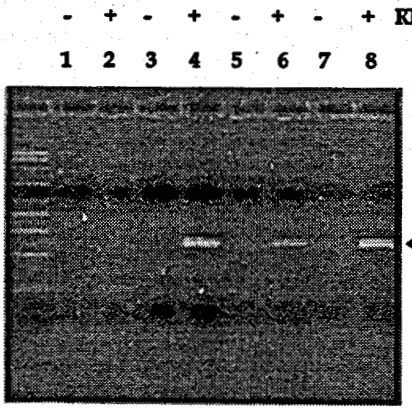

Figure 6. Gel Electrophoresis of RT-PCR Analysis of pCR-Blunt-Tbu Constructs. Lanes 1, 2: wild-type *D. radiodurans* with no plasmid inserted. Lanes 3, 4: *E. coli* transformed with pCR-Blunt-Tbu-kat. Lanes 5, 6: *D. radiodurans* transformed with pCR-Blunt-Tbu-sigmaX. Lanes 7, 8: *D. radiodurans* transformed with pCR-Blunt-TBU-kat. The arrow indicates the reverse transcriptase Tbu product at 300 bp.

To examine the role of the sigmaX gene during *D. radiodurans* growth, an insertional mutation was made in the sigmaX gene using duplication inactivation. Initial analysis of the sigmaX mutant strain indicates that the mutant has a two-fold slower growth rate than wild-type *D. radiodurans*. Starvation survival has been initiated.

We have initiated experiments to determine the expression pattern of the other four putative *Deinococcus* stress factors. The 3-ft end, including downstream external sequences of *ftsK*, *ahpC*, *pspA* and *cspA*, has been inserted in front of a *lacZ* reporter gene. Properly constructed clones will be transformed into *Deinococcus* and the expression of *lacZ* monitored during exponential and stationary phases.

We have also investigated the *katA* gene, which encodes the major catalase enzyme. The *E. coli* katA gene is induced in cells entering the stationary phase (Mulvey et al. 1990). Furthermore, it has been shown that catalase activity in cultures of *D. radiodurans* increases as cells enter the stationary phase (Wang and Schellhorn 1996). Because of this evidence, we investigated whether the *katA* promoter is good for the expression of Tbu under nutrient-limiting conditions. A transcriptional fusion was inserted between the *tbu* operon and a 2.4 kbp upstream region of *katA*. The resultant pCR-Blunt-Tbu-katA construct was transformed into *D. radioduran,s* and RT-PCR analysis was performed. Figure 3 (lanes 7 and 8) shows that the resultant *D. radiodurans* strain expresses Tbu at a high level.

Because *katA* is also induced by ionizing radiation (Tanaka et al. 1996), the role of *katA* in radiation and peroxide resistance was investigated. We have constructed a catalase mutant (*katA*) in *D. radiodurans* and found that the *katA* mutant lost major catalase activity and it became substantially more sensitive to hydrogen peroxide. Moreover, the *katA* mutant was slightly and reproducibly more sensitive to ionizing radiation than the wild type at a high radiation exposure.

These findings suggest that the major catalase is involved in the extreme hydrogen peroxide resistance of *D. radiodurans* and to a lesser extent is involved in ionizing radiation resistance (Wong et al. 1998). Thus expressing heterologous genes useful for bioremediation with *katA* promoter might be ideal for bioremediation at the mixed-contaminant site with radionuclides.

Planned Activities

1. Determine the complete sequences of rRNA of starved and recovery cells to develop oligonucleotide probes for monitoring the physiological state of soil bacteria.

2. Study stress responses to trichloroethylene, a major contaminant at DOE sites.

3. Because over-expressing *robA* or *pspA* genes in E. coli can enhance its resistance to metal and organic solvent, we will attempt to over-express these genes in both *S. aromaticivorans* and *D. radiodurans*.

4. Further analyze all *Deinococcus* strains expressing Tbu, including Northern analysis, timing of expression, and analysis of these strains' degradative ability for trichloroethylene and toluene in pure culture studies.

References

Mulvey MR, J Switala, A Borys, and PC Loewen. 1990. "Regulation of transcription of katE and katF in Escherichia coli." *J. Bacteriol.*, 172:6713-20.

Tanaka A, H Hirano, M Kikuchi, S Kitayama, and H Watanabe. 1996. "Changes in cellular proteins of *Deinococcus radiodurans* following gamma-irradiation." *Radiation & Environmental Biophysics*, 35(2):95-99).

Wang P and HE Schellhorn. 1995. "Induction of resistance to hydrogen peroxide and radiation in *Deinococcus radiodurans*." *Can. J. Microbiol.*, 41:170-176.

Publications and Presentations

Wong KK, SM Varnum, and LM Markille. October 1997. "Genetic analysis of stress responses in *Deinococcus radiodurans* R1." Presented at the American Society for Microbiology conference on E. coli and small genomes, Snowbird, Utah.

Wong KK, SM Varnum, and LM Markille. January 1998. "Genetic analysis of stress responses in *Deinococcus radiodurans* R1." Presented at the DOE-NABIR workshop, Reston, Virginia.

Wong KK, LM Markille, P Hradecky, and SM Varnum. 1998. "Targeted mutagenesis by duplication insertion in the radioresistant bacterium *Deinococcus radiodurans*: application to the catalase gene, *katA*." Submitted for publication in the *Journal of Bacteriology*.

Molecular-Level Processes Governing the Interaction of Contaminants with Iron and Manganese Oxides

(First Year of Funding: FY 1996)

Principal Investigator

S.A. Chambers
Pacific Northwest National Laboratory
P.O. Box 999, MSIN K8-93
Richland, WA 99352
(509) 376-1766 (phone)
(509) 376-1044 (fax)
sa.chambers@pnl.gov

G.E. Brown, Jr.
Stanford University
Department of Geological and Environmental Sciences
Stanford, CA 94305-2115
(650) 723-9168 (phone)
gordon@pangea.stanford.edu

Contributors

J.E. Amonette
D.A. Dixon
T.J. Kendelewicz
S.A. Joyce
S.R. Rustad
S. Thevuthasan

Postdoctoral Associates

Ping Liu
Daniel Grolimund
N.S. Foster-Mills
Sang In Yi

Research Objective

The central tenet of this program is that *a fundamental understanding of specific mineral surface-site reactivities will substantially improve reactive transport models of contaminants in geologic systems and will allow more effective remediation schemes to be devised.* To this end, we are carrying out a program of research that focuses on the fundamental mechanisms of redox chemistry of contaminants on mineral surfaces. Because much of this chemistry in sediments involves the Fe(III)/Fe(II) and Mn(IV)/Mn(II) couples, we are focusing on mineral phases containing these species. Our approach is to conduct carefully controlled experiments on model, single-crystal Fe and Mn oxide mineral surfaces grown by molecular beam epitaxy, natural Fe oxide single crystals, and synthetic mineral powders. In this way, we can use the results from the model surfaces, which are very well defined in terms of surface composition, structure, and defect densities, to understand the results obtained on more complex mineral specimens. Likewise, we are using a variety of experimental probes, along with molecular modeling theory, to determine clean mineral surface structure and morphology, details of the chemisorption and decomposition of water, and the interface structure and redox chemistry of important contaminants such as CrO_4^{-2} on these surfaces. In what follows, we highlight the most important results obtained from June 1, 1997 to June 1, 1998.

Problem Statement

Contamination of subsurface sediments with radionuclides, organic solvents, and RCRA metals is one of the many challenging environmental problems at DOE weapons sites. Addressing this problem requires 1) accurately assessing the risks associated with these subsurface contaminants (in particular, a prediction of transport rates and degradation products in the subsurface), and 2) developing reliable and economical remediation schemes. These two activities, in turn, critically depend on an adequate understanding of the chemistry that occurs when contaminants encounter the solid surfaces (largely minerals) present in the subsurface. In addition to adsorption and precipitation at these surfaces, many of the contaminants (e.g., Pu, U, Cr(VI), CCl_4, TCE, and perchloroethylene) can undergo electron-transfer reactions that can substantially alter the species and thereby either help or hinder the remediation process. Predicting the movement of redox-sensitive contaminants through subsurface materials poses a difficult challenge, made more difficult by a lack of fundamental knowledge about the mechanisms and rates of redox reactions with exposed mineral phases. Manipulation of the redox status of aquifers, and the contaminants they contain, by the in-situ reduction of iron-bearing minerals or the addition of elemental iron are two examples of proposed remediation techniques that take advantage of redox chemistry at solid surfaces to remove contaminants from groundwater. Although these remediation techniques have shown some success in laboratory-, intermediate-, and

field-scale demonstrations, this success has been somewhat fortuitous in that little is actually known about the manner in which they work and the manner by which they might fail. Clearly, both risk assessment and remediation activities can benefit from a better understanding of the molecular-level mechanisms of redox reactions at well-defined mineral surfaces.

Research Progress

Clean Surface Structure and Morphology of Iron Oxide Surfaces

The first step in gaining a molecular-level understanding of contaminant interactions with model minerals is to understand the structure and morphology of the clean mineral surfaces with which the contaminants interact. To this end, we have employed surface-sensitive photoelectron diffraction (PED) to determine the atomic composition of the surface layer and the extent of atomic relaxation in the top few layers of α-Fe_2O_3(0001) (hematite) grown by molecular beam epitaxy (MBE) on α-Al_2O_3(0001). The XPD experiments were carried out using synchrotron radiation at the Advanced Light Source at Lawrence Berkeley National Laboratory (LBNL) to achieve as much surface sensitivity as possible. We have also used scanning tunneling microscopy (STM) at Pacific Northwest National Laboratory (PNNL) to obtain real-space images of MBE-grown Fe_3O_4(001) on MgO(001).

Detailed comparison of scanned-angle photoelectron diffraction measurements with simulations employing quantum mechanical scattering theory for trial geometries via R-factor analysis reveal that α-Fe_2O_3(0001) is terminated with a single layer of Fe atoms, and that the percentage relaxations of the first four layers are -41%, +18%, -8% and +47% of the respective bulk values. A typical set of angular distributions is shown in Figure 1, including experiment and theory with

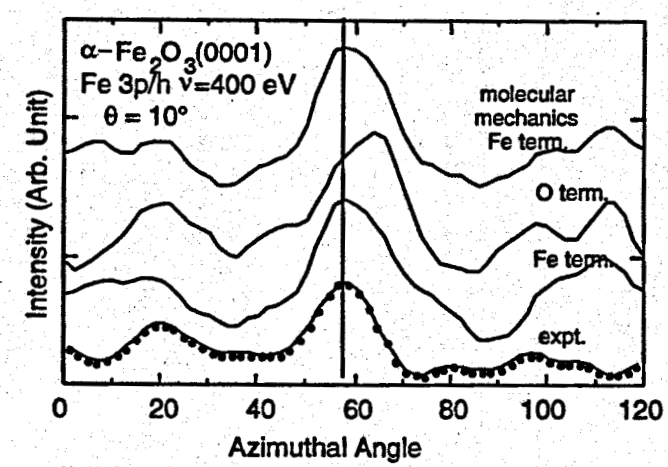

Figure 1. Photoelectron Diffraction Determination of the Surface Termination and Interlayer Relaxations of MBE Grown α-Fe_2O_3(0001) on α-Al_2O_3(0001)

Fe- and O-termination after structural optimization. This structure is in good agreement with that predicted by our molecular mechanics calculations, a PED simulation of which is also included in the figure. These rather large surface relaxations, which are similar in both magnitude and sign to those determined to exist on α-Al_2O_3(0001), are driven by the associated decrease in surface energy. We have calculated the surface energies of relaxed and bulk-terminated (unrelaxed) α-Fe_2O_3(0001) to be 1.64 and 4.24 J m^{-2}, respectively.

Several MBE-grown Fe_3O_4(001) (magnetite) surfaces have been examined using ultrahigh vacuum STM. For all samples studied, two-dimensional islands and atomic-height steps are always observed. Some notable differences in the surface topography are observed for samples grown under different conditions. The resulting step densities (defined as the ratio of the number of atoms at a step edge to the total number in the surface) can vary from as high as ~0.20 to lower than 0.05. A dramatic example of the range of step densities that can be achieved is shown in Figure 2.

For the same size scanned area, the height variation is ~9 nm for the rough film and ~1.2 nm for the smooth film, a difference of a factor of 7.5. The ability to systematically vary the step densities is crucial to ultimately understanding the role of steps in the heterogeneous chemistry that occurs on the magnetite surface. While variations in step density are observed for the different films, a number of common features have been seen for all of the samples studied. The steps and island edges are preferentially oriented along two orthogonal directions. Comparison with low-energy electron diffraction (LEED) patterns indicates that the steps run along the <110> crystallographic directions. The measured step heights are always ~2Å. The stacking of Fe_3O_4 along (001) can be thought of as alternating layers of tetrahedral Fe(III) and octahedral

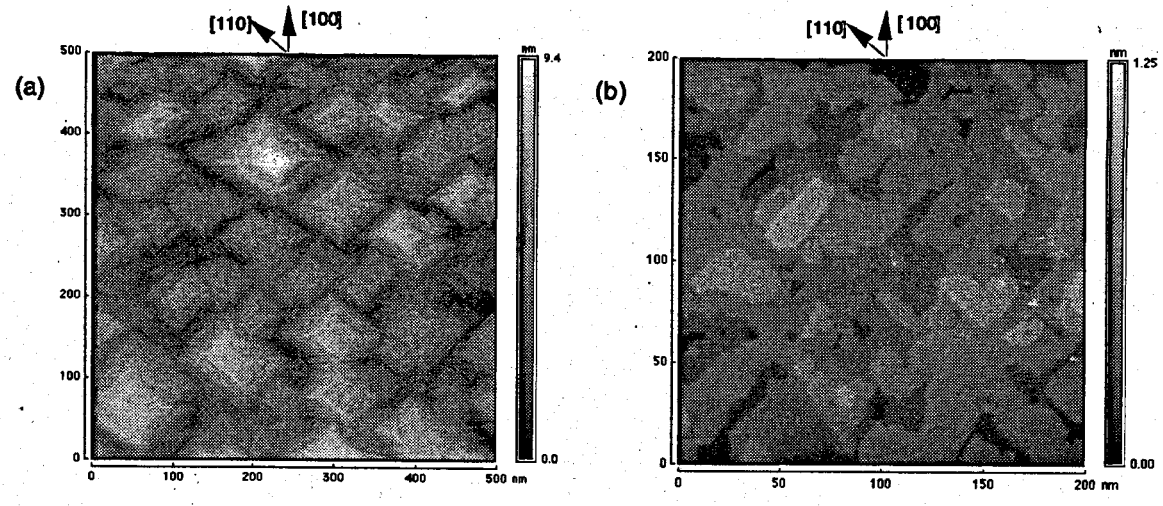

Figure 2. STM Images of (a) "Rough" and (b) "Smooth" MBE-Grown Fe_3O_4(001) on MgO(001) Using Different Growth Temperature Profiles to Achieve Different Step Densities. Notice the substantial difference in vertical relief.

Fe(II) and Fe(III) along with oxygen. The separation between these atomic layers is 1.05Å. The STM results are consistent with a model in which the (001) surface is terminated exclusively by either a tetrahedral Fe or an octahedral Fe layer, but not by both. Given that both the coordination number and the charge states of the iron in these layers are different, significant differences in the surface chemistry are expected depending upon the terminating layer.

Redox Chemistry of Chromate on Iron Oxide Surfaces

The next step in the overall goal of understanding contaminant interactions at a molecular level is to understand the effect of water—the universal solvent—on well-defined mineral surfaces. Accordingly, the interaction of water with α-Fe_2O_3 and Fe_3O_4 single-crystal surfaces has been studied using O 1s photoemission, Fe $L_{2,3}$-edge near-edge x-ray absorption fine structure (NEXAFS), and O K-edge NEXAFS data. These data have been compared with similar data for α-FeOOH (goethite) and limonite (a poorly ordered, naturally occurring iron oxyhydroxide). In addition, we have carried out parallel studies of the interaction of water with the α-Al_2O_3 surfaces because of their likely structural similarity with the same surfaces of α-Fe_2O_3. Our objective here is to gain a better molecular-level understanding of the significantly greater thermodynamic stability of the α-Fe_2O_3 surfaces relative to the α-Al_2O_3 surfaces in contact with water. In addition to these studies, we have also conducted investigations of the interaction of Cr(VI)-containing aqueous solution with vacuum-prepared α-Fe_2O_3 and Fe_3O_4 surfaces using UHV Cr L-edge, Fe L-edge, and O K-edge NEXAFS measurements and ambient Cr K-edge grazing-incidence XAFS measurements.

Photoemission (O 1s) and Fe L-edge and O K-edge XAFS data were collected on MBE-grown α-Fe_2O_3(0001) (c-plane) and (1-102) (r-plane) along with Fe_3O_4(001) on natural hematite and magnetite surfaces and on natural polycrystalline samples of goethite and limonite. The goethite and limonite data show clear signatures of OH^- groups coordinating iron that serve as fingerprints for the dissociative chemisorption of water on water-exposed hematite and magnetite surfaces (Figure 3). The measured threshold water vapor pressures for the hydroxylation of the α-Al_2O_3(0001) and α-Fe_2O_3(0001) surfaces are $\approx$ 1 Torr and $\approx 10^{-4}$ Torr, respectively. These threshold pressures are generally in agreement with results from previous experiments reported in the literature. While the measured threshold pressure for α-Al_2O_3(0001) is similar to the calculated threshold pressure for the conversion of corundum to gibbsite [$Al(OH)_3$] based on an equilibrium thermodynamic model, the measured threshold pressure for α-Fe_2O_3(0001) is more than five orders of magnitude lower than the calculated threshold pressure for the conversion of hematite to Fe-oxyhydroxide (FeOOH) or Fe-hydroxide [$Fe(OH)_3$]. We offer a possible explanation for this curious result in the molecular modeling section.

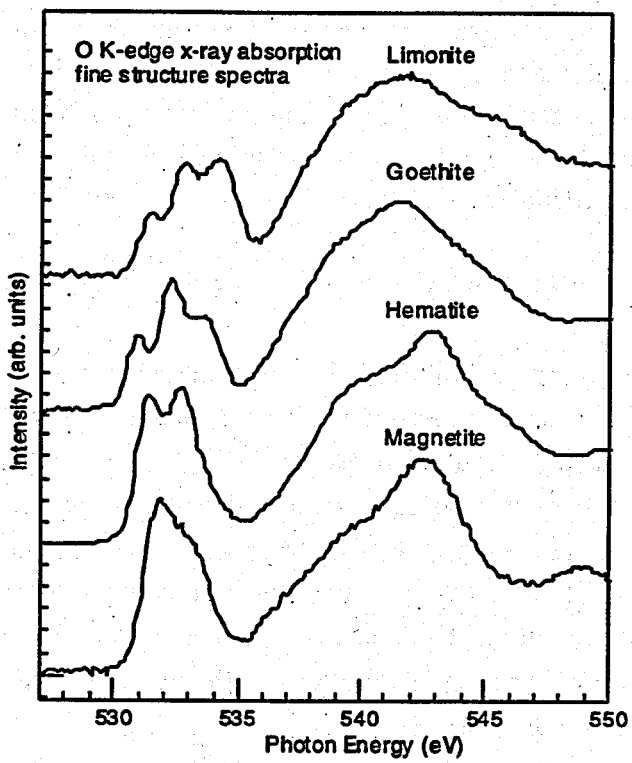

Figure 3. O K-Edge XAFS Spectra of Iron Oxides and Hydroxides

The reaction of water with (001) and (111) surfaces of natural magnetites prepared in UHV was monitored using chemical shifts of O 1s and Fe 2p core level photoemission spectra. We found that the initial reactions of water with these surfaces are quite similar to those for the (0001) and (1-102) hematite surfaces and involve dissociation of water. In fact, for all clean surfaces of hematite and magnetite examined, independent of orientation, we observed almost no water uptake for doses less than 10^5 Langmuir, indicating almost identical and small sticking coefficients for this exposure. However, there is a quantitative difference observed in O 1s photoemission spectra for clean surfaces of hematites and magnetites exposed to higher water doses at higher vapor pressures. While hydroxyl coverages for hematite remain in the submono-layer range for water doses as high as 10^9 Langmuir, the magnetite (001) and (111) surfaces react very strongly with water, resulting in hydroxylation extending several layers deep.

Moving next to the interaction of CrO_4^{-2} with iron oxides, we have performed Cr $L_{2,3}$-edge and O K-edge XAFS studies of the reaction of 5 mM Na_2CrO_4 solutions (0.1 M $NaNO_3$ background electrolyte) with various Fe oxide surfaces, including $Fe_3O_4(111)$, α-$Fe_2O_3(0001)$, and α-$Fe_2O_3(1\text{-}102)$ (see Figure 4a). Also obtained were the Cr $L_{2,3}$-edge spectra of Cr_2FeO_4 (chromite) and $PbCrO_4$ (crocoite), which serve as model compounds for Cr(III) and Cr(VI), respectively. Significant differences in the Cr(III) and Cr(VI) L-edges are observed. These differences make Cr(III) and Cr(VI) easy to identify and quantify in samples with both oxidation

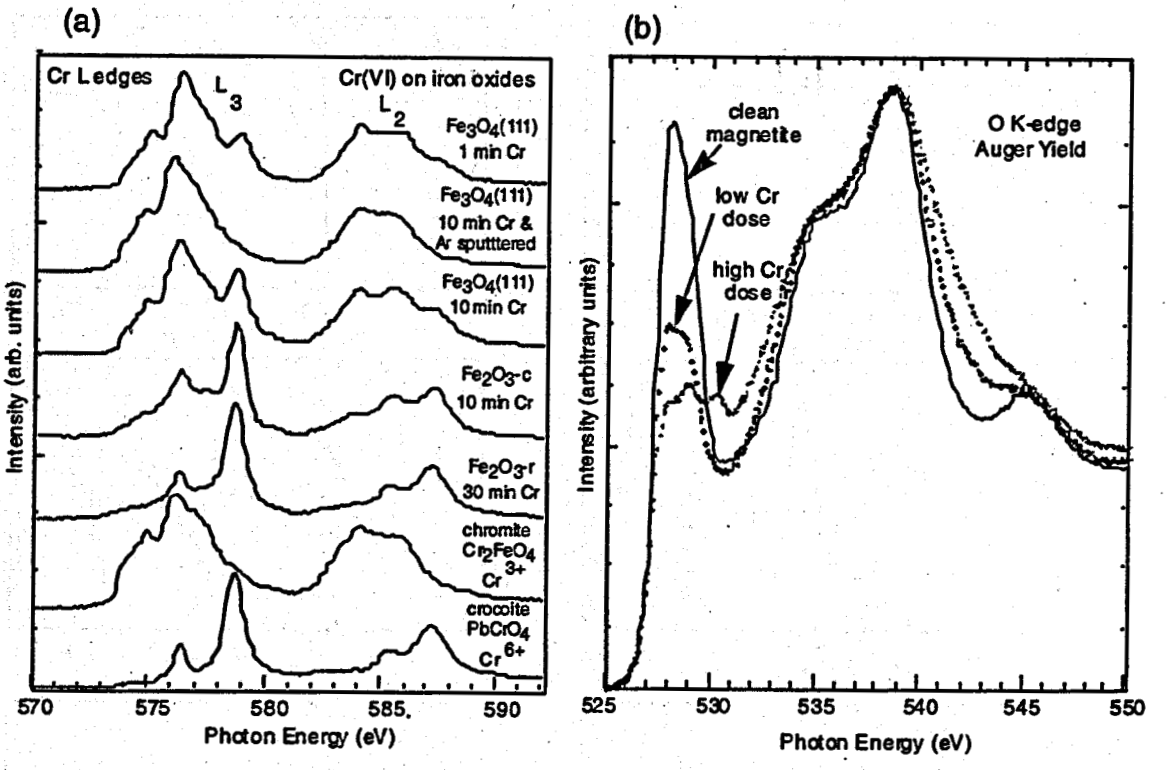

Figure 4. (a) Cr $L_{2,3}$ Edge Spectra of Cr Sorbed on Iron Oxides and Two Model Compounds; (b) O K-eEdge KLL Auger Yield for Magnetite and Cr-Dosed Magnetite

states present. Cr L-edge spectra of Fe_3O_4 (111) samples reacted with the Na_2CrO_4 solution for 1 minute in a N_2-filled glovebox connected to a gate valve on the UHV chamber showed that about 80% of the chemisorbed Cr had been reduced to Cr(III). Exposure of a Fe_3O_4(111) surface to this solution for 10 minutes, followed by Ar ion sputtering was found to produce only Cr(III) on the surface. This experiment shows that Cr(III) is more strongly bound to the surface than Cr(VI). O K-edge Auger yield data for Cr(VI)-reacted magnetite produced a spectrum (using the O KLL Auger line) having O K-edge features that look like those of goethite (c.f. Figures 3 and 4b). These data suggest that the (111) surface of magnetite converts into a goethite-like phase after reaction with a 10^{-5}M Na_2CrO_4 solution. In an earlier study by our group, a similar reaction rim found on magnetite reacted with chromate solution was found and suggested to be maghemite.

We have also completed the first grazing-incidence x-ray absorption fine structure (GI-XAFS) spectroscopy study of CrO_4^{-2} on single-crystal hematite surfaces. Chromate from a 10^{-5}-M Na_2CrO_4 solution (0.1 M $NaNO_3$ background electrolyte) was reacted with reduced thin-film hematite (0001) (heat-treated at 800°C) and unreduced (unheated) hematite (0001). The data in Figure 5 show that near total reduction of Cr(VI) to Cr(III) occurred on the reduced (0001) hematite surface (Figure 5-right), as indicated by the absence of a pre-edge feature in

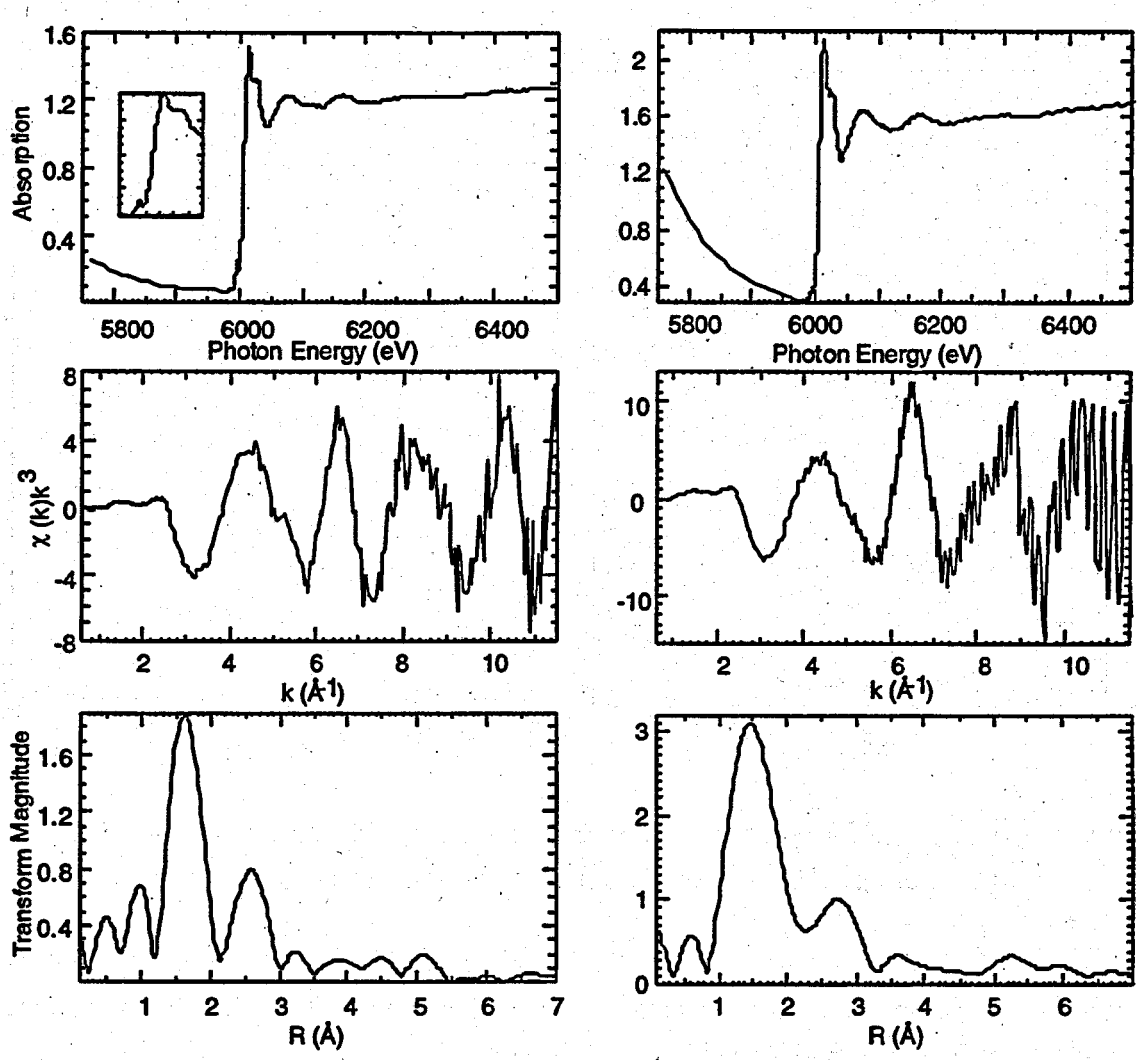

Figure 5. Grazing-Incidence Cr K-Edge XAFS Data for Aqueous Cr(VI) Reacted with: (i) an Unreduced Thin-Film Hematite (0001) Surface [left column of figures] and, (ii) a Partially Reduced Thin-Film Hematite (0001) Surface [right column of figures]. Reduction was accomplished by heating the surface in vacuum to 800°C. The pre-edge feature in the Cr K-edge spectrum for the unreduced hematite (see inset of the XANES spectrum in upper left figure) is indicative of the presence of some Cr(VI) [about 20% of the total Cr is Cr(VI) and 80% is Cr(III)], and its absence in the XANES spectrum of the partially reduced surface is indicative of little or no Cr(VI). The background subtracted and k^3-weighted EXAFS spectra are shown in the middle figures in each panel, and the Fourier transforms (FT) of these EXAFS data (FT magnitude vs. interatomic distance) are shown in the lowest figure in each panel. The distances are uncorrected for phase shifts. The first main feature in the FT in each case, centered at ≈ 1.5 Å, is due to Cr-O correlations and the second FT feature, centered at ≈ 2.6 Å, is due to Cr-Fe and possibly Cr-Cr correlations.

front of the Cr K-edge. However, considerable reduction also occurred on the unreduced hematite (0001) surface (Figure 5-left), indicating that trace amounts of Fe(II) or some other impurity reductant must be present.

Interestingly, no Fe(II) could be detected in the Fe L-edge XAFS spectra for the unreduced hematite (0001) surface, nor were any impurities detected by XPS. This puzzling result is being investigated. These EXAFS data are being analyzed to determine the structure of the Cr surface complexes and their mode of attachment to the hematite surfaces, and the present results are summarized in the caption for Figure 5. A similar GI-XAFS study of the interaction of Cr(VI) with magnetite surfaces is planned for next fall.

Kinetics of Chromate Sorption on Iron Oxide Surfaces

To examine the dynamics of contaminant chemistry with mineral surfaces, we are using pulsed laser photoacoustic spectroscopy (PLAS) to nondestructively monitor the levels of Cr(VI) in solutions contacting iron oxides. This novel technique relies on the absorption of light by the analyte and the subsequent generation of an acoustic wave from heat released as the analyte returns to the ground state. The advantage of this technique is that the data are collected without destroying any sample and can be monitored in real time, thus allowing us to perform time-resolved sorption experiments at trace levels of Cr(VI), e.g., > 1 ng mL^{-1}).

Three different types of Cr(VI) sorption experiments have been conducted using the photo-acoustic technique and powdered synthetic hematite samples. First, an adsorption isotherm was performed at pH 5.7 using an initial Cr(VI) concentration of 140 ng mL^{-1} and different amounts (2-20 mg) of hematite. The results could be fit to the Langmuir isotherm equation and yielded a maximum Cr(VI) adsorption capacity for this form of hematite of 2.5×10^5 ng g^{-1}. Assuming each Cr(VI) molecule occupies about 0.03 nm^2, maximal adsorption of Cr(VI) would cover 0.09 m^2 g^{-1}. The specific surface of the hematite, determined by the BET-N_2 method, was 6.2±0.3 m^2 g^{-1}. Thus, the fractional surface coverage of Cr(VI) on the hematite at maximum sorption was about 1.4%.

The second type of experiment involves assessing the kinetics of Cr(VI) sorption (and desorption, as prompted by displacement by phosphate). Our experiments to date have been mainly to demonstrate the feasibility of the technique (Figure 6a). The mixing kinetics in the system were on the order of five minutes (as estimated from the rate of growth of the absorbance signal when Cr(VI) was initially added to the system). The rate of adsorption was slower than the rate of mixing. Desorption kinetics, using a 25-fold more concentrated phosphate solution, were essentially indistinguishable from mixing kinetics, suggesting very rapid desorption. Slower rates are expected at lower concentrations of phosphate.

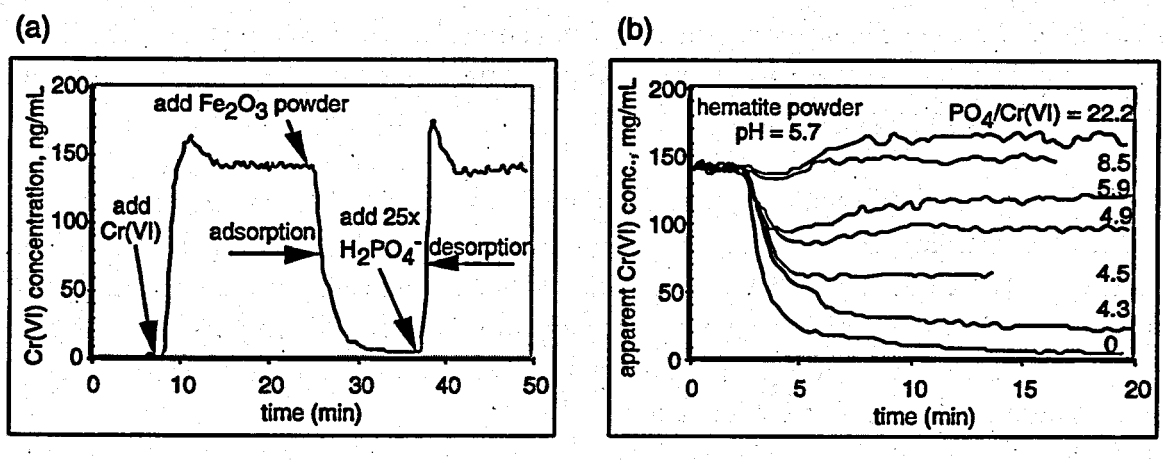

Figure 6. (a) Kinetics of Adsorption and Desorption of Cr(VI) on Hematite Powder as Measured by LPAS. Cr(VI) desorption is driven by addition of concentrated phosphate solution, which apparently displaces Cr(VI) from the hematite surface. (b) Competitive adsorption of chromate and phosphate on hematite powder. Notice that the mixture must be substantially rich in phosphate for desorption of Cr(VI) to occur.

The third type of experiment involves assessing the effects of competing anions (in this instance, phosphate) on the sorption kinetics and equilibria of Cr(VI). We observed that phosphate concentrations at least four times more concentrated than Cr(VI) were needed to affect Cr(VI) adsorption (Fig. 6b). Complete inhibition of Cr(VI) sorption was seen at phosphate levels >8 times higher. In this experiment, we also saw an apparent 7–8% increase in the Cr(VI) concentration at the highest levels of phosphate. This stems from a slight increase in the solution pH from addition of the hematite powder and a corresponding increase in Cr(VI) absorptivity.

Our current interpretation of these results is that Cr(VI) and phosphate each have sorption sites for which the individual adspecies are favored. As the phosphate concentration increases, phosphate sorption sites become occupied, and non-sorbed phosphate anions (mainly $H_2PO_4^-$) are more available to compete with Cr(VI) for the Cr(VI) sorption sites, resulting in Cr(VI) desorption. An alternative interpretation is that Cr(VI) is simply adsorbed more strongly than phosphate on hematite. This attractively simple explanation, however, runs counter to other measurements of relative phosphate and Cr(VI) adsorption affinities, as well as to our molecular-mechanics calculations, as discussed in the next section.

Molecular Modeling of Chromate/Iron Oxide Interactions

The major focus of the molecular modeling activities has been to create a molecular-level model that can be used to discriminate between possible chromate surface species present at iron-oxide-water interfaces. In constructing the model, density functional theory (DFT) calculations were carried out on $H_{(0-4)}CrO_4^{(-2+2)}$ species. DFT calculations were also used to develop

were carried out on $H_{(0-4)}CrO_4^{(-2-+2)}$ species. DFT calculations were also used to develop molecular mechanics force field parameters for describing the sorption of tetrahedral oxyanions H_nTO_4 (T=Cr, P, Si) on iron oxide surfaces. P and Si were chosen because they may be taken as rough analogs of Cr(V) and Cr(IV). Because there are few data available for these species, the utility of the concept of understanding the basicity of the T-O bond by treating various tetrahedral species as cations with formal charges needed to be tested through analog compounds. Other oxoacids (H_2SO_4, H_3AsO_4, and H_3VO_4) were also run with DFT as a check on the performance of DFT in correlating the relative acidities of these compounds. The force field is an ionic model using formal charges (H=+1, Cr=+6, P=+5, Si=+4, O=-2) with polarizable oxygen ions. The O-O and O-H parameters were taken from prior investigations of water and have been successfully applied to ferric oxide and oxyhydroxide polymorphs α-Fe_2O_3, and α,β,γ-FeOOH. The predicted surface structure of α-Fe_2O_3 (0001) agrees fairly well with that measured by photoelectron diffraction, as described previously. For the oxyanions, the ionic model accurately reproduces changes in bond lengths and energetics from the DFT calculations as the tetrahedral oxyanions are successively deprotonated from H_4TO_4 to TO_4. Both the DFT calculations and the force field model protonation/deprotonation energetics correlate well with known solution pK_a values for all species (Figure 7). The ionic model was tested against hydrated Fe(II)-Fe(III)-(Cr, P, Si)O_4-H_2O crystal structures with generally good results, yielding lattice constants within 5% of experiment. Application of the model to Fe(III)$(H_2O)_5(H_nTO_4)$ complexes shows that phosphate binds ferric iron more strongly than chromate, in agreement with experiments on complexes in aqueous solution. The ability of the ionic model to account for both the structure

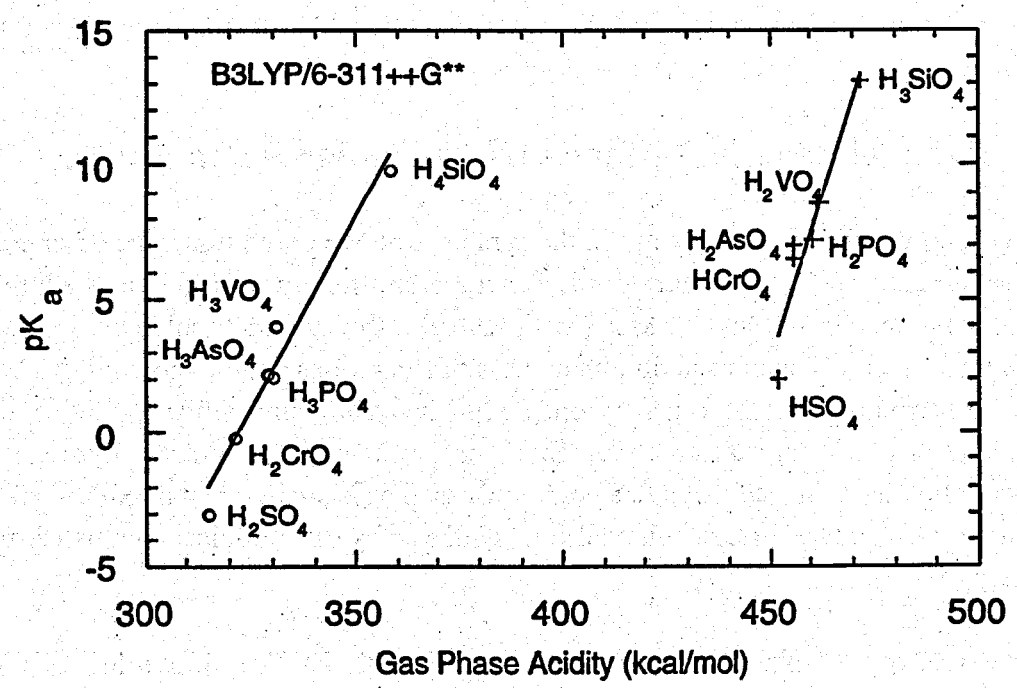

Figure 7. Measured pK_a Versus Calculated Gas-Phase Acidity for Several Oxoacids

and protonation energetics in the tetrahedral oxyanions is remarkable and makes the ionic model a feasible option for future investigation of surface complexation reactions using molecular dynamics techniques.

We have also carried out DFT calculations on the relative acidities of iron and aluminum compounds to help explain the vast differences in experimentally determined threshold hydration pressures for α-Fe_2O_3(0001) and α-Al_2O_3(0001), as discussed previously. Our initial hypothesis is that the threshold pressure is greater on the aluminum surface for the same reasons that aqueous aluminum is a weaker acid. If water at the aluminum oxide surface also dissociates less readily than on the iron oxide surface, the hydration capacity of the surface should decrease because of steric crowding of water molecules. These steric effects should be accommodated to some extent by dissociative adsorption. We have shown in other work that DFT electronic structure calculations are capable of reproducing the relative acidities of Al(III), Fe(III), and Cr(III) hexaaquo ions. These serve as analogs for singly coordinated M-OH_2 sites that presumably exist on iron and aluminum oxide surfaces. In addition, triple-coordinated M_3O sites will also exist on the surface and the proton affinities of these sites will also play a role in the uptake of water on the mineral surface. There are no direct data on the acidities of these species. Indirectly, it has been assumed that Al_3O sites are more acidic than Fe_3O sites because of differences in polynuclear speciation schemes between the two metals. To help resolve this question, we have carried out DFT electronic structure calculations on $M_3O_{13}H_{(18\text{-}19)}^{2+}$ (M=Al, Cr, Fe) on the IBM SP parallel computer using the NWChem code developed at PNNL. There was little difference in the gas-phase acidities of the M_3O sites. Therefore, the acidic $FeOH_2$ sites should govern the dissociation of water and lower the hydration threshold pressure for water on the iron oxide surface.

Growth of Model Mineral Surfaces by Molecular Beam Epitaxy

We have conducted exploratory work in the synthesis of Mn oxide films, the other class of redox-active minerals identified in our proposal as important for study. Mn oxides exhibit a range of compositions, from MnO_2 to MnO, with several stable and metastable phases occurring over this range. The most stable and dominant class of Mn oxides are the dioxides, MnO_2, of which there are two inequivalent forms, pyrolusite (β-MnO_2) and ramsdellite (γ-MnO_2). Pyrolusite exhibits a rutile crystal structure, while ramsdellite is orthorhombic. Pyrolusite is reasonably well lattice-matched to TiO_2, a commonly available single-crystal oxide surface. It is, therefore, a good candidate for thin epitaxial film synthesis by oxygen-plasma-assisted molecular beam epitaxy (MBE).

We have used oxygen-plasma-assisted MBE to grow epitaxial films of pyrolusite (β-MnO_2) on TiO_2(110) for thicknesses of 1 to 6 bilayers (BL). We define a BL to be a layer of Mn and lattice O and an adjacent layer of bridging O within the rutile structure. The resulting surfaces

have been characterized in situ with several techniques. Well-ordered, pseudomorphic overlayers form at substrate temperatures between 400 and 500°C (Figure 8). Mn-Ti intermixing occurs over the time scale of film growth for substrate temperatures in excess of 500°C. Films grown at 400–500°C exhibit classic Stranski-Krastanov growth, whereas those grown at higher temperatures are atomically flat. 1-BL films grown at 450°C form a well-ordered surface cation layer of Mn on the rutile structure with, at most, a 10% indiffusion to the second cation layer. Thicker films rapidly fall into disorder because of the simultaneous formation of pyrolusite and ramsdellite, which is orthorhombic and not lattice-matched to TiO_2(110). However, thin films of rutile pyrolusite are preferentially stabilized by the TiO_2 substrate.

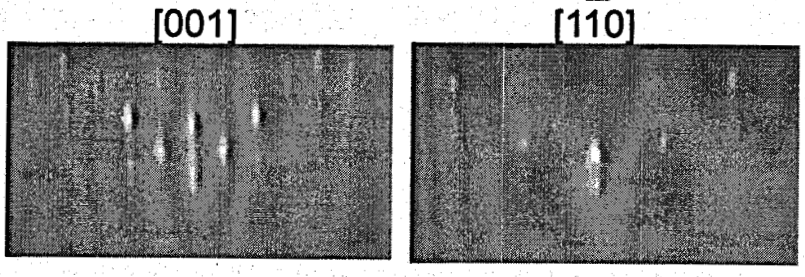

Figure 8. Reflection High-Energy Electron Diffraction Patterns for an Ultrathin Epitaxial Film of β-MnO_2 on TiO_2(110)

Summary

Work conducted under this program over the last year has concentrated on obtaining detailed, molecular-level information on the interaction of aqueous Cr(VI) and its solvent with well-defined iron oxide surfaces. Theory and experiment have been combined in a highly synergistic way. Experiment is used to validate theoretical models, and theory is then used to provide information that cannot be readily obtained experimentally and to shed light on puzzling experimental results. Insight has been gained on the sorption and redox chemistry of Cr(VI) and phosphate, a competing anion in the natural environment, on iron oxide. However, much remains to be learned over the next year, as described below.

Planned Activities

Clean and Hydrated Iron Oxide Surface Structure and Atomic Scale Morphology

Immediate future activities will focus on high-resolution imaging of the clean (2x 2)R45° reconstruction of Fe_3O_4(001) to determine which termination, the tetrahedral or octahedral, is favored and under what conditions. In particular, because the tetrahedral termination has cation vacancies whereas the octahedral termination has anion vacancies, bias-dependent imaging

should be able to distinguish between these two alternatives. It is expected that this activity will involve significant interactions with the theoretical components of this project, both in aiding in the interpretation of the STM images and in helping to refine the structures that are modeled. In conjunction with this activity, we will use low-energy photoelectron diffraction at the LBNL Advanced Light Source (ALS) to determine, via diffraction, the surface termination of Fe_3O_4(001), as well as the interlayer spacings in the near-surface region. The combination of diffraction and real-space imaging of this important surface should allow us to determine the surface structure in considerable detail.

These studies will be followed by experiments in which the Fe_3O_4 (001) surface is exposed to simple probe molecules, most notably H_2O, to directly image the role of the defects such as step edges and the ion vacancies in the adsorption.

During the summer of 1998, we will initiate crystal truncation rod (CTR) x-ray scattering studies at the Advanced Photon Source (ANL) of both sapphire and hematite (0001) and (1-102) surfaces under a humid atmosphere to provide needed information about the structure of these surfaces after exposure to water. Assuming success in this work, we will extend these CTR studies to the magnetite (001) surface under wet conditions. The results of these studies will complement the completed x-ray photoelectron diffraction studies of the clean hematite (0001) carried out at the ALS under UHV conditions and the planned XPD study of the magnetite surface.

Redox Chemistry of Chromate and TCE on Iron Oxide Surfaces

We plan to fully analyze our GI-XAFS data on the interaction of Cr(VI) on synthetic thin-film hematite samples (reduced and unreduced) collected in March 1998 and to extend these studies to Cr(VI) interactions with thin-film magnetite. This work should lead to a model of Cr(III) surface complexes on reduced hematite and magnetite. We will also continue our soft x-ray XAFS studies of Cr in other model compounds, including Cr_2O_3, CrOOH, CrO_2, and K_2CrO_4, and will examine the effect of different exposure times of a 50 μM Cr(VI) solution to magnetite (111) surfaces. We will also carry out solid-state depositions of Cr onto magnetite surfaces in UHV and study these reaction products with soft x-ray Cr L-edge, O K-edge, and Fe L-edge spectroscopy. These studies will provide additional information on changes in electronic structure of sorbed Cr on magnetite and will provide interesting comparisons with the results of our studies of aqueous solution-deposited Cr. We also plan to initiate a study of the reaction of TCE in solution with magnetite surfaces using C K-edge and Cl L-edge measurements. To provide constraints on the mechanism of the reduction reaction of Cr(VI) with magnetite surfaces, we will initiate valence bond modeling of Cr in various structures and will compare these results with those from more fundamental theoretical studies of the sorption of Cr(VI) and its reduction on magnetite surfaces. A primary objectives in this work is to provide insights to

the mechanism of Cr(VI) reduction to Cr(III) via electron transfer reactions on the magnetite surface that results in the oxidation of three Fe(II) to Fe(III). This study should also lead to predictions of sites of different reactivities on the magnetite surfaces and potential bonding arrangements of Cr(III) on the magnetite surface.

Kinetics of Chromate Sorption on Iron Oxide Surfaces

Future LPAS experiments will focus on 1) determining the absolute changes in phosphate and Cr(VI) speciation (surface and solution) that occur during the sorption process on hematite, 2) extension of this approach to understand the competitive effects of sulfate and carbonate species on Cr(VI) sorption on hematite, 3) further improvement in the time-resolution of the kinetic studies through minimization of mixing kinetics, 4) studies of Cr(VI) interactions with powdered magnetite samples, and 5) sorption kinetics and equilibria measurements for Cr(VI) sorption on the MBE-synthesized hematite and magnetite thin films at ultra-trace levels of Cr(VI).

Molecular Modeling of Chromate/Iron Oxide Interactions

Using our Fe(II,III)-(Cr, Si, P)O_4 potentials, which have now been rather rigorously tested on crystalline solids, in conjunction with our iron oxide-water potential models, we will conduct molecular dynamics investigations of chromate sorption to solvated Fe(II)-Fe(III) oxide surfaces (hematite and magnetite). These numerical experiments will generate hypothetical chromate-iron oxide surface complexes that will be used in the interpretation of both GI-XAFS and laser photo-acoustic experiments. In particular, we will calculate the affinity of chromate and phosphate to different sites known to exist on these surfaces to address the puzzling result uncovered by LPAS, as discussed earlier in this report. In addition, we will carry out energy-minimization calculations on vacuum-terminated and hydroxylated Fe_3O_4(001) surfaces to aid in the interpretation of STM images, as described above. Electronic structure calculations will be carried out on H_x(Cr(IV,V,VI)O_y) compounds to better understand the chemistry of intermediates in the process of chromate reduction.

Growth of Model Mineral Surfaces by Molecular Beam Epitaxy

Three research activities are planned, and the members of the program team will be supplied with samples for their experiments. First, we plan to determine the evolution of the surface morphology of α-Fe_2O_3(0001) on α-Al_2O_3 as a function of growth rate and crystal orientation. The large lattice mismatch of this system (5.7%) results in island growth followed by island coalescence. We seek to understand the growth mode and gain control over the resulting step density on the resulting surfaces. Doing so will enable us to tailor the surface step density so the effect of such defects on contaminant interactions can be better understood. Second, we plan to grow α-Fe_2O_3(0001) with substitutional Al impurities. Such phases are also important minerals,

and the effect of substitutional Al on the surface chemistry of α-Fe_2O_3 has never been explored in a controlled and systematic way. Finally, we will attempt to grow α-FeOOH by thin film deposition techniques using a water molecular beam, in addition to oxygen and Fe molecular and atomic beams. This mineral is ubiquitous in the terrestrial environment, and it represents a logical next step in our overall goal of understanding the behavior of relevant mineral surfaces that are sufficiently well defined, both structurally and compositionally, so as to be amenable to definitive study.

Publications

Chambers SC and SA Joyce. 1998. "Surface Termination and Reconstruction of Fe_3O_4 (001) and γ-Fe_2O_3(001)." Submitted to *Surf. Sci. Lett.*

Chambers SA and Y Liang. 1998. "Growth of Ultrathin β-MnO_2 on TiO_2(110) by Oxygen-Plasma-Assisted Molecular Beam Epitaxy." Submitted to *Surf. Sci.*

Foster NS, JE Amonette, and ST Autrey. 1998. "In-Situ Detection of Chromate Using Photoacoustic Spectroscopy." Submitted to *Analytical Chemistry.*

Foster NS, ST Autrey, JE Amonette, JR Small, and EW Small. 1998. "Laser Photoacoustic Spectroscopy—What is it Good For?" Submitted to *American Laboratory.*

Gao Y, YJ Kim, and SA Chambers. 1998. "Preparation and Characterization of Epitaxial Iron Oxide Films." Submitted to *J. Mat. Res.*

Kendeleweicz T, P Liu, GE Brown Jr., EJ Nelson, and SA Chambers. 1998. "Near Ledge Study of Adsorption of Cr^{6+} from Liquid Solution on Hematite and Magnetite Surfaces." Submitted to *Surf. Sci.*

Liu P, T Kendelewicz, GE Brown Jr., EJ Nelson, and SC Chambers. 1998. "Reaction of Water with α-Al_2O_3 and α-Fe_2O_3 (0001) Surfaces: Synchrotron X-ray Photoemission Studies." Submitted to *Surf. Sci.*

Rustad JR and DA Dixon. 1998. "Density Functional Calculations of the Acidities of Oxyanions." Submitted to *J. Chem. Phys.*

Rustad JR and DA Dixon. 1998. "Surface hydrolysis of Fe, Cr, and Al oxides," in preparation.

Rustad JR and DA Dixon. 1998. "The Effectiveness of an Ionic Model Describing Oxyanion Sorption on Ferric Oxide Surfaces," in preparation.

Thevuthasan S, DE McCready, W Jiang, YJ Kim, Y Gao, SA Chambers, NR Shivaparan, and RJ Smith. 1998. "Rutherford Backscattering and Channeling Studies of Epitaxially Grown Iron Oxide Films on Various Substrates," in preparation.

Thevuthasan S, YJ Kim, SA Chambers, P Liu, T Kendelewicz, GE Brown, J Morais, R Denecke, and CS Fadley. 1997. "The Surface Structure of α-Fe_2O_3(0001) by Low Energy X-Ray Photoelectron Diffraction." *Advanced Light Source Compendium of User Abstracts and Technical Reports*, in press. Also submitted to *Surf. Sci.*, in press.

Thevuthasan S, W Jiang, DE McCready, and SA Chambers. 1998. "Rutherford Backscattering and Channeling Studies of Mg and Fe Diffusion at the interface of γ-Fe_2O_3(001)/MgO(001)," in preparation.

Trainor TP, JP Fitts, D Grolimund, JR Bargar, S Chambers, and GE Brown Jr. 1997. "Grazing-Incidence XAFS Studies of Adsorption Complexes at Metal Oxide-Water Interfaces." *1997 Activity Report*. Stanford Synchrotron Radiation Laboratory, Palo Alto, California, in press.

Presentations

Chambers SA, S Thevuthasan, YJ Kim, SA Joyce, and Y Liang. August 1998. "Surface Structure Determination of MBE Grown Iron and Manganese Oxides." National Meeting of The American Chemical Society, Boston, invited.

Chambers SA. June 1998. "Epitaxial Growth of Ultrathin β-MnO_2 on TiO_2(110) by Oxygen-Plasma-Assisted Molecular Beam Epitaxy." 20th Surface Analysis/10th Annual Pacific Northwest AVS Symposium, Richland, Washington.

Chambers SA. May 1998. "Surface and Interface Structure of MBE-Grown Fe and Mn Oxides." Naval Research Laboratories, Washington D.C., invited.

Chambers SA. May 1998. "Surface and Interface Structure of MBE-Grown Fe and Mn Oxides," Department of Physics, University of Maine, Orono, Maine, invited.

Foster-Mills NS, JE Amonette and SA Chambers. June 1998. "Aqueous Sorption of Cr(VI) on Hematite Using Laser Photoacoustic Spectroscopy." 20th Surface Analysis/10th Annual Pacific Northwest AVS Symposium, Richland, Washington.

Grolimund D, T Kendelewicz, TP Trainor, P Liu, JP Fitts, and GE Brown Jr. August 1998. "Identification of Cr Species at the Solution-Hematite Interface after Cr(VI)-Cr(III) Reduction Using GI-XAFS and Cr L-edge NEXAFS." *Xth International XAFS Conference*, Chicago.

Jiang W, S Thevuthasan, YJ Kim, SA Chambers, GS Herman, DE McCready, NR Shivaparan, and RJ Smith. March 1998. "Mg and Fe Diffusion at the γ-Fe_2O_3(001)/MgO Interface." American Physical Society March Meeting, Los Angeles.

Jiang W, S Thevuthasan, DE McCready, and SA Chambers. June 1998. "Rutherford Backscattering and Channeling Studies of Mg and Fe Diffusion at the Interface of γ-Fe_2O_3(001)/MgO(001)." 20th Surface Analysis/10th Annual Pacific Northwest AVS Symposium, Richland, Washington.

Joyce SA and SA Chambers. June 1998. "The Microscopic Structure of Iron Oxide Surfaces." June 1998. 20th Surface Analysis/10th Annual Pacific Northwest AVS Symposium, Richland, Washington.

Kendelewicz T, P Liu, GE Brown Jr., and EJ Nelson. August 1998. "Reaction of Water with (100) and (111) Surfaces of Magnetite (Fe_3O_4)." *14th International Vacuum Congress*, Birmingham, UK.

Kendelewicz T, P Liu, GE Brown Jr., EJ Nelson MI McCarthy, and SA Chambers. August 1998. "Spectroscopic Studies of the Reaction of Water with Metal Oxide Surfaces." Goldschmidt Conference, Toulouse, France.

Kendelewicz T, P Liu, GE Brown Jr., EJ Nelson, and SA Chambers. August 1998. "Reaction of Water with Clean (0001) and (1-102) Surfaces α-Fe_2O_3 " *14th International Vacuum Congress*, Birmingham, UK.

Kendelewicz T, P Liu, GE Brown Jr., EJ Nelson, and SA Chambers. August 1998. "Reduction of the (0001) Surface of Hematite (α-Fe_2O_3) Prepared Under UHV Conditions." *14th International Vacuum Congress*, Birmingham, UK.

Kendelewicz T, P Liu, GE Brown Jr., EJ Nelson, and SA Chambers. August 1998. "Fe $L_{2,3}$ and O K Near Edge Structure of Iron Oxides and Hydroxides." *14th International Vacuum Congress*, Birmingham, UK.

McCready DE, S Thevuthasan, W Jiang, YJ Kim, Y Gao, SA Chambers, NR Shivaparan, and RJ Smith. June 1998. "Rutherford Backscattering and Channeling Studies of Epitaxially Grown Iron Oxide Films on Various Substrates." 20th Surface Analysis/10th Annual Pacific Northwest AVS Symposium, Richland, Washington.

Rustad JR and DA Dixon. April 1998. "Surface hydrolysis of Fe, Cr, and Al oxides." Physical Chemistry Division, University of Washington, Seattle, invited.

Rustad JR. June 1998. "The Effectiveness of an Ionic Model Describing Oxyanion Sorption on Ferric Oxide Surfaces." Annual Symposium of the Clay Minerals Society, invited.

Thevuthasan S, GS Herman, YJ Kim, YGao, SA Chambers, NR Shivaparan, RJ Smith, BJMorris, and TT Tran. October 1997. "Ion Scattering Studies of Epitaxially Grown Iron Oxide Films on MgO and Al_2O_3 Substrates." 44th National Symposium of the American Vacuum Society, San Jose, California.

Thevuthasan S, YJ Kim, SA Chambers, P Liu, T Kendelewicz, DE Brown Jr, J Morais, R Denecke, and CS Fadley. March 1998. "Surface Structure Determination of Hematite Using Low-Energy X-Ray Photoelectron Diffraction." American Physical Society March Meeting, Los Angeles.

Thevuthasan S, YJ Kim, SA Chambers, P Liu, T Kendelewicz, GE Brown Jr, J Morais, R Denecke, and CF Fadley. June 1998. "The Surface Structure Determination of α-Fe_2O_3 by Intermediate-Energy X-Ray Photoelectron Diffraction." 20th Surface Analysis/10th Annual Pacific Northwest AVS Symposium, Richland, Washington.

Mineral Surface Processes Responsible for the Decreased Retardation (or Enhanced Mobilization) of ^{137}Cs from High-Level Waste Tank Discharges

(First Year of Funding - FY 1997)

Principal Investigator:

Dr. John M. Zachara
Pacific Northwest National Laboratory
P.O. Box 999, MSIN K8-96
Richland, WA 99352
(509) 376-3254 (phone)
(509) 376-3650 (fax)
jm_zachara@pnl.gov

Co-Principal Investigators:

R. Jeffrey Serne
Pacific Northwest National Laboratory
P.O. Box 999, MSIN K6-81
Richland, WA 99352
(509) 376-8429 (phone)
(509) 376-5368 (fax)
rj_serne@pnl.gov

Dr. Paul D. Ellis
Pacific Northwest National Laboratory
P.O. Box 999, MSIN K8-98
Richland, WA 99352
(509) 372-3888 (phone)
(509) 376-2303 (fax)
pd_ellis@pnl.gov

Dr. Paul M. Bertsch
University of Georgia
Savannah River Ecology Laboratory
P.O. Drawer E/Bldg 737A
Aiken, SC 29801
(803) 725-2472 (phone)
(803) 725-3309 (fax)
bertsch@srel.edu

Research Objective

Experimental research will determine how the sorption chemistry of cesium (Cs) on vadose zone sediments changes after contact with solutions characteristic of high-level wastes (HLW) in underground storage tanks at the Hanford Site. The central hypothesis is that the high ionic strength of tank wastes (i.e., > 5 mol/L $NaNO_3$) will suppress all surface-exchange reactions of Cs except those to the highly selective frayed edge sites (FES) of the micaceous fraction. We further speculate that the concentrations, ion selectivity, and structural aspects of the FES will change after contact with the harsh chemical conditions of HLW and that these changes will be manifest in the macroscopic sorption behavior of Cs. We believe that migration predictions of Cs can be improved substantially if such changes are understood and quantified.

The research will integrate studies of ion exchange thermodynamics on the FES with high-resolution surface microscopies and spectroscopy to probe the structure of FES in Hanford sediments and to describe how the chemical environment of sorbed Cs changes when HLW supernatant liquids promote silica dissolution and aluminum precipitation. Newly available atomic force microscopies and high-resolution electron-beam microscopies afford previously unavailable opportunities to visualize and characterize FES. The overall goal is to provide knowledge that will improve transport calculations of Cs in the tank farm environment by

- Identifying how the macroscopic sorption behavior of Cs on the micaceous fraction of the Hanford sediments changes after contact with simulants of HLW tank supernatants over a range of relevant chemical ([OH], [Na], [Al], [K, NH_4]) and temperature conditions (23°–80°C).

- Reconciling observed changes in sorption chemistry with microscopic and molecular changes in adsorption-site distribution, chemistry, mineralogy, and morphology/structure of the micaceous sorbent fraction.

- Integrating mass-action-solution-exchange measurements with changes in the structure/site distribution of the micaceous-sorbent fraction to yield a multicomponent/site-exchange model relevant to high ionic strength and hydroxide concentrations for predicting environmental Cs sorption.

Problem Statement

Environmental Management Concerns

- Single-shell tanks (SSTs) containing HLW have leaked supernatant liquids containing large amounts of radioactive ^{137}Cs (10^6 Ci) and other contaminants into the Hanford vadose zone.

- In select locations ^{137}Cs has exhibited "expedited" migration (up to 50 m when predicted migration distances are <10 m) saturated zone. The reasons for "expedited" migration are unclear.

- Deep ^{137}Cs migration has been observed beneath the SX tank farm at Hanford with redox wastes as the carrier, causing significant regulatory and stakeholder concern.

Scientific Context

- Micaceous 2:1 layer silicates are the primary environmental sorbents of Cs. Cs^+ is strongly sorbed by specific structural sites on these solids that exhibit nanometer scale dimensions with unique steric and geometric attributes.

- Micaceous 2:1 layer silicates exist as a small mass fraction of Hanford vadose zone sediments. These are known to impart significant Cs^+ sorptivity to Hanford subsurface sediments.

Science Issues

- Redox wastes were self-concentrating by boiling and contain molar plus concentrations of Na^+, NO_3^-, OH^-, and $Al(OH)_4^-$. The sorption behavior of Cs^+ from this complex waste matrix is not known.

- The chemical composition and temperature of the redox wastes is harsh and will induce dissolution and precipitation reactions upon contact with Hanford vadose zone sediments, possibly changing mineral surface structure and the selectivity of the micaceous fraction for Cs^+. The extent, kinetics, and impacts of these reactions on contaminant fixation and migration are unknown.

- No literature information exists upon which to base scientifically credible estimates of Cs^+ adsorptive-retardation beneath SSTs that have leaked high pH/high ionic strength waste waters.

Research Progress

The project was initiated in September 1997. Research has been directed into two areas of study that involve 1) contaminated materials from Hanford borehole SX-41-09-39 collected near waste tank SX-109, and 2) the Cs retention characteristics of a mica-containing composite sediment from the Hanford formation.

SX-109. Our central research hypothesis was that surface chemical reaction of Cs with the micaceous fraction in the Hanford sediments was the adsorption reaction responsible for Cs retardation from tank wastes. Furthermore, we speculated that changes to the micaceous fraction resulting from chemical interaction with HLW components would decrease the extent and strength of Cs adsorption to this phase. We thought it prudent to first verify the central tenet of our research by examining sediments that were contaminated with ^{137}Cs obtained beneath tank SX-109, an SST containing self-boiling redox wastes that had leaked HLW supernatant liquids into the Hanford vadose zone.

Three samples were obtained from the upper levels of borehole SX-41-09-39 in December 1997. The coring was a DOE-EM-supported activity that extended the borehole beneath SX-109 from 39.6 m to 65 m (5 m below groundwater) to define the distribution of HLW components in the vadose zone. The three Cs-contaminated samples each contained in excess of 10^4 pCi/g ^{137}Cs. These ^{137}Cs concentrations are about 10^4-10^6 times lower than those expected in sediment immediately proximate to tank leakage points. Shown in Figure 1 are representative results from one of the samples (2C/2D collected at 133.2-ft depth). The material was fine-grained (48% was silt size or less), and ^{137}Cs was distributed variably through the different particle size fractions. On a pCi/g basis the highest concentrations were observed in the medium sand (7.22×10^4 pCi/g). Mica grains were clearly evident in the sand and silt fractions. Taking into account the mass percent of the different particle size fractions, it was concluded that the silt and clay was the primary repository of ^{137}Cs in terms of the whole sediment (e.g., 60% of the radioactivity was found there, as shown in Figure 1).

The cation exchange capacity of the contaminated sediments was measured, and it was found that ^{137}Cs occupied only a small fraction of the exchange sites in spite of high radioactive content. For example, the exchange capacity of 2C/2D was 134 meq/kg, and the ^{137}Cs concentration (3.41×10^4 pCi/g) represented slightly less than 1% of the total exchange capacity on a meq/kg basis. The mineralogic content of the particle size fractions of 2C/2D was determined by x-ray

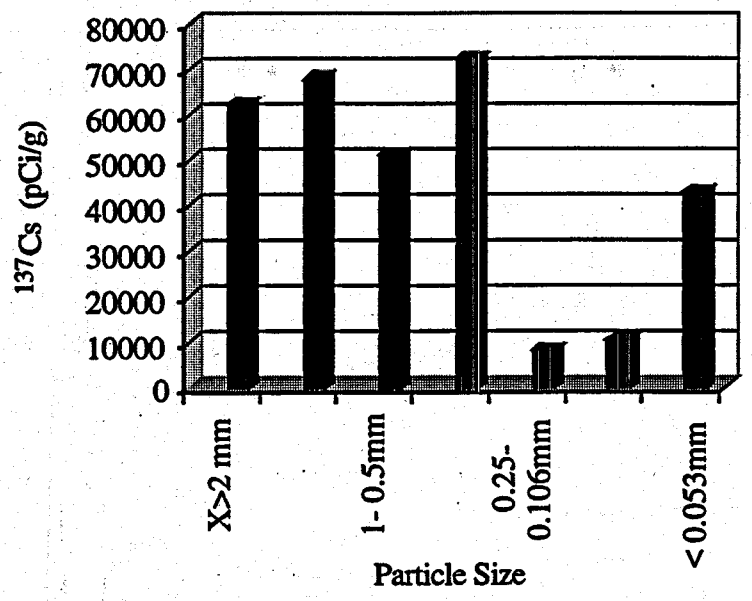

	mass%	pCi/g - ^{137}Cs	pCi/g - %
x > 2 mm	2.15	62200	3.92
very coarse sand	2.58	68000	5.14
coarse sand	3.48	51300	5.23
medium sand	1.92	72200	4.06
fine sand	12.8	8010	3.00
very fine sand	28.0	10700	8.77
silt/clay	47.9	42800	60.0
bulk sample		34150	

Figure 1. Characteristics of ^{137}Cs-Contaminated Materials from Hanford Site (Borehole SX-41-09-39 at 133.2 ft)

diffraction (XRD). Each fraction contained approximately 10–15% mica, and the silt-clay comprised 40–50% mica, micaceous weathering products (vermiculite), and other phyllosilicates (kaolinite and smectite) (Figure 2). Diffraction peaks for mica, which is known to fix Cs^+, were clearly evident, implicating it as the primary sorbent. Mineralogic transformations or precipitates originating from reaction with OH^- or $Al(OH)_4^-$ present in the SST supernate were not observed

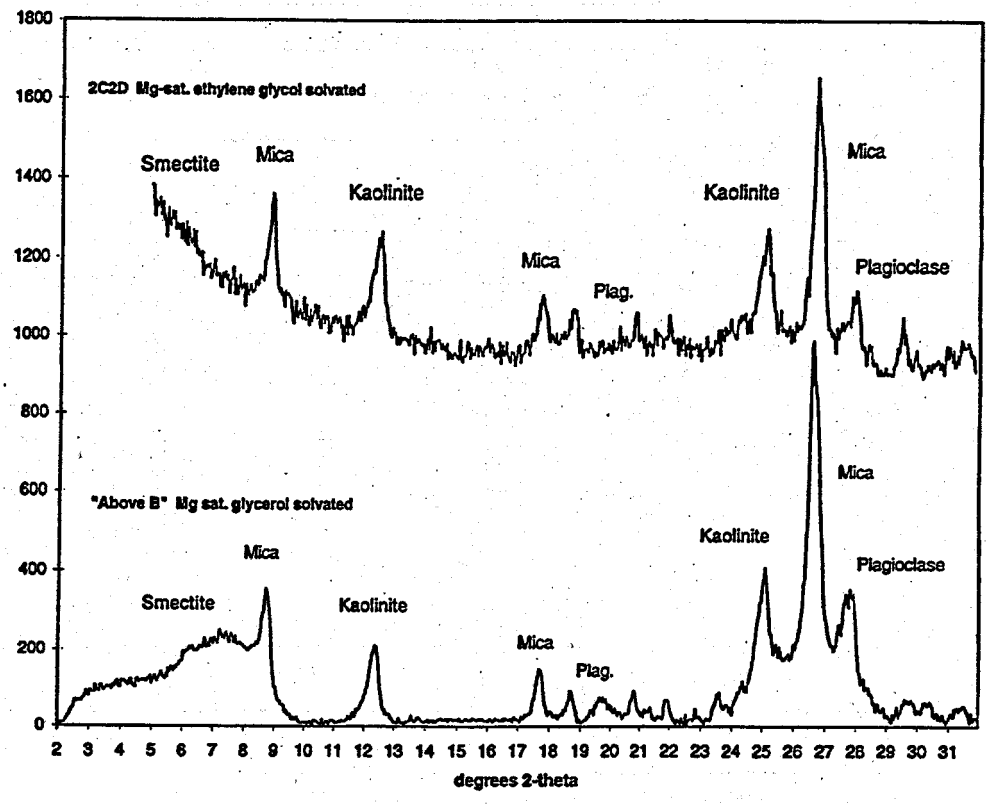

Figure 2. X-Ray Diffractograms of Clay-Sized Isolates (<2 μm) of 2C/2D (4.28×10^4 pCi/g ^{137}Cs) and 'Above B' Hanford Sediments

because the sample originated from a depth that was distant from the pH neutralization front. The XRD traces for the clay fraction from 2C/2D were virtually identical to the XRD patterns for clay from the uncontaminated 'Above B' composite sediment that is discussed below. The contaminated samples were equilibrated in water to determine the concentration of soluble HLW constituents. Not only were these constituents present in low concentrations, but the ^{137}Cs was found to be virtually undesorbable in 10^{-3} mol/L Na^+ electrolyte. Additional experiments are planned to assess the desorption issue.

Above B Sediment. A bulk reference sample (≈ 20 kg) that was representative of the 50–100-ft depth interval in the Hanford formation of 200 West Area was obtained by compositing 250–500 g subsamples of cores that were collected during the placement of RCRA monitoring wells around the southern end of the SX tank farm. Core subsamples from these boreholes were saved at the Hanford core library. The composited materials were not contaminated, and these were taken from core depth intervals above the B-contact in the upper Hanford formation. The sediments are Pleistocene age (13,000–700,000 yBP) silty sands of glacio-fluvial origin.

Several characterizations have been performed on the 'Above B' composite, including particle size distribution, mineralogy, and chemical composition. Others under way include cation exchange capacity with different index ions and surface area. The sediments are of complex mineralogy, reflecting diverse geologic provenance of granitic, metamorphic, and basaltic terrains. Most significant to this project is the mica content and mineralogy and that of the associated expansible 2:1 layer silicate fraction (vermiculite, smectite). Micas are present in all size fractions from coarse to fine. Their mass content through sand and silt is relatively constant at 10–20%, increasing to over 40% in the clay-sized fraction (<2 μm). The micas are of three general types (Figure 3): muscovite, biotite, and vermiculitized biotite, and these appear uniformly distributed through most particle size fractions. Smectite, which is presumed to be detrital in origin, is a significant component of the clay fraction.

Cs^+ interaction experiments have been performed on two materials (<63 μm and 125–250 μm) from the composite to investigate if the sorption behavior of Cs^+ is sensitive to mica particle size. Cs^+ sorption to the <63 μm sediment was highly sensitive to Na^+ concentration and occurred rapidly (Figure 4). Identical behavior was noted for the 125–250 μm sediment (not shown). Significant long-term uptake of Cs^+, often reported by others, was not observed. Rather, there was a long-term trend toward desorption of sorbed Cs^+ that was more pronounced at lower Na^+ concentrations. This desorption was accompanied by an increase in $K^+_{(aq)}$ resulting from feldspar dissolution. The results were qualitatively consistent with an initial rapid ion exchange reaction:

$$NaX + Cs^+ = CsX + Na^+$$

where X is an equivalent of isomorphic surface charge associated with the 2:1 layer silicate fraction, followed by back exchange with K^+,

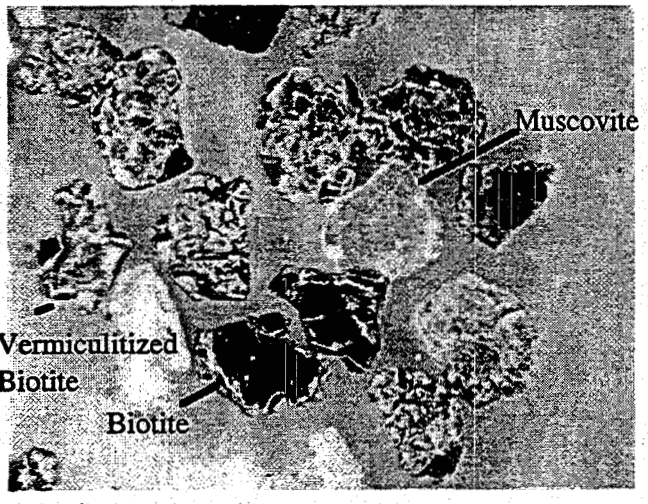

Figure 3. Sand-Sized Mica Grains Form Hanford Sediments

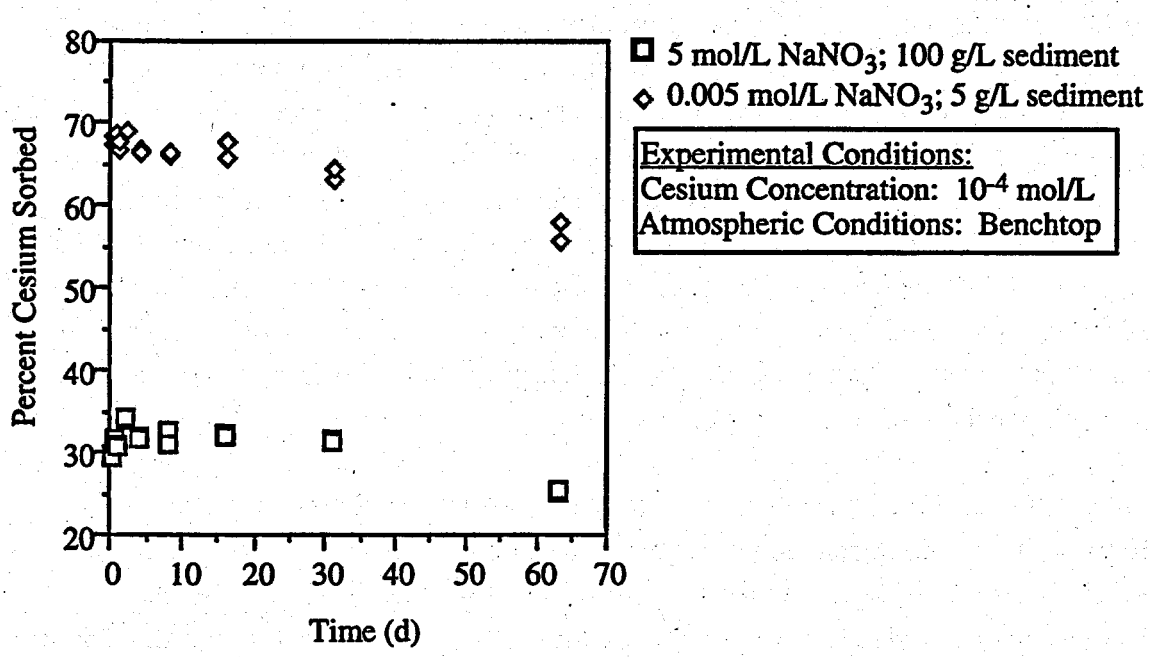

Figure 4. Time-Dependent Cesium Sorption on Ringold 'Above B' Sediment; <63 μm Size Fraction

$$CsX + K^+ = KX + Cs^+.$$

The ion exchange process with respect to Na^+ was investigated over a concentration range that was relevant to HLW discharge: $Na^+ = 0.005$ to ≈ 9 mol/L (saturated $NaNO_3$) and $Cs^+ = 10^{-7}$ to 10^{-2} mol/L (Figure 5). The two particle sized fractions, and presumably the sorbing micaceous fraction within them, exhibited nearly identical behavior with respect to both Na^+ and Cs^+ concentration. The coarser material exhibited less sorption of Cs^+ than did the fine fraction, as expected from surface area considerations. The resulting isotherms (Figure 5a) exhibited a slope <1, indicating that Cs^+ sorption strength decreased with increasing concentration. Mass distribution coefficients [K_d = (mol/g - Cs)/(mol/L - Cs)] are a commonly used measure of solid-liquid partitioning and sorption strength. Distribution coefficients derived from the isotherm data (Figure 5b), showed no regions of constancy but uniformly decreased with increasing Cs^+ concentration, implying that sorption sites in the sediment are heterogeneous in their affinity for Cs^+.

Not readily discernable from the log-log plots in Figure 5 was that high salt very much suppressed the ion-exchange sorption reaction of Cs^+. Distribution coefficients for Cs^+ in high-salt solution are shown in Figure 6. To reinforce the magnitude of the salt effect, it was observed that the high value noted for the Cs-K_d with the <63 μm fraction in 5 mol/L $NaNO_3$ was 135, but

A.) Sorbed Versus Final Aqueous Concentration

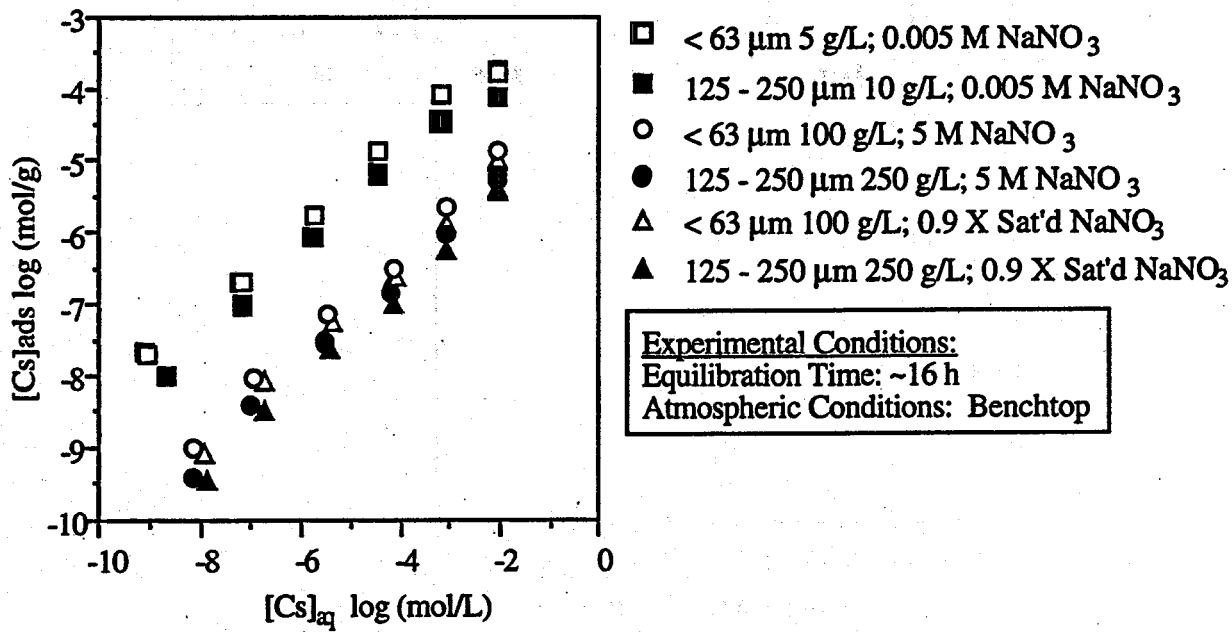

B.) K_d Versus Final Aqueous Concentration

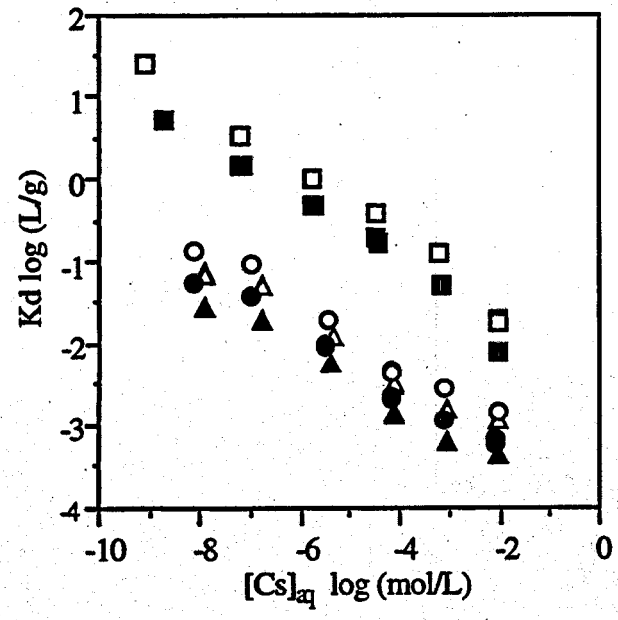

Figure 5. Cesium Sorption on Hanford 'Above B' Size Fractions in 0.005 mol/L, 5 mol/L, and Saturated $NaNO_3$ Electrolyte

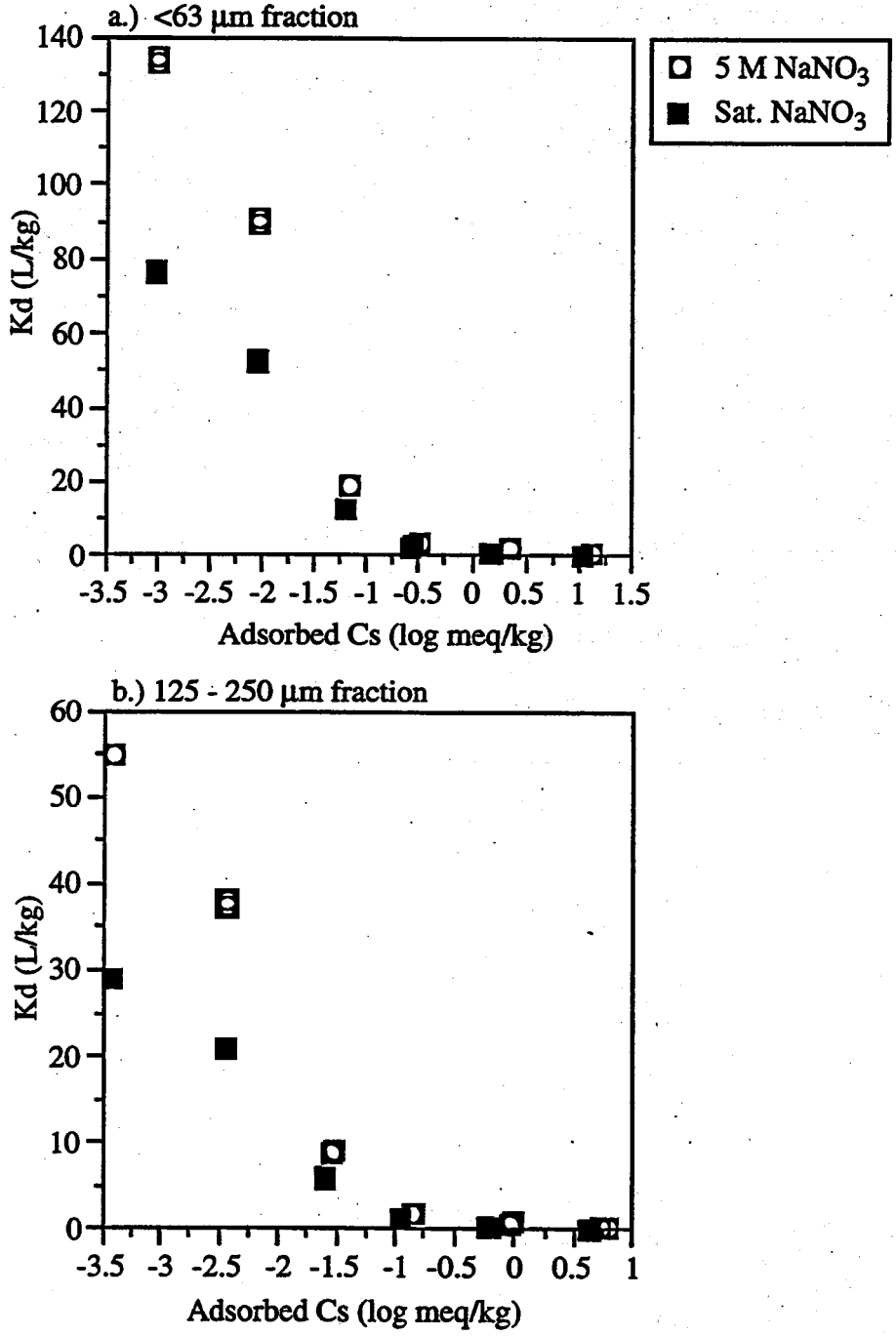

Figure 6. Distribution Coefficients for Cs^+ on 'Above B' Particle-Size Separates in High Salt Solution (5 mol/L and saturated $NaNO_3$)

it was 25,000 in 0.005 mol/L $NaNO_3$ at an identical Cs concentration (not shown). Unexpectedly high K_d's were observed at Cs^+ surface concentrations below 10^{-1} meq/kg in high-salt solution, as expected from surface area considerations. The resulting isotherms (Figure 7a) exhibited a slope <1, indicating that Cs^+ sorption strength decreased with increasing concentration. Mass distribution coefficients [K_d = (mol/g - Cs)/(mol/L - Cs)] are a commonly used measure of solid-liquid partitioning and sorption strength. Distribution coefficients derived from the isotherm data (Figure 7b), showed no regions of constancy but uniformly decreased with increasing Cs^+ concentration, implying that sorption sites in the sediment are heterogeneous in their affinity for Cs^+.

a. Microscopic Image

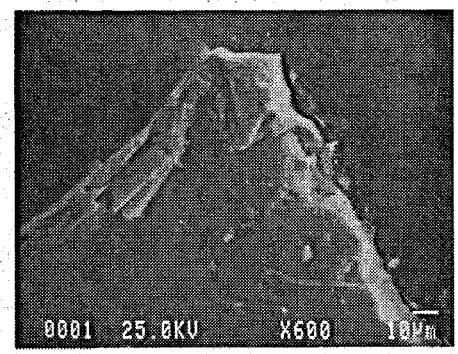

b. Cs^+ Distribution

Figure 7. Electron Microscopic and Backscattered Cs^+ Images of Cs^+-Treated Muscovite from the 'Above B' Composite

Planned Activities

During the remainder of FY 1998, researchers will complete experiments and modeling for two manuscripts: one on the mineralogic residence and desorbability of ^{137}Cs in contaminated Hanford vadose zone sediments and the other on Cs sorption thermodynamics and kinetics in the 'Above B' sediment. The latter manuscript will require 1) Cs^+ x-ray absorption measurements on Hanford micas with different Cs^+ concentrations and after different contact times, and 2) development of a high ionic strength, multicomponent ion-exchange model for Cs^+.

FY 1999 activities will focus on the impacts of high-base, variable-temperature-induced mineral dissolution on Cs^+ sorption in Hanford sediments and isolated mica fractions. We will identify whether the selectivity of the mica fraction for Cs^+ is changed by molar concentrations of hydroxide and whether changes result from competitive ion effects (e.g., K^+ release by dissolution) or structural destabilization of the FES. The latter issue will be resolved by application

of scanning probe microscopy and high-resolution transmission electron microscopy. In FY 2000, similar studies will be performed using high-base waste stimulants containing $Al(OH)_4^-$ at the same concentrations as those in the SSTs. At issue is whether $Al(OH)_4^-$ precipitation that follows base neutralization will cause marked changes to Cs^+ sorption selectivity, kinetics, and reversibility. Important questions to be resolved include the nature of the precipitated Al phase and whether it causes hydroxy pillaring and alteration of the structural environment of the FES. A combination of microscopy, solution-phase thermodynamic measurements, and chemical modeling will be used to interpret results and resolve hypotheses.

Presentations

Zachara JM. March 10, 1998. "^{137}Cs Geochemistry in the Hanford Vadose Zone." Presented to the Hanford Vadose Zone Expert Panel Review, Richland, Washington.

Serne RJ. March 10, 1998. "Characterization of Sediments from the SX-41-09-39 Borehole Extension." Presented to the Hanford Vadose Zone Expert Panel Review, Richland, Washington.

Serne RJ, and JM Zachara. September/October 1998. "Sr and Cs Adsorption to Hanford Sediments Underlying Leaking Single Shell Tanks." 41st Annual Meeting of the Association of Engineering Geologists, Seattle, Washington.

Health Effects

Mechanisms Involved in Trichloroethylene-Induced Liver Cancer: Importance to Environmental Cleanup

(First Year of Funding: FY 1996)

Principal Investigator

Richard J. Bull, Ph.D.
Pacific Northwest National Laboratory
P.O. Box 999, MSIN P7-56
Richland, WA 99352
(509) 373-6218 (phone)
(509) 376-6767 (fax)
Dick.bull@pnl.gov

Co-Investigator

Brian D. Thrall
Pacific Northwest National Laboratory
P.O. Box 999, MSIN P7-56
Richland, WA 99352
(509) 376-3809 (phone)
Brian.thrall@pnl.gov

Contributors

Lyle B. Sasser (PNNL)
John H. Miller (PNNL)
Irvin R. Schultz (PNNL)

Research Objective

The objective of this project is to develop critical data for changing risk-based cleanup standards for trichloroethylene (TCE). Cleanup costs for chlorinated solvents found on U.S. Department of Energy (DOE) sites are most frequently driven by TCE because it is both the most widespread contaminant and is generally present at the highest concentrations. Data that would permit increases in risk-based standards for TCE would reduce complex-wide cleanup costs by several billion dollars. The U.S. Environmental Protection Agency (EPA) is reviewing its risk assessment for TCE. Dr. Richard J. Bull, Pacific Northwest National Laboratory, is working with EPA on this review. Scheduling tasks in the project is carefully keyed to the final rulemaking process to ensure that the data generated have the greatest potential benefit to DOE.

Problem Statement

The main impetus for this research is that recent data indicate that TCE induces a shift in the mutation spectra observed in the H-ras codon 61 in mouse liver tumors. Such effects have been generally interpreted as indicating that the chemical is acting as a mutagen. However, data obtained in this project argue strongly that selection (or promotion) is most likely involved.

The project is organized around two interrelated tasks:

Task 1 addresses the tumorigenic and dosimetry issues for the metabolites of TCE that produce liver cancer in mice, dichloroacetate (DCA) and trichloroacetate (TCA). Early work had suggested that TCA was primarily responsible for TCE-induced liver tumors, but several more mechanistic observations suggest that DCA may play a prominent role. This task is aimed at determining the basis for the selection hypothesis and seeks to prove that this mode of action is responsible for TCE-induced tumors. This project will supply the basic dose-response data from which low-dose extrapolations would be made.

Task 2 seeks specific evidence that TCA and DCA are capable of promoting the growth of spontaneously initiated cells from mouse liver in vitro. The data provide the clearest evidence that both metabolites act by a mechanism of selection rather than mutation. These data are necessary to select between a linear (i.e., no threshold) and nonlinear low-dose extrapolation model.

Research Progress

Tumorigenesis Studies

Biologically based models for assessing health risk from TCE exposure will be useful only if it can be firmly established which metabolite is responsible for the carcinogenic effects of TCE and the likely mode of action by which this metabolite(s) operates. A key argument that DCA is the metabolite primarily responsible for TCE-induced liver tumors is that the incidence and spectra of H-ras mutations are similar in tumors induced by DCA and TCE (Anna et al. 1994).

We have now sequenced codon 61 of the H-ras protooncogene in a total of 30 TCA-induced and 64 DCA-induced liver tumors. The TCA-induced tumors were examined at a single time point and dose (2 g/L for 52 weeks), whereas DCA-induced tumors were obtained at 0.5 and 2 g/L and at 52 and 87 weeks. Literature data have been derived primarily from mice treated for a full two years. Our data are provided in Figure 1. First, the mutation frequency observed in TCA-induced tumors is not dissimilar from that of control animals. This frequency, however, is distinct from that observed with other peroxisome proliferators (Maronpot et al. 1995). Moreover, for the purposes of this project, the mutation spectra are not consistent with that observed with TCE (fraction of tumors positive for AAA = 0.16, CGA = 0.13, CTA = 0.22). In contrast to

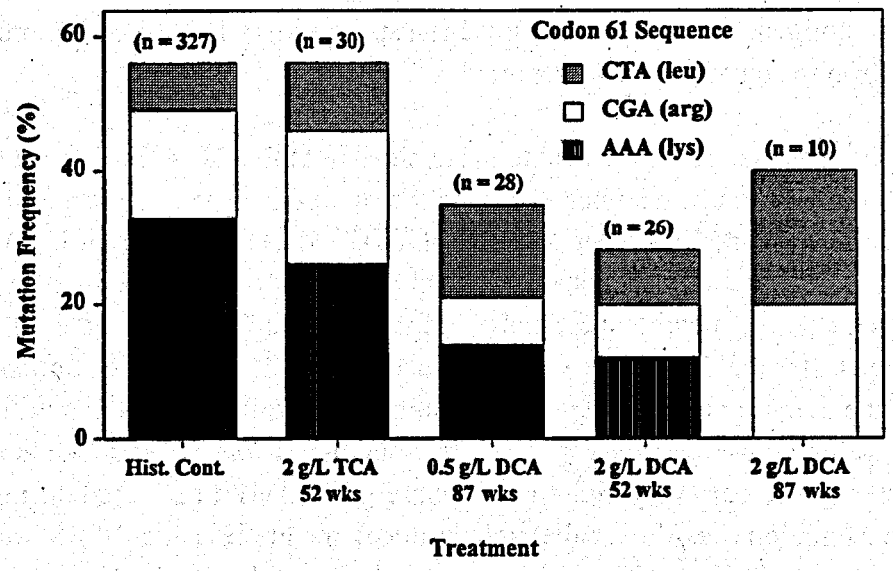

Figure 1. Mutation Frequency and Spectra from Tumors Induced by Carcinogenic Metabolites of Trichloroethylene, Trichloroacetate (TCA) and Dichloroacetate (DCA). Historical control frequency and spectra is taken from Maronpot et al., 1995.

previously published data (Anna et al. 1994; Fereira-Gonzalez et al. 1996), however, the mutation frequency obtained in DCA-induced tumors at these early time points were significantly below those observed with TCE and DCA. However, a relative enhancement of the CTA mutation appears as was previously reported. These discrepancies suggest that mutation in H-ras codon 61 appears to be a late event in mouse liver tumorigenesis and certainly not sufficient basis for the tumorigenic response. This conclusion is supported by the observations that the mutation frequency increases with duration of treatment with DCA and that the mutated forms of H-ras are expressed in only some of the cells within the tumor. Therefore, changes in H-ras mutation frequency and spectra do not provide evidence that DCA or TCE are acting by a genotoxic mechanism.

An initiation/promotion study was designed to determine whether DCA- or TCA-induced liver cancer is caused by mechanisms that select a particular H-ras genotype. Three chemical initiators were selected that give rise to liver tumors when injected into B6C3F1 neonatal mice. Vinyl carbamate (VC) induces tumors with H-Ras-61-leu mutation, N-hydroxy-2-acetylaminofluorene (N-OH-2-AAF) produces the H-Ras-61-lys mutation, and diethylnitrosamine (DENA) produces tumors without H-ras mutations. DCA apparently does selectively increase the size of lesions carrying a CTA mutation (produced by initiation with vinyl carbamate) relative to its increase in tumor numbers. Increases in size and number were proportional with the other tumor initiators that had other impacts on the mutation spectra in H-ras-61. TCA did not produce any evidence of selectivity toward tumors induced by any initiator. These data are consistent with our original hypothesis. However, it may allow a basis for evaluating the extent to which DCA contributes to the tumorigenesis of TCE if the mutation spectra in TCE-induced tumors in our ongoing study confirm the data previously reported.

Pharmacokinetic results: Issues related to the dosimetry of the DCA that is produced from the metabolism of TCE have become much clearer in the past year. There are two issues: 1) the amount of DCA that is generated from a given dose of TCE and 2) the amount of DCA that must be in the liver to induce a carcinogenic response. As previously reported, DCA treatment results in substantial decreases in the metabolic clearance of the compound when mice are on chronic treatment at the high doses that have been used to induce cancer. Considerable confusion has been generated in the literature concerning the actual blood levels of DCA that result from the metabolism of TCE. In the past year it was discovered that blood concentrations induced by 2 g DCA/L of drinking water are very high (approximately 500 μM) if measured during the period of water consumption (i.e., during the night in mice) and are less than 10 μM during the day. Lowering the concentration in drinking water by only four-fold to 0.5 g/L resulted in peak concentrations of only 2-5 μM during the night but were immeasurable during the day (limit of quantitation = 1 μM). This is because the metabolism of DCA at these low doses is extremely rapid over the range of 5-10 minutes. A concentration of 0.5 g/L of drinking water gives rise to an 80% tumor incidence in mice when administered for a lifetime; thus it indicates that low

systemic concentrations of DCA are sufficient to induce cancer. Data from our initiation/ promotion studies indicate that 0.1 g DCA/L does not induce cancer. Concentrations of DCA seen in the blood from a dose of 1000 mg/kg TRI (the lowest carcinogenic dose tested by the National Toxicology Program) are maximally 1-2 μM. The key question is the dose of DCA that is in the liver. This problem is illustrated in Figure 2. The curves are hypothetical blood and liver concentration profiles that might be observed with mice drinking water at the levels identified based upon our preliminary data. At doses that saturate (or inhibit metabolism), the concentrations in the liver and blood should be approximately equal. As doses decrease, however, the amount in blood will become a much less accurate indication of the concentration in the liver, because a large fraction of the DCA will be metabolized as it passes through the liver. To understand the dosimetry of DCA derived from TCE treatment, a PBPK model needs to be developed that describes the conversion of TCE to DCA in the liver and then accounts for the concentration of DCA in the liver before it diffuses into the systemic circulation. This latter parameter can be estimated only by determining the rate of hepatic clearance of DCA when it is administered. This effort goes significantly beyond the goals of the present project. Thus the resources available are not sufficient to provide a model that deals comprehensively with the clearance, but approximations have been sufficient to allow estimates of the maximum concentrations of DCA that might be formed in mice, rats, and humans. We have proposed follow-on studies to deal with the diurnal variation issue in response to the Low-Dose Initiative of the Office of Biological

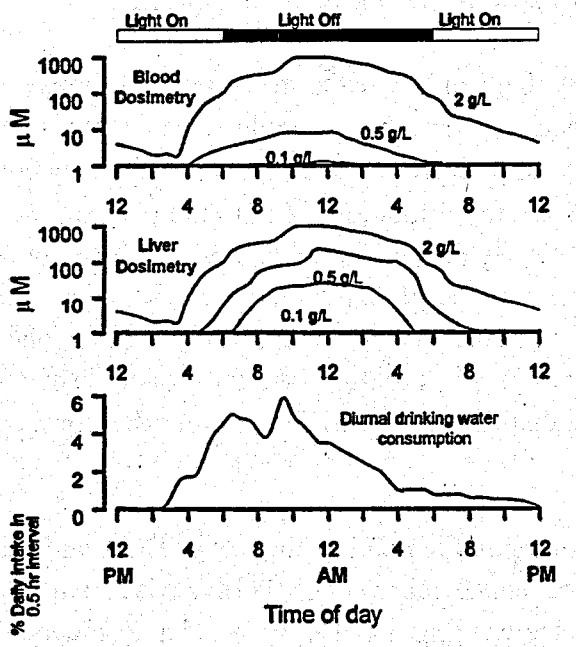

Figure 2. Hypothetical Relationships Between Drinking Water Consumption, Concentrations of DCA in Drinking Water, and Blood and Liver Concentrations of DCA in B6C3F1 Mice. Blood levels from 0.5 and 2 gL treatments reflect fluctuations actually measured.

and Environmental Research (OBER). However, the data that will be finalized in this project should provide an upper bound on the contribution DCA might make to the carcinogenic response to TCE.

Establishing Selective Advantage as a Mode of Action for DCA and TCA

An important issue with the hepatocarcinogenic activity of TCE in mice revolves around the contribution of DCA and TCA to this response at both high and low doses. The hypothesis in this program is that neither metabolite causes tumors by a genotoxic mode of action but rather through promoting the clonal expansion of preexisting initiated (precancerous) cells. If this is correct, it becomes important to determine which proposed metabolite has the potency necessary to account for the tumor-promoting activity of TCE.

The potency of a nongenotoxic tumor promoter depends on the ability of the compound to stimulate the survival and replication of initiated cells, and measuring this effect requires the actual isolation of initiated cells. A reliable characteristic of initiated cells is the ability to proliferate under anchorage-independent conditions such as in culture over soft agar. Although growth over soft agar has been extensively studied using continuous cell lines (which are by definition already initiated), less is known about the response in primary cells.

We have established an assay that can be used to measure the response of initiated primary hepatocytes to putative carcinogens in vitro. For example, hepatocytes isolated from male B6C3F1 mice four weeks after a single injection of a tumor-initiating (genotoxic) agent show an increase in anchorage-dependent colony formation after culture over soft agar (Figure 3). The number of colonies formed was clearly dependent on the initiator dose. Furthermore, DNA sequence analysis of colonies formed after N-OH-2-acetylaminofluorene initiation demonstrate that the colonies contain a significant increase in mutations in the H-ras oncogene, consistent with the known mutagenic activity of this initiator (data not shown). Thus both genetic and dose-response evidence indicate that the hepatocellular colonies that form over agar are truly "initiated" cells.

The assay was also used to measure the relative potency of DCA and TCA to promote the clonal growth of initiated hepatocytes (Stauber et al. 1998). As is shown in Figure 4, incubation of hepatocytes from untreated mice with TCA or DCA caused a dose-dependent increase in anchorage-independent colonies that form over soft agar. Both DCA and TCA were about equally effective in promoting colony formation in vitro. In vitro, the effective concentration of either haloacetate to promote an increase in colony formation was between 200 and 500 μM. Furthermore, analysis of gene expression markers on DCA- or TCA-promoted colonies indicated

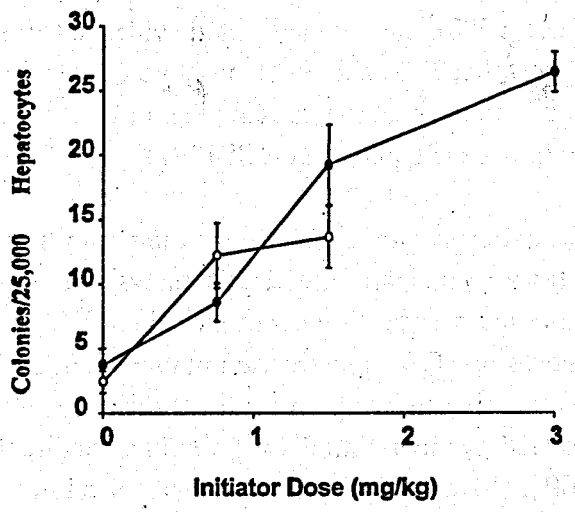

Figure 3. Effects of Initiators on Hepatocellular Colony Formation. Hepatocytes from male B6C3F1 mice were given a single injection of either vinyl carbamate (closed symbol) or acetylaminofluorene (open symbol). After four weeks, hepatocytes were isolated and the number of anchorage-independent colonies that formed over agar was determined after 10 days in culture.

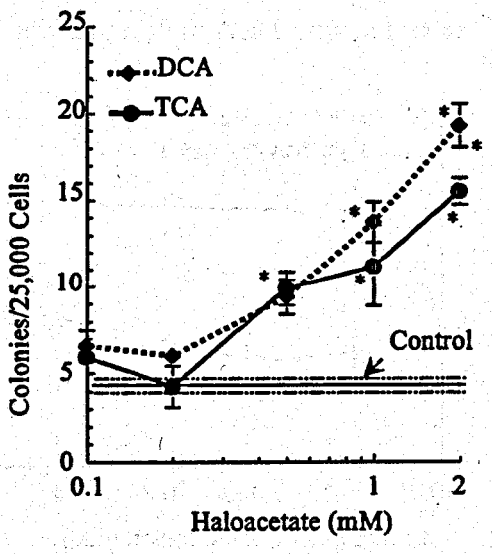

Figure 4. Effect of DCA and TCA on Anchorage- Independent Hepatocellular Colony Formation In Vitro. Hepatocytes were isolated from untreated mice and cultured over agar in the presence of the DCA or TCA for 10 days. The number of anchorage-independent colonies was scored by microscopy. *Differs from untreated control ($p < 0.05$).

that the phenotype of these colonies reflects the phenotype of tumors promoted by chronic exposure in vivo (Stauber et al. 1998). Given the limited evidence for mutagenicity by these chemicals, these studies suggest that TCA and DCA promote the survival and growth of different populations of spontaneously initiated hepatocytes (Stauber et al. 1998), similar to previous reports for chronic in vivo exposure (Stauber and Bull 1997).

Although DCA and TCA exposures are equally potent in promoting anchorage-independent growth in vitro, comparing these results with the kinetic analysis of potential DCA and TCA formation after TCE exposure raises a question about the role of DCA in tumors induced by TCE. At the carcinogenic doses of TCE typically used in bioassays, sustained blood concentrations of ≥200 μM TCA are easily achieved. In contrast, such concentrations of DCA are neither measurable nor predicted by kinetic models. Even in mice directly exposed to DCA, blood levels of DCA of >200 μM are reached for a transient period immediately after exposure (Kato-Weinstein et al. 1998). Thus, the in vitro sensitivities of primary hepatocytes to TCA appear to support a greater role for TCA than DCA as the primary carcinogenic metabolite of TCE.

There may be a component of DCA-induced tumor promotion in vivo that is not accounted for by in vitro experimentation. This was confirmed when we examined hepatocellular colony formation over agar with hepatocytes isolated from mice pretreated for two weeks with a minimal carcinogenic dose of DCA (0.5 g/L) in drinking water (Figure 5). Surprisingly, hepatocytes isolated from mice that were pretreated with DCA in drinking water were dramatically

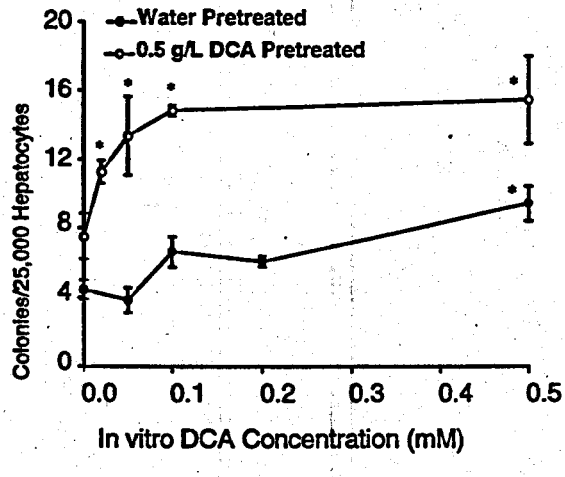

Figure 5. Effect of in vivo DCA Pretreatment on the Sensitivity of Hepatocytes to Subsequent in vitro DCA Exposure. Hepatocytes were isolated from mice pretreated with either water or 0.5 g/L DCA in water for two weeks. The cells were then cultured over agar in the presence of 0-0.5 mM DCA for 10 days, and anchorage-independent colonies were scored. * Differs from controls lacking DCA in vitro ($p < 0.05$).

sensitive to subsequent in vitro DCA treatment than hepatocytes isolated from untreated mice. In hepatocytes isolated from DCA-pretreated mice, an increase in colony formation above untreated controls was observed with only 20 μM DCA in vitro. For comparison, concentrations ≥200 μM DCA were necessary to stimulate colony formation in hepatocytes from naïve mice, indicating that DCA pretreatment in vivo caused an increase in hepatocellular sensitivity by ≥10-fold. Still, if 20 μM DCA is a minimally effective concentration to promote the clonal expansion of initiated cells during chronic exposure, it is an order of magnitude greater than the limit of quantitation for DCA in the blood of mice or that predicted to occur from TCE exposure.

As indicated above, the rapid metabolism of DCA suggests blood concentration is not necessarily a good indicator of tissue levels for this putative metabolite. Therefore, additional studies of the rate of formation of DCA in liver tissue are needed before direct comparisons of potency can be made between TCA and DCA. Future studies will focus on whether sufficient concentrations of DCA are formed in the liver after TCE exposure to promote clonal expansion or the predominant promoting activity is the result of TCA formation.

We have also discovered that substantial increases in serum insulin concentrations are associated with DCA treatment in mice, but only at the lowest dose that is effective in inducing tumors and during the nighttime hours (see Figure 6). This is something missed in our earlier studies and in the clinical studies that have been conducted with DCA. In part this is because the effects that occur at high doses used therapeutically completely mask this response, probably through a feedback loop. Increases in insulin concentrations and their impacts would not be well modeled by our in vitro experiments. In addition, this result provides a mechanistic basis for the large accumulations of glycogen that occur at the lower doses of DCA. Recent reports have associated increased serum insulin concentrations with occupational exposures to trichloroethylene (Goh et al. 1998). Insulin can also contribute to the tumorigenic effects of DCA as the tumors induced by DCA express high levels of insulin receptors, and insulin is known to act as a weak mitogen and as a suppressor of apoptosis. Experiments are being conducted to determine whether this response is specific to DCA or if it is also observed with TCA to see if this may be a discriminator of the relative activity of these metabolites in TCE-induced liver cancer.

Structural bases of selectivity: Ras proto-oncogene products are membrane-associated guanine nucleotide-binding proteins that couple growth regulatory signals from cell surface tyrosine-kinase receptors to cytoplasmic second messenger pathways. Agents that elevate cyclic AMP (cAMP) activity can block stimulation of the MAP kinase pathway by oncogenic Ras. We have investigated through modeling whether there might be a structural basis of the selection of

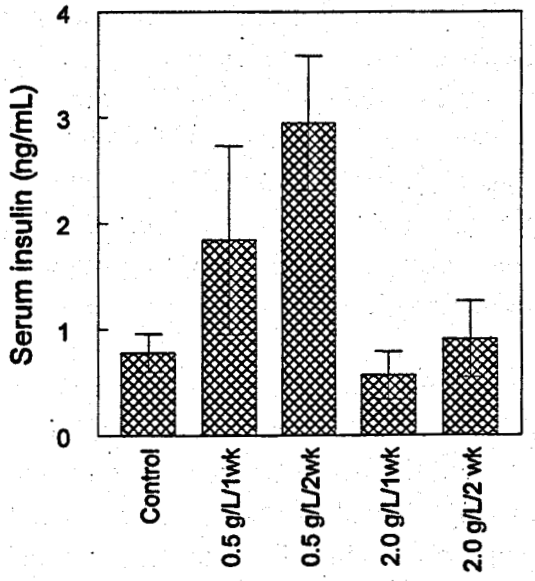

Figure 6. Effects of Dichloroacetate in Drinking Water on Serum Insulin Concentrations at 3 AM (i.e., during the period of active water consumption)

the CTA mutation in H-ras-61 by DCA and TCE. Essentially, we believe this to involve differences in charged and uncharged mutants that affect the affinity of Ras for its effector due to phosphorylation of Raf-1 at serine 43 by protein kinase A. Follow-on funding is being sought under the Low-Dose Initiative of the Office of Biological and Environmental Research (OBER).

Implications for EM

This research identifies two plausible modes of action by which TCE produces liver tumors in mice. These modes of action do not require the compounds to be mutagenic. The bulk of the experimental evidence suggests that neither TCE nor the two hepatocarcinogenic metabolites are mutagenic. The results from the colony formation assay clearly establish that these metabolites cause colony growth from initiated cells that spontaneously occur in the liver of B6C3F1 mice. In the case of DCA, a second mechanism, involving the release of insulin, occurs at a lower dose. However, this has not yet been shown to be responsible for liver tumor induction. This is being pursued with a proposal to the Low-Dose Initiative advertised by the OBER. Even if this is shown to be responsible for the tumors at lower doses of TCE, it involves modification of normal endocrine function. Because doses are decreased to levels that do not induce these increases, there should be no risk from this metabolite either. Therefore, there is clearly a rational basis for considering a margin of exposure for low-dose extrapolation of liver cancer risks for TCE based on our results.

Technical questions still arise from whether TCA or DCA is primarily responsible for the induction of liver cancer. If TCA could be shown solely responsible for the tumors, it would simplify the argument for low-dose extrapolation. There are two reasons for this. First, the EPA has already received advice that risks from peroxisome proliferators should be dealt with by the margin of exposure rather than the linear low-dose extrapolation; and second, TCA does not induce liver tumors in rats. However, even if DCA is formed in mice and contributes to the development of liver tumors, its formation is much lower in other species, including the human (data from our previous SERDP proposal on chloral hydrate and other work on volunteers by our colleagues at Wright Patterson Air Force Base). In addition, our data demonstrate that it is acting by a promoting mechanism.

Dr. Richard J. Bull, a member of our research team, is preparing the final draft on the mode of action paper being used by EPA as a test case for their new Proposed Cancer Risk Assessment Guidelines. The arguments discussed above have been generally accepted by EPA and will form the basis for their decision. Since kidney tumors in rats are also produced with TCE, the effect of this work will be to change the potency estimate from that derived from liver tumor induction in the mouse to kidney tumor induction in mice. This should decrease the estimated risk per unit dose by approximately 10-fold. Informal discussions have been conducted with the Office of Water of the EPA. If the new guidelines are adopted in treating liver tumor induction by TCE, they intend to determine whether the drinking water MCL will need to be revised.

References

Anna CH, RR Maronpot, MA Pereira, JF Foley, DE Malarkey, and MW Anderson. 1994. *Carcinogenesis,* 15:2255-2261.

Block C, R Janknecht, C Herrmann, N Nassar, and A Wittinhofer. 1996. "Quantitative structure-activity analysis correlating Ras/Raf interaction in vitro with Raf activation in vivo." *Nature Struct. Biol.,* 3:244-251.

Ferreira-Gonzalez A, AB DeAngelo, S Nasim, and CT Garrett. 1995. *Carcinogenesis,* 16:495-500.

Goh VH-H, SE Chia, and CN Ong. 1998. "Effects of chronic exposure to low doses of trichloroethylene on steroid hormone and insulin levels in normal men." *Environ. Health Persp.,* 106:41-44.

Hafner S, HS Adler, H Mischak, P Janosch, G Heidecker, A Wolfman, S Pippig, M Lohse, M Ueffing, and W Kolch. 1994. "Mechanism of inhibition of Raf-1 by protein kinase A." *Mol. Cell. Biol.*, 14:6696-6703.

Maronpot RR, T Fox, DE Malarkey, and TL Goldsworthy. 1995. "Mutations in the *ras* proto-oncogene: clues to etiology and molecular pathogenesis of mouse liver tumors." *Toxicology,* 101:125-156.

Nassar N, H Gudrun, C Herrmann, C Block, R Janknecht, and A Wittinhofer. 1996. "Ras/Raf effector specificity determined by charge reversal." *Nature Struct. Biol.*, 3:723-724.

Stauber AJ and RJ Bull. 1997. "Differences in phenotype and cell replicative behavior of hepatic tumors inducted by dichloroacetate (DCA) and trichloroacetate (TCA)." *Toxicol. Appl. Pharmacol.*, 144:235-246.

VanRenterghem B, MD Browning, and JL Maller. 1994. "Regulation of mitogen-activated protein kinase activation by protein kinases A and C in a cell-free system." *J. Biol. Chem.*, 269:24666-24672.

Publications

Kato-Weinstein J, MK Lingohr, BD Thrall, and RJ Bull. 1998. "Effects of dichloroacetate on carbohydrate metabolism in B6C3F1 mice." Submitted to *Toxicology.*

Merdink JL, A Gonzalez-Leon, RJ Bull, and IR Schultz. 1998. "The extent of dichloroacetate formation from trichloroethylene, chloral hydrate, trichloroacetate, and trichloroethanol in B6C3F1 mice." *Toxicological Sciences*, in press.

Mounho BJ, AJ Stauber,, RJ Bull, and BD Thrall. 1998. "Peroxisome proliferator-induced activation of extracellular signal-regulated kinase (Erk) pathway contributes to hepatocellular clonal expansion." Submitted to *Carcinogenesis.*

Orner GA, JA Malone, LC Stillwell, RS Cheng, AJ Stauber, L Sasser, BD Thrall, and RJ Bull. 1998. "Factors that affect H-ras mutation frequency and spectra of chemically-induced liver tumors in B6C3F1 mice." *Toxicol. Appl. Pharmacol*, in preparation.

Stauber AJ, RJ Bull, and BD Thrall. 1998. "Dichloroacetate and trichloroacetate promote clonal expansion of anchorage-independent hepatocytes, in vivo and in vitro." *Toxicol. Appl. Pharmacol*, in press.

Presentations

Gonzalez-Leon A, JL Merdink, IR Schultz, and RJ Bull. 1998. "Dichloroacetate auto-inhibits its degradation in the cytosol." Society of Toxicology, 37th Annual Meeting #426.

Kato-Weinstein J, BD Thrall, and RJ Bull. 1998. "The effect of haloacetates on carbohydrate metabolism in B6C3F1 mice." Society of Toxicology, 37th Annual Meeting #308.

Lingohr MK, BD Thrall, and RJ Bull. 1998. "Dichloroacetate (DCA) affects proteins involved in insulin signaling in mouse liver cells." Society of Toxicology, 37th Annual Meeting #61.

Merdink JL, IR Schultz, and RJ Bull. 1998. "Formation of dichloroacetic acid in B6C3F1 mice from trichloroethylene or its metabolites." Society of Toxicology, 37th Annual Meeting #1621.

Mounho BJ and BD Thrall. 1998. "Tumor promotion by peroxisome proliferators may involve the activation of mitogenic activated protein kinases (ERK1/ERK2).P Society of Toxicology, 37th Annual Meeting #51.

Orner GA, LC Stillwell, RS Cheng, LB Sasser, RJ Bull, and BD Thrall. 1998. "Effects of trichloroacetate (TCA) and dichloroacetate (DCA) on H-ras in male B6C3F1 mice." Society of Toxicology, 37th Annual Meeting #60.

Schultz IR, A Gonzalez-Leon, JL Merdink, and RJ Bull. 1998. "Comparative toxicokinetics and metabolism of halo-acetic acids in F344 rats." Society of Toxicology, 37th Annual Meeting #1045.

Stauber AJ, RJ Bull, and BD Thrall. 1998. "Dichloroacetate and trichloroacetate promote clonal expansion of anchorage-independent hepatocytes." Society of Toxicology, 37th Annual Meeting #62.

PNNL-11899
UC-400
UC-721

Distribution

No. of Copies

OFFSITE

John Ahearne
Sigma Xi
99 Alexander Drive
Research Triangle Park, NC 27709

Professor Mansoor Alam
Department of Materials
New Mexico Tech
Socorro, NM 87801

G. Ballew
Pacific Rim Enterprise Center
660 George Washington Way, Suite B
Richland, WA 99352

J.R. Beall
Office of Energy Research
U.S. Department of Energy
19901 Germantown Road (ER-72)
Germantown, MD 20874-1290

Richard Begley
101 Red Oak Lane
Aiken, SC 29803

Jimmy Bell
Bell Consultants, Inc.
137 Bowsprit Lane
Kingston, TN 37763

Professor John D. Berg
Department of Chemical Engineering (BF-10)
University of Washington
Seattle, WA 98195

No. of Copies

Edgar Berkey
Concurrent Technologies Corporation
320 William Pitt Way
Pittsburgh, PA 15238

Paul Bertsch
University of Georgia
Savannah River Ecology Laboratory
P.O. Drawer E/Bldg 737 A
Aiken, SC 29801

Robert C. Birtcher
Argonne National Laboratory
Building 212
9700 South Cass Avenue
Argonne, IL 60439

David R. Boone
Department of Environmental Science and Engineering
Oregon Graduate Institute of Science and Technology
2000 Northwest Walker Road
Beaverton, OR 97006

Gerald Boyd
Office of Environmental Management
U.S. Department of Energy
19901 Germantown Road (5B-014)
Germantown, MD 20874-1290

Michelle Broido
U.S. Department of Energy
19901 Germantown Road, MSIN F-240
Germantown, MD 20874-1290

No. of
Copies

G. Brown
Stanford University
Department of Geological and
Environmental Sciences
Stanford, CA 94305-2115

Barry Burks
Oak Ridge National Laboratory
P.O. Box 2008, Bldg. 7601, MSIN-6304
Oak Ridge, TN 37831-6304

B. Calloway
Westinghouse Savannah River Company
Savannah River Technology Center
Building 773-A/Rm A-229
Mail Stop 28
Aiken, SC 29802

John Carberry
Dupont
Experimental Station
Building 249/119
P.O. Box 80249
Wilmington, DE 19880-0249

P.M. Castle
Lockheed Martin Idaho Technologies
Company
P.O. Box 1625, MSIN 5205
Idaho Falls, ID 83415

Gregory Choppin
Florida State University
Department of Chemistry (B-164)
600 W College Ave.
Tallahassee, FL 32606-3006

Paul Clayton
Vice President for Academic Affairs
and Provost
Oregon Graduate Institute
P.O. Box 91000
Portland, OR 97291-1000

Jim Cochran
Washington State Univ. at Tri-Cities
100 Sprout Road
Richland, WA 99352-1643

Roger G. Collis
Environmental Technology Partnership
Department of Community, Trade, and
Economic Development
State of Washington
2001 Sixth Avenue, Suite 2700
Seattle, WA 98121

L. Coleman
Washington State Department of Ecology
1315 W. 4th
Kennewick, WA 99336

Julie Conner
U.S. Department of Energy
Idaho Operations Office
785 DOE Place
Idaho Falls, ID 83402

Allen Croff
Martin Marietta Energy Systems, Inc.
Oak Ridge National Laboratory
P.O. Box 2008
Oak Ridge, TN 37831-6178

Rico Cruz
Nez Perce Indian Nation
P.O. Box 365
Main Street and Beaver Grade
Lapwai, ID 83450

John H. Cushman
Department of Mathematics and
Department of Agronomy
Purdue University
West Lafayette, IN 47907

No. of
Copies

P.M. Davidson
Office of Energy Research
U.S. Department of Energy
19901 Germantown Road (ER-15)
Germantown, MD 20874-1290

Professor Morton M. Denn
Lawrence Berkeley National Laboratory
Chemical Engineering Department
University of California
Berkeley, CA 94720-1462

S.L. Domoter
Office of Environmental Management
U.S. Department of Energy
19901 Germantown Road (EH-412)
Germantown, MD 20874-1290

Gary Eller
Los Alamos National Laboratory
NMT-6 Advanced Technology Group
MSIN E5-10
Nuclear Material Technology Division
Los Alamos, NM 87544

Tom Engel
Hanford Advisory Board
University of Washington
Department of Chemistry
Bagley Hall Room 109
Seattle, WA 98195-1700

Robert Erdmann
P.O. Box 922
Grass Valley, CA 95945

H.H. Farrell
Office of Energy Research
U.S. Department of Energy
19901 Germantown Road
Germantown, MD 20874-1290

No. of
Copies

Dennis Faulk
U.S. Environmental Protection Agency
MAF Plaza
712 Swift, Suite 5 (B5-01)
Richland, WA 99352

M.M. Fletcher
Belle W. Baruch Institute for Marine
Biology and Coastal Research
University of South Carolina
Columbia, SC 29208

David Geiser
U.S. Department of Energy EM-52.1
19901 Germantown Road
1183/Cloverleaf Bldg.
Germantown, MD 20874-1290

Joe Gentilucci
JAG Technical Services, Inc.
127 Savannah Drive
Aiken, SC 29803

Kurt D. Gerdes
Office of Science & Technology
U.S. Department of Energy (EM-541)
19901 Germantown Road
1186 Cloverleaf Bldg.
Germantown, MD 20874-1290

P.W. Gibbons
P.O. Box 1970, MSIN H5-61
Richland, WA 99352-1300

Mark Gilbertson
U.S. Department of Energy (EM-52)
19901 Germantown Road
5A-031/FORS
Germantown, MD 20874-1290

No. of
Copies

T.R. Ginn
172 Everson Hall
Department of Civil and Environmental Engineering
University of California, Davis
Davis, CA 95616-5294

Dib Goswami
Washington State Department of Ecology
1315 W. 4th
Kennewick, WA 99336

D.J. Grimes
Office of Energy Research
U.S. Department of Energy
19901 Germantown Road
Germantown, MD 20874-1290

Barbra Harper
Yakama Indian Nation
1933 Jadwin, Suite 110
Richland, WA 99352

Stuart Harris
Confederated Tribes of the Umatilla Indian Reservation
Old Mission Hwy 30
Pendleton, OR 97801

Paul Hart
Morgantown Energy Technology Center
3610 Collins Ferry Road
Morgantown, WV 26507-0880

Peter E. Haustein
Brookhaven National Laboratory
P.O. Box 5000
Upton, NY 11973

Thomas Hirons
Los Alamos National Laboratory
P.O. Box 1663, MSIN J591
Los Alamos, NM 87545

No. of
Copies

Roland Hirsch
U.S. Department of Energy
Medical Applications and Biophysical Research Division
19001 Germantown Road (ER-73)
Germantown, MD 20874-1290

Earl Holtzscheiter
Westinghouse Savannah River Company
Savannah River Technology Center
Building 773-A/Rm A-229
Mail Stop 28
Aiken, SC 29802

Ken Hubbard
Assistant to Associate Provost for Research and Economic Development
Dean of Graduate School
University of Montana
University Hall 118
Missoula, MT 59812-1329

Tom Isaacs
Lawrence Livermore National Laboratory
P.O. Box 808, MS/L-19
Livermore, CA 94551

Professor Art Janata
School of Chemistry and Biochemistry
Georgia Institute of Technology
Atlanta, GA 30332-0400

Moses Jaraysi
Washington State Department of Ecology
1315 W. 4th
Kennewick, WA 99336

Arvid Jensen
Lockheed Martin Idaho Technologies Company
P.O. Box 1625
Idaho Falls, ID 83415-3204

No. of Copies

Dawn Kaback
Colorado Center for Environmental Management
999 18th St, Ste 2750
Denver, CO 80202

Michael Knotek
U.S. Department of Energy
Office of the Undersecretary
19001 Germantown Road
7E-079/FORS
Germantown, MD 20874-1290

Roy Koch
Vice Provost for Research
Dean of Graduate Studies
Portland State University
P.O. Box 751
Portland, OR 97207-0751

Bruce Kowalski
Chemistry Department (BG-10)
University of Washington
Seattle, WA 98195

Jerome J. Kukor
Biotechnology Center, Foran Hall
Cook College Campus, Rutgers University
The State University of New Jersey
59 Dudley Road
New Brunswick, NJ 08901-8520

Alvin Kwiram
Vice Provost for Research
University of Washington
312 Gerberding Hall
Box 351237
Seattle, WA 98195-1237

Jim Lee
Sandia National Laboratories
P.O. Box 5800, MSIN 0734
Albuquerque, NM 87185-5800

No. of Copies

Brenda Lewis
Westinghouse Savannah River Company
P.O. Box 616
Aiken, SC 29802

Paul Lurk
U.S. Department of Energy (EM-542)
19901 Germantown Road
1168/Cloverleaf Bldg.
Germantown, MD 20874-1290

Theodore E. Madey
Rutgers University
P.O. Box 849
Piscataway, NJ 08855-0849

R.S. Marianelli
Office of Energy Research
U.S. Department of Energy
19901 Germantown Road (ER-14)
Germantown, MD 20874-1290

J.A. Martin
Sandia National Laboratories
P.O. Box 5800
Albuquerque, NM 87185-0709

M.R. Martin
Lockheed Martin Idaho Technologies Company
P.O. Box 1625, MSIN 2424
Idaho Falls, ID 83415

Todd Martin
Hanford Advisory Board
West 1408 Broadway
Spokane, WA 99201

R.N. Massey
Office of Environmental Management
U.S. Department of Energy
19901 Germantown Road (EM-64)
Germantown, MD 20874-1290

No. of Copies

L.W. McClure
Lockheed Martin Idaho Technologies Company
P.O. Box 1625, MSIN 3710
Idaho Falls, ID 83415

Linda McCoy
U.S. Department of Energy
Idaho Operations Office
785 DOE Place
Idaho Falls, ID 83402

C. Phil McGinnis
Martin Marietta Energy Systems, Inc.
Oak Ridge National Laboratory
P.O. Box 2008
Oak Ridge, TN 37821-6273

M.E. McIlwain
Lockheed Martin Idaho Technologies Company
P.O. Box 1625, MSIN 2210
Idaho Falls, ID 83415

D. Meisel
Argonne National Laboratory
9700 South Cass Avenue
Argonne, IL 60439

W.D. St. Michel
Lockheed Martin Idaho Technologies Company
P.O. Box 1625, MSIN 1061
Idaho Falls, ID 83415

D.L. Miller
Lockheed Martin Idaho Technologies Company
P.O. Box 1625, MSIN 2208
Idaho Falls, ID 83415

No. of Copies

W.S. Millman
Office of Energy Research
U.S. Department of Energy
19901 Germantown Road (ER-14)
Germantown, MD 20874-1290

Jerry Morin
Westinghouse Savannah River Company
Savannah River Technology Center
P.O. Box 616
Aiken, SC 29802

Professor Susan J. Muller
Chemical Engineering Department
University of California
Berkeley, CA 94720-1462

Michael Nastasi
Los Alamos National Laboratory
P.O. Box 1663, Mail Stop K7-65
Los Alamos, NM 87545

Alexandra Navrotsky
Department of Chemical Engineering and Material Science
University of California-Davis
Davis, CA 95616

Tina Nenoff
Sandia National Laboratories
P.O. Box 5800
Albuquerque, NM 87185-0709

Professor Ronald Olsen
Department of Microbiology and Immunology
5605 Medical Science Building II
University of Michigan Medical School
Ann Arbor, MI 48109-0620

No. of Copies

J.M. Owendoff
Office of Environmental Management
U.S. Department of Energy
19901 Germantown Road (5A-014)
Germantown, MD 20874-1290

Robert T. Paine
Department of Chemistry
University of New Mexico
Albuquerque, NM 87131

Frank Parker
Vanderbilt University
400 24th Avenue South
New Engineering Building, Room 108C
Nashville, TN 37235

A.A. Patrinos
Office of Energy Research
U.S. Department of Energy
19901 Germantown Road (ER-70)
Germantown, MD 20874-1290

David Pepson
U.S. Department of Energy (EM-38)
19901 Germantown Road
472/TREV
Germantown, MD 20874-1290

Michael R. Pfister
U.S. Department of Energy, EM-1
Environmental Management Advisory Board
1000 Independence Ave., SW, Rm. 5B-171
Washington, DC 20585

Ken Picha
U.S. Department of Energy (EM-32)
Office of Eastern Operations
19901 Germantown Road 343/TREV
Germantown, MD 20874-1290

No. of Copies

Kevin Price
DOE-ID/OPE
850 Energy Drive
Idaho Falls, ID 83402

Bill Prindle
1556 Crestline Drive
Santa Barbara, CA 93105

Professor Kenneth N. Raymond
Department of Chemistry
University of California at Berkeley
Berkeley, CA 94720

Les Shephard
Sandia National Laboratories
P.O. Box 5800
Albuquerque, NM 87185-0726

Doug Riggs
Legislative Director
Office of Congressman Doc Hastings, 4th District, Washington
1323 Longworth Building
Washington, DC 20515

Professor William R. Rossen
Petroleum and Geosystems Engineering Department
The University of Texas at Austin
Austin, TX 78712-1061

Professor D. Max Roundhill
Department of Chemistry
Texas Tech University
Lubbock, TX 79409-1061

Richard Scanlan
Dean of Research
Oregon State University
Administration Services Bldg A312
Corvallis, OR 97331

No. of
Copies

Wally Schulz
5314 Arbustos Court, NE
Albuquerque, NM 87111

D.R. Sherwood
U.S. Environmental Protection Agency
MAF Plaza
712 Swift, Suite 5 (B5-01)
Richland, WA 99352

Jean'ne Shreeve
Vice President for Research and
Graduate Studies
Professor of Chemistry
University of Idaho
Moscow, ID 83843-4199

Leon T. Silver
Div. of Geological and Planetary Sciences
California Institute of Technology, 170-25
1200 East California Street
Pasadena, CA 91125

Robert Smith
Vice Provost for Research
Dean of Graduate School
Washington State University
Pullman, WA 99164-1030

R.N. Snelling
Lockheed Martin Idaho Technologies
Company
P.O. Box 1625, MSIN 2213
Idaho Falls, ID 83415

Stan Sobczyk
Nez Perce Indian Nation
P.O. Box 365
Main Street and Beaver Grade
Lapwai, ID 83450

No. of
Copies

Peter Spencer, Director
Center for Research on Occupational and
Environmental Toxicology L606
Oregon Health Sciences University
3181 SW Sam Jackson Park Road
Portland, OR 97202-3098

Alex Stone
Washington State Department of Ecology
1315 W. 4th
Kennewick, WA 99336

Harold Sullivan
Los Alamos National Laboratory
P.O. Box 1663
Los Alamos, NM 87545

John Swanson
1318 Cottonwood
Richland, WA 99352

Robert Swenson
Vice President for Research
Montana State University
Montana Hall 207
Bozeman, MT 59717

Larry Tavlarides
Syracuse University
334 Hinds Hall
Syracuse, NY 13244

Tom Thomas
Lockheed Martin Idaho Technologies
Company
P.O. Box 1625, MSIN 3458
Idaho Falls, ID 83415-3423

Major Thompson
Westinghouse Savannah River Company
Building 773-A, C140
P.O. Box 616
Aiken, SC 29802

No. of
Copies

Steadman Upham
Vice Provost for Research and
Graduate Education
Dean of Graduate School
University of Oregon
112 Johnson Hall
Eugene, OR 97403-1226

Nancy Uziemblo
Washington State Department of Ecology
1315 W. 4th
Kennewick, WA 99336

George Vandegrift
Argonne National Laboratory
Building 205
9700 South Cass Avenue
Argonne, IL 60439

Paul Wang
Special Technologist Laboratory
5520 Ekwill St., Suite B
Santa Barbara, CA 93111-2335

Jack Watson
Oak Ridge National Laboratory
P.O. Box 2008
Bldg 4500N, MS-6178
Oak Ridge, TN 37831-6178

Tom Weber
6622 West Victoria
Kennewick, WA 99336

JR Wilkinson
Confederated Tribes of the
Umatilla Indian Reservation
Old Mission Hwy 30
Pendleton, OR 97801

No. of
Copies

Tom Winston
Ohio Environmental Protection Agency
401 East 5th Street
Dayton, OH 45402

Tom Woods
Yakama Indian Nation
1933 Jadwin, Suite 110
Richland, WA 99352

Jim Wright
U.S. Department of Energy
Savannah River Operations Office
P.O. Box A
Aiken, SC 29802

Lin Yarborough
U.S. Department of Energy
Albuquerque Operations Office
P.O. Box 5400
Albuquerque, NM 87185-5400

ONSITE

4 **Bechtel Hanford, Inc.**

Steven C. Foelber	H0-09
Kim Koegler	H0-05
Stephen K. Pulsford	X3-41
Jerry D. White	H0-05

3 **Duke Engineering and Services**

Roger E. Bauer	S7-14
Robert J. Cash	S7-14
Jerry D. Johnson	S7-14

4 **Fluor Daniel Hanford**

Tom L. Anderson	K9-46
Mike Yates	H5-20
Greg Berlin	K9-46
Wayne Green	K9-46

No. of Copies

4 **Lockheed Martin Hanford Corporation**

John N. Appel	H6-37
W. Blaine Barton	R2-12
Ken A. Gasper	H6-37
Jim O. Honeyman	G3-21

23 **U.S. Department of Energy Richland Operations Office**

Jay Austenborg	S7-41
Linda K. Bauer	H0-12
Dennis A. Brown	K8-50
Jeff A. Frey	K8-50
Marcus J. Glasper	K8-50
Charles A. Hansen	S7-41
James P. Hanson	K8-50
Maureen A. Hunemuller	S7-50
Jackson E. Kinzer	S7-50
Pete M. Knollmeyer	A5-11
Cathie S. Louie	B4-55
Lance S. Mamiya	K8-50
Billie M. Mauss	K8-50
John L. Murphy	H0-12
John P. Neath	K8-50
Lloyd L. Piper	A7-50
Robert M. Rosselli	K8-50
Shannon W. Saget	K8-50
Fred R. Serier	H0-12
K. Mike Thompson	H0-12
Deborah E. Trader	K8-50
Joseph J. Waring	S7-55
Don D. Wodrich	S7-50

189 **Pacific Northwest National Laboratory**

Richard C. Adams	K1-43
Robert W. Allen	K9-69
Jack Bagley	K1-74
Sharon A. Bailey	K5-08
Eddie G. Baker	P8-38
Mari Lou Balmer	K8-93
William R. Barchet	K9-30
William F. Bonner	K9-14
Donald M. Boyd	K5-02
Joseph W. Brothers	K9-20
Tom M. Brouns	K9-91
Merwin L. Brown	K5-02
James L. Buelt	P7-41
Richard J. Bull	P7-56
Bruce C. Bunker	K8-93
Don M. Camaioni	K2-44
James A. Campbell	P8-08
Scott A. Chambers	K8-93
Steven D. Colson	K2-14
Louis R. Corrales	K1-96
James P. Cowin	K8-88
Joseph L. Devary	K6-96
John L. Daschbach	K8-93
David A. Dixon	K1-83
Terrence J. Doherty	K6-49
Dennis D. Doneen	K6-48
Thomas H. Dunning	K2-20
Richard M. Ecker	K6-91
Robert E. Einziger	K2-45
Paul D. Ellis	K8-98
Gregory J. Exarhos	K2-44
Linda L. Fassbender	K8-11
Andrew R. Felmy	K8-96
Xiangdong Feng	P8-37
Mark D. Freshley	K9-36
Donald M. Friedrich	K8-96
Teresa A. Fryberger (5)	K2-20
James L. Fuller	K6-48
Bobi A. Garrett	K8-09
Suzanne M.K. Garrett	K8-18
Phillip A. Gauglitz	K6-28
Roy E. Gephart (5)	K9-76
Bob L. Gruel	K8-60
Mark S. Hanson	K9-02
Paul D. Hart	K9-25
John S. Hartman	K5-25
Benjamin P. Hay	K9-77
Scott W. Heaberlin	K8-31
Michael A. Henderson	K8-93
Langdon K. Holton	K6-51
Landis D. Kannberg	K5-20
Paul K. Kearns	K6-51

No. of Copies		No. of Copies	
Karen Knutsen	K2-14	Brian M. Rapko	P7-25
David W. Koppenaal	P7-07	Shirley A. Rawson	K2-20
W.L. (Bill) Kuhn	K2-21	L. Rene	K1-96
John P. LaFemina	K9-91	Bernard F. Saffell, Jr.	K5-22
Carlton D. Lee	K7-22	Jeffrey D. Saffer	P7-58
Janice R. Lewis	K1-51	R. Jefferey Serne	K6-81
Philip E. Long	K6-91	Steve N. Schlahta	K9-69
Greg J. Lumetta	P7-25	Paul A. Scott	K9-46
William J. Madia	K1-46	L John Sealock	K2-10
Judith A. Mahaffey	K8-38	Alireza Shekarriz	K7-15
Steven C. Marschman	P7-27	Billy D. Shipp	K9-01
Wayne J. Martin	K9-14	Steve C. Slate	K9-14
Louis Martucci	K7-10	Gary L. Smith	P7-41
B. Peter McGrail	K6-81	Kelvin L. Soldat	K3-53
Gary W. McNair	P7-75	Steven L. Stein	BSRC/S171
Gary L. McVay	K2-50	Terri L. Stewart	K9-91
Barry J. Merrill	K6-49	Gerry M. Stokes	K9-95
Ellyn M. Murphy	K3-61	B. Ray Stults	K9-76
Jon L. Olson	BSRC/S128	Yali Su	K8-93
Norman J. Olson	K9-46	Guillermo Terrones	K7-15
Thomas M. Orlando	K8-88	Jim J. Thomas	K7-10
Thomas L. Page	K9-18	Brian D. Thrall	P7-56
Terri Paluszkiewicz Sequim/MS	L5-304	Jud W. Virden	K2-44
Charles H.F. Peden	K8-93	Terry L. Walton	K1-46
Larry R. Pederson	K2-44	William J. Weber	K2-44
Loni M. Peurrung (30)	K6-28	Walter C. Weimer	P7-27
Linda R. Pond	K8-23	Raymond E. Wildung	P7-54
Brent A. Pulsipher	K5-12	Yong Wang	K8-93
Marilyn J. Quadrel	K9-70	Kwong K. Wong	P7-56
Rod K. Quinn (20)	K9-69	John M. Zachara	K8-96
Linfeng Rao	P7-50	TFA Library (2)	K9-69
		Information Release (7)	K1-06